Experimental and *Ab Initio* Investigations into the Fundamentals of Corrosion, in the Context of Supercritical Water Oxidation Systems

by

Jason Alexander Cline

Submitted to the Department of Chemical Engineering
in partial fulfillment of the requirements for the degree of

Doctor of Philosophy

at the

MASSACHUSETTS INSTITUTE OF TECHNOLOGY

February 2000

Author .....
Department of Chemical Engineering
December 16, 1999

Certified by .....
Jefferson W. Tester
H. P. Meissner Professor of Chemical Engineering
Thesis Supervisor

Certified by .....
Ronald M. Latanision
Professor of Materials Science and Engineering
Thesis Supervisor

Accepted by .....
Robert Cohen
St. Laurent Professor of Chemical Engineering
Chairman, Committee on Graduate Students

Experimental and *Ab Initio* Investigations into the Fundamentals of Corrosion, in the context of Supercritical Water Oxidation Systems

by

Jason Alexander Cline

Submitted to the Department of Chemical Engineering
on February 9, 2000, in partial fulfillment of the
requirements for the degree of
Doctor of Philosophy

Abstract

Supercritical water oxidation (SCWO) is a process which runs at 250 bar and 400-600° C to effect rapid and complete destruction of aqueous organics. The SCWO process streams are very corrosive and pose a materials performance challenge to even noble metals and the most advanced alloys.

Corrosion in chlorinated, acidic streams at transitional temperatures (100–400° C) in a Hastelloy C-276 tube is examined through post-failure analysis and controlled exposure experiments. Dealloying and intergranular corrosion were observed. Dealloying rate was found to be strongly correllated with temperature and dielectric constant. Intergranular corrosion behavior was found to be affected by the alloy hardness.

In order to understand the fundamental chemistry of localized chloride-assisted corrosion initiation, a density-functional calculation of Cr_2O_3 was performed and validated against experimental data. The (0001) surface of α-Cr_2O_3 was computed and found to experience strong relaxations in the terminal oxygens. The surface was found to be susceptible to attack by electron-rich species; this might be defeated by p-doping the oxide. Further, the chemically relevant states at the surface assumed a ferromagnetic order. Effects of a variable dielectric medium upon the chemistry of the surface were assessed for the bare surface and adsorption of H and Cl.

Thesis Supervisor: Jefferson W. Tester
Title: H. P. Meissner Professor of Chemical Engineering

Thesis Supervisor: Ronald M. Latanision
Title: Professor of Materials Science and Engineering

DEDICATION

For my friends and family whose shining lights have joined the stars:

Vikki Caterina
Clyde Chynoweth
Kenneth Hogg, Jr.

Amos S. Cline
Mary H. Crain
Russell Lyden, Sr.
Alfreda Lyden

Acknowledgments

First, many thanks to my wife, LISA, who was very understanding about my sometimes-hyperextended work hours, weekend meetings, and late nights spent hacking codes on our Linux box or running into the laboratory to monitor an experiment.

Secondly, I thank my father, JESSE CLINE and my mother, BARBARA CLINE, for feeding and clothing me as a child, nurturing my physical and academic growth. Thanks also for putting me through undergrad.

I am also grateful for the financial support of the U. S. Army Research Office through ROBERT W. SHAW under the University Research Initiative (URI) grant DAAL03-92-G-0177 and AASERT award DAAH04-95-1-0302 (projects 30345-CH-URI and 34173-CH-AAS, respectively).

I thank my former karate instructors at the NI BU KAN dojo of the Okinawan Gojukan Karatedo system (Vineland, New Jersey). JAMES LORETTA Shihan and CHARLES FERILLO Sensei (who by now have ascended far beyond the titles I have listed for them) taught me and many others to have patience, discipline, and spirit. I still work hard to find the true way in my training.

I thank JOHN RIECK, formerly of Vineland High School, for teaching AP Chemistry, and for really showing me what chemistry is all about.

Thanks also to the Tester research group, including PHIL MARRONE, JOANNA DINARO BLANCHARD, MARC HODES, FREDERIC VOGEL, RANDY WEINSTEIN, MATT DIPIPPO, MIKE KUTNEY, BRIAN PHENIX, MATT REAGAN, and JOSH TAYLOR, for their advice, assistance, and comraderie. Never before have I ridden 100 miles on a bike in a single day, nor skiied so fast as I had with this group. Thanks to fellow New Jerseyan MARC HODES for inviting me to those esoteric lectures. I particularly want to thank JOANNA DINARO BLANCHARD for organizing numerous group outings, and for contributing more than just her share of heart to this group. Finally, thanks especially to JEFF TESTER, who was a tremendously supportive advisor and leader (in spite of his hectic schedule) and was always there for us and the group. I could write pages on each of these people but I would never finish in time to defend!

I thank SAMMY THE FISH for being a good fish to Lisa and me while I was writing my thesis. He's a silly fish. He's a good fish.

From the Corrosion Laboratory, I'd like first to thank my immediate lab-mates GARY LEISK and SUZANNE WALLACE for numerous discussions on *all* kinds of topics, and for not immediately dismissing me as insane. I thank D. BRYCE MITTON for many things: teaching me metallography, numerous technical discussions, his post-

failure analysis of the SCWO preheaters, and for just being a good guy to talk to. Thanks also to GEETHA BERERA who instituted the Friday Lunch Meetings. Best of luck to newer lab-mates NICOLAS CANTINI, who just graduated and returned to Bordeaux, and NOAM ELIAZ who will be continuing on in the lab. Also good luck to TAREQ AL-NUAIM who will become the last remaining grad student in the Corrosion Laboratory group for a little while. Thanks also to visiting scientist JAE-HONG YOON of Changwon University in Korea for performing some SEM analysis of samples (Figure 4-20); I wish him well in continuing the SCWO work. Thanks also to SHI-HUA ZHANG, EN-HOU HAN, KATHERINE HAUTANEN, NATALIE CAPUTY and MIKE QUINTANA for their participation in the earlier SCWO work. Thanks also to RON LATANISION, who had the generosity and broad-mindedness to let me divide an essentially experiment-based research project into one which also incorporated a lot of theoretical physics.

I want to thank the people involved in the theoretical side of my research. TOMÁS A. ARIAS, now at Cornell, spent many one-on-one hours teaching me the density functional theory, sometimes at a rate that my chemical-engineering-oriented mind could just barely handle. Thanks also to DIANE RIGOS, a.k.a. ANGELIKI ARTEMIS RIGOS, of Merrimack College, who would trek down to MIT to guide me with her chemical intuition. Thanks to both of you guys for the help and the fun time working on the paper and the supercomputer. Major credit also goes to SOHRAB ISMAIL-BEIGI for writing the new `dft++` code, which I used and modified to suit this project, to DIÇLE YESILLETEN for investigating some low-cutoff chromium pseudopotential options, and to TAIRAN WANG and KENNETH ESLER for making `dft++` MPI-compatible. Also thanks to GABOR CSANYI, TORKEL ENGENESS, and DARREN SEGALL for help with the computers at various times and being otherwise very fun people to talk to.

Thanks also to ANTHONY GARRATT-REED and DAVID BELL of the MIT Center for Materials Science and Engineering shared electron microscopy facility for their expert guidance with the ESEM and EDX.

Thanks to CHRIS N. HILL of EAPS and to the MIT Laboratory for Computer Science for use of the Pleiades and Xolas supercomputer clusters.

Of course one cannot forget the secretaries and administrative assistants extraordinaire who have helped me along the way, including BONNIE CAPUTO of the Energy Lab, CONNIE BEAL and ELEANOR BONSAINT of the Corrosion Lab. Thanks also to GILIAN KILEY of the Energy Lab for making those routine memos just a little bit more entertaining. And I can't forget JANET FISCHER and ELAINE AUFIERO for

guiding me through the Chemical Engineering Department, from the first day to the last, and for cutting me out of the red tape when I got stuck in it.

I'd like to make a special mention of my LaTeX-using comrades, MARC HODES and FREDERIC VOGEL. (Are we the last of the loyalists?) May this free software never perish from the earth.

This document was produced with LaTeX and GNU Emacs on a Pentium II Linux box and also on a DECstation 3100 Model 300X (Alpha AXP) running Digital UNIX 4.0d. Therefore I must thank: LINUS TORVALDS for inventing Linux, DONALD KNUTH and LESLIE LAMPORT for TeX and LaTeX, and RICHARD STALLMAN and other contributors from the Free Software Foundation for GNU Emacs and all of the free software which went into producing this thesis.

Contents

List of Figures

List of Tables

Chapter 1

Introduction—Supercritical Water Oxidation (SCWO) and the Corrosion Challenge

1.1 Background on Supercritical Water Oxidation

Properties of water in the critical region. Pure water has a critical point at 374° C and 221 bar. Near this critical point water has a large heat capacity, typically 2 to 6 times that of liquid water, and its isothermal compressibility is very large ($\approx$ 0.04 bar^{-1}). In this region, the solvation properties of water also change dramatically—correlating directly with density changes that are sensitive to pressure and temperature.[1] For example, at 250 bar, sodium chloride is very soluble (37 wt%) at 25° C, but at 550° C the solubility is only 120 ppm. Water's ability to shield charge diminishes as its dielectric constant decreases from 80 at ambient conditions to approximately 2 at 250 bar and 400° C. Conversely, in the critical region, non-polar compounds and non-condensible gases become soluble. For example, benzene above 300° C and 250 bar is completely miscible in water over all concentrations (Rebert and Kay 1959; Connolly 1966). Gases such as oxygen (Japas and Franck 1985a), nitrogen (Japas and Franck 1985b), carbon dioxide (Mather and Franck 1992), and even methane (Krader and Franck 1987) are also completely soluble in supercritical water. With these solvation characteristics, supercritical water is an excellent medium

[1] Although the supercritical solutions discussed in this thesis are multicomponent systems, frequently with properties that significantly deviate from the pure-water case, the term "critical point" used in this thesis always refers to pure water conditions to provide a constant frame of reference.

to carry out oxidation of organics contained in aqueous waste streams.

Destruction efficiency. Supercritical water oxidation (SCWO) systems provide high destruction efficiencies for organics within short residence times. Typical destruction and removal efficiencies (DRE) can exceed 99.999% for normal operating conditions of 250 bar, 600° C, and residence times of 60 seconds or less. These DRE levels meet requirements for destruction of EPA-controlled substances and DOD chemical weapons stocks. A SCWO system is entirely self-contained, allowing for capture and storage of reaction products for analysis and further treatment, if necessary. Under normal operating conditions, hydrocarbons are converted to carbon dioxide and water. Although carbon dioxide is a greenhouse gas, it can be recovered at pressure and liquefied for reuse or sequestration. Heteroatoms such as phosphorus and sulfur react to form to phosphate and sulfate anions, which, depending on pH control, will remain as their respective acids, or, if neutralized, may precipitate at supercritical conditions as solid salts (such as NaCl and Na_2SO_4 when NaOH is used). Nitrogen heteroatoms are abstracted to form primarily N_2, with trace amounts of N_2O, but not NO_x, which forms under higher temperature conditions (Webley *et al.* 1991; Webley *et al.* 1990; Webley 1990).

1.1.1 Applications of SCWO

Environmental Protection Agency (EPA) regulated wastes. Dilute aqueous wastes containing organic residues can be effectively treated using SCWO to acceptable destruction and removal efficiency (DRE) levels for a wide range of toxic compounds, from low-molecular-weight solvents (such as methanol, methylene chloride, and trichloroethylene), to common aromatics (such as benzene, toluene, and phenol), to high-molecular-weight polycyclic aromatics (such as polychlorinated biphenyls).

NASA human waste treatment. NASA has investigated SCWO for use in remediating biomass and human metabolic waste for long-term space flight. As resources in space are scarce, and payload size and weight is critical, it becomes necessary for spacecraft personnel to quickly and efficiently treat and recycle cellulosic metabolic waste materials which would normally be remediated on a longer time scale by the Earth's ecosystem. SCWO has been shown to be effective in oxidizing cellulosic biomass and urine (Webley *et al.* 1990).

Department of Defense (DOD) chemical demilitarization. The chemical weapons stockpile of the United States has been targeted for destruction. To this end, various technologies for hazardous waste destruction are under evaluation for feasibility, reliability, and cost-effectiveness. Among these are SCWO, incineration, molten metal treatment, electrochemical oxidation, and flash photolysis. The chemical weapons stockpile presents a considerable challenge to SCWO in terms of operational logistics, as the chemical agents are frequently transported in non-toxic form as "hydrolysate," which is a hydrolyzed form of the agent formed by reaction with sodium hydroxide. This detoxification process dramatically increases the pH, which also changes the corrosion regime, and could have a major impact on the treatment process selected. Further such agents as mustard gas[2] and VX[3] contain sulfur, chlorine, and phosphorus heteroatoms, which will produce H_2SO_4, NaCl, and Na_3PO_4 in the product stream.

Department of Energy (DOE) mixed waste remediation. The DOE is considering SCWO as an option for removing the organic components of mixed low-level radioactive wastes (MLLW). As the inorganic components, which harbor the majority of the radioactivity, are sparingly soluble in supercritical water, the SCWO process lends itself naturally to separation of the radioactive inorganic components, while simultaneously mineralizing all organic components to CO_2, H_2O, and N_2 and acid products for any heteroatoms present, for example HCl, H_2SO_4, and H_3PO_4.

Commercial SCWO and Competing Technologies. SCWO has recently gone commercial. In 1994, EcoWaste Technologies (Austin, TX) successfully used SCWO to treat wastewater sludges. General Atomics acquired the MODAR process (Natick, MA) and has demonstrated that it can be used for the destruction of US DOD chemical weapons and solid rocket propellants. Japanese companies have also developed an interest in SCWO: Organo and Hitachi are in the process of developing commercial SCWO processes.

While incineration is the chief competitor to SCWO for concentrated wastes, other waste treatment technologies target the same market. These include catalytic oxidation, molten metal treatment, electrochemical oxidation, flash photolysis, and microbial degradation. SCWO is particularly well-suited to dilute aqueous wastes with

---

[2] 1,1'-thiobis[2-chloroethane].

[3] Methylphosphonothioic acid S-[2-[bis(1-methylethyl)amino]ethyl] O-ethyl ester.

total organic carbon (TOC) contents from 1 to 20 wt%, which are too concentrated for absorptive (activated carbon) remediation and too dilute for effective incineration or molten metal reforming.

1.1.2 Limitations of SCWO

Just as supercritical water oxidation is well-suited to rapid destruction of organic compounds, the thermal environment of sub- and supercritical water is generally too aggressive for most organic synthesis reactions. Notable exceptions are selective hydrolysis reactions, and the Kolbe-Schmitt synthesis of carboxylic acids (Holliday *et al.* 1997; Krammer *et al.* 1999). While the idea of a tunable solvent, in terms of dielectric constant and density is attractive from the point of reaction kinetics optimization for rate and selectivity, the critical temperature for water is 374° C. As many organic compounds oxidize or hydrolyze readily at such temperatures, the scope of organic reactants for which this is a viable synthesis medium is very limited. The high pressures needed also are a drawback in that pumping power requirements and system containment are important concerns for SCWO to meet operability and economic criteria as a waste treatment option.

1.2 Overview

1.2.1 Process Equipment and Flowsheets

A typical SCWO system, as depicted in Figure 1-1, begins with two or three feed streams—an oxidizer stream, an organic stream (the destruction target), and possibly an auxiliary fuel stream. Usually these feed streams are brought up to pressure separately, and preheated separately. Reactant streams proceed to the reactor, which may be either a vessel reactor or continuously fed stirred-tank reactor (CSTR), or a tubular, plug-flow type reactor (PFR).

CSTR. The vessel and continuous stirred-tank reactors have prolate vertical aspect ratios. They employ two major temperature zones which are designed to facilitate solids handling and mitigate corrosion. The top zone is the hot reaction zone, which operates isobarically at supercritical pressures with temperatures ranging from 400–650° C. Most of the oxidation takes place in this top zone, producing mainly CO_2 and H_2O. The large differences in local fluid density (which depend strongly on temperature and concentration) drive the mixing;

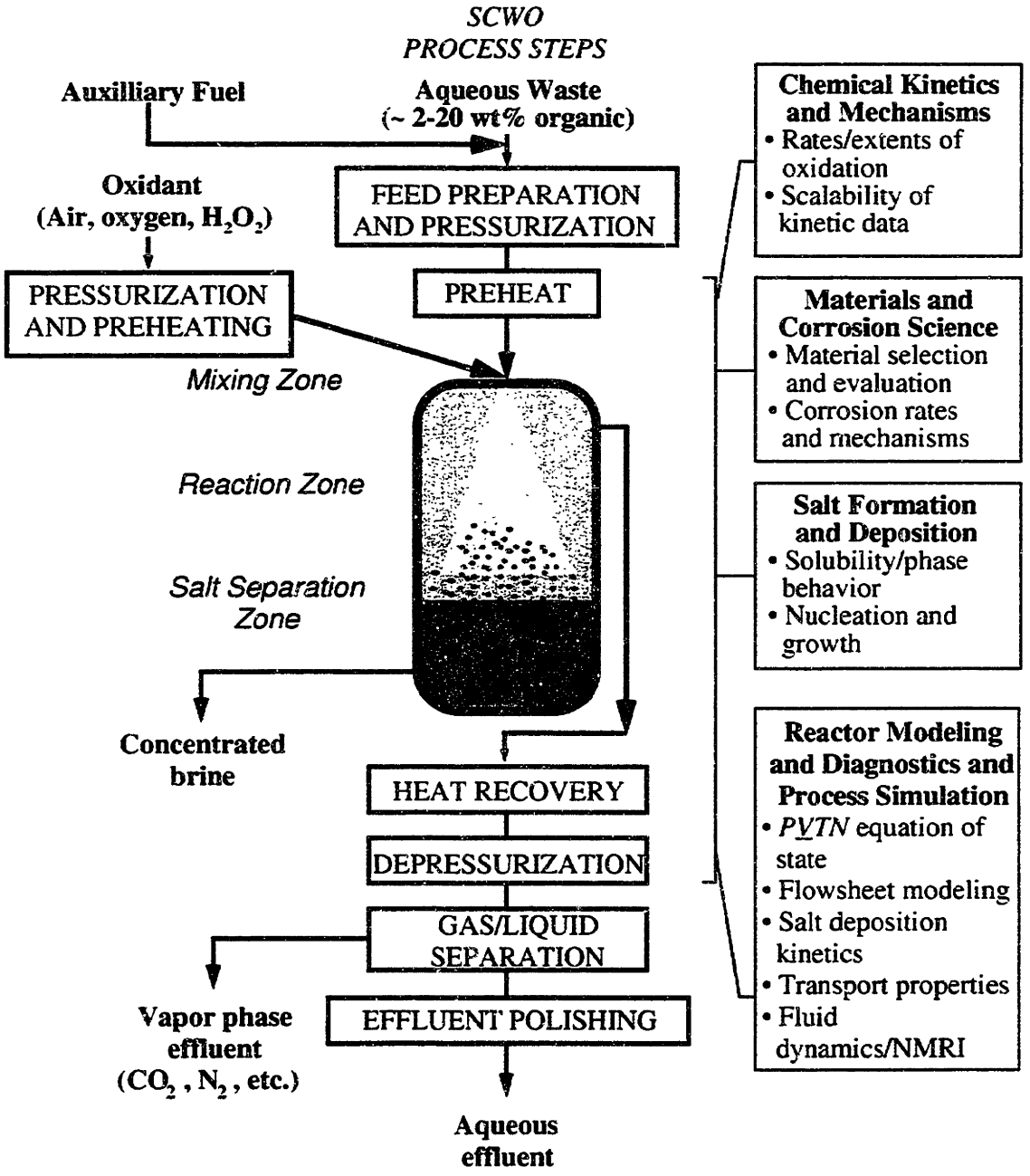

Figure 1-1 General process flowsheet for supercritical water oxidation showing major process steps and relevant areas of research.

the buoyancy forces create substantial convective transport rates. Depending on the pH of the feed streams, heteroatoms such as P and S which oxidize in the hot zone (to PO_4^{3-} and SO_4^{2-}), can either precipitate out as salts, for example, Na_2SO_4, or persist as acids, such as H_2SO_4. Solid precipitates settle into the lower, cooler zone, while lower-density fluid-phase products are carried upwards through an exhaust port. The lower zone is a cool zone in which a dense brine, liquid-like phase, redissolves the salt which precipitated in the upper (hot) reaction zone. The brine phase is normally continuously removed to prevent crystallization of salt on the reactor walls.

PFR. The plug-flow reactor serves the same purpose as the CSTR, but is generally a very long small-diameter tube. Rather than having different temperature zones in the PFR, solids management is controlled by fluid velocity. The linear velocity of the fluid is always kept above that which is required to suspend any resultant crystals in a slurry. In some schemes mechanical action is used to enhance re-entrainment and to remove any sticky salt deposits that may have deposited on surface. In a newer design (LaJeunesse *et al.* 1997; Haroldsen *et al.* 1996), the reactor is fitted with small jets that transpire water through the reactor wall to create a boundary layer of relatively pure water to prevent attack from aggressive species and/or precipitation of sticky salts.

Leaving the reactor, the fluid phase products reject their entrained solids, cool down and de-pressurize. Often heat recuperation or integration is used, where hot product effluent is cooled by incoming reactant streams to preheat the feed to reaction conditions. Such heat integration reduces the required heating value of the target waste fed to be self-sustaining. This autogenic condition corresponds to a state where the net heat of combustion per unit feed produces enough thermal energy to sustain the reaction without additional heating.

In certain applications, the process reactor is placed in a deep well with the reaction zone at the bottom of the well, where supercritical pressures exist due to the hydraulic gradient. This configuration has the advantage that the pumping power requirements are much less than for SCWO plants located on this surface.

Each portion of the flow sheet in Figure 1-1 is connected to one or more areas of research:

Feed preparation and pressurization. While the feed streams may seem inherently simple to handle, it is often necessary to estimate the fuel value of the target waste. Additionally, there is the strategy of pH control, which requires anal-

ysis of the feed for halogens, sulfur, and phosphorus; a corresponding amount of neutralizing agent may be added to the feed to promote effluent neutrality. There are also different methods of obtaining high concentrations of oxygen in the feed—using a pure oxygen feed is one, but another is using hydrogen peroxide, which catalytically decomposes to O_2 and water (Croiset *et al.* 1997).

Heat exchangers. The heat exchangers must endure thermal and mechanical (pressure) load cycling, and are commonly the site of the most aggressive localized corrosion in the system. Current research aims to identify thermodynamic (T, P, x_i) conditions which promote corrosion initiation in the preheater sections under acidic conditions.

Reactor. Upon entering the reactor, the feed streams mix. As mixing time is an important parameter in determining reaction effectiveness, quantitative characterization of mixing rates has been conducted (Phenix *et al.* 1999). In addition, reaction kinetics measurements have also been performed to determine overall "global" reaction rate expressions and to characterize reaction networks to illustrate how more rate-limiting or "refractory" compounds are produced as intermediates from the faster initial oxidation and/or hydrolysis of more labile compounds. The reactor is also an area in which the kinetics of corrosion are very relevant. General corrosion rates in the reactor have been observed at rates up to 750 mpy for Hastelloy C-276 and Inconel 625. Corrosion can also be aggravated by salt precipitation, which as a deposit can promote crevice corrosion, or when entrained can cause erosion-corrosion or flow-assisted-corrosion (FAC).

1.2.2 Critical Engineering Issues Affecting Development

Key engineering issues affecting the commercial development of SCWO technology include salt and solids management, knowledge of reaction rates, and materials performance.

Salt and solids management. Many of the feed stocks for SCWO produce insoluble salts. Corrosion and metal atoms in the feed stream can also produce insoluble oxides. While the oxides can be entrained by control of fluid velocity near process surfaces, the salts are often very sticky, and tend to adhere to reactor walls and block the process streams (Hong *et al.* 1995). Further, these entrained solids can cause erosion of process piping and valves.

Reaction rates. Fluid density and solvent effects such as molecular-scale clustering can play a major role in determining reaction rates. Solution pH, a parameter often used in predicting and controlling corrosion, becomes difficult to measure or even define, as the ionic dissociation constant of water plunges near the critical point of water (Marshall and Franck 1981). Water's dielectric constant, highly tunable in the critical region (Uematsu and Franck 1980), determines the ability of the medium to support polarized transition states, and therefore to support ionic reactions or reactions in which transition states have a large dipole moment. Whereas ionic reactions are supported at 250 bar and T<300° C, at 250 bar and above 450° C free-radical reactions are preferred. With the high water densities at 500 bar it is expected that ionic reactions are again a major reaction pathway for all temperatures.

Materials performance. General corrosion or "wastage" occurs in the main reactor when an aggressive feed stocks (containing S, P, and halogen atoms) are encountered. Corrosion-resistant alloys such as Inconel 625 and Hastelloy C-276 have been observed to corrode at a rate of 740–750 mpy (18.8–19.0 mm/y) (Mitton *et al.* 1995). Worse, however, is the localized corrosion observed in the heat exchangers used for preheating and cooling of process streams. Localized attack, such as stress corrosion cracking (SCC) is difficult to detect because the amount of material lost is small. Stress corrosion cracking accelerates in a preferred direction and is isolated to localized sites, and so can quickly cause through-wall failure.

1.2.3 Fundamental and Applied Research

SCWO technology provides an opportunity for significant process improvement utilizing insights obtained from both fundamental and applied research. Reactor and process design technology of SCWO systems is still hindered by the sparsity of thermodynamic data for hydrothermal aqueous and supercritical solutions of salts and metal oxides and hydroxides. A more fundamental understanding of the fluid mechanics and mass and heat transfer in such systems would aid in development of mixing strategies as well as the resolution of many key solids-deposition and entrainment issues. Mixing effects can be critical for optimal reaction and residence time: vessel reactors rely on convective transport to homogenize the reaction mixture, but required residence times could be reduced if the manner in which the reactants are mixed as they enter the reaction vessel were optimized (*e.g.*, using jet-impingement mixing). A combined knowledge of heat transfer, natural and forced flows, fluid mixing and diffusion rates, and salt solubility/deposition is required to prevent salt

fouling of heat exchange surfaces.

Detailed molecular-level understanding of the reaction kinetics for the limiting reactions for a particular feed stock may lead to the development of reactors whose size and shape are specifically optimized for high conversion with proper solids handling appropriate to its task. Knowledge of the water chemistry produced by this feed stock and its products, in conjunction with an understanding of the thermodynamic stability limits of the reactor material (or its protective surface layer) will allow process designers to select materials based on cost, containment and safety criteria for specific applications. Such kinetic and thermodynamic factors ultimately depend on molecular-level interactions between the solvent and solute. Thus improved understanding of these phenomena will augment the experimental criteria currently used to select equipment and set system design parameters.

1.3 Engineering Issues and Technical Challenges

1.3.1 Water Chemistry

Behavior of K_w and D_s. Self-dissociation behavior (indicated by the magnitude of K_w) and dielectric strength ($D_s \equiv \epsilon/\epsilon_0$) drop off markedly in water at supercritical pressures as temperatures approach and exceeds the critical point. As shown in Figure 1-2 for example, at 250 bar, the dielectric strength of water drops from 80 at 25° C to less than 2 above 450° C. Also at 250 bar, pK_w ranges from 14 at 25° C to approximately 22 at 450° C—an eight order of magnitude change in the molal ion product $K_w = [H^+][OH^-]$ of water.

Aqueous chemistry and electrochemistry in SCW. Molecular simulations of solutions performed by Johnston *et al.*, investigate the pH and dissociation of boric and sulfuric acids at supercritical conditions (Wofford *et al.* 1998; Xiang *et al.* 1996). This work has yet to be experimentally verified. Research continues for development of electrodes for electrochemical parameters in hydrothermal and supercritical water (Lvov and Macdonald 1997; Ding and Seyfried 1996), but the techniques have not been developed to a degree such that they are used widely. Work by Bard and coworkers has overcome numerous technical challenges (*e.g.*, corrosion, electrode design) to explore some high-pressure electrochemistry of hydroquinone and iodide (Liu *et al.* 1997). At temperatures up to 385° C, this work not only produced some measurements for diffusion coefficients in near- and supercritical water, but also provided insight into

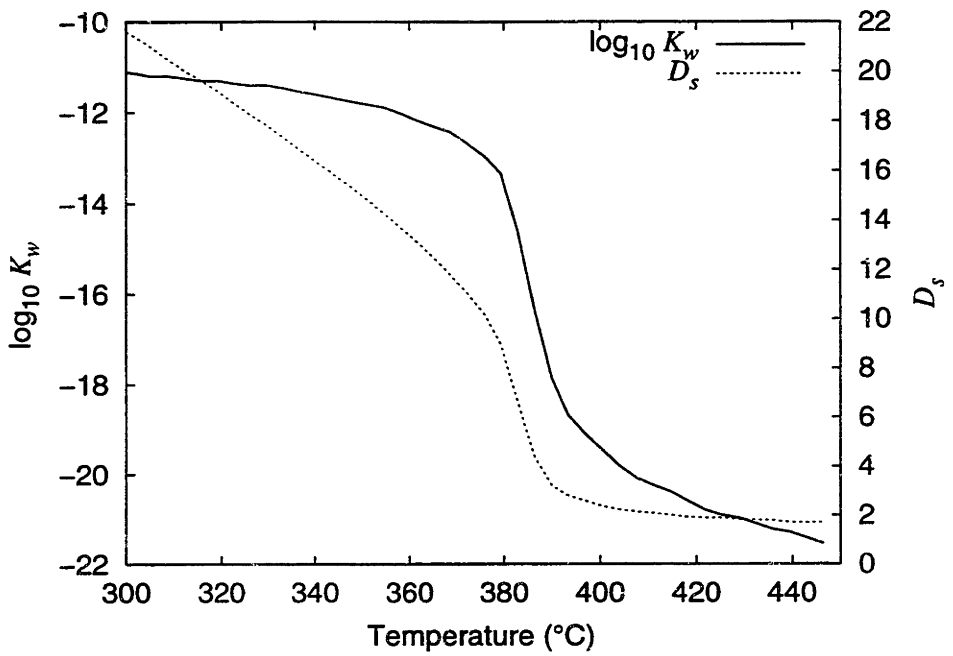

Figure 1-2 Ion product K_w and dielectric constant D_s of pure water at 250 bar. From Uematsu and Franck (1980) using Haar *et al.* (1984).

the redox behavior of iodine and hydroquinone. From the magnitude of their diffusion coefficients, aqueous ions were found to exhibit normal Stokes-Einstein behavior.

Hydrogen bonding. Another aspect of water that is markedly different at hydrothermal and supercritical conditions is hydrogen bonding (Gorbaty and Kalinichev 1995; Mizan *et al.* 1995; Chialvo *et al.* 1996; Chialvo and Cummings 1996; Mizan *et al.* 1996a; Mizan *et al.* 1996b; Bellissent-Funel *et al.* 1997; Ikushima 1997; Kalinichev and Bass 1997; Botti *et al.* 1998; Gorbaty and Gupta 1998; Ikushima *et al.* 1998). Figure 1-3 shows radial distribution functions for a 21 wt% aqueous brine solution for temperatures spanning 177–427° C under 250 bar of pressure. Radial distribution functions (RDF's, expressed mathematically as $g(r)$) express the local density of a "target" species at a certain distance r from the "source" species. Figure 1-3(a) shows the RDF for water and water while Figure 1-3(b) shows the RDF for Na^+ and Cl^- ions, as computed from molecular dynamics (see Reagan *et al.* (1999) for details). Whereas room-temperature water has an RDF with many peaks, the structure of hydrothermal and supercritical water has a less-well-defined structure.

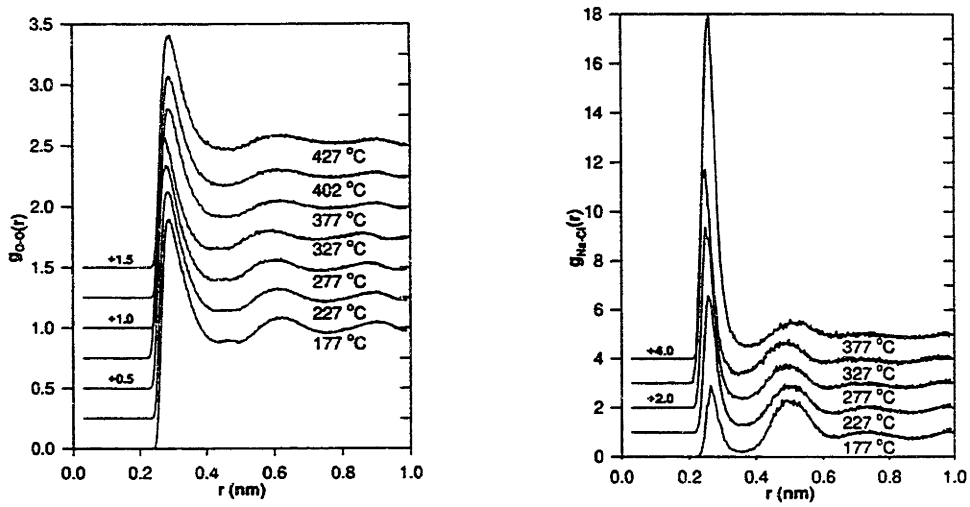

(a) (b)

Figure 1-3 Water-water (a) and Na-Cl (b) radial distribution functions from a molecular dynamics simulation of a 21 wt% NaCl-H_2O solution at 250 bar. Energy for water interactions is computed using the simple point charge (SPC) intermolecular potential model for pure water. Energy for interactions of the solvated ions is handled using a Huggins-Mayer potential plus Coulombic and Lennard-Jones attraction potentials. From Reagan *et al.* (1999).

1.3.2 Solution Thermodynamics

Equations of state. Equations of state which can predict the $PVTx_i$ behavior of SCW solutions are needed to design and simulate process steps in SCWO. A volume-translated, hard spheres, van der Waals equation of state was developed which accurately captures the density behavior of dense liquid and supercritical fluid phases (Kutney *et al.* 1997). Other, more complex equations of state are available, such as the one developed by Anderko and Pitzer (1993) for the NaCl-H_2O system. These equations, which typically require fitting many adjustable parameters, have successfully been used to represent a large amount of data. The SCWO community has also benefitted from the extensive work of geochemists, as much effort has gone into characterizing ionic solutions at hydrothermal conditions (Shock and Helgeson 1988; Tanger and Helgeson 1988). Recent efforts have discovered a marked similarity between the Zeno line observed in high density PVT data with predictions from equations of state and molecular dynamics simulations using an SPC-E water potential. The Zeno line is a locus of points in density-temperature space for which the compressibility factor (Z) of a fluid is again 1.0, similar to the ideal-gas state, except the densities and

temperatures are far from ideal gas conditions. Numerical simulations predict the observed experimental Zeno behavior as closely as, or in some instances, more closely than other equations of state.

Molecular simulations. The simulation of dense NaCl brine solutions at near- and supercritical conditions using Monte Carlo and molecular dynamics techniques has been an active area in one research group at MIT. The major interest lies in exploring whether relatively simple intermolecular potential models for ion-ion and water-ion interactions can predict complex phase equilibria such as mixture critical points, phase transformations, and solid salt formation in supercritical water (Reagan *et al.* 1999). Figure 1-3(b) shows a typical RDF for Na–Cl at 250 bar and 177–377° C, where the growth in the initial peak indicates a strong tendency towards ion pair formation as temperature increases.

1.3.3 Chemical Kinetics

Experimental methods. Several groups perform kinetics experiments on model compounds in isothermal, isobaric plug flow reactors (PFR) (Tester *et al.* 1991; Webley *et al.* 1991; Webley and Tester 1991; Holgate and Tester 1993; Tester *et al.* 1993; Holgate and Tester 1994; Rice *et al.* 1994; Brock and Savage 1995; Brock *et al.* 1996; Hanush *et al.* 1996). The MIT group has extensively used a PFR reactor system shown in Figure 1-4. Two feed streams, an aqueous oxygen stream and an aqueous model-compound-containing stream, flow through separate preheaters into a mixing tee, where the plug flow reactor begins. The preheaters and the tee are made of Hastelloy C-276 and the PFR is made of Inconel 625. The preheaters and the reactor (each coiled) are heated by immersion in a heated fluidized sand bath. After the reactor, flow proceeds to a shell-and-tube cool-down heat exchanger, then to a back-pressure regulator, and finally on to separators and analytical equipment. Kinetics measurements using this apparatus are restricted to conditions in which the reactants are dilute enough that the reacting stream does not deviate measurably from isothermal conditions. Oxygen concentrations are limited either by the amount of hydrogen peroxide added into the feed stream, as the H_2O_2 catalytically decomposes to O_2 and water, or in other configurations that use a O_2 saturator, with concentrations set by the Henry's Law equilibrium of O_2 at various pressures over water at room temperature (Webley and Tester 1991).

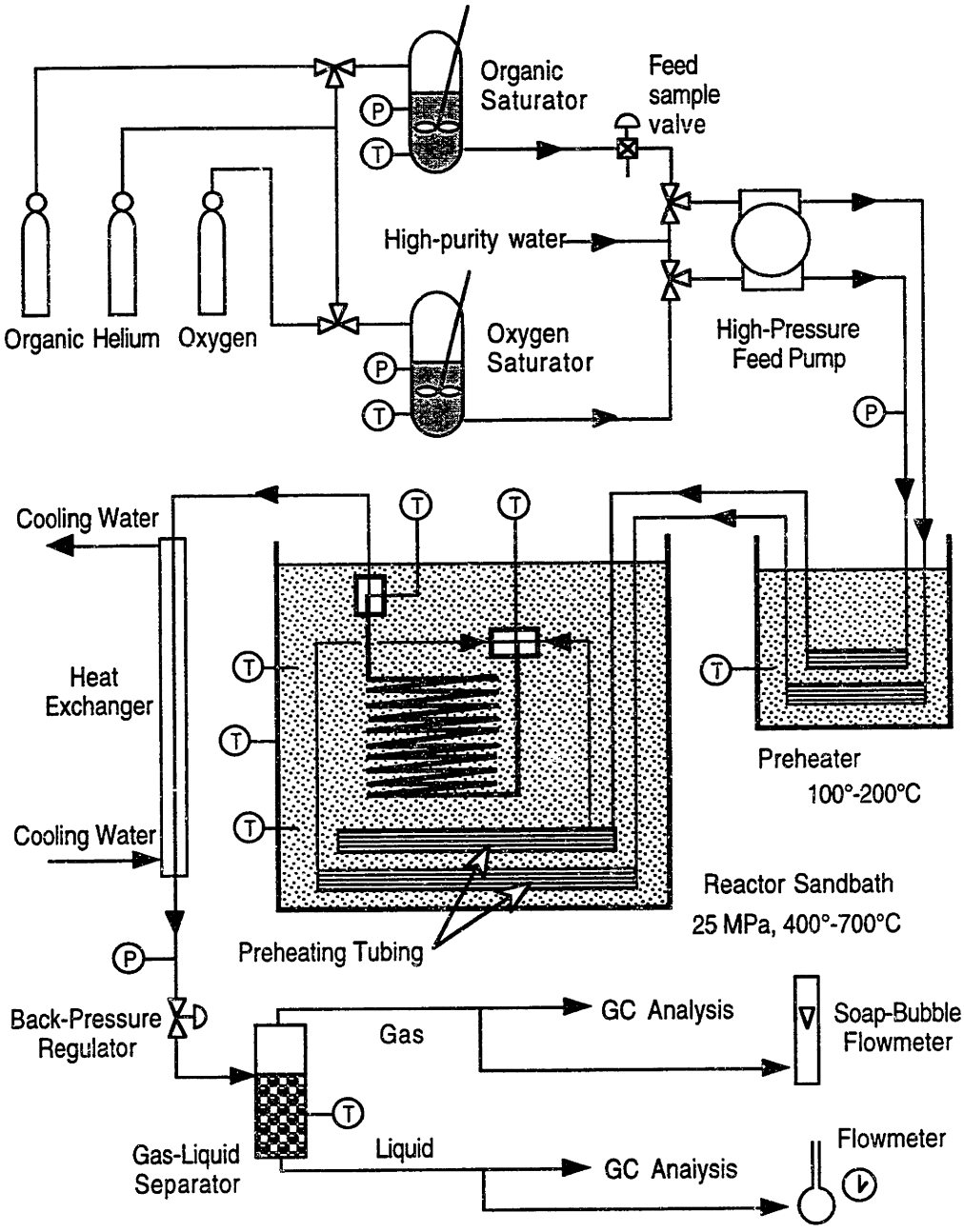

Figure 1-4 Bench-scale apparatus for kinetic studies of hydrolysis and oxidation in a tubular PFR reactor system (Holgate and Tester 1993; Webley 1990; Phenix 1998; Marrone 1998; DiNaro 1999).

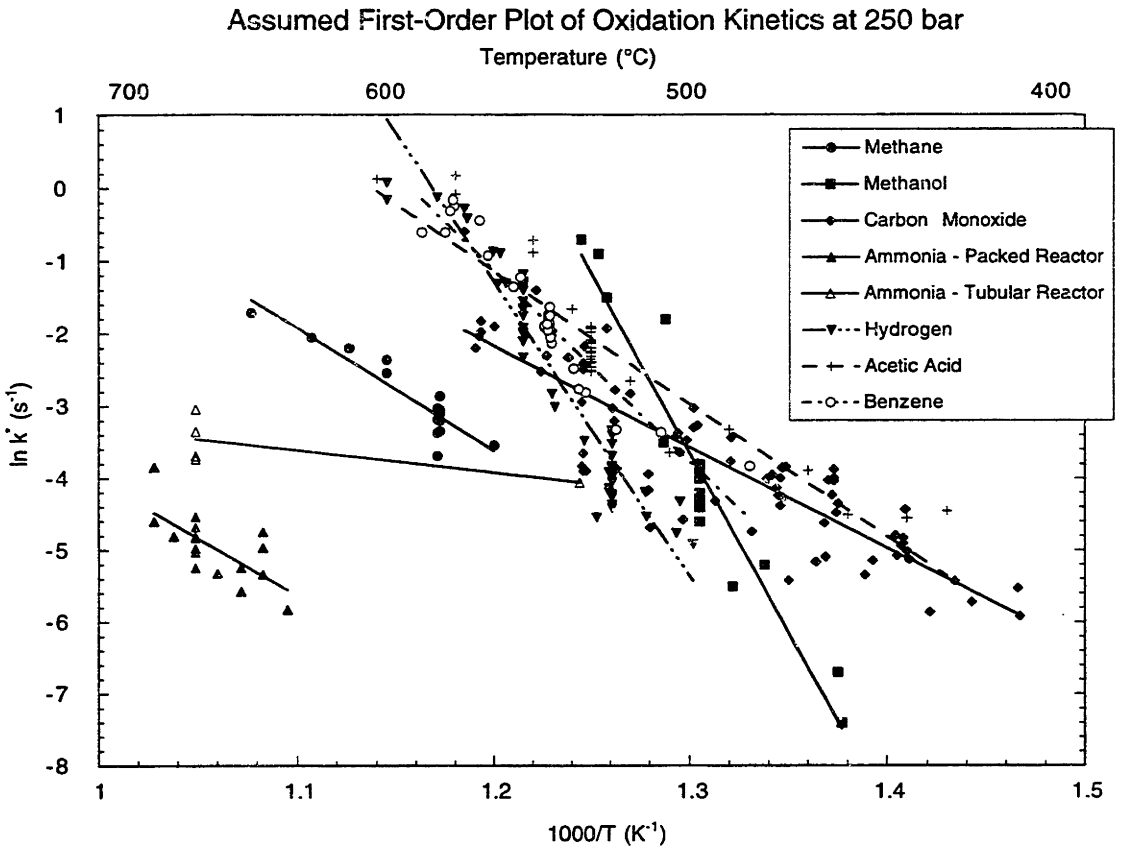

Figure 1-5 Arrhenius behavior of assumed-first-order oxidation rate constants for several model compounds in supercritical water.

Experiments. Kinetic measurements have been performed at MIT under conditions of controlled temperature, residence time, composition, pressure, and density (and, for catalytic effects, surface-to-volume ratio of reactor material Inconel 625) for various compounds, including benzene, methanol, phenol, glucose, acetic acid, ammonia, carbon monoxide, hydrogen, MTBE, methylene chloride, and thiodiglycol (Webley *et al.* 1991; Webley and Tester 1991; Tester *et al.* 1991; Holgate and Tester 1993; Tester *et al.* 1993; Holgate and Tester 1994; DiNaro *et al.* 1999; Taylor and Tester 1999; Salvatierra *et al.* 1999). Figure 1-5 illustrates the Arrhenius behavior of first-order rate constants for several model compounds.

Elsewhere, numerous other oxidation kinetics studies have been performed, including studies of phenol (Oshima *et al.* 1998); alkyl aromatics (Holliday *et al.* 1998); pulp and paper mill sludge (Blaney *et al.* 1996); methanol (MeOH), phenol (PhOH), methylethylketone (MEK), ethylene glycol (EG), acetic acid (HOAc), methylene chlo-

ride (CH_2Cl_2), 1,1,1-trichloroethane ($C_2H_3Cl_3$), ethanol (EtOH), and *n*-propanol (*n*-PrOH) (Croiset and Rice 1998); HOAc, NH_3 (Lee *et al.* 1996); TrimSol (Garcia 1996); 2,4-dichlorophenol (Lin *et al.* 1998); *p*-nitroaniline (Lee *et al.* 1997); isopropyl alcohol (Hunter *et al.* 1996); methane to MeOH (Lee and Foster 1996); GB, VX, mustard (Downey *et al.* 1995); and hydroquinone (Thammanayakatip *et al.* 1998). While many of the initial kinetics investigations were studies of global destruction rates of target waste mixtures (such as sludges, solid rocket propellants, and chemical weapons agents), later studies tended to focus mostly on single model compounds under very narrowly controlled reaction conditions.

The model compounds chosen are those which are more refractory, and thus rate-limiting, in the overall oxidation process, and include benzene, acetic acid, formaldehyde, methane, and ammonia, and their related products hydrogen and carbon monoxide. Specific attention is given to the extent of catalytic effect exerted by the reactor walls (often Inconel 625 or Hastelloy C-276), the determination of global rate laws, and chemical pathways for hydrolysis and oxidation.

Kinetics modeling. Oxidation reactions at high temperatures are often modeled using traditional combustion free-radical reaction networks. This approach has been adapted to model oxidation at the high densities in SCWO systems. In particular, reactions between water and related free radicals are now very significant, as water is the primary third-body collider. Also radical quenching can be important.

A key issue in practical free-radical modeling is determining which of the hundreds of plausible reactions are important in terms of capturing the behavior of the reaction system. In addition, developing a quantitative appreciation for the effects of uncertainties in specified elementary reaction rate constants and thermochemistry on global oxidation rates is crucial.

Often at SCW conditions the data needed to support free-radical modeling are incomplete, making quantitative predictions untractable. Nonetheless, fundamental knowledge of the reaction system can be of great value in providing estimates. An alternative approach is to consider lumped macroscopic reaction steps. A case in point is the S_N2 hydrolysis reaction of methlyene chloride with water, where the only previous experimental data was limited to conditions at 80 to 150° C in liquid water (Fells and Moelwyn-Hughes 1958). When these data were extrapolated to supercritical conditions, there was a wide disparity with new experimental data. As will be explained below, this disagreement between extrapolated and measured reaction rates is the direct result of a change in the medium properties, and can be quantitatively

described with theory developed by Kirkwood (1934).

Effects of medium. Hydrolysis and oxidation reactions are sensitive to the density of their molecular environment. The effectiveness of intermolecular interactions between the solvent and reactants influences the rates of both hydrolysis and oxidation reactions. In order to resolve the aforementioned disparities between measured CH_2Cl_2 hydrolysis rates and extrapolations from published data, the effect of changes in solvent properties was investigated. Theory developed much earlier by Kirkwood (1934) relates the Gibbs free energy of activation (used in conventional transition state theory) to the radii and dipole moments of the transition state complex, reactants, and products, and to the solvent's dielectric constant. Estimates for the transition state dipole moment and radius were then derived by computing the transition state charge density distribution using *ab initio* methods (Marrone *et al.* 1998; Marrone 1998). By compensating for the effect of the medium on the free energy of the reaction transition state, the disparity between measured and predicted hydrolysis rates based on extrapolating low-temperature rate data was resolved.

In a more rigorous study, Tester *et al.* (1998) place the electron density distribution of the transition state (from the previous *ab initio* study) into a molecular dynamics simulation using SPC water molecules. Here an averaged inhomogeneous dielectric structure of the fluid can be approximated rather than assuming a constant dielectric environment for the medium. Another similar study was pursued by Pomelli and Tomasi (1997) focusing on methyl chloride (CH_3Cl), which made extensive use of quantum mechanical methods.

Another consideration is the role of the reactor materials themselves on reactions, which might either catalyze or poison the reactions. Investigations of Webley *et al.* (1991), Webley and Tester (1991), and Holgate and Tester (1993) compared results from Inconel 625 plug-flow and packed-bed reactors to show that ammonia oxidation is sensitive to the extra surface area in the packed bed, while methanol and methane oxidation rates were independent of surface area effects over this range. Holgate, using the same apparatus, later showed that CO and H_2 oxidation is slowed slightly by the extra metal surface area, probably through termination of free-radical species (see Holgate (1993), Holgate and Tester (1993), and Holgate and Tester (1994) for details). Later, work of Salvatierra *et al.* (1999) determined that reactions with CH_2Cl_2 are neither catalyzed nor poisoned by the Inconel 625 reactor surface.

Figure 1-6 Potassium sulfate (K_2SO_4) salt deposits. These deposits formed at supercritical conditions (T > 374° C, P = 250 bar) in laminar flow from a 4 wt% K_2SO_4 solution. From Hodes (1998).

1.3.4 Macrotransport Rates

Salt deposition. Metal oxides and salts are two main categories of insoluble inorganic compounds which are produced during SCWO. The metal oxides come both from the feed stream, which may contain metals, or from the reactor wall, where corrosion has taken place, and the oxide has become detached. These solid metal oxides are generally brittle and relatively inert chemically and are easily entrained in the process stream (particularly in PFR type systems). The salts, in contrast, can be very sticky, and under prevailing supercritical process conditions are relatively insoluble (Hong *et al.* 1995). These sticky salts can hinder heat transfer, harbor corrosive agents, and tend to aggregate and obstruct flow.

An MIT-NIST collaboration (Hodes *et al.* 1997; Hodes 1998) focused on describing the deposition of salt in supercritical water under simulated SCWO process conditions. Experiments at NIST examined the behavior of an immersed, heated cylinder exposed to a constant flow of salt-containing supercritical water to study salt deposition on a surface (see Figure 1-6). Here deposition kinetics and morphology were quantitatively related to diffusion and convective transport phenomena.

Diffusion and mixing. In a separate study, M. Kutney, K. Smith and J. Tester are working with D. Cory of MIT's Francis Bitter Magnet Laboratory to explore the use of NMR to quantitatively capture molecular and bulk fluid motion in supercritical water solutions. This method has the advantage that it is completely non-intrusive. Using a gradient-field pulsed-NMR approach, an electromagnetic signature is assigned to the water molecules in arbitrarily thin cross sections of a control volume at an initial time. These signatures are tracked as time evolves in order to measure the rate of displacement to determine molecular diffusivities or fluid velocities in a 2-D cross section.

1.3.5 Materials Performance

In general, the materials of construction for SCWO systems (especially in critical components such as the reactor, salt separator, preheater, and heat recovery units) must be able to withstand high temperatures, high pressures, and corrosive process streams. Heat transfer media must additionally be able to withstand the thermal stresses induced by large temperature changes. Proper selection of materials, from both performance-oriented and economical points of view, requires an understanding of the rates and mechanisms of corrosion and erosion, and how adaptations in the process conditions may be able to sustain materials performance at acceptable levels.

General corrosion / wastage. In the presence of more "aggressive" feed stocks (*i.e.*, compounds containing halogens, sulfur, and/or phosphorus), significant general corrosion occurs (Garcia and Mizia 1995). During corrosion tests at MODAR (now General Atomics) using a halogenated mixed solvent, TrimSol, as the feed stock, Mitton *et al.* (1995) exposed coupons of various alloys to the environment for 66.2 hours. High general corrosion rates were found, *e.g.*, 2000 mpy (50.8 mm/y) for 316L, 740 to 750 mpy (18.8 to 19.0 mm/y) for Inconel 625 and Hastelloy C-276. Metallurgical and electrochemical analysis of these coupons indicates that a thick but non-protective oxide layer was generated in this highly oxidizing, chlorinated environment, in which much intergranular corrosion was also observed (Mitton *et al.* 1999). Ceramics are not immune to attack, either. Research of Boukis *et al.* (Boukis *et al.* 1997; Schacht *et al.* 1997; Schacht *et al.* 1998) investigates corrosion of zirconia ceramics in the presence of mineral acids, and le Clercq (1996) describes attack of supercritical sea water on an alumina-lined reactor.

With sufficient thermodynamic data, proper materials selection for SCWO systems may be assisted by using Pourbaix diagrams to identify conditions commensurate

with corrosion or oxide-film passivation. To produce Pourbaix diagrams of SCWO systems, we must extend thermodynamic data into higher temperature and pressure regimes. Huang *et al.* (1989) derive methods for such extensions, and identify the requirement for heat capacity data (for entropy contribution) and enthalpy data (explicitly or using heat capacity, thermal expansivity and isothermal compressibility) in order to obtain the free energy change of reaction at hydrothermal temperatures and pressures. Kriksunov and Macdonald (1995b) combine this approach with the HKF equation of state (Anderko and Pitzer 1993; Shock and Helgeson 1988; Tanger and Helgeson 1988) to more accurately determine the Pourbaix diagram for metals in SCW. See Section 3.4 for more on equations of state.

Localized Corrosion. It has been generally noted that the worst corrosion in SCWO systems occurs in the heat exchangers, where the fluid is hot but subcritical and can sustain ionic reactions (Mitton *et al.* 1996; Garcia and Mizia 1995; Peters 1996; Hong 1995). In the heat exchangers, the dominant mode of corrosion observed is localized, usually as stress corrosion cracking. Mitton *et al.* (1996) examined multiple through-wall preheater failures generated during the MIT group's CH_2Cl_2-related experiments. As these failures occurred in hot acidified streams containing HCl, pH and water chemistry control was recommended. Localized corrosion is difficult to detect and quantify, as only a very small amount of material is actually removed before the process piping is compromised—but due to locally accelerated rates, failure can occur very rapidly.

Erosion. Entrained solids (oxides, salts) can erode process piping, particularly at bends, valves, and other discontinuities. These effects are exacerbated when the materials of construction obtain their corrosion resistance by maintaining a passive layer, as this will be the first component to erode—continually providing a fresh metal surface for oxidation.

1.4 Research Needs

1.4.1 Density Effects on Reaction Rates/Mechanisms

Density of the medium may have a strong effect on chemical reaction rates, not only by concentration of specific reactants in the system, but also through changes in dielectric constant and therefore the ability of the medium to sustain dipoles and/or

ionic charge separations. Another density effect is that of the water medium as a "third body" for reactions, which in conjunction with molecular cage effects would promote deactivation of active species (Holgate and Tester 1994; DiNaro 1999). Also, under SCWO conditions, water itself is a reactant, and as such can contribute significantly to the free-radical pool, and will promote reactions which require water or consume water reaction by-products.

1.4.2 Electrochemical Data for Hydrothermal Salt Solutions, P>25 MPa and T>300° C

By obtaining and using data and/or equations of state for conditions above 300° C, Pourbaix diagrams relevant to SCWO systems can be generated which would vastly expedite the selection of proper combinations of materials and water chemistries for best materials performance. Work by MacDonald *et al.* (Kriksunov and Macdonald 1995a; Kriksunov and Macdonald 1995b; Kriksunov and Macdonald 1997), uses the data of Helgeson *et al.* (Shock and Helgeson 1988; Tanger and Helgeson 1988; Anderko and Pitzer 1993)[4], from the HKF equation of state for hydrothermal systems, to predict the Pourbaix diagram for iron above 300° C, without requiring approximations such as the Criss-Cobble entropy correspondence principle (Criss and Cobble 1964).

The majority of the corrosion data for high pressure steam systems exist for temperatures below 300° C. To this end, there is a need for widely available pH and reference electrode technology (Kriksunov *et al.* 1994; Sunkara *et al.* 1996; Eklund *et al.* 1997; Liu *et al.* 1997; Lvov and Macdonald 1997) which can continually withstand SCW operational conditions. Once more widely available, electrochemical impedance spectroscopy and other modern tools of electrochemistry can be used to map out the stabilities of various materials under a wide range of operating conditions and chemistries.

1.4.3 Pourbaix Diagrams for Alloys

The majority of Pourbaix diagrams available are for single-element systems at near-ambient temperatures. As a first approximation, a pseudo-pure component approach can be applied to multicomponent alloys, but the properties of atoms in alloys are most often different from pure component behavior. However, as yet there is no

[4] The paper by Tanger and Helgeson (1988) is a revision of the HKF EOS.

general work for Pourbaix diagrams which include non-ideal effects of alloying, such as incorporating models for activity coefficients of the alloyed elements explicitly.

1.4.4 Molecular Modeling of Solvation, Corrosion Initiation, and Metal-Ion Interactions.

Numerous molecular dynamics simulations have explored the fundamentals of ion solvation (Johnston *et al.* 1995; Balbuena *et al.* 1996; Chialvo and Cummings 1996; Chialvo *et al.* 1996; Biswas and Bagchi 1998; Reagan *et al.* 1999) and hydrogen bonding (Mizan *et al.* 1995; Mizan *et al.* 1996a; Kalinichev and Bass 1997; Gorbaty and Gupta 1998; Reagan *et al.* 1999) in supercritical water, and have in many cases been able to provide semi-quantitative information regarding solvation structure, including solvation and clustering in sub- and supercritical water (see Figure 1-3(b), for example). But molecular modeling can be extended—for instance to examine transition states for reactions other than CH_2Cl_2 hydrolysis in various solvent environments for detailed reaction modeling. A fuller understanding of solvation and solvent cage effects can be used in modeling the effectiveness of collisions between reacting species. Further, for purposes of catalysis or corrosion modeling, models are needed which take into account interactions between the aqueous ions and the metal reactor walls.

1.4.5 In-situ Process Diagnostics

Spectroscopy. Spectroscopy can be used to directly measure concentrations of reactants, and sizes and populations of particulate matter as well as to characterize solvation dynamics, clustering and or structural changes induced by reactant-solvent interactions. Steeper and Rice (1995) used Raman spectroscopy to measure concentrations of CH_4, O_2, N_2, CO and CO_2 *in situ* during SCWO of methane. Johnston and co-workers have used absorption spectra to probe pH in water at conditions of approximately 350° C and 240 bar, using indicators such as 2-naphthol (Wofford *et al.* 1998). A broader extension of spectroscopic methods would benefit industrial applications by providing detailed data regarding the progress of the reaction, perhaps changes in water chemistry relevant to corrosion control. Another relevant application is determination of particle size distributions using dynamic light scattering techniques. Such methods can be used to characterize nucleation and growth kinetics of the insoluble species.

Electrochemical noise analysis. Electrochemical noise analysis is being investigated as a means to detect corrosion *in situ* (Sunkara *et al.* 1996; Liu *et al.* 1994). Such analysis would provide a valuable tool from both a safety and operational standpoint, as engineers could monitor systems continuously to assess corrosion effects. Other descriptions of research needs can be found in Tester and Cline (1999), Tester *et al.* (1991) and Peters (1996).

1.5 Summary

This chapter presents supercritical water oxidation and its subsidiary research requirements and outlines the rationale for defining the objectives of this thesis. The application of fundamental knowledge obtained from well-defined experiments and from macro-transport and molecular modeling has had a direct impact on many aspects of process selection and performance enhancement, in, for example, salt and solids handling. Clearly there is still much more to be gained by steering process engineering science with knowledge of fundamental phenomena at a molecular level (Tester *et al.* 1991; Gloyna and Li 1995; Peters 1996; Macdonald 1997; Tester and Cline 1999).

Of particular interest to the author are the problems of materials performance as outlined in Section 1.3.5. Materials performance issues may have the greatest impact upon the economic success of the technology, as it will directly affect the initial capital outlay, the operating cost (in terms of both repairs and planned replacements), the market (reactor may be tailored to certain feed streams), and safety engineering. Were it not for the materials performance issues, the rapid chemical kinetics, the thermal autogenicity of the system, and the self-contained nature of the SCWO system would make this technology a clear winner. By fostering a fundamental understanding of the chemistry and metallurgy of the system, new strategies[5] can be developed and implemented to alleviate the economic burden of the now-mediocre materials performance.

[5] Example strategies used in other systems include materials tailored to the feed, new material coatings or treatments, identification of crucial planned-replacement piping, cathodic protection, anodic protection, sacrificial coupons, and water chemistry control.

Bibliography

Anderko, A. and K. S. Pitzer (1993). Equation-of-state representation of phase equilibria and volumetric properties of the system NaCl-H_2O above 573 K. *Geochim, [Comochimj, Aeta* **57**, 1657–80.

Balbuena, P. B., K. P. Johnston, and P. J. Rossky (1996). Molecular dynamics simulation of electrolyte solutions in ambient and supercritical water. 2. Relative acidity of HCl. *J. Phys. Chem.* **100** (7), 2716–22.

Bellissent-Funel, M.-C., T. Tassaing, H. Zhao, D. Beysens, B. Guillot, and Y. Guissani (1997). The structure of supercritical heavy water as studied by neutron diffraction. *J. Chem. Phys.* **107** (8), 2942–2949.

Biswas, R. and B. Bagchi (1998). Ion solvation dynamics in supercritical water. *Chem. Phys. Lett.* **290** (1–3), 223–228.

Blaney, C. A., L. Li, E. F. Gloyna, and S. U. Hossain (1996). Supercritical water oxidation of pulp and paper mill sludge (as an alternative to incineration). In *Minimum Effluent Mills Symp.*, pp. 79–93. TAPPI Press, Atlanta, GA.

Botti, A., F. Bruni, M. A. Ricci, and A. K. Soper (1998). Neutron diffraction study of high density supercritical water. *J. Chem. Phys.* **109** (8), 3180–4.

Boukis, N., N. Claussen, K. Ebert, R. Janssen, and M. Schacht (1997). Corrosion screening tests of high-performance ceramics in supercritical water containing oxygen and hydrochloric acid. *J. Eur. Ceram. Soc.* **17** (1), 71–77.

Brock, E. E., Y. Oshima, P. E. Savage, and J. R. Barker (1996). Kinetics and mechanism of methanol oxidation in supercritical water. *J. Phys. Chem.* **100** (39), 15834–15842.

Brock, E. E. and P. E. Savage (1995). Detailed chemical kinetics model for supercritical water oxidation of C_1 compounds and H_2. *AIChE Journal* **41** (8), 1874–88.

Chialvo, A. A. and P. T. Cummings (1996). Microstructure of ambient and supercritical water. Direct comparison between simulation and neutron scattering experiments. *J. Phys. Chem.* **100** (4), 1309–16.

Chialvo, A. A., P. T. Cummings, and H. D. Cochran (1996). Solvation structure, hydrogen bonding, and ion pairing in dilute supercritical aqueous NaCl mixtures. *Int. J. Thermophys.* **17** (1), 147–56.

Connolly, J. (1966). Solubility of hydrocarbons in water near the critical solution temperature. *J. Chem. Eng. Data* **11** (1), 13.

Criss, C. M. and J. W. Cobble (1964). The thermodynamic properties of high temperature aqueous solutions. IV. Entropies of the ions up to 200°C and the correspondence principle. *J. Am. Chem. Soc.* **86**, 5390.

Croiset, E. and S. F. Rice (1998). Direct observation of H_2O_2 during alcohol oxidation by O_2 in supercritical water. *Ind. Eng. Chem. Res.* **37** (5), 1755–1760.

Croiset, E., S. F. Rice, and R. G. Hanush (1997). Hydrogen peroxide decomposition in supercritical water. *AIChE Journal* **43** (9), 2343–2352.

DiNaro, J. L. (1999). PhD thesis in Chemical Engineering, Massachusetts Institute of Technology, Cambridge, MA.

DiNaro, J. L., J. W. Tester, K. Swallow, and J. B. Howard (1999). Experimental measurements of benzene oxidation in supercritical water. To be submitted to *AIChE Journal*.

Ding, K. and W. E. Seyfried, Jr. (1996, 14 June). Direct pH measurement of NaCl-bearing fluid with an in situ sensor at 400°C and 40 megapascals. *Science* **272**, 1634–6.

Downey, K. W., R. H. Snow, D. A. Hazlebeck, and A. J. Roberts (1995). Corrosion and chemical agent destruction: Research on supercritical water oxidation of hazardous military wastes. In K. P. Johnston and J. M. L. Penninger (Eds.), *Innovations in Supercritical Fluids: Science and Technology*, ACS Symposium Series #608. American Chemical Society.

Eklund, K., S. N. Lvov, and D. D. Macdonald (1997). The measurement of Henry's constant for hydrogen in high subcritical and supercritical aqueous systems. *J. Electroanal. Chem.* **437** (1-2), 99–110.

Fells, I. and E. A. Moelwyn-Hughes (1958). The kinetics of the hydrolysis of methylene dichloride. *J. Chem. Soc.*, 1326.

Garcia, K. M. (1996). Data acquisition testing in supercritical water oxidation using machine cutting oils and metals. In *Proceedings of the ASME Heat Transfer Division*, Volume 4, pp. 169–176.

Garcia, K. M. and R. E. Mizia (1995). Corrosion investigation in supercritical water oxidation process environments. See Heat Transfer Division (Am. Soc. Mech. Eng.) (1995), pp. 299–309.

Gloyna, E. F. and L. Li (1995). Supercritical water oxidation research and development update. *Environ. Prog.* **14** (3), 182–92.

Gorbaty, Y. E. and R. B. Gupta (1998). The structural features of liquid and supercritical water. *Ind. Eng. Chem. Res.* **37** (8), 3026–3035.

Gorbaty, Y. E. and A. G. Kalinichev (1995). Hydrogen bonding in supercritical water. 1. Experimental results. *J. Phys. Chem.* **99**, 5336–40.

Haar, L., J. S. Gallagher, and G. S. Kell (1984). *NBS/NRC Steam Tables*. Hemisphere Publishing Corp.

Hanush, R. G., S. F. Rice, T. B. Hunter, and J. D. Aiken (1996). Operation and performance of the supercritical fluids reactor (SFR). Technical Report SAND96-8203, Sandia National Laboratories, Livermore, CA.

Haroldsen, B. L., D. Y. Ariizumi, B. E. Mills, B. G. Brown, and D. C. Rousar (1996). Transpiring wall supercritical water oxidation test reactor design report. Technical Report SAND96-8213, Sandia National Laboratories, Livermore, CA.

Heat Transfer Division (Am. Soc. Mech. Eng.) (1995). *Proceedings of the ASME Heat Transfer Division*, Volume 2. Heat Transfer Division (Am. Soc. Mech. Eng.).

Hodes, M. S. (1998, September). *Measurements and Modeling of Deposition Rates from Near-Supercritical, Aqueous, Sodium Sulfate and Potassium Sulfate Solutions to a Heated Cylinder*. PhD thesis in Mechanical Engineering, Massachusetts Institute of Technology, Cambridge, MA.

Hodes, M. S., K. A. Smith, W. S. Hurst, W. J. Bowers, Jr., and P. Griffith (1997). Measurements and modeling of deposition rates from a near supercritical aqueous

sodium sulfate solution to a heated cylinder. In *ASME Proceedings of the National Heat Transfer Conference*, Volume 12, pp. 107–119.

Holgate, H. R. (1993). *Oxidation Chemistry and Kinetics in Supercritical Water: Hydrogen, Carbon Monoxide, and Glucose.* PhD thesis in Chemical Engineering, Massachusetts Institute of Technology, Cambridge, MA.

Holgate, H. R. and J. W. Tester (1993). Fundamental kinetics and mechanisms of hydrogen oxidation in supercritical water. *Comb. Sci. and Tech.* **88**, 369–97.

Holgate, H. R. and J. W. Tester (1994). Oxidation of hydrogen and carbon monoxide in sub- and supercritical water: Reaction kinetics, pathways, and water-density effects. 2. Elementary reaction modeling. *J. Phys. Chem.* **98**, 810–22.

Holliday, R. L., B. Y. M. Jong, and J. W. Kolis (1998). Organic synthesis in subcritical water. Oxidation of alkyl aromatics. *J. Supercrit. Fluids* **12** (3), 255–260.

Holliday, R. L., J. W. King, and G. R. List (1997). Hydrolysis of vegetable oils in sub- and supercritical water. *Ind. Eng. Chem. Res.* **36** (3), 932–935.

Hong, G. T. (1995). Hydrothermal oxidation: Pilot scale operating experiences. In *Off. Proc.—Int. Water Conf.*, pp. 439–96.

Hong, G. T., F. J. Armellini, and J. W. Tester (1995). The NaCl-Na_2SO_4-H_2O system in supercritical water. See White (1995).

Huang, S., K. Daehling, T. E. Carleson, P. Taylor, C. Wai, and A. Propp (1989). Thermodynamic analysis of corrosion of iron alloys in supercritical water. In K. P. Johnston and J. M. L. Penninger (Eds.), *Supercritical Fluid Science and Technology*, ACS Symposium Series #406. American Chemical Society.

Hunter, T. B., S. F. Rice, and R. G. Hanush (1996). Raman spectroscopic measurement of oxidation in supercritical water. 2. Conversion of isopropyl alcohol to acetone. *Ind. Eng. Chem. Res.* **35** (11), 3984–3990.

Ikushima, Y. (1997). An *in situ* laser Raman spectroscopy study on the structure of supercritical water. *Koatsuryoku no Kagaku to Gijutsu* **6** (1), 24–29.

Ikushima, Y., K. Hatakeda, N. Saito, and M. Arai (1998). An in-situ Raman spectroscopy study of subcritical and supercritical water: The peculiarity of hydrogen bonding near the critical point. *J. Chem. Phys.* **108** (14), 5855–5860.

Japas, M. L. and E. U. Franck (1985b). High pressure phase equilibria and PVT-data of the water–nitrogen to 673K and 250 MPa. *Ber. Bunsenges Phys. Chem.* **89**, 793.

Japas, M. L. and E. U. Franck (1985a). High pressure phase equilibria and PVT-data of the water–oxygen system including water–air to 673K and 250 MPa. *Ber. Bunsenges Phys. Chem.* **89**, 1268.

Johnston, K. P., P. B. Balbuena, T. Xiang, and P. J. Rossky (1995). Simulation and spectroscopy of solvation in water from ambient to supercritical conditions. In K. P. Johnston and J. M. L. Penninger (Eds.), *Innovations in Supercritical Fluids: Science and Technology*, ACS Symposium Series #608, pp. 77–92. American Chemical Society.

Kalinichev, A. G. and J. D. Bass (1997). Hydrogen bonding in supercritical water. 2. Computer simulations. *J. Phys. Chem. A* **101** (50), 9720–9727.

Kirkwood, J. G. (1934). Theory of solutions of molecules containing widely separated charges with special applications to zwitterions. *J. Chem. Phys.* **2** (7), 351.

Krader, T. and E. U. Franck (1987). The ternary sytems H_2O-CH_4-NaCl and H_2O-CH_4-$CaCl_2$ to 800K and 250 MPa. *Ber. Bunsenges. Phys. Chem.* **91**, 627.

Krammer, P., S. Mittelstadt, and H. Vogel (1999, February). Investigating the synthesis potential in supercritical water. *Chemical Engineering & Technology* **22** (2), 126–130.

Kriksunov, L. and D. Macdonald (1997). Potential-pH diagrams for iron in supercritical water. *Corrosion* **53** (8), 605–611.

Kriksunov, L., D. D. Macdonald, and P. J. Millett (1994, November). Tungsten/tungsten oxide pH sensing electrode for high temperature aqueous environments. *J. Electrochem. Soc.* **141** (11), 3002–5.

Kriksunov, L. B. and D. D. Macdonald (1995a). Corrosion testing and prediction in SCWO environments. See Heat Transfer Division (Am. Soc. Mech. Eng.) (1995), pp. 281–288.

Kriksunov, L. B. and D. D. Macdonald (1995b, Feb. 6–9). Development of Pourbaix diagrams for metals in supercritical aqueous media. In *Proceedings of First International Workshop on Supercritical Water Oxidation*, Jacksonville, FL.

Kutney, M. C., V. S. Dodd, K. A. Smith, H. J. Herzog, and J. W. Tester (1997). A hard-sphere, volume-translated van der Waals equation of state for supercritical process modeling: Part I, pure components. *Fluid Phase Equilibria* **128**, 149–171.

LaJeunesse, C. A., B. L. Haroldsen, S. F. Rice, and B. G. Brown (1997). Hydrothermal oxidation of Navy shipboard excess hazardous materials. Technical Report SAND97-8212, Sandia National Laboratories, Livermore, CA.

le Clercq, M. (1996, June). Ceramic reactor for use with corrosive supercritical fluids. *AIChE Journal* **42** (6), 1798.

Lee, A., O. S. Saulters, C. S. Connon, and H. G. Castillo (1996). Destruction of ammonia and acetic acid by hydrothermal oxidation. In *Proceedings of the ASME Heat Transfer Division (335)*, Volume 4, pp. 189–201. HTD (Am. Soc. Mech. Eng.).

Lee, D. S., K. S. Park, Y. W. Nam, Y.-C. Kim, and C. H. Lee (1997). Hydrothermal decomposition and oxidation of p-nitroaniline in supercritical water. *J. Hazard. Mater.* **56** (3), 247–256.

Lee, J. H. and N. R. Foster (1996). Direct partial oxidation of methane to methanol in supercritical water. *J. Supercrit. Fluids* **9** (2), 99–105.

Lin, K. S., H. P. Wang, and M. C. Li (1998). Oxidation of 2,4-dichlorophenol in supercritical water. *Chemosphere* **36** (9), 2075–2083.

Liu, C., D. D. Macdonald, E. Medina, J. J. Villa, and J. M. Bueno (1994, September). Probing corrosion activity in high subcritical and supercritical water through electrochemical noise analysis. *Corrosion Science* **50** (9), 687.

Liu, C., S. R. Snyder, and A. J. Bard (1997). Electrochemistry in near-critical and supercritical fluids. 9. Improved apparatus for water systems (23-385°C). The oxidation of hydroquinone and iodide. *J. Phys. Chem. B* **101** (7), 1180–1185.

Lvov, S. N. and D. D. Macdonald (1997). Potentiometric studies of supercritical water chemistry. In *Proc. Electrochem. Soc., High Temperature Materials Chemistry*, Volume 39, pp. 746–754.

Macdonald, D. D. (1997, January). Defining the corrosion chemistry of supercritical water oxidation systems. In *Proc. of the Tri-Service Conference on Corrosion*, Volume 1, Springfield, VA. National Technical Information Service.

Marrone, P. A. (1998). *Hydrolysis and oxidation of model organic compounds in sub- and supecritical water: Reactor design, kinetics, measurements, and modeling.* PhD thesis in Chemical Engineering, Massachusetts Institute of Technology, Cambridge, MA.

Marrone, P. A., T. A. Arias, W. A. Peters, and J. W. Tester (1998). Solvation effects on kinetics of methylene chloride reactions in sub- and supercritical water: Theory, experiment, and *ab initio* calculations. *J. Phys. Chem. A* **102** (35), 7013–28.

Marshall, W. L. and E. U. Franck (1981). Ion product of water substance, 0–1000°C, 1–10,000 bars. *J. Phys. Chem. Ref. Data* **10** (2), 295–304.

Mather, A. E. and E. U. Franck (1992). Phase equilibria in the system carbon dioxide–water at elevated pressures. *J. Phys. Chem.* **96** (1), 6.

Mitton, D. B., Y. S. Kim, J. H. Yoon, S. Take, and R. M. Latanision (1999). Corrosion of SCWO constructional materials in Cl^- containing environments. In *Corrosion 99*, Number 257, Houston, TX. NACE. Meeting Location: San Antonio, TX.

Mitton, D. B., P. A. Marrone, and R. M. Latanision (1996, March). Interpretation of the rationale for feed modification in SCWO systems. *J. Electrochem. Soc.* **143** (3), L59–L61.

Mitton, D. B., J. C. Orzalli, and R. M. Latanision (1995). Corrosion studies in supercritical water oxidation systems. In K. P. Johnston and J. M. L. Penninger (Eds.), *Innovations in Supercritical Fluids: Science and Technology*, ACS Symposium Series #608. Washington, DC: American Chemical Society.

Mizan, T. I., P. E. Savage, and R. M. Ziff (1995). A molecular dynamics investigation of hydrogen bonding in supercritical water. In K. P. Johnston and J. M. L. Penninger (Eds.), *Innovations in Supercritical Fluids: Science and Technology*, ACS Symposium Series #608, pp. 47–64. American Chemical Society.

Mizan, T. I., P. E. Savage, and R. M. Ziff (1996a). Comparison of rigid and flexible simple point charge water models at supercritical conditions. *J. Comput. Chem.* **17** (15), 1757–1770.

Mizan, T. I., P. E. Savage, and R. M. Ziff (1996b). Temperature dependence of hydrogen bonding in supercritical water. *J. Phys. Chem.* **100** (1), 403–8.

Oshima, Y., K. Hori, M. Toda, T. Chommanad, and S. Koda (1998). Phenol oxidation kinetics in supercritical water. *J. Supercrit. Fluids* **13** (1–3), 241.

Peters, ed., W. A. (1996). Data needs to support modeling of supercritical water oxidation reactors and processes for chem demil applications. Technical Report MIT-EL 96-002, MIT Energy Laboratory, Cambridge, MA.

Phenix, B. D. (1998). *Hydrothermal oxidation of simple organic compounds.* PhD thesis in Chemical Engineering, Massachusetts Institute of Technology, Cambridge, MA.

Phenix, B. D., J. L. DiNaro, J. W. Tester, J. B. Howard, and K. A. Smith (1999). The effects of mixing and oxidant choice in laboratory-scale measurements of supercritical water oxidation kinetics. To be submitted to *Ind. Eng. Chem. Res.*

Pomelli, C. S. and J. Tomasi (1997). *Ab Initio* study of the S_N2 reaction $CH_3Cl + Cl^- \rightarrow Cl^- + CH_3Cl$ in supercritical water with the polarizable continuum model. *J. Phys. Chem. A* **101** (19), 3561–3568.

Reagan, M., J. Harris, and J. W. Tester (1999). Molecular simulations of dense hydrothermal NaCl-H_2O solutions from subcritical to supercritical conditions. *J. Phys. Chem. B* **103** (37), 7935–7941.

Rebert, C. J. and W. B. Kay (1959). The phase behavior and solubility relations of the benzene–water system. *AIChE Journal* **5**, 285.

Rice, S. F., R. R. Steeper, and C. A. LaJeunesse (1994). Supercritical water oxidation of colored smoke, dye, and pyrotechnic compositions. Technical Report SAND94-8203, Sandia National Laboratories, Livermore, CA.

Salvatierra, D., J. D. Taylor, P. A. Marrone, and J. W. Tester (1999). Kinetic study of hydrolysis of methylene chloride from 100 to 500° C. Accepted for publication in *Ind. Eng. Chem. Res.*

Schacht, M., N. Boukis, N. Claussen, E. Dinjus, K. Ebert, R. Janssen, and F. Meschke (1997). Reactor for investigations of the corrosion of ceramics in HCl containing SCWO environments and first experimental results. In *Proceedings of the 4th International Symposium on Supercritical Fluids (ISSF97)*, pp. 147–150. Meeting date: 11-14 May, 1997 in Sendai, Japan.

Schacht, M., N. Boukis, E. Dinjus, K. Ebert, R. Janssen, F. Meschke, and N. Claussen (1998). Corrosion of zirconia ceramics in acidic solutions at high pressures and temperatures. *J. Europ. Ceram. Soc.* **18**, 2373–76.

Shock, E. L. and H. C. Helgeson (1988). Calculation of the thermodynamic and transport properties of aqueous species at high pressures and temperatures: Correlation algorithms for ionic species and equation of state predictions to 5 kb and 1000°C. *Geochimica et Cosmochimica Acta* **52**, 2009.

Steeper, R. R. and S. F. Rice (1995). Optical monitoring of the oxidation of methane in supercritical water. See White (1995), pp. 652–4.

Sunkara, M. K., A. K. Rawat, and P. J. Moran (1996). Corrosion monitoring in supercritical water media. In R. H. Jones and D. R. Baer (Eds.), *Proc. Symp. New Tech. Charact. Corros. Stress Corros.*, pp. 303–313. Minerals, Metals & Materials Society, Warrendale, PA.

Tanger, IV, J. C. and H. C. Helgeson (1988). Calculation of the thermodynamic and transport properties of aqueous species at high pressures and temperatures: Revised equations of state for the standard partial molal properties of ions and electrolytes. *American Journal of Science* **288**, 19.

Taylor, J. D. and J. W. Tester (1999). Experimental measurements of MTBE hydrolysis and oxidation in supercritical water. Work in progress.

Tester, J. W. and J. A. Cline (1999). Hydrolysis and oxidation in sub- and supercritical water: Connecting process engineering science to molecular interactions. In *Corrosion 99*, Number 252, Houston, TX. NACE. Meeting Location: San Antonio, TX.

Tester, J. W., H. R. Holgate, F. J. Armellini, P. A. Webley, W. R. Killilea, G. T. Hong, and H. E. Barner (1991). Oxidation of hazardous organic wastes in supercritical water: A

review of process development and fundamental research. In D. W. Tedder and F. G. Pohland (Eds.), *Emerging Technologies for Hazardous Waste Management III*, ACS Symposium Series #518, pp. 35–76. American Chemical Society.

Tester, J. W., P. A. Marrone, M. D. DiPippo, K. Sako, M. T. Reagan, T. A. Arias, and W. A. Peters (1998). Chemical reactions and phase equilibria of model halocarbons and salts in sub- and supercritical water. *J. Supercrit. Fluids* **13**, 225–240.

Tester, J. W., P. A. Webley, and H. R. Holgate (1993). Revised global kinetic measurements of methanol oxidation in supercritical water. *Ind. Eng. Chem. Res.* **32** (1), 236–9.

Thammanayakatip, C., Y. Oshima, and S. Koda (1998). Inhibition effect in supercritical water oxidation of hydroquinone. *Ind. Eng. Chem. Res.* **37** (5), 2061–2063.

Uematsu, M. and E. U. Franck (1980). Static dielectric constant of water and steam. *J. Phys. Chem. Ref. Data* **9** (4), 1291–1306.

Webley, P. A. (1990). *Fundamental oxidation kinetics of simple compounds in supercritical water*. PhD thesis in Chemical Engineering, Massachusetts Institute of Technology, Cambridge, MA.

Webley, P. A., H. R. Holgate, D. M. Stevenson, and J. W. Tester (1990). Oxidation kinetics of model compounds of metabolic waste in supercritical water. In *20th Intersociety Conference on Environmental Systems*, #901333, Warrendale, PA. Society of Automotive Engineers. Meeting Location: Williamsburg, VA.

Webley, P. A. and J. W. Tester (1991). Fundamental kinetics of methane oxidation in supercritical water. *Energy and Fuels* **5**, 411–419.

Webley, P. A., J. W. Tester, and H. R. Holgate (1991). Oxidation kinetics of ammonia and ammonia-methanol mixtures in supercritical water in the temperature range 530–700°C at 246 bar. *Ind. Eng. Chem. Res.* **30** (8), 1745–54.

White, Jr., H. J. (Ed.) (1995). *Physical Chemistry of Aqueous Systems, Proceedings from the 12th International Conference on the Properties of Water and Steam*, New York. Begell House.

Wofford, W. T., E. F. Gloyna, and K. P. Johnston (1998). Boric acid equilibria in near-critical and supercritical water. *Ind. Eng. Chem. Res.* **37** (5), 2045–2051.

Xiang, T., K. P. Johnston, W. T. Wofford, and E. F. Gloyna (1996). Spectroscopic measurement of pH in aqueous sulfuric acid and ammonia from sub- to supercritical conditions. *Ind. Eng. Chem. Res.* **35** (12), 4788–4795.

Chapter 2

Objectives and Approach

2.1 Corrosion Science in Supercritical Water

As observed in Chapter 1, supercritical water oxidation (SCWO) reactors and heat exchange media are susceptible to severe corrosion in the presence of chlorinated feed stocks.[1] Perhaps the most critical corrosion regime is the localized corrosion and stress corrosion cracking (SCC) exhibited in the heat-exchange media (Mitton *et al.* 1996), which is associated with HCl-containing streams at temperatures in the range of 290–380° C. Figure 2-1 shows a through-wall failure produced in a bench-scale SCWO preheater tube (0.010 in thick), when exposed to a feed of CH_2Cl_2 and water for an aggregate exposure time of 40 h. Such a failure represents an average penetration rate of 2.2 in/y. Localized corrosion such as this speckles the surface with "pits," with the inter-pit spacing dependent on the material, the chloride concentration and the oxidation potential. Local corrosion removes little actual metal, but insidiously compromises the material structure such that sudden and catastrophic failure can occur.

Still severe, but perhaps less dramatic, is the general corrosion which has been observed at the higher temperatures and lower fluid densities ($T \geq$500° C, $\rho \leq$0.2 g/cc). Inconel 625 and Hastelloy C-276 have been observed to corrode at rates of approximately 750 mpy under conditions of high oxidation potential and high chloride concentrations (see Section 1.3.5, page 30) during SCWO of TrimSol.[2] General corrosion

[1] Many of the candidates for SCWO treatment are chlorinated, so the capability to successfully treat them is a process engineering objective.

[2] TrimSol is a cutting fluid of proprietary composition used in nuclear applications; it contains phosphates, chlorides and other aggressive species at high concentrations (*e.g.*, $[Cl^-]$=3000 ppm in the SCWO reactor).

Figure 2-1 A through-wall crack in a 1/16-in Hastelloy C-276 preheater tube exposed to a feed of CH_2Cl_2 for 40 h. The top of the photo is the inner surface of the tube, while the outer surface is at the bottom. From Mitton *et al.* (1995).

experienced during this exposure is significantly slower than the penetration rate of the local corrosion, especially since the TrimSol system contained high levels of other aggressive species (chlorides, phosphates, *etc.*). Here, the metal is still attacked intergranularly, but with a broad and uniform penetration at high local rates.

Sections 2.1.1 and 2.1.2 below detail the mechanistic differences in the types of corrosion. In the context of these corrosion mechanisms, the specific thesis research objectives will then be introduced.

2.1.1 Localized Corrosion

Localized corrosion takes place upon passive-film-protected materials, and involves local inhomogeneities in the passive oxide film (Jones 1996). Without a passive film, corrosion reactions can occur across the metal uniformly. With a non-porous barrier oxide (or other passive film) in place, the oxidation potential of a system can rise without any subsequent oxidation—the metal is protected. In an electrochemical system, when the film is somehow disrupted, the entire oxidative capacity of the environment is focused on the tiny area at which bare metal is exposed. Because the system is electrically continuous, the species in the environment are drawn to the metal by the field caused by its electrical potential. In an electrochemical system, the cathodic reaction and the anodic reaction are not necessarily adjacent, because the current can flow through the conductive metal. In local corrosion, this leads to a dramatic effect upon the current density because the tiny bare-metal site's anodic current must offset the cathodic current. Since the cathode area (which may, for instance, include the passive film itself) is vast compared to the area of the exposed bare metal, the current density at the exposed metal site is large, and the corrosion rate there is, correspondingly, also very large. The resulting attack is deep and rapid, producing a void or "pit" in the metal. This type of local electrochemical attack requires that charge, in the form of ions, be carried through the aqueous medium. Thus localized corrosion is generally associated with a relatively high polar-solvent density. (See Jones (1982) for a review of local corrosion.)

2.1.2 General Corrosion

At lower water densities, a different form of corrosion is relevant: the general oxidative attack of the alloy. At these higher densities individual ions are generally only sparingly soluble, because the dielectric strength of water is low ($D_s \equiv \epsilon\epsilon_0 < 6$), making its solvation characteristics similar to an organic solvent. Instead of reacting

with aqueous ions, the alloy reacts with oxygen (or other oxidizing species) directly, transferring charge directly from reactants to products at the site of the heterogeneous reactions. Damage is caused at the surface of the alloy. For the reaction to persist, its products (such as oxides or metal halides) must either porous, volatile, or otherwise discontinuous. If a continuous, adherent, chemically resistant oxide film develops atop the alloy, it will be protected from the corrosive environment.

2.1.3 Effect of Film Formation on Corrosion

The instantiation of either local or general corrosion is dependent on the solubility and/or morphology of the metal oxides. If the oxide is porous, or if it does not adhere well to the underlying metal matrix, then it may present little more than a diffusion barrier between the bare metal and the environment. If the oxide is soluble, then there is nothing to protect the metal at all. If the oxide is non-porous and adherent, then the metal will be protected.

In an alloy, there is more than one element. This complicates the corrosion process, as alloying elements may preferentially dissolve (dealloying). This potentially makes the corrosion layer more complex, as it may be composed of any combination of alloying elements, oxides or hydroxides of alloying elements, and perhaps voids where other alloying elements have dissolved.

The corrosion problem in SCWO is very broad, and spans the full spectrum of corrosion chemistry (from "wet" to "dry"). In all situations the metal is going to be oxidized, although the consequences of the change in oxidation state vary based upon the properties of the medium. It is thus the interplay between the material, the corrosion products, and the environment which determine the corrosion rate and mechanism, and it is this interplay which must come under scrutiny.

2.2 Focus

The entire interplay, of course, merits the work of many theses, and so the scope of the investigation must be narrowed. This investigation of corrosion addresses in essence two very basic problems: (1) the problem of not knowing when it occurs, and (2) the problem of understanding the relationship between the immediate SCWO environment and the commencement of corrosion.

2.2.1 Defining Corrosion Conditions

"The Problem of Not Knowing When Corrosion Occurs"

To address this issue, one must experimentally observe corrosion in a (supercritical-water + aggressive-agent)-containing system. Previous studies (see Section 1.3.5) were chiefly of a lumped-effect design, in which the materials are exposed to multiple aggressive agents simultaneously in order to screen for the best performers. This type of experiment can very effectively sort materials based on overall performance, but in the case of SCWO it must be noted that even the best performers had some serious deficiencies. For instance, a protective layer of gold simply dissolved in an HCl-containing stream at 24 MPa and temperatures of ≈350° C (Boukis *et al.* 1996). The lumped-effect type of exposure study does not, however, lend itself to any detailed mechanistic interpretation, and thus its utility in suggesting a possible corrective action is quite limited.

> For example, consider a hypothetical metal M with passive film P. Unbeknownst to the observer, aggressive agent X causes the film P to develop some abnormal porosity, allowing aggressive agents Y and Z to attack M right through it. Without isolating the effect of X, it might never be known that P is otherwise impervious to Y and Z.

In the absence of a clear "winner" in the lumped-effect studies, there is much to be gained by developing a fundamental and systematic understanding of the complex interplay between the metals, their oxides, and the hydrothermal constituents. To effect this, we must first start by examining the effect of one hydrothermal constituent upon one material. Chapter 4 contains a detailed study of corrosion of Hastelloy C-276 by hydrothermal hydrochloric acid.

2.2.2 Understanding Environmental Influences

"The Problem of Understanding the Relation Between the Immediate SCWO Environment and the Commencement of Corrosion"

To address this topic requires some foreknowledge of the metal-water interface. SCWO reactors provide a highly oxidizing environment, making it likely that oxides are present atop the metal surfaces. It is not *a priori* obvious whether the oxides are

protective or if in fact the oxygen can penetrate the oxide (via diffusion or a mechanical defect) to the metal. On the other hand, the heat exchangers in SCWO systems, which experience the severe localized corrosion, might be exposed to either oxidizing or oxygen-depleted conditions. Usually, localized corrosion is observed only when general corrosion is stifled, *i.e.*, when a passive oxide film is present on the metal—indicating that a passive film is present upon the heat exchanger material, at least in the neighborhood of the localized attack.[3] With metal oxide being present in both the reactor and in the heat exchangers, and furthermore with the oxide properties being pivotal to the initiation of the very-dangerous localized corrosion, it is of the broadest interest to study an interface with an oxide film.

Localized corrosion has been studied for many years by electrochemical means (Jones 1996; Jones 1982), providing great insight on the chemistry which surrounds the formation and propagation of pits and cracks. However, within this same literature there is vast disagreement as to the critical step of "initiation," which precedes the formation of the neo-pit (or neo-crack). While new advances in technology are beginning to make atomic-resolution observation of an *in situ* passive film more accessible (McKrell and Galligan 1995), still it is forseeably difficult to observe and characterize the actual initiation reaction as it takes place. The difficulty is greatly magnified when it is compounded with the high-temperature and high-pressure conditions of a hydrothermal water system.[4] With the key elements of a mechanistic model for corrosion initiation still experimentally inaccessible, we must turn to a more theoretically-based approach. Density functional theory is a tool developed by Nobel laureate Walter Kohn (Hohenberg and Kohn 1964; Kohn and Sham 1965). Both the complexity and applicability of the density functional model will be justified in Chapters 5 and 6, where an *ab initio* description of the α-Cr_2O_3 (0001) surface and its interactions with hydrogen and chlorine is presented.

---

[3] It cannot be completely ruled out at this point, however, that the localized attack might simply be a manifestation of metal inhomogeneities: differences in grain-boundary composition, or, in a pure material, changes in the Fermi level at the grain boundaries, could incite an electrochemical reaction which attacks the metal preferentially at the grain boundaries. This type of attack, however, is expected to rapidly excavate individual grains from the metal surface, causing observable grain-shaped irregularities in the metal surface.

[4] An interesting experiment would be to provide a room-temperature and pressure solvent with a D_s equivalent to supercritical water, and do an *in situ* AFM or STM study.

2.3 Specific Research Objectives and Approach

The following are the specific objectives of the work, pertaining to the studies mentioned in Sections 2.2.1 and 2.2.2.

2.3.1 Experimental objectives

To design experiments which expose Hastelloy C-276 to hydrothermal HCl. This apparatus is capable of making repeatable, safe, multiple-day exposures. The instrumentation is also capable of sensing events and taking the proper corrective action. Temperature and pressure data are logged. The experiment exposes pressure-bearing tubing to the aggressive environment at a constant pressure and temperature over a defined time period. The experiment uses Hastelloy C-276 and HCl to take advantage of a direct comparison with post-failure analyses (Marrone 1998; Mitton *et al.* 1996).

To determine the temperature dependence of the corrosion phenomena. A map of corrosion as a function of temperature for Hastelloy C-276 in an acidified non-oxygenated SCWO system at $\approx$ 246 bar is developed. This corrosion is characterized in terms of its form, its chemistry/metallurgy, and its rate.

To further validate the heat transfer model used in kinetics studies. Kinetics measurements performed by Marrone (Marrone *et al.* 1998; Marrone *et al.* 1995; Marrone 1998) employ heat transfer models in order to determine the temperature history of the fluid in his preheater tubing, and to back out the reaction rate constant. The Marrone heat transfer computer model is modified to describe the experiment designed for this work. The model is then compared to explicit temperature measurements in this system.

To describe the corrosion phenomena in terms of thermodynamics, kinetics, and mechanical variables. The corrosion susceptibility is expressed in terms of the effects of the environment (such as temperature, changes in D_s, *etc.*) as well as the materials properties (*e.g.*, grain size). The thermodynamic stability of the species involved, as reported in the available literature, is compared with the phenomena observed. A unified description of the corrosion susceptibility in terms of thermodynamic variables is attempted.

Another factor influencing the growth of cracks is the stress distribution in the metal. Stress corrosion cracking (SCC) requires a susceptible material, a corrosive environment, and stress. External stress is delivered to the point of a crack through the geometry of the material (expressed through stress intensity factors) and through the properties of the material and its microstructure. In particular, the grain size has an influence on the yield stress of a material (Dieter 1986), and therefore its yield curve. Overall, the stress at the crack tip is proportional to the tangential stress. The tangential stress tends to pull the crack open, allowing the corrosion to proceed deeper into the metal (Jones 1996). As the through-wall tube failures (page 42) occurred in a load-bearing wall, the tangential stress is expected to be a factor in determining the cracking rate. Thus, a peripheral output of this work is to examine the influence of stress upon the cracking rate. Cracking is further complicated by dealloying behavior (Sieradzki and Newman 1987); the interplay between the two will be examined.

2.3.2 Theoretical modeling objectives

To develop a first-principles model of an oxidized surface. In order to develop a model of the local corrosion susceptibility of the system at various temperatures (and therefore fluid densities) as detailed above, it is helpful to have a model for corrosion initiation which can account for the changes in reactivity as a function of fluid properties. The fundamentals of the initiation process are not well understood at the mechanistic level (Jones 1982). The model of the passive surface must be able to account for the effect of the water medium, as well as being explicit in terms of chemical bonding and reactivity.

To employ the first-principles model to predict susceptibility to corrosion initiation. A chemistry-explicit model of the oxidized surface will be developed to predict the surface reactivity with H^+ and Cl^- in hydrothermal and supercritical water. This model will be explicit not only in the positions of atoms and the interatomic potential energies, but also in terms of electron density and energies of orbitals. A model for the important passive-film component Cr_2O_3 will be developed. The electronic states and crystal structure of a perfect crystal of α-Cr_2O_3 will be computed and validated. From this, a model for the oxidized surface will be computed and optimized under density functional theory. The highest-energy occupied and lowest-energy unoccupied orbitals will then be used to explore the chemical reactivity of the surface.

To determine the effect of the medium upon the reactive susceptibilities. Through the dielectric constant D_s, the effect of the medium upon the reactions under consideration is assessed. To obtain a general magnitude and trend of the effect of a dielectric upon the α-Cr_2O_3 surface, a slab-dielectric will be incorporated into the density-functional calculation. The response of the orbitals of Cr_2O_3 to the induced field will be assessed. The magnitude of the effects of the dielectric upon the adsorption energies will be explored.

2.3.3 Anticipated Results

This thesis is organized into three major sections: experimental, theoretical, and summary. In the experimental portion it will be shown that the corrosion of Hastelloy C-276 with hydrothermal HCl produces a profile which depends on temperature through the activation energies and changes in diffusivity. A probable mechanism for the development of intergranular stress corrosion cracking (IGSCC) in narrow-diameter Hastelloy C-276 tubes will be presented. Finally, it will be shown that the most dramatic corrosion penetration occurs in a narrow temperature regime in which dealloying and intergranular corrosion act synergistically to create an environment conducive to IGSCC. It will be shown that, for a given material and wall stress, changes in dealloying behavior influence directly the extent of penetration and crack development.

Chapter 5 of the theoretical portion presents the development of a quantum-mechanical model of crystalline Cr_2O_3 with a thorough validation against experimental data. It will be shown that the local spin-density approximation (LSDA) provides a satisfactory description of the crystal, and that seemingly subtle effects such as electron spin affect basic macroscopic parameters of the solid, such as bulk modulus. The oxygen-terminated (0001) surface is modeled in a slab geometry and the surface oxygens undergo significant relaxations. The surface is found to be vulnerable to electron-donating species, and it is projected that p-doping the surface may help decrease this chemical susceptibility. The electronic states relevant to bonding also exhibit a surprising uniformity of spin-polarization which may impact surface reactions or catalytic activity.

Chapter 6 presents a first-order *ab initio* investigation of the effect of a strong dielectric (such as water) upon the chemical reactivity of the α-Cr_2O_3 (0001) surface. This computation employs a simple slab dielectric. The work shows that the reactivity of a bare Cr_2O_3 (0001) surface is almost unaffected by the presence of a dielectric.

However, calculations of the effect of the dielectric upon the adsorption energies of adsorbed species such as Cl suggest that the presence of water may strongly enhance the adsorption of Cl onto the surface.

Bibliography

Boukis, N., G. Franz, C. Friedrich, W. Habicht, and K. Ebert (1996). Corrosion screening tests with Ni-base alloys in supercritical water containing hydrochloric acid and oxygen. In *Proceedings of the ASME Heat Transfer Division*, Number 4, pp. 159–167.

Dieter, G. E. (1986). *Mechanical Metallurgy*. New York: McGraw-Hill.

Hohenberg, P. and W. Kohn (1964). *Phys. Rev.* **136**, 864B.

Jones, D. A. (1982). Localized corrosion. In R. N. Parkins (Ed.), *Corrosion Processes*, Chapter 4, pp. 161–207. New York: Applied Science Publishers.

Jones, D. A. (1996). *Principles and Prevention of Corrosion*. Upper Saddle River, NJ: Prentice Hall.

Kohn, W. and L. J. Sham (1965). Self-consistent equations including exchange and correllation effects. *Phys. Rev.* **140**, 1133A.

Marrone, P. A. (1998). *Hydrolysis and oxidation of model organic compounds in sub- and supecritical water: Reactor design, kinetics, measurements, and modeling*. PhD thesis in Chemical Engineering, Massachusetts Institute of Technology, Cambridge, MA.

Marrone, P. A., T. A. Arias, W. A. Peters, and J. W. Tester (1998). Solvation effects on kinetics of methylene chloride reactions in sub- and supercritical water: Theory, experiment, and *ab initio* calculations. *J. Phys. Chem. A* **102** (35), 7013–28.

Marrone, P. A., R. P. LaChance, J. L. DiNaro, B. D. Phenix, J. C. Meyer, J. W. Tester, W. A. Peters, and K. C. Swallow (1995). Methylene chloride oxidation and hydrolysis in supercritical water. In K. W. Hutchenson and N. Foster (Eds.), *Innovations in Supercritical Fluids: Science and Technology*, ACS Symposium Series #608. Washington, D.C.: American Chemical Society.

McKrell, T. J. and J. M. Galligan (1995). Kinetic study of the passive film on 304 stainless steel using a scanning tunneling microscope. In R. Sharma, P. L. Gai, M. Gajdardziska-Josifovska, R. Sinclair, and L. J. Whitman (Eds.), *In Situ Electron and Tunneling Microscopy of Dynamic Processes*, Pittsburgh, PA, pp. 199–204. Materials Research Society. Meeting in Boston, MA, 27–30 November, 1995.

Mitton, D. B., P. A. Marrone, and R. M. Latanision (1996, March). Interpretation of the rationale for feed modification in SCWO systems. *J. Electrochem. Soc.* **143** (3), L59–L61.

Mitton, D. B., J. C. Orzalli, and R. M. Latanision (1995). Corrosion studies in supercritical water oxidation systems. In K. P. Johnston and J. M. L. Penninger (Eds.), *Innovations in Supercritical Fluids: Science and Technology*, ACS Symposium Series #608. Washington, DC: American Chemical Society.

Sieradzki, K. and R. C. Newman (1987). Stress-corrosion cracking. *J. Phys. Chem. Solids* **48** (11), 1101–13.

Chapter 3

A Review of Electrochemical Thermodynamics at Elevated Temperatures and Pressures

Computing the thermodynamics of electrochemistry at elevated temperatures and pressures requires reformulation following reconsideration of the assumptions which are valid for room-temperature electrochemistry models. Several works (Macdonald and Butler 1973; Lee 1981; Huang *et al.* 1989; Kriksunov and Macdonald 1995; Kriksunov and Macdonald 1997) describe different approaches and approximations for high-temperature and high-pressure extensions to this modeling. In general, the theory is presented using standard electrochemical nomenclature, which makes it somewhat less accessible to the chemical engineering community. Many efforts, particularly those related to geochemistry, use well-established computer models such as `SupCrt92` (Johnson *et al.* 1992) and therefore do not report the nature of the thermodynamic assumptions in the calculations or models employed, except to first cite the computer program and then detail the properties of the particular system studied.

This chapter begins by introducing the reader to the elementary electrochemistry of corrosion. Next, an extension to elevated conditions will be presented, followed by its application to Pourbaix diagrams, and ending with a discussion of sources of data.

3.1 The Nernst Equation

The equation which connects electrical physics to solution chemistry is the Nernst equation. Below, the Nernst equation is derived from familiar thermodynamic con-

cepts. (See Odenweller (1990) for an alternative derivation with specific applications to semiconductor electrodes.)

The total differential energy of a system is usually expressed as

$$dU = \delta Q - \delta W = T\,dS - P\,dV \tag{3.1}$$

Here let us introduce a new term in the energy equation, the work term for electrons. The electron work is the potential that the electrons traverse multiplied by their charge, or

$$(\text{electron work}) = \mathbb{F}\mathbb{E}\,dn_e \tag{3.2}$$

where $\mathbb{E} \equiv \mathcal{V}_2 - \mathcal{V}_1$ is the change in electrical potential, $\mathbb{F}$ is the Faraday constant, and n_e is the number of electrons. The net energy change corresponds to the removal of an electron from one substance and the addition of an electron to a different substance.

The electrical work is incorporated into the equation for internal energy:

$$dU = T\,dS - P\,dV - \mathbb{F}\mathbb{E}\,dn_e \tag{3.3}$$

The last term of Equation 3.3, $\mathbb{F}\mathbb{E}\,dn_e$, has a negative contribution, which will now be verified. By convention, U decreases when the system considered performs work or otherwise moves to a state of lower potential or internal energy. Consider the system of the electron. The electron is at a potential $\mathcal{V}_1$. Somewhere else accessible by the electron the potential is $\mathcal{V}_2$, where $\mathcal{V}_2 > \mathcal{V}_1$. Naturally the electron, with its negative charge, is attracted to the more-positive $\mathcal{V}_2$ potential, and minimizes its energy by moving to the region of more-positive potential. In this picture, for an electron moving up into a more-positive potential, the sign must be negative, as the system of the electron is losing energy and moving to a more favorable state.

The second Legendre transform of Equation 3.3 is the Gibbs free energy,

$$dG = -S\,dT + V\,dP - \mathbb{F}\mathbb{E}\,dn_e \tag{3.4}$$

which will now be used to analyze an electrochemical process at constant T and P. Consider the half-reaction:

$$\mathrm{M}^{+}_{(\mathrm{aq})} + e^{-} \rightarrow \mathrm{M}_{(\mathrm{m})} \tag{3.5}$$

It is known that electrochemical reactions such as these need no external input, *i.e.*, a

battery with a resistor across its terminals needs not take energy from its surroundings to operate. This half-reaction can be split into two processes: an electrical and a chemical process. In the electrical picture, the system is an electron, and the electron is moving from one potential to another. In the chemical picture, the system is the metal ion or atom, M^+ or M, where the $M \rightleftarrows M^+$ reaction is driven by the change of potential of the electron in the other reaction. Thus the system of {electron + metal atom/ion} is subdivided into {electron} and {metal atom/ion}.

For the {electron} system, the sole change is the reversible movement of the electron from one potential to another. Integrating across such a process at constant pressure and temperature, we obtain

$$\Delta G = -n_e \mathbb{F} \mathbb{E} \tag{3.6}$$

Complementary to this electrical process is a chemical process within the system {metal atom/ion}. In this system the metal changes oxidation state and enters solution. This can also be visualized as one species being removed while another species takes its place.

The free energy change of this chemical process is described by

$$\Delta G = \sum_i \nu_i \mu_i \tag{3.7}$$

where $i \in \{M_{(m)}, M^+_{(aq)}\}$, ν_i is the reaction coefficient for species i (by convention negative for reactants, positive for products) and μ_i is the chemical potentials of species i. Because the electrical and chemical processes are complementary, their net effect on the surroundings is zero. The ΔG from one process equals the ΔG of its complement. Equating these, we obtain

$$\Delta G = -n_e \mathbb{F} \mathbb{E} = \sum_i \nu_i \mu_i \tag{3.8}$$

Since chemical potential is a relative value, we must include a reference state for each compound. To adhere to the convention, an electrochemical reference state $\mu_i^\square$ is used, which refers to a state of infinite dilution extrapolated to unit molality at the temperature and pressure of the system (see notes at the end of this section). Subtracting Equation 3.8 between an arbitrary condition ($\mathbb{E}$, μ_i) and a reference state

$(\mathbb{E}^{\square}, \mu_i^{\square})$, we obtain

$$-n_e\mathbb{F}(\mathbb{E} - \mathbb{E}^{\square}) = \sum_i \nu_i (\mu_i - \mu_i^{\square}) \tag{3.9}$$

$$= RT \sum_i \nu_i \ln a_i \tag{3.10}$$

where a_i is the activity of species i. This can be rearranged to the more familiar form of the Nernst equation,

$$\mathbb{E} = \mathbb{E}^{\square} - \frac{RT}{n_e\mathbb{F}} \ln \left[\prod_i a_i^{\nu_i} \right] \tag{3.11}$$

Thus we have an explicit relation between the electrical potential and the chemical activities of species participating in the net electrochemical reaction of a system.

A Word on Reference States In many mixture applications, the activity coefficient γ_i of species i is defined in terms of mole fraction x_i. This can be expressed with a pure-component reference state in terms of mixture fugacity $\hat{f}_i$ and pure-component fugacity f_i (using nomenclature of Tester and Modell (1997, Chapter 9)):

$$\hat{f}_i = \gamma_i x_i f_i(T, P, x_i{=}1) \qquad \text{such that} \qquad \gamma_i \to 1 \text{ as } x_i \to 1 \tag{3.12}$$

or with an infinite-dilution reference fugacity f_i^{**}, extrapolated to unit mole fraction:

$$\hat{f}_i = \gamma_i^{**} x_i f_i^{**}(T, P, x_i^{**}{=}0) \qquad \text{such that} \qquad \gamma_i^{**} \to 1 \text{ as } x_i \to 0 \tag{3.13}$$

Electrolyte applications employ a *practical* reference state which is based upon molality instead of mole fraction. For non-electrolyte purposes, the relation maintains its familiar form:

$$\hat{f}_i = \gamma_i^{*} m_i f_i^{+}(T, P, m_i^{+}{=}1) \qquad \text{such that} \qquad \gamma_i^{*} \to 1 \text{ as } m_i \to 0 \tag{3.14}$$

But electrolyte behavior is such that there is no linear limiting slope as concentration approaches zero. Instead, the limiting slope depends upon molality at a certain exponent:

$$\lim_{m \to 0} \hat{f}_{ij} = \hat{f}_{ij}^{\infty} = k m^{\nu} \tag{3.15}$$

Here, $\nu \equiv \nu_+ + \nu_-$ the sum of the moles of ions produced when one mole of electrolyte ij dissociates, and k is a limiting slope which can be estimated from Debye-Hückel theory. The equation for the mean ionic fugacity of electrolyte ij is thus:

$$\hat{f}_{ij}(T,P,m) \equiv k(\gamma_\pm m)^\nu = \frac{k(\gamma_\pm m)^\nu}{k/(\nu_+^{\nu_+}\nu_-^{\nu_-})} \hat{f}_{ij}^{\square}(T,P,m^{\square}=1) \tag{3.16}$$

where

$$\gamma_\pm \equiv \frac{a_\pm}{m_\pm} = \left(\gamma_i^{\nu_i}\gamma_j^{\nu_j}\right)^{1/\nu} \qquad a_\pm = a_i^{\nu_i}a_j^{\nu_j} \tag{3.17}$$

for cation i and anion j, $a_\pm$ is the mean ionic activity, and $\gamma_\pm$ is the mean activity coefficient. Constants ν_i and ν_j are the atom coefficients in the salt $C_{\nu_i}A_{\nu_j}$.

3.2 The Basic Pourbaix Diagram

A graphical means of showing the stability of metals and metal oxides as a function of electrochemical potential and acidity levels was developed by Pourbaix as an engineering tool to provide an heuristic visualization of the corrosion resistance of metals in dilute aqueous ionic solutions (Pourbaix 1964). The Pourbaix diagram (see Figure 3-1) is a thermodynamic stability diagram for a metal, its oxides, and hydroxides with equilibrium oxidation potential $\mathbb{E}$ plotted as a function of pH at a particular temperature and pressure. Pourbaix diagrams typically consider one elemental metal at a time. The solid materials are considered pure and separate. The practical-basis activities $\{a_i\}$ of the aqueous species are usually taken at 10^{-6} g·equiv/L while activities for solids and solvents are assumed to be unity.

The diagrams are constructed by applying the Nernst equation (3.11) to the chemical reactions expected in the chemical system. The $\Delta G^{\square}$ and ΔG of the reaction are converted through the Nernst equation to electrochemical potentials $\mathbb{E}^{\square}$ and $\mathbb{E}$. Dependence of the reaction free energy on the activities of OH^- or H^+ are computed through the definition $\text{pH} \equiv -\log a_{H^+}$ and ion dissociation constant K_w of water, as needed. A linear equation is formed by substituting the conventional activities into the equation.

Each line drawn on the Pourbaix diagram represents the equilibrium potential $\mathbb{E}$ and pH of a particular chemical reaction. In between the lines are domains in which a particular oxidation state of a metal compound in a particular state of aggregation is thermodynamically stable. Horizontal lines represent reactions which do not have

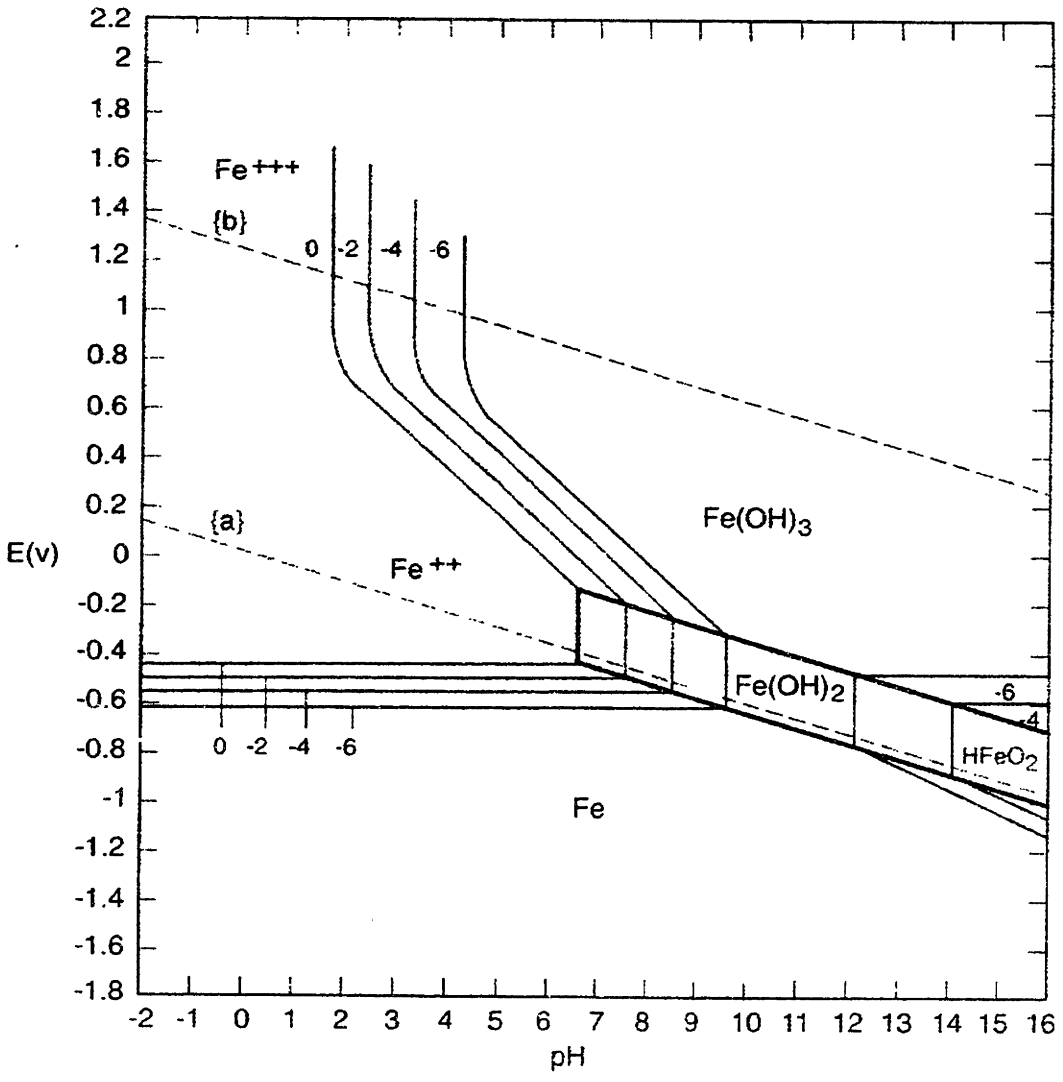

Figure 3-1 Pourbaix diagram for iron at 25° C and 1 atm pressure. Adapted from Jones (1996).

a pH-dependence but involve a change in oxidation state; vertical lines correspond to reactions which are pH-controlled and generally correspond to changes in state of aggregation or extent of hydrolysis. For instance, in a Pourbaix diagram for iron (Figure 3-1), the reaction $Fe^{2+} + 2e^- \rightarrow Fe$ is a horizontal line. Below the line, solid iron is stable. At an oxidation potential above the line, the iron dissolves.

3.2.1 A Typical Reaction Set

A Pourbaix diagram is only as good as the underlying model. Similarly to free-radical reaction networks, a number of species are involved in multiple reactions which are interdependent. However, in this case the mathematical relationships are not kinetic rate expressions, but thermodynamic relations of electrochemical equilibria. Because these involve charge-transfer reactions, the interplay is even more subtle—not only do concentrations of ions matter by changing the chemical potentials in the system, but the electrons being transferred have electrical potentials which can also drive reaction equilibria. A reaction set for iron specifically for hydrothermal conditions is given by Townsend (1970):

$$3Fe + 4H_2O \rightleftarrows Fe_3O_4 + 8H^+ + 8e^- \tag{3.18}$$

$$2Fe_3O_4 + H_2O \rightleftarrows 3Fe_2O_3 + 2H^+ + 2e^- \tag{3.19}$$

$$2Fe^{3+} + 3H_2O \rightleftarrows Fe_2O_3 + 6H^+ \tag{3.20}$$

$$Fe \rightleftarrows Fe^{2+} + 2e^- \tag{3.21}$$

$$Fe + 2H_2O \rightleftarrows HFeO_2^- + 3H^+ + 2e^- \tag{3.22}$$

$$3Fe^{2+} + 4H_2O \rightleftarrows Fe_3O_4 + 8H^+ + 2e^- \tag{3.23}$$

$$3HFeO_2^- + H^+ \rightleftarrows Fe_3O_4 + 2H_2O + 2e^- \tag{3.24}$$

$$2Fe^{2+} + 3H_2O \rightleftarrows Fe_2O_3 + 6H^+ + 2e^- \tag{3.25}$$

$$2HFeO_2^- \rightleftarrows Fe_2O_3 + H_2O + 2e^- \tag{3.26}$$

Note that only reactions 3.18 and 3.26 have no pH dependence and so will appear as horizontal lines. Reaction 3.20 has no net charge, and is the only reaction which can be represented by a vertical line.

Two special reactions are also commonly noted on the Pourbaix diagram: the hydrogen and oxygen redox reactions. The hydrogen reaction can be written either of the following two ways. The reactions, in acidic and alkaline media, respectively,

are:

$$2H^+ + 2e^- \rightleftarrows H_2 \tag{3.27}$$

$$2H_2O + 2e^- \rightleftarrows H_2 + 2OH^- \tag{3.28}$$

where the difference between the two is the simple addition of OH^- to either side of the equation. Similarly, the oxygen reaction in acidic and alkaline media, respectively, is:

$$O_2 + 4H^+ + 4e^- \rightleftarrows 2H_2O \tag{3.29}$$

$$O_2 + 2H_2O + 4e^- \rightleftarrows 4OH^- \tag{3.30}$$

These reactions do not directly affect the thermodynamic stability of the metal and related compounds, but as can be seen from reactions 3.18–3.26 are involved in the conversion of some key reactants in the reaction network. Thus they are superimposed onto the Pourbaix diagram, usually as dashed lines. In between the (lower) hydrogen line and the (upper) oxygen line, water is chemically stable. Below the hydrogen line, H_2 gas is evolved. Above the oxygen line, O_2 gas is evolved.

3.2.2 Example

To plot a line on a Pourbaix diagram, one starts with the reaction of interest and its corresponding standard free energy, and then expresses this free energy as a function of activities using the Nernst equation. The Pourbaix conventions for activity are then substituted, and the result is a linear equation which can be plotted in $\mathbb{E}$–pH space. As an example, the hydrogen reduction reaction in acidic media (Reaction 3.27) is considered. The Nernst equation for this reaction is:

$$\mathbb{E} = \mathbb{E}^\square - \frac{RT}{2\mathbb{F}} \ln \left[\frac{a_{H_2}^2}{a_{H^+}^2} \right] \tag{3.31}$$

$$\therefore \quad \mathbb{E} = \mathbb{E}^\square - \frac{RT}{\mathbb{F}} \left[\ln a_{H_2} + 2.303\,\mathrm{pH} \right] \tag{3.32}$$

If the equation is presented with OH^- instead of H^+ as a reactant, the water dissociation reaction must be used to convert between them. For a more detailed example of Pourbaix diagram construction, see Jones (1996, Ch. 2).

3.3 Non-Standard Conditions

Standard Pourbaix diagrams are very popular for ambient-temperature design and troubleshooting applications, and more recently, at temperatures up to 300° C for power-generating applications. Existing electrochemical computations for temperatures up to 300° C, however plentiful, deal with dense water ($\rho = 0.78\,\mathrm{g}\cdot\mathrm{cm}^{-3}$ at 500 bar to $\rho = 0.72\,\mathrm{g}\cdot\mathrm{cm}^{-3}$ at 100 bar), whereas at 380° C and 250 bar the water is significantly less dense ($\rho = 0.45\,\mathrm{g}\cdot\mathrm{cm}^{-3}$). It is expected, then, that the behavior at these conditions will not be a simple extrapolation of the previous temperature trends, but must include the effect of the changing solvent properties of the water. For these applications, then, more data is required than is currently available. Without further information in the high-P,T regime it is the only recourse to knit the existing data with extrapolations based on lower temperature data and equations of state which explicitly consider the effect of the changing solvent structure on the $\overline{\Delta G_i}$'s.

As shown in Equation 3.8, the potential $\mathbb{E}$ depends on the free energy of reaction. The free energy change for a chemical reaction is the stoichiometric sum of the chemical potentials of its reactants,

$$\Delta G_{rxn}(T, P, x_1, \ldots, x_{n-1}) = \sum_i \nu_i \mu_i(T, P, x_1, \ldots, x_{n-1}) \tag{3.33}$$

where the $\{\nu_i\}$ are the reaction coefficients (by convention negative for reactants, positive for products) and the $\{\mu_i\}$ are the chemical potentials of each species i, as noted earlier. Each μ_i can be related to its chemical potential at a standard state, μ_i°, by integrating through the general expression[1]

$$d\mu_i = d\overline{G}_i = -\overline{S}_i\,dT + \overline{V}_i\,dP + \sum_{m=1}^{n}\left(\frac{\partial \mu_m}{\partial N_i}\right)_{T,P,N_{j\neq i}} dN_m \tag{3.34}$$

The Gibbs free energy change from standard state can be represented as an excess function:

$$\mu_i - \mu_i^\square = \overline{\Delta G}_i^{\mathrm{EX}} + \overline{\Delta G}_i^{\mathrm{ID}} \tag{3.35}$$

[1] Overbars denote partial molar properties, defined as $\overline{B}_i \equiv (\partial B/\partial N_i)_{T,P,N_{j\neq i}}$ for arbitrary extensive property B.

where for constant T and P the ideal Gibbs free energy change is

$$\overline{\Delta G}_i^{\mathrm{ID}} = RT \ln \frac{x_i}{x_i^{\square}} \tag{3.36}$$

The standard partial molar excess Gibbs free energies are sometimes available from equations of state, such as the HKF Equation of State (Tanger and Helgeson 1988). The standard partial molar excess Gibbs free energy is referenced to the electrochemical reference state ($\mu^{\square}$) which employs an infinite-dilution reference state extrapolated to a fictitious unit-molality state. It can be shown that while $\overline{\Delta G}_i^{\mathrm{ID}}$ depends on the reference state, $\overline{\Delta G}_i^{\mathrm{EX}}$ does not, so long as pressure and temperature are kept constant (Tester and Modell 1997, p. 356).

For the electrolytes, it might also be convenient, when available, to use activity models of the form

$$\mu_i - \mu_i^{\square} = RT \ln a_i \tag{3.37}$$

$$= RT \ln \gamma_i + \overline{\Delta G}_i^{\mathrm{ID}} \tag{3.38}$$

where a_i is the activity of the species. These are often expressed in terms of mean ionic activity of a binary solute ij, in which case the activity would be $a_{\pm} \equiv a_i^{\nu_i} a_j^{\nu_j}$ and its activity coefficient $\gamma_{\pm} \equiv (\gamma_i^{\nu_i} \gamma_j^{\nu_j})^{1/\nu}$. Constants ν_i and ν_j are the atom coefficients in the salt $\mathrm{C}_{\nu_i}\mathrm{A}_{\nu_j}$.

3.3.1 An Example at Hydrothermal Conditions

For the reaction

$$\mathrm{Fe}_{(\mathrm{aq})}{}^{3+} + e^- \rightleftarrows \mathrm{Fe}_{(\mathrm{aq})}{}^{2+} \tag{3.39}$$

the corresponding Nernst equation is

$$\mathbb{E} = \mathbb{E}^{\square} - \frac{RT}{n_e \mathbb{F}} \ln \left[\frac{a_{\mathrm{Fe}^{2+}}}{a_{\mathrm{Fe}^{3+}}} \right] \tag{3.40}$$

where $n_e = 1$.

To obtain the proper line for high T and P, most of the work involved is spent

T	$\mu_{Fe^{2+}}$			$\mu_{Fe^{3+}}$			$\Delta G^{\square}$	$\mathbb{E}^{\square}$
[° C]	P^{sat}	500 bar	≈250 bar	P^{sat}	500 bar	≈250 bar	[cal·mol^{-1}]	[mV (SHE)]
250	-15.52	-16.04	-15.65	13.22	12.23	12.97	-28.62	+1.24
300	-13.70	-14.45	-13.89	18.01	16.64	17.66	-31.55	+1.37
350	-11.89	-12.68	-12.09	22.51	21.39	22.23	-34.32	+1.49

Table 3.1 Computation of the standard Gibbs free energy of reaction for conversion between iron(II) and iron(III). Data from Oelkers *et al.* (1995). Saturation pressure P^{sat} was taken to be the pure water saturation pressure of 165 bar (Haar *et al.* 1984). Results for 250 bar were linearly interpolated.

obtaining a proper $\mathbb{E}^{\square}$ value. Rewriting Equation 3.8 for the reference state,

$$\Delta G^{\square} = -n_e \mathbb{F} \mathbb{E}^{\square} = \sum_i \nu_i \mu_i^{\square} \tag{3.8'}$$

Using the HKF Equation of State calculations of Oelkers *et al.* (1995) for $\overline{\Delta G_i}^{\square}$ of Fe^{2+} and Fe^{3+}, we find that $\mathbb{E}^{\square}$ is relatively easily computed for the given conditions (Table 3.1.) For the reaction at 300° C and 250 bar, the corresponding Pourbaix diagram line is defined by:

$$\mathbb{E} = (1.37 \times 10^{-3}\,\mathrm{V}) - (4.94 \times 10^{-2})\,\mathrm{V}\,\ln\left[\frac{10^{-6}}{10^{-6}}\right] = (1.37\,\mathrm{mV}) \tag{3.41}$$

Thus, with access to thermodynamic data in the correct form, the construction of a Pourbaix diagram for higher temperature and pressure is achievable with relative ease. For instance, Mitton *et al.* (1996) composed a Pourbaix-type diagram for the Ni-Cr-Mo-Fe system at 300° C (Figure 3-2).

When explicit data for $\overline{\Delta G_i}^{\square}$ are not available, they must be inferred by other means. With some data, an equation of state can be used to extrapolate and interpolate between state points. Lacking this, or proper substitutes thereof, there are some simpler models which can be employed to estimate properties at high temperature and pressure. Generally speaking, the thermodynamic data for the aqueous species at hydrothermal conditions is not available, while for solid materials the data are often tabulated.

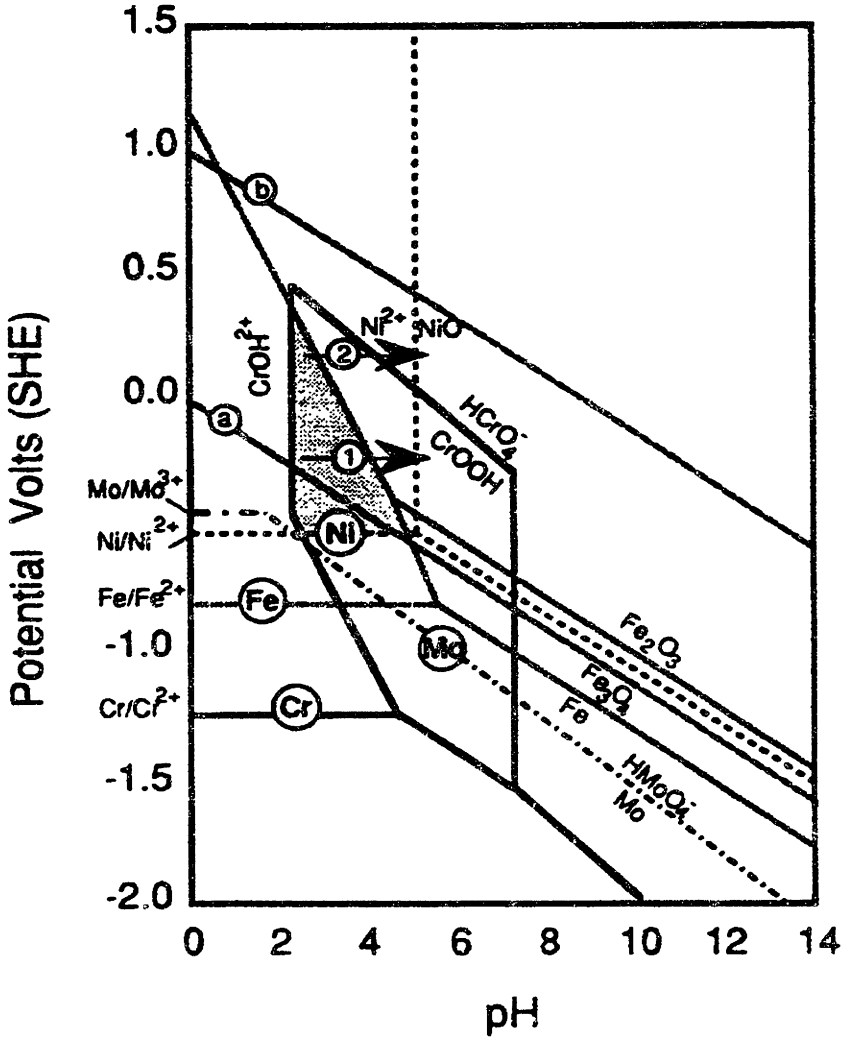

Figure 3-2 Superimposed Pourbaix diagram for Ni, Cr, Mo, and Fe at 300° C. From Mitton *et al.* (1996).

3.4 Thermodynamic Models for Aqueous Species

3.4.1 HKF Equation of State

While there are many equations of state (EOS) available for describing the thermodynamic properties of aqueous species, perhaps the most popular EOS used in the corrosion literature today for describing the behavior of aqueous ions at high pressure and temperature (Kriksunov and Macdonald 1995; Anderko *et al.* 1997; Kriksunov and Macdonald 1997) is the Helgeson-Kirkham-Flowers (HKF) EOS (Oelkers *et al.* 1995). This EOS has a fairly extensive library of compounds treated in its library, and also has a FORTRAN program, `SupCrt92` (Johnson *et al.* 1992), which provides a convenient interface between the engineer and the model. It also treats electrostriction explicitly. (Electrostriction, a phenomenon in which the density of an ion's first solvation shell is of a higher density than the bulk, is significant at intermediate and lower solvent densities and is therefore relevant to supercritical water conditions.) In general, the HKF EOS splits the partial molal properties of an aqueous ion into solvation and nonsolvation contributions.

$$\overline{B}_j^\circ = \Delta\overline{B}_{n,j}^\circ + \Delta\overline{B}_{s,j}^\circ \tag{3.42}$$

where B is an arbitrary partial molal property and subscripts n and s refer to nonsolvation and solvation contributions, respectively. Electrostriction effects are divided between the solvation and nonsolvation contributions. Solvation effects include the interactions between ion and solvent, including the electrostatic interactions causing electrostriction. Nonsolvation effects are the contributions from the intrinsic properties of the ion as well as the mechanical contributions from structural collapse around the ion during electrostriction.

Solvation contributions are handled via the Born equation (Born 1920)

$$\Delta\overline{G}_{s,j}^\circ = \omega_j \left(\frac{1}{D_s} - 1\right) \tag{3.43}$$

where ω_j is the conventional Born coefficient of aqueous species j, defined by

$$\omega_j \equiv \omega_j^{abs} - Z_j \omega_{H^+}^{abs} \tag{3.44}$$

$$\omega_j^{abs} \equiv \frac{N_A e^2 Z_j^2}{2 r_{e,j}} \tag{3.45}$$

where $\omega_{H^+}^{abs}$ is the absolute Born coefficient of the hydrogen ion, N_A is Avogadro's

number, e is an elementary charge, and Z_j and $r_{e,j}$ correspond respectively to the charge and effective electrostatic radius of j. The electrostatic radius is described in terms of crystallographic radius $r_{x,j}$ as

$$r_{e,j} = r_{x,j} + |Z_j|\Gamma_Z \tag{3.46}$$

where

$$\Gamma_Z \equiv k_z + g \tag{3.47}$$

where k_z is a constant (0.94 for cations, 0.0 for anions) and g is a complex function of density which is described by the following equations:

$$g = 0.5(-b + \sqrt{b^2 - 4c}) \tag{3.48}$$

$$b = 3.72 - 2\eta \left(\sum_{i=-1}^{4} \sum_{j=0}^{4} a_{ij} T^i \rho^j \right)^{-1} \tag{3.49}$$

$$c = 3.4571 - 3.72\eta \left(\sum_{i=-1}^{4} \sum_{j=0}^{4} a_{ij} T^i \rho^j \right)^{-1} \tag{3.50}$$

where ρ is the specific density of water, the twenty-one $\{a_{ij}\}$ are solvent-property curve-fit parameters,[2] and $\eta \equiv N_A e^2/2$ is a unit factor. With a functional estimate for ω_j the solvation contribution to partial molal properties is determined from

$$\Delta\overline{V}^{\circ}_{s,k} = -\frac{\omega_k}{(D_s)^2} \left(\frac{\partial D_s}{\partial T} \right)_T \tag{3.51}$$

$$\Delta\overline{\kappa}^{\circ}_{s,k} = \frac{\omega_k}{(D_s)^2} \left[\left(\frac{\partial^2 D_s}{\partial P^2} \right)_T - \frac{2}{D_s} \left(\frac{\partial D_s}{\partial P} \right)^2_T \right] \tag{3.52}$$

$$\Delta\overline{(C_p)}^{\circ}_{s,k} = \frac{\omega_k T}{(D_s)^2} \left[\left(\frac{\partial^2 D_s}{\partial T^2} \right)_P - \frac{2}{D_s} \left(\frac{\partial D_s}{\partial T} \right)^2_P \right] \tag{3.53}$$

The nonsolvation contribution to the partial molal properties is handled through

[2] The $\{a_{ij}\}$ do not form a full 5×6 matrix.

temperature- and pressure-dependent functions.

$$\Delta\overline{V}^{\circ}_{n,k} = a_{1,k} + a_{2,k}\mathfrak{F}_2(P) + a_{3,k}\mathfrak{F}_1(T) + a_{4,k}\mathfrak{F}_2(P)\mathfrak{F}_1(T) \tag{3.54}$$

$$-\Delta\overline{\kappa}^{\circ}_{n,k} = (a_{2,k} + a_{4,k}\mathfrak{F}_1(T))\left(\frac{\partial\mathfrak{F}_2(P)}{\partial P}\right)_T \tag{3.55}$$

$$\Delta\overline{(C_p)}^{\circ}_{n,k} = c_{1,k} + c_{2,k}\mathfrak{F}_1(T) \tag{3.56}$$

where

$$\mathfrak{F}_1(T) = 1 + \Theta_k\left(\frac{1}{T-\Theta_k}\right) \qquad\qquad \mathfrak{F}_2(P) = \frac{1}{\Psi + P}$$

The constants $a_{1,k}, \ldots, a_{4,k}$, $c_{1,k}$, $c_{2,k}$, Θ_k and Ψ are all solvent-dependent constants.

3.4.2 Other $PVTx_i$ Equations of State

Other equations of state which describe solubility phenomena near and above the critical point of pure water is the Pitzer-Anderko EOS (Anderko and Pitzer 1993). General purpose cubic equations of state may also apply: Peng-Robinson, Redlich-Kwong-Soave, Renon-Swartz (Tester and Modell 1997, Chapter 9).

3.4.3 Activity Coefficient Models for Aqueous Ions

An alternative to a full $PVTx_i$ equation of state is to use activity coefficients to account for non-ideal effects that scale with changes in solvent density or dielectric constant.

Debye-Hückel Theory The most fundamental of these models is an extended Debye-Hückel theory. The Debye-Hückel model is based upon the difference in work needed to charge an ion in a dilute solution vs. in a pure solvent, where the solvent is assumed to be a structureless dielectric continuum.

$$kT\ln\gamma_i = \frac{(z_i e)^2}{8\pi\epsilon_0 D_s}\frac{\kappa}{1+\kappa b} + \frac{\overline{V_i}\,kT}{8\pi N_A\, b^3}\left[1 + \kappa b - \frac{1}{1+\kappa b} - 2\ln(1+\kappa b)\right] \tag{3.57}$$

where

$$\kappa^2 \equiv \frac{\mathbb{F}^2}{\epsilon_0 D_s kT}\sum_{j}^{\text{all ions}}\langle C_j^{\circ}\rangle\, z_j^2 \tag{3.58}$$

and

N_A = Avogadro's number

b = ion radius

$\overline{V_i}$ = partial molar volume of species i

z_i = charge on ion i

The $\overline{V_i}$-term in Equation 3.57 is often negligible, producing the simpler expression

$$kT \ln \gamma_i \approx \frac{(z_i e)^2}{8\pi\epsilon_0 D_s} \frac{\kappa}{1+\kappa b} \tag{3.59}$$

Pitzer Ion Interaction Model The ion interaction model developed by Pitzer extends the Debye-Hückel equation in a manner consistent with the McMillan-Mayer osmotic-pressure virial expansion. For any i:1 or 1:j electrolyte:

$$\ln \gamma_\pm = |z_+ z_-| f^\gamma + m \left(\frac{2\nu_+\nu_-}{\nu}\right) B_\pm^\gamma + m^2 \left(\frac{2(\nu_+\nu_-)^{3/2}}{\nu}\right) C_\pm^\gamma \tag{3.60}$$

where

$$f^\gamma = -3A_\phi \left[\frac{\sqrt{I}}{1+b\sqrt{I}} + \frac{2}{b}\ln\left(1+b\sqrt{I}\right)\right]$$

$$A_\phi = \frac{1}{3}(2\pi(1000)N_A\rho_s)^{1/2}\left[\frac{e^2}{4\pi\epsilon_0 D_s kT}\right]^{3/2}$$

$$B_\pm^\gamma = 2\beta_0 + \frac{2\beta_1}{\alpha^2 I}\left[1-(1+\alpha\sqrt{I}-0.5\alpha^2 I)\exp(-\alpha\sqrt{I})\right]$$

$$C_\pm^\gamma = \frac{3}{2}C_\pm^\phi$$

I = ionic strength

m = molal concentration

β_0, β_1, $C_\pm^\phi$ are fitted parameters

α, b are constants

Meissner Corresponding States Model Meissner and Tester (1972) developed a set of Γ_{ij} vs. I curves which are analogous to the compressibility charts for

compressibility factor. The model is defined by

$$\Gamma^{\circ}_{ij} = \left[1 + B(1+0.1I)^{q^{\circ}_{ij}} - B\right] \Gamma^{DH}_{ij}$$

$$\log_{10} \Gamma^{DH}_{ij} = \frac{-0.5107\sqrt{I}}{1 + C\sqrt{I}}$$

$$B = 0.75 - 0.065\, q^{\circ}_{ij}$$

$$C = 1 + 0.055\, q^{\circ}_{ij} \exp(-0.023\, I^3)$$

where q°_{ij} is an empirical parameter. The extension to mixtures involves a sum on the individual contributions.

$$\log_{10} \Gamma^{mix}_{ij} = \frac{|z_i|}{|z_i| + |z_j|} \sum_{j'}^{\text{anions}} \frac{(|z_i| + |z_{j'}|)^2}{2|z_i z_{j'}|} X^*_{j'} \log_{10} \Gamma^{\circ}_{ij'} + \frac{|z_i|}{|z_i| + |z_j|} \sum_{i'}^{\text{cations}} \frac{(|z_{i'}| + |z_j|)^2}{2|z_{i'} z_j|} X^*_{i'} \log_{10} \Gamma^{\circ}_{i'j} \quad (3.61)$$

where $X^*_{i \text{ or } j}$ are fractional ionic strengths:

$$X^*_{j'} \equiv \frac{I_{j'}}{I} = \frac{m_{j'} z^2_{j'}}{\sum_{\text{all ions}} m_i z^2_i} \qquad X^*_{i'} \equiv \frac{I_{i'}}{I} = \frac{m_{i'} z^2_{i'}}{\sum_{\text{all ions}} m_j z^2_j}$$

Chen Local Composition Model The model developed by Chen *et al.* (1982) combines three types of theories to consider cation-centered cells, anion-centered cells, and molecule-cetered cells. The long-range effects of an extended Debye-Hückel model are combined with a Born approximation contribution and a short-range local contribution.

As this model incorporates the complexity of three different models, it will not be mathematically expressed here.

These electrolyte models were first developed for ambient or near-ambient conditions. While they can be extremely accurate for ambient conditions, performance may deteriorate at higher temperatures (Tester and Modell 1997, p. 545).

3.5 Critique

While the Pourbaix diagram is a useful heuristic tool for materials selection and design, its applicability to supercritical water oxidation systems is not straightforward.

For instance, when there are significant quantities of metallic contaminants or anions such as sulfate, phosphate, or chloride, many more reactions become possible which need to be taken into account. Further, it may be more practical to have a system with the oxygen concentration itself, rather than the electrochemical oxidation potential, on the vertical axis, especially in systems where the oxygen concentration fluctuates the most widely.

Work by Anderko *et al.* (1997) has broken ground by beginning to generalize the Pourbaix diagram treatment beyond elemental metals and hydroxides to include sulfates, sulfides, ammonia, and chlorides. These *real-solution* stability diagrams have the potential not only to describe alloys and their stability in water, but also in the presence of other cations such as sulfates. They are generated by using the thermodynamic information available not only for half-reactions between metals and hydroxides, but also for the other non-metal species and all of their expected products.

With the knowledge that aggressive species such as chloride also change the corrosion resistance of normally "passive" films (such as Cr_2O_3), it also becomes necessary to examine not only the relative thermodynamic stability of the participant species but also to assess the impact of the aggressive species upon the corrosive susceptibility. A Pourbaix diagram that shows a stable passive film for a highly chlorinated system cannot be trusted until the behavior of the film in the presence of chlorides is well characterized. Despite the increases in descriptive capability afforded by extended treatments, Pourbaix and real-solution stability diagrams are still hueristic corrosion-engineering tools which depend upon experimental knowledge of passive layers to evaluate corrosion resistance.

Bibliography

Anderko, A. and K. S. Pitzer (1993). Equation-of-state representation of phase equilibria and volumetric properties of the system NaCl-H_2O above 573 K. *Geochim, [Comochim], Aeta* **57**, 1657–80.

Anderko, A., S. J. Sanders, and R. D. Young (1997). Real-solution stability diagrams: A thermodynamic tool for modeling corrosion in wide temperature and concentration ranges. *Corrosion* **53** (1), 43–53.

Born, V. M. (1920). Volumen und Hydrationswärme der Ionen. *Zeitschr. Physik* **1**, 45–48.

Chen, C. C., H. I. Britt, J. F. Boston, and L. B. Evans (1982). Local composition model for excess Gibbs energy of electrolyte solutions. Part 1: Single solvent, single completely dissociated electrolyte systems. *AIChE Journal* **28** (4), 588–596.

Haar, L., J. S. Gallagher, and G. S. Kell (1984). *NBS/NRC Steam Tables.* Hemisphere Publishing Corp.

Huang, S., K. Daehling, T. E. Carleson, P. Taylor, C. Wai, and A. Propp (1989). Thermodynamic analysis of corrosion of iron alloys in supercritical water. In K. P. Johnston and J. M. L. Penninger (Eds.), *Supercritical Fluid Science and Technology*, ACS Symposium Series #406. American Chemical Society.

Johnson, J. W., E. H. Oelkers, and H. C. Helgeson (1992). SUPCRT92: A software package for calculating the standard molal thermodynamic properties of minerals, gases, aqueous species, and reactions from 1 to 5000 bar and 0 to 1000° C. *Computers and Geosciences* **18** (7), 899–947.

Jones, D. A. (1996). *Principles and Prevention of Corrosion.* Upper Saddle River, NJ: Prentice Hall.

Kriksunov, L. and D. Macdonald (1997). Potential-pH diagrams for iron in supercritical water. *Corrosion* **53** (8), 605–611.

Kriksunov, L. B. and D. D. Macdonald (1995, Feb. 6–9). Development of Pourbaix diagrams for metals in supercritical aqueous media. In *Proceedings of First International Workshop on Supercritical Water Oxidation*, Jacksonville, FL.

Lee, J. B. (1981, August). Elevated temperature potential-pH diagrams for the Cr-H_2O, Ti-H_2O, Mo-H_2O, and Pt-H_2O systems. *Corrosion* **37** (8), 467.

Macdonald, D. D. and P. Butler (1973). The thermodynamics of the aluminum-water system at elevated temperatures. *Corrosion Science* **13**, 259–74.

Meissner, H. P. and J. W. Tester (1972). Activity coefficients of strong electrolytes in aqueous solutions. *Ind. Eng. Chem. Proc. Des. Dev.* **11** (1), 128–133.

Mitton, D. B., P. A. Marrone, and R. M. Latanision (1996, March). Interpretation of the rationale for feed modification in SCWO systems. *J. Electrochem. Soc.* **143** (3), L59–L61.

Odenweller, T. (1990, August). On the theory of the semiconductor/electrolyte-interface (I). *J. Electrochem. Soc.* **137** (8), 2457–61.

Oelkers, E. H., H. C. Helgeson, E. L. Shock, D. A. Sverjensky, J. W. Johnson, and V. A. Pokrovskii (1995). Summary of the apparent standard partial molal Gibbs free energies of formation of aqueous species, minerals, and gases at pressures 1 to 5000 bars and temperatures 25 to 1000°C. *J. Phys. Chem. Ref. Data* **24** (4), 1401.

Pourbaix, M. (1964). *Atlas of Electrochemical Equilibria.* London: Pergamon Press.

Tanger, IV, J. C. and H. C. Helgeson (1988). Calculation of the thermodynamic and transport properties of aqueous species at high pressures and temperatures: Revised equations of state for the standard partial molal properties of ions and electrolytes. *American Journal of Science* **288**, 19.

Tester, J. W. and M. Modell (1997). *Thermodynamics and Its Applications* (3rd ed.). Upper Saddle River, NJ: Prentice Hall.

Townsend, Jr., H. E. (1970). Potential-pH diagrams at elevated temperature for the system Fe-H_2O. *Corrosion Science* **10**, 343–58.

Chapter 4

Experiments

This chapter presents experimental investigations of Hastelloy C-276 tubing in hydrothermal HCl. Section 4.1 reviews and analyzes failures which occurred during reaction-kinetics experiments. Section 4.2 presents the experiment which was developed to reproduce and analyze in depth the corrosion which produced the kinetics-experiment failures (see also Cline *et al.* (2000)).

4.1 Methylene Chloride Experiments

A number of CH_2Cl_2 hydrolysis and oxidation experiments were performed in sub- and supercritical water using a plug flow, tubular reactor system. The original purpose of these experiments was to determine the kinetics of CH_2Cl_2 decomposition under these oxidative and nonoxidative pyrolysis or hydrolysis conditions. Detailed descriptions of the apparatus, experimental operating procedures and run conditions, and analytical techniques used for identification of products are given elsewhere (Marrone 1998; Marrone *et al.* 1995; Tester *et al.* 1998; Marrone *et al.* 1998). A description of the heated section of the experimental apparatus is repeated here as it is relevant to the heat transfer analysis and temperature profile modeling discussed subsequently.

The coiled preheater tubing and main tubular reactor of the experimental system were heated in a fluidized sand bath (see Figure 1-4 on page 25). There were two separate preheater coils; one for a pressurized aqueous feed solution of CH_2Cl_2 and another for a pressurized O_2/water solution (for oxidation runs) or just pressurized pure deionized water (DW) for hydrolysis runs. Each preheater coil was approximately 3 m in length, with the lower 2.75 m submerged in the hot, fluidized sand. The tubing had an ID of 0.108 cm and a wall thickness of 0.025 cm, and was made out of welded, drawn, solution-annealed Hastelloy C-276. (See Tables 4.4 and 4.5

for details.) Both feeds entered their respective preheaters at ambient temperature and were heated to a specified operating temperature before reaching a mixing tee and the main reactor. For the oxidation runs, oxidizing conditions existed only in the main reactor, after the point at which the aqueous O_2 and CH_2Cl_2 feed solutions were mixed. Hydrolysis conditions always existed in the CH_2Cl_2 feed preheater coil in all experiments. Measured mixing tee temperatures were usually within about 5° C of the sand bath temperature. The main reactor tube was 4.71 m in length, had a 0.171 cm ID and 0.232 cm wall thickness, and was constructed of Inconel 625. The main reactor was always kept at turbulent (*i.e.*, nearly plug) flow and isothermal conditions, while laminar conditions did exist in sections of the preheater tubing during some experiments. The reactor exit temperature was measured just before the fluid exited the sand bath and entered a heat exchanger where the reaction products were cooled to ambient temperature, followed by reduction of pressure to atmospheric.

Temperature, residence times, and feed concentrations were varied considerably over all of the experiments performed. Reactor temperatures were always kept supercritical and maintained within a few degrees of the sand bath temperature, which was varied from 450 to 600° C. Temperatures in the preheater tubing ranged from ambient at the entrance to the operating sand bath temperature. Ambient CH_2Cl_2 feed concentrations at the entrance to the preheater tubing ranged from 0.006 to 0.038 M. After accounting for subcritical hydrolysis in the preheater (Marrone *et al.* 1998), the effects of decreasing density with increasing fluid temperature, and dilution from mixing with the O_2 feed solution (or deaerated distilled water (DDW) in hydrolysis experiments), CH_2Cl_2 concentrations at the entrance to the main reactor were calculated to range from 0.0002 to 0.0006 M. Concentrations of CH_2Cl_2 in the effluent from the reactor under ambient conditions were measured to be 1×10^{-5} to 9×10^{-3} M. O_2 concentrations at the entrance to the main reactor ranged from 0.0006 to 0.0021 M. Residence times in the main reactor ranged between 4 and 9 s, while residence times in the preheater tubing (calculated from temperature profile models described below) were generally longer, from 7 to 17 s. All experiments were isobaric at approximately 246 bar.

Severe corrosion, resulting in through-wall failure, was observed in four separate CH_2Cl_2 feed preheater coils over the course of these experiments. In each case, the failure occurred in a region between 7 and 29 cm downstream of the point at which the tubing entered the sand bath. Tube life before failure ranged from 45 to 104 hrs of use at operating temperatures (see Table 4.1). The liquid effluent pH measured at ambient temperature typically ranged between 1.5 and 2.5, due primarily to HCl

Preheater Tube #	Total Time of Exposure to CH_2Cl_2 Feed† (h)	Position of Tube Failure Relative to the Beginning of the Tube (cm)	Position of Tube Failure Relative to the Point Where Heating Begins (cm)
1	104	41	11
2	45	59	29
3	56	37	7

Table 4.1 Corrosive failure data for preheater tubing.

† At operating temperatures.

formed from CH_2Cl_2 hydrolysis. HCl concentrations in the ambient effluent varied from 4 to 25 mM.

Measured values of CH_2Cl_2 conversion varied from 26±9% to 91±1% for pure hydrolysis experiments and from 30±9% to 99.9±0.1% for oxidation experiments (Marrone *et al.* 1995). The significant conversions observed during hydrolysis experiments, along with the evidence of corrosion occurring early in the preheater tubing, strongly suggest that hydrolysis of CH_2Cl_2 in the preheater tubing was fairly rapid and substantial. From a kinetics perspective, knowledge of the axial temperature profile along the preheater tubing as a function of position and time is essential if one is to properly infer hydrolysis kinetic parameters from the data. From a corrosion perspective, however, temperature-time profiles are also important for characterizing the conditions under which the observed corrosion phenomena occurred in this sub- and supercritical water system.

4.1.1 Failure Analysis of Preheaters

Three of the four organic preheater tubes (apparatus in Figure 1-4 on page 25) that failed prematurely during the CH_2Cl_2 experiments described above were examined. Each failed by developing an intergranular crack. Ni, Mo, and Fe were depleted in the corrosion layer, but the corrosion layer exhibited no volume changes, suggesting dealloying. Grain boundaries, visible in the metal, also extended into the corrosion layer. Time-to-failure for these three preheaters allows estimation of a minimum crack propagation rate of 21.4 to 39.8 mm/y, which is within the normal range for stress corrosion cracking (SCC). Failures were observed only within an approximately 22-cm

region near the inlet of the preheater, despite variations in experiment flow rate, feed composition, and sand bath temperature.

Preheaters #2 and #3 were cut into sections of 30 mm, which were cold-mounted, polished, and viewed on an optical and confocal laser scanning microscope (CLSM). Figures 4-1(a) and 4-1(b) illustrate the extent of the intergranular and dealloying corrosion (in terms of % of tube wall) as a function of distance from the preheater inlet. A temperature profile for typical operating conditions is depicted. The locations of the final through-wall cracks are indicated by arrows. Both failures occurred within regions which exhibited a fairly high corrosion rate. In general, the extent of dealloying was less than but approximately proportional to that of cracking.

Figure 4-1(b) shows two main peaks in extent of cracking. The maximum at 375 mm is attributed to environmental conditions, but the peak at 550 mm corresponds to a region in which there is a tight (radius $\approx$ 10 mm) 90° bend, suggesting that stress may be a significant contributor to the magnitude of intergranular cracking.

Figure 4-2 is an ESEM image of the tube cross-section 1.5 cm upstream from the first preheater failure site. Both generally uniform dealloying and intergranular cracking are visible. Also visible is a banded structure, which appears in many of the preheater samples. In the cooling-tube experiment (Section 4.2) we find that this banded structure does not occur unless there are multiple thermal cycles, indicating that the bands correspond to the operational cycles (thermal and chemical) to which the tube was exposed. The only detectable difference in composition between light and dark bands was the oxygen concentration, which, as found in a previous study (Mitton *et al.* 1995), is higher in the lighter-colored bands.

Deeper within the banded structure, a chevron pattern, which has good registry with the grain boundaries, is visible. That the upper bands do not exhibit this chevron pattern indicates that originally the corrosion front was uniform—without cracking or other grain-boundary preference—and later evolved such that the grain boundaries were preferentially attacked. The pattern becomes successively wider as one proceeds to deeper lamellae; the angle of the chevron point is constant. This corresponds to the grains being attacked preferentially at the grain boundaries, becoming rounded off. The pattern does not appear at every grain boundary, suggesting that the angle of the striations corresponds to an attack-governing feature, such as a crystal plane, in the constituent grains.

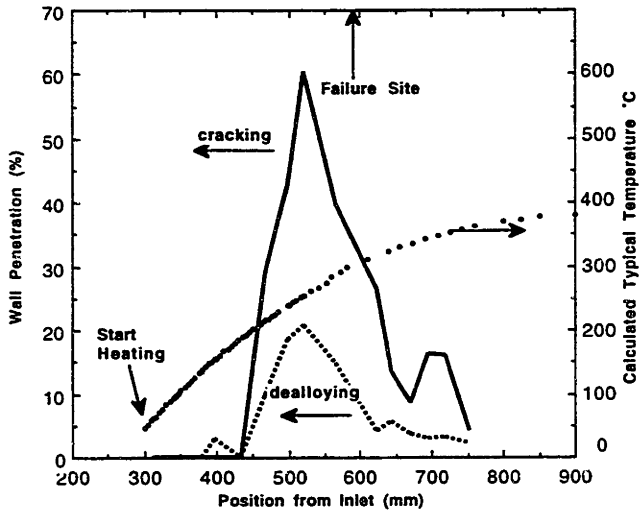

(a) Preheater #2

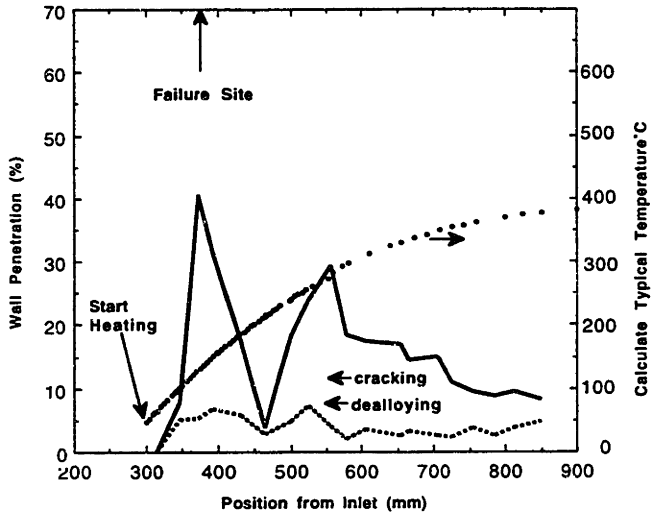

(b) Preheater #3

Figure 4-1 Extent of intergranular corrosion and dealloying for Preheaters #2 and #3 as a function of distance from the preheater inlet. From Mitton *et al.* (1998).

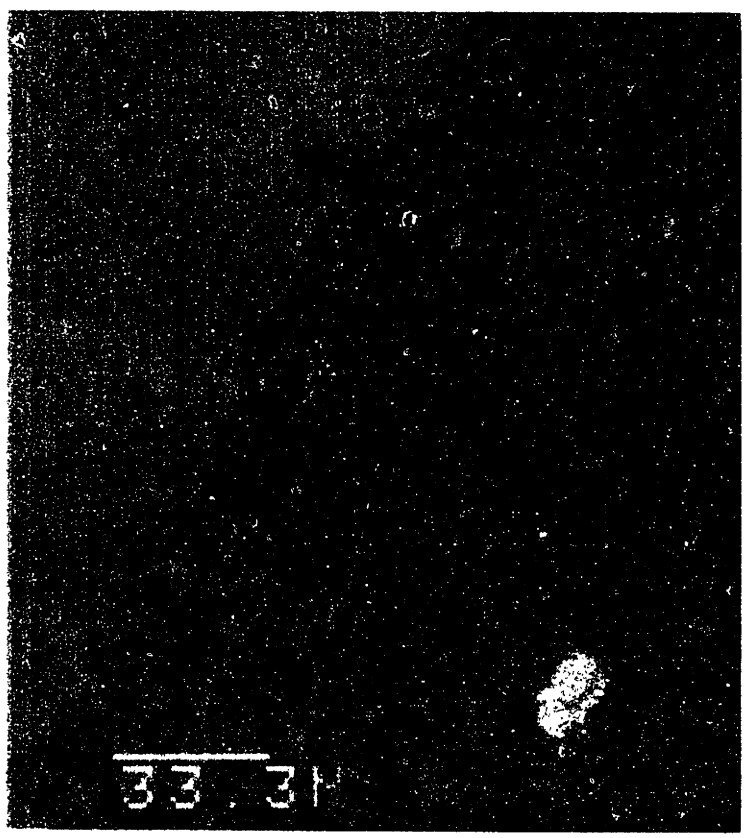

Figure 4-2 Banded structure of corrosion layer in Preheater Tube #1, as observed by ESEM. Sample is from a section of tube 4 cm upstream of the through-wall rupture.

Potential Failure Mechanisms

It is generally accepted that SCC requires (1) a susceptible material, (2) tensile stress, and (3) an aggressive environment. The preheaters examined have the same nominal composition. Except in the case of Preheater #3, in which there was a tight 90° bend, stresses in the tubing are generally random. Because of a lack of extraordinary concentrations of stress or variations in composition, the restriction of the failures to the same 22-cm region in three different preheaters must be an effect of the chemical environment. Below we detail some phenomena relevant to SCC to help explain the relationship between the tube corrosion and its immediate environment.

Kelly *et al.* (1993) established a strong connection between dealloying and cracking for some systems from electrochemical impedance investigations. In this *film-induced cleavage model* of SCC, a crack originating in a dealloyed layer achieves crack-tip velocity sufficient to be injected into the underlying metal. The ability of a dealloyed film to inject a crack into the alloy is a function of the film's porosity (larger pores hinder) and its coherence with the underlying metal. The preheater material never exhibited cracking where it did not also exhibit dealloying.

Referring to the chevron pattern (Figure 4-2) discussed above, it is also apparent that *local chemistry changes* may become increasingly important in influencing the penetration rate as the number of operational cycles increases. Whereas initially the bands are flat or slightly indented, later the intrusion is much deeper. It does not flatten out but rather retains an approximately constant aspect ratio. The grain boundaries appear to serve as a channel, allowing the solvent to contact the alloy deeper, sooner. This pointed interface, in combination with the increasingly-thick corrosion layer atop it, may then begin to function as a crevice. At the wedge-shaped interface penetrates further into the metal, the diffusion barrier presented by the porous corrosion layer and the surrounding uncorroded alloy begins to support diffusion-limited chemistry, such as acidification and high chloride concentrations at the interface. As the interface moves deeper, then, it is expected that the local chemistry becomes increasingly acidified and chlorinated. After reaching a certain pH or $[Cl^-]$, SCC will begin. The blunting effects of the dealloying may be further retarded by electrochemical protection due to the deep local corrosion reactions—similar to the way in which the metal adjoining a pit is protected by the reaction at the pit bottom.

Finally, the effect of *existing defects* in the material cannot be discounted. The inner surface of the Hastelloy C-276 tube possesses many defects and discontinuities which are potential crack initiation sites. A crack was observed at such a defect in

a section of tube with a "typical" operating temperature of 83–116° C. The absence of non-defect-oriented cracks in this region of the tube may indicate that a defect is required under such low temperatures for crack initiation to occur.

The preheaters examined have failed under corrosion behavior which includes both dealloying and cracking, and at a crack propagation velocity which is consistent with stress corrosion cracking. In general the extent of the dealloyed layer is less than that of cracking, and no cracking is observed where a dealloyed layer is absent. Although each of the tubes has a thermal history with some variation in flow rate (and therefore thermal profile), the conditions of the most severe corrosion have been identified to occur at hot subcritical conditions. The cracking may occur by mechanisms of film-induced cleavage or diffusion-limited local chemistry changes, and, at lower temperatures, attack at existing defects.

4.1.2 Heat Transfer Modeling

The water temperature in the preheater tubing was only measured at the preheater's endpoints. To characterize the corrosion in terms of temperature, a model was developed which describes the temperature profile of the tube for a given set of run conditions. This section provides details of the heat transfer analysis used to characterize the corrosion.

General approach In order to develop the necessary temperature-time profiles in the preheater tubing for each experimental run, the basic modeling approach of Holgate *et al.* (1992) was used. The variation of bulk fluid temperature T with the axial distance z along the preheater tubing was obtained from a differential heat balance on the feed solution flowing through the tubing:

$$\frac{dT}{dz} = \frac{2\pi r_i U_i (T_{\text{fsb}} - T)}{\dot{m} C_p(T)} \tag{4.1}$$

where r_i is the internal radius of the tube, T_{fsb} is the sand bath temperature, $\dot{m}$ is the mass flow rate of the feed solution, C_p is the heat capacity of the feed solution, and U_i is the overall heat transfer coefficient (based on inner surface area of the tube). Because of the dilute feed solutions used, the heat contribution from the enthalpy of reaction of CH_2Cl_2 hydrolysis was negligible and so omitted from Equation 4.1. Starting from the point at which the tubing first enters the sand bath, Equation 4.1 was integrated over a small segment dz of the tubing using a fourth-order Runge-Kutta technique (Press *et al.* 1992) to yield T at the end of that segment. Properties within

a segment were computed using the incoming fluid temperature. The residence time increase, $\Delta\tau$, over any segment n was calculated from incoming solution temperature T_n according to hold-up volume and pseudo-constant density:

$$\Delta\tau_n = \frac{\rho(T_n)\pi r_i^2(\Delta z)_n}{\dot{m}} \tag{4.2}$$

where $\rho(T_n)$ is the temperature-dependent density of the feed solution at 246 bar. This process was repeated until the end of the tubing was reached. Initially the step size dz was chosen to be 0.1% of the heated length of the tubing, but this was modified as the calculation progressed down the length of the tubing depending on the value of T calculated from the previous segment. In all calculations, the concentrations of the CH_2Cl_2 and O_2 feed solutions were considered sufficiently dilute to permit the use of density values for pure water at the given temperature and pressure. All physical properties were calculated using the NBS/NRC steam tables (Haar *et al.* 1984).

Overall heat transfer coefficient U_i was considered to be a function of z and was calculated for each segment using the usual sum of resistances formula:

$$\frac{1}{U_i} = \frac{1}{h_i} + \frac{t_w d_i}{k_w d_{LM}} + \frac{d_i}{d_o h_o} \tag{4.3}$$

where h_i and h_o are the internal and external heat transfer coefficients, respectively; d_i, d_o, and d_{LM} are the inner, outer, and log-mean tube diameter, respectively; t_w is the wall thickness; and k_w is the wall thermal conductivity.

Calculation of heat transfer coefficients Calculation of h_i in this system required consideration of a number of important factors and phenomena including substantial changes in physical properties (particularly near the critical point), geometric and flow effects, and the proper coupling of forced and natural convection. A detailed analysis is provided by Marrone (1998). Six correlations were taken from the literature to cover the three different spatial orientations of sections of the tubing (vertical downflow, horizontal flow, and vertical upflow) and whether the flow was laminar or turbulent. Sources of these correlations are listed in Table 4.2. All of these correlations are given in terms of the Nusselt number Nu and can generally be written as follows:

$$Nu = \frac{h_i d_i}{k} = f\left(Re, Pr, Gr, \frac{\rho_w}{\rho}, \frac{\bar{C}_p}{C_p}\right) \tag{4.4}$$

Tube Orientation	Flow Direction	Flow Type	Correlation Source
Vertical	Upward, downward	Laminar	Churchill, 1984
Vertical	Upward, downward	Turbulent	Watts and Chou, 1982
Horizontal		Laminar	Morcos and Bergles, 1975
Horizontal		Turbulent	Robakidze *et al.*, 1983

Table 4.2 Sources of empirical correlations used for calculation of internal heat transfer coefficients, h_i.

where Re is the Reynolds number, Pr is the Prandtl number, Gr is the Grashof number, ρ_w and ρ are the fluid densities at the wall and in the bulk, respectively, $\overline{C}_p$ is the average heat capacity between wall and bulk temperatures, and C_p is the bulk heat capacity.

Values for the tube wall conductivity, k_w, were calculated from a temperature-dependent empirical equation fit to thermal conductivity data for Hastelloy C-276 (Alloy Digest, Inc. 1985). The external heat transfer coefficient, h_o, was assumed constant over the tubing length for a given sand bath temperature. Because the tubing submerged in the sand bath was loosely bundled and not spaced, the correlation of Vreedenberg (1958), which describes heat transfer between a fluidized bed and a horizontal tube, could not be directly applied. Rather, values for h_o were *chosen* for each experiment so that the model predicted the measured value of the mixing tee temperature at the end of the preheater tubing. For the entire range of operating conditions, the necessary values of h_o ranged from 69 to 316 W/m^2-K, varying by less than a factor of 5. Uncertainty in the measured mixing tee temperature had only a modest effect on calculated h_o values; a $\pm$ 1° C change in the mixing tee temperature resulted in only a 3% change in h_o. The assumption that h_o was constant is reasonable, given the uniform thermal conditions that existed in the fluidized sand bath in which the preheater tubing and main reactor were immersed. Because there is no data for the preheater temperature at any middle location, the choice of h_o can only be an upper bound, as the fluid may reach the equilibrium mixing-tee temperature before it physically reaches the end of the preheater tubing. This upper bound is a reasonable estimator of the actual behavior, as the experimentally fitted values of h_o slightly undershoot the values of about 260–450 W/m^2-K calculated from the correlation of Vreedenberg.

As in earlier experiments with a similar preheater by Holgate *et al.* (1992), most of the heat transfer resistance occurred external to the preheater tubing. Typically, h_i

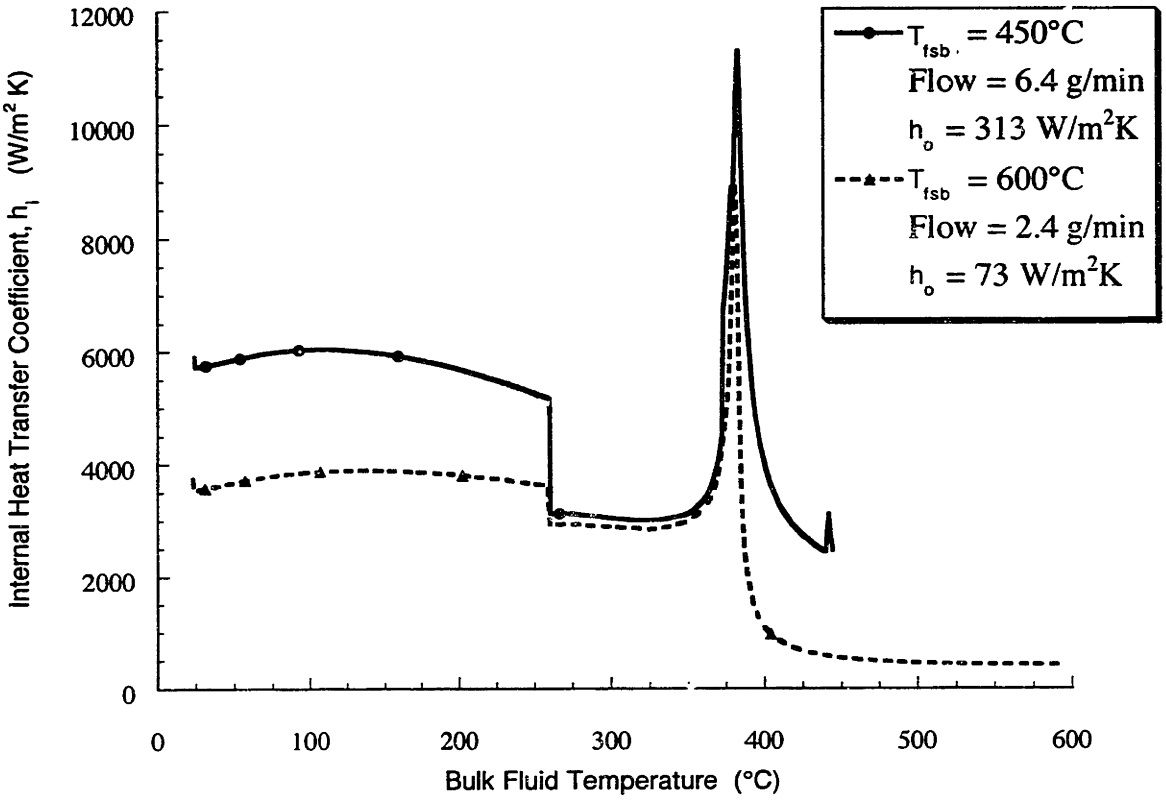

Figure 4-3 Values of the internal heat transfer coefficient as a function of bulk fluid temperature for two experimental runs, calculated using the correlations in Table 4.2. After Cline *et al.* (2000).

was about an order of magnitude larger than h_o. Nonetheless, at various conditions along the tube, internal and wall resistances could not be neglected.

Estimated values for the internal heat transfer coefficient versus bulk temperature along the length of the preheater tubing are shown in Figure 4-3 for two experiments representing the two extremes in sand bath temperature (450 and 600° C) and flow rate (6.4 and 2.4 g/min). Note that the curves end at the temperature of the mixing tee, which approaches the sand bath temperature. Both curves exhibit the expected peak in h_i near the pseudocritical point. The fact that fluid flow was laminar throughout the entire tubing in the high sand-bath-temperature (T_{fsb}) / low-flow ($\dot{m}$) case probably accounts for its generally lower h_i values relative to the low-T_{fsb} / high-$\dot{m}$ case, where the flow became turbulent around 375° C.

Predicted heat transfer and temperature profile results The behavior of the overall heat transfer coefficient U_i with temperature for these same two experimental

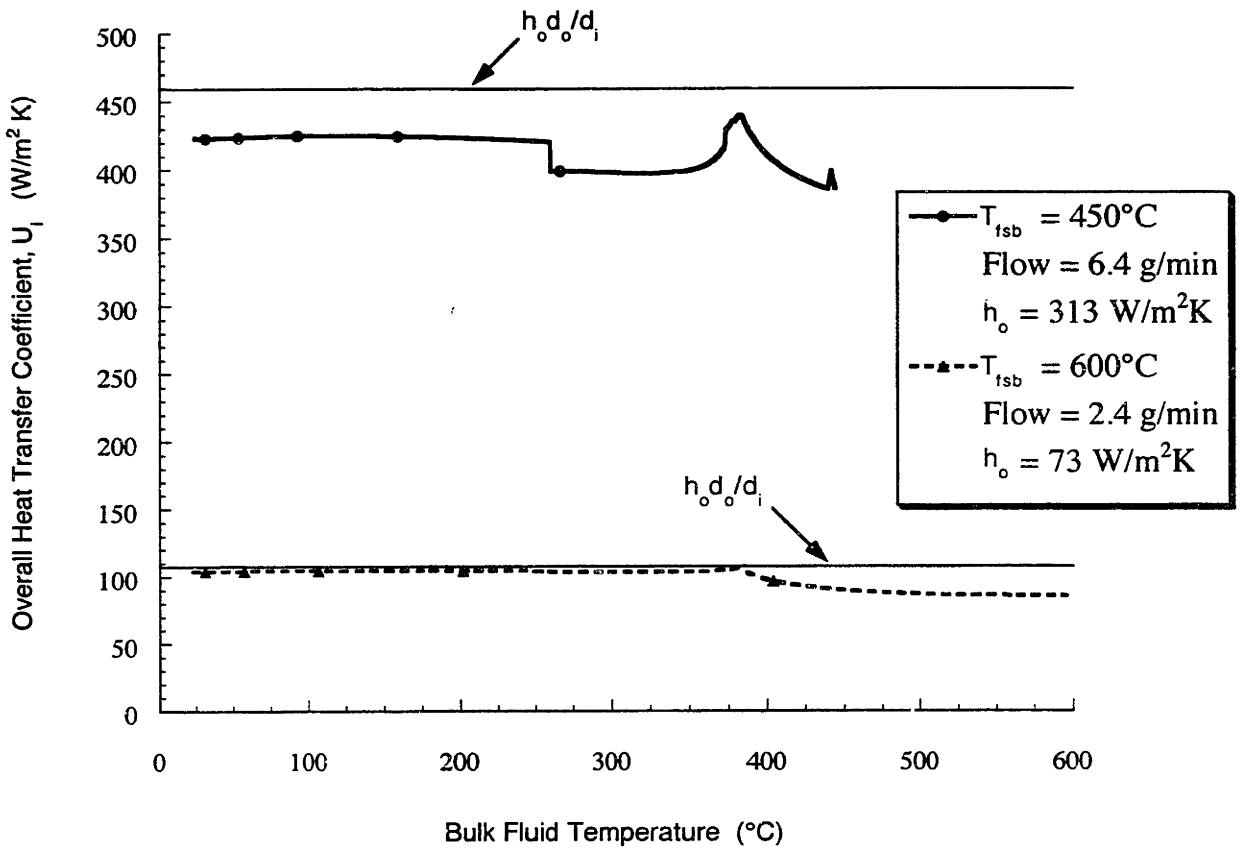

Figure 4-4 Calculated values of the overall heat transfer coefficient as a function of bulk fluid temperature for two experimental runs. The value used for the external heat transfer coefficient (h_o) is listed for each run; internal heat transfer coefficients were those calculated for Figure 4-3. After Cline *et al.* (2000).

runs differs considerably, as shown in Figure 4-4. This is primarily due to changes in the external heat transfer coefficient. For the low-T_{fsb} / high-$\dot{m}$ case, the external heat transfer coefficient h_o was 313 W/m^2-K and $h_o d_o/d_i$ was 460 W/m^2-K, which was high enough to cause U_i to be affected by changes in internal heat transfer coefficient h_i and wall conductivity k_w. For the high-T_{fsb} / low-$\dot{m}$ case, h_o=73 W/m^2-K and $h_o d_o/d_i$=107 W/m^2-K, so that the external resistance dominated the heat transfer in most of the tubing and U_i largely mimicked h_o except near the end of the tubing. The results in Figures 4-3 and 4-4 are typical for the experiments reported for these experiments.

According to the criteria presented by Jackson and Hall (1979), Protopopov (1977), and Watts and Chou (1982), the variation of the parameter Gr/Re^2 with temperature (Figure 4-5) shows that natural convection was generally non-negligible

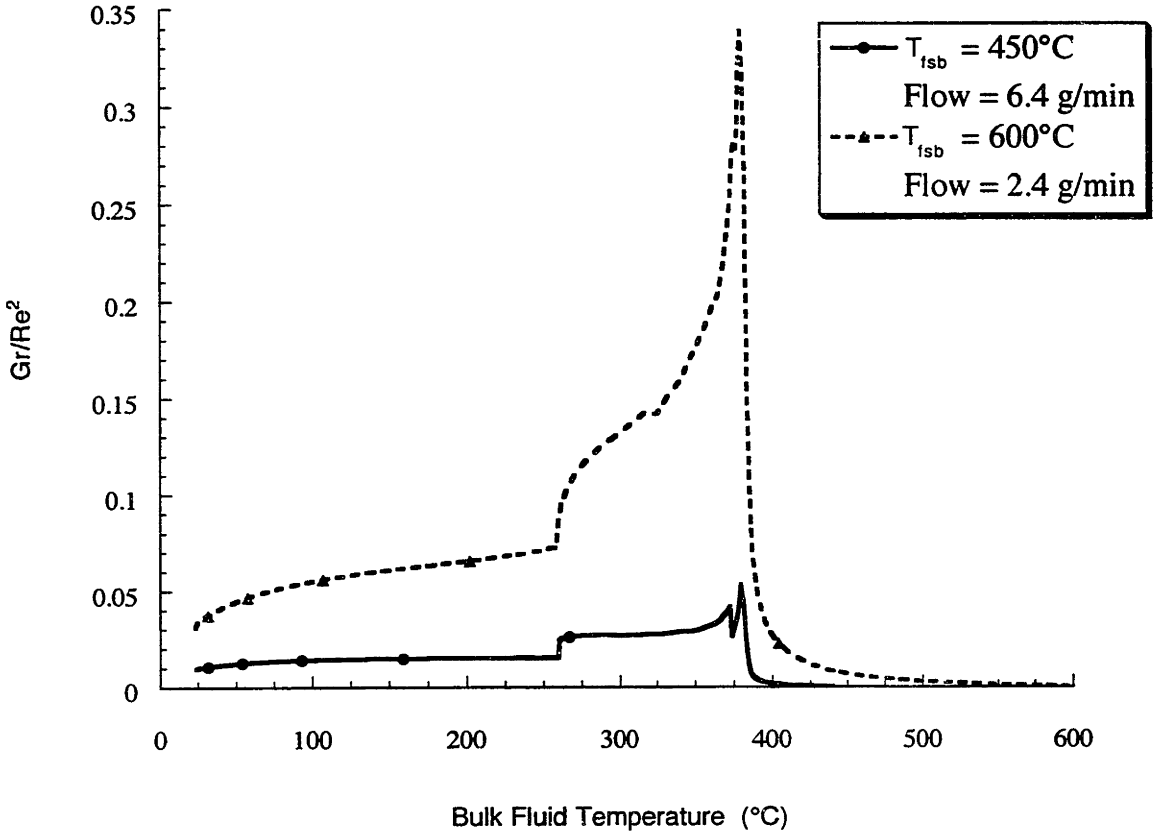

Figure 4-5 Calculated values of the natural convection parameter Gr/Re^2 as a function of bulk fluid temperature for two experimental runs. After Cline *et al.* (2000).

in our experiments and probably appreciable in some cases. Not surprisingly, the runs at high-T_{fsb} / low-$\dot{m}$ like those shown had the highest values of Gr/Re^2, because these runs had laminar flow conditions throughout the preheater tubing and thus smaller values of Re. Also as expected, the highest values of Gr/Re^2 occurred near the pseudocritical point, where density differences between wall and bulk fluid were the greatest.

Predicted temperature-time histories in the preheater tubing are displayed for several experiments in Figure 4-6. Each curve represents a different sand bath temperature and mass flow rate ranging from 450° C and 6.4 g/min to 600° C and 2.4 g/min. In general, $\dot{m}$ was decreased as T_{fsb} was increased in order to maintain the same constant residence time of 6 s in the supercritical main reactor. This effect causes the preheater residence time to increase with T_{fsb}. Each curve in Figure 4-6 ends at the time the fluid exits the preheater tubing. For all experiments, calculated residence times in the preheater tubing ranged from 7 to 17 s. In all cases, these were

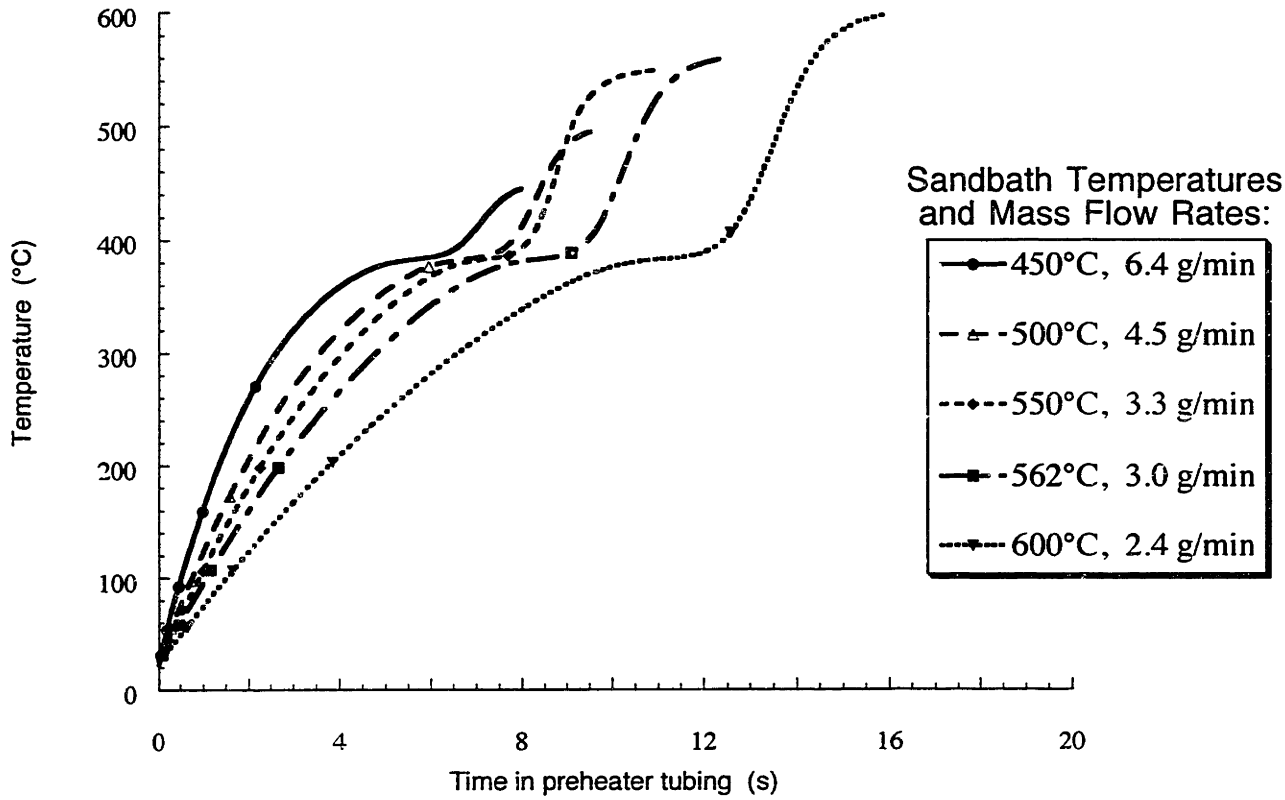

Figure 4-6 Calculated temperature-time profiles in the preheater tubing for various experimental runs at different sand bath temperatures and flow rates. The end of the curve corresponds to the point where fluid exits the preheater tubing. After Cline *et al.* (2000).

greater than the corresponding residence times in the supercritical isothermal main reactor.

One can see in Figure 4-6 that the spacing between the temperature-time profiles below the pseudo-critical temperature T_{pc} increases with increasing T_{fsb} and/or decreasing $\dot{m}$. Most of the low temperature and high flow runs below sand bath temperatures of 550° C have very similar profiles below T_{pc}, with the total time required to attain T_{pc} for the 450 and 550° C profiles differing by only about 2 s. All temperature—time profiles level off near T_{pc}, but remain below 390° C for about 70 to 80% of the total residence time of fluid in the preheater tubing. It is only above the pseudo-critical region that all the profiles differ from one another.

Interpretation of corrosion data The heat transfer analysis provides a means for describing corrosion effects in the CH_2Cl_2 feed preheater tubing. As discussed above, post-failure analysis revealed that each tube ruptured at one location after

Preheater Tube #	Position of Tube Failure Relative to the Point Where Heating Begins (cm)	Bulk Fluid Temperature (° C)‡	Inner Wall Temperature (° C)‡
1	11	130–190	150–200
2	29	250–330	270–350
3	7	100–140	110–150

Table 4.3 Bulk and wall temperatures predicted at points of corrosive failure in preheater tubing. The range of results is due to the changes in the operating conditions over the numerous experiments a particular preheater experienced.

‡ Calculated from heat transfer model; see text.

undergoing various extents of corrosion over an extended region (about 40 cm long in Preheater #2, somewhat longer in Preheater #3 as shown in Figures 4-1(a) and 4-1(b)) beginning at the point where the tube first entered the fluidized sand bath. The rupture location and the calculated temperature range over all experiments at the failure site for the bulk fluid and the inner wall of the tube are presented in Table 4.3. Note that these temperatures never exceed the pseudo-critical point. The highest wall temperature for any experiment that is predicted by the model at the end of the 40 cm region where all corrosion evidence ends is 380° C. Corrosion was insignificant in the region of the preheater calculated to always be supercritical, such as where the end of the preheater tubing enters the mixing tee (see Figure 1-4 on page 25). These findings confirm that the corrosion was confined to a region of hot, but subcritical, temperatures, which is the regime in which thermally activated ionic reactions are rapid and corrosion should be particularly swift and damaging.

4.2 Cooling-Tube Experiments

The CH_2Cl_2 SCWO experiments, as quantified by the heat transfer model results, indicate a broad range of temperatures (110–350° C, from Table 4.3) over a substantial length of tubing where localized corrosion was greatly accelerated. Because these experiments were not intended as corrosion experiments *per se*, the variables important to corrosion (O_2, Cl^- concentrations, wall temperature) were not kept constant over the exposure lifetime of the material—making it more difficult to correlate material performance to specific operating conditions. That the internal heat transfer coeffi-

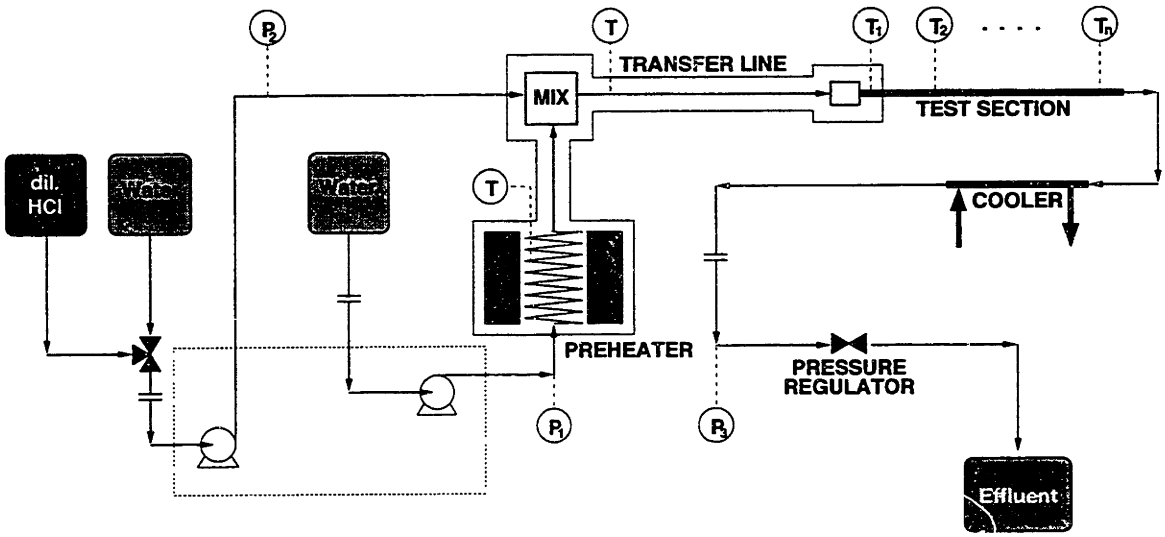

Figure 4-7 Flowsheet of the HCl/SCWO corrosion experiment.

cient h_i was significant in the low-T_{fsb} / high-$\dot{m}$ case further complicates interpretation by increasing the ambiguity of the temperature of corrosion. In order to more precisely define the temperature ranges of highest corrosion susceptibility, experiments were performed which expose a given section of metal to a single temperature and a constant water chemistry. The temperature profile is reversed to a cooling profile in air, making h_o limiting.

Procedure The system shown in Figure 4-7 draws from three feed-carbuoys, two of which contain deionized water (DW), and the third dilute aqueous hydrochloric acid (1830 ppm HCl).

System pressure is developed by a continuously-running two-head piston-type HPLC feed pump (Eldex, model AA-100-S) upstream end in the system and a back-pressure regulator (BPR) (Tescom, model 26-1722-24-090) downstream. Pressure is maintained at approximately 3600 psig (246 bar) and is approximately constant throughout the system. The feed to one pump head is switchable between HCl and DW so that a thermal steady-state can be achieved without an aggressive agent present.

The high-pressure portion of the apparatus is made completely of corrosion resistant materials, with an effort to limit the number of different alloys employed. With the exceptions of the snubbers on the pressure transducers, test section itself, and the

fittings downstream of the test section, the materials of construction for the system are entirely Inconel 625. (Pressure snubbers and downstream fittings are made from 316 stainless steel.)

The pump feeding the high-pressure portion is set such that the two feeds are mixed in a ratio of 4:1 which, when acid is being fed in the slower stream, produces a stream of 365 ppm aqueous HCl (corresponding to a pH of 2.0 if measured under ambient conditions). This is the concentration to which the test sections of tubing were exposed. It was selected to be within the 150–910 ppm HCl effluent-concentration range detected during the CH_2Cl_2 experiments. As before, a second fluid phase is not expected because the pressure is maintained well above the critical pressure of pure water (221 bar), and because the solution is very dilute.

The pressurized DW-only stream is sent through a radiantly-heated preheater coil to bring the fluid temperature to 500° C. This stream then proceeds to an insulated mixing tee, where it is mixed with the room-temperature acid-or-DW stream from the other pump head. At the 4:1 (water:acid) flow ratio, assuming adiabatic mixing, the fluid exits the mixing tee at 390–400° C. From the mixing tee, the flow proceeds through an insulated heat-traced transfer line of 30–40 cm, then enters the test section.

The test section is a tube which is instrumented approximately every 10 cm along its length with Type K thermocouples (0.010-in diameter, sheathed) starting at the hot end. The tube is only insulated from the transfer line to the first thermocouple. Each thermocouple is wrapped around and cemented to the tube and covered with a fold (3–5 mm thick) of aluminosilicate-wool insulation. (See Figure 4-8.) Seven thermocouples in all are used to monitor the test section. After passing through the test section the flow proceeds to a shell-and-tube heat exchanger where it is cooled to room temperature. The cooled stream then passes through the back-pressure regulator (BPR) and then to effluent storage. Pressure is measured just upstream of the BPR, as well as in each feed stream, by piezoelectric transducers (Figure 4-7).

Hastelloy C-276 tubing of two different diameters was tested. The tubes were welded and solution annealed at the time of manufacture. Details regarding tube composition and processing conditions are provided in Tables 4.4 and 4.5. As the sections were part of the process piping, they bore the full system pressure. Table 4.6 presents the data pertinent to each corrosion experiment. Although five runs were performed, the results from only the two with the most steady and reliable operating conditions and temperature measurements (3 and 5) are presented. Runs 1 and 2 employed a sub-optimal temperature measurement scheme. Run 4 experienced some flowrate excursions which greatly affected the measured temperature profile. Unless

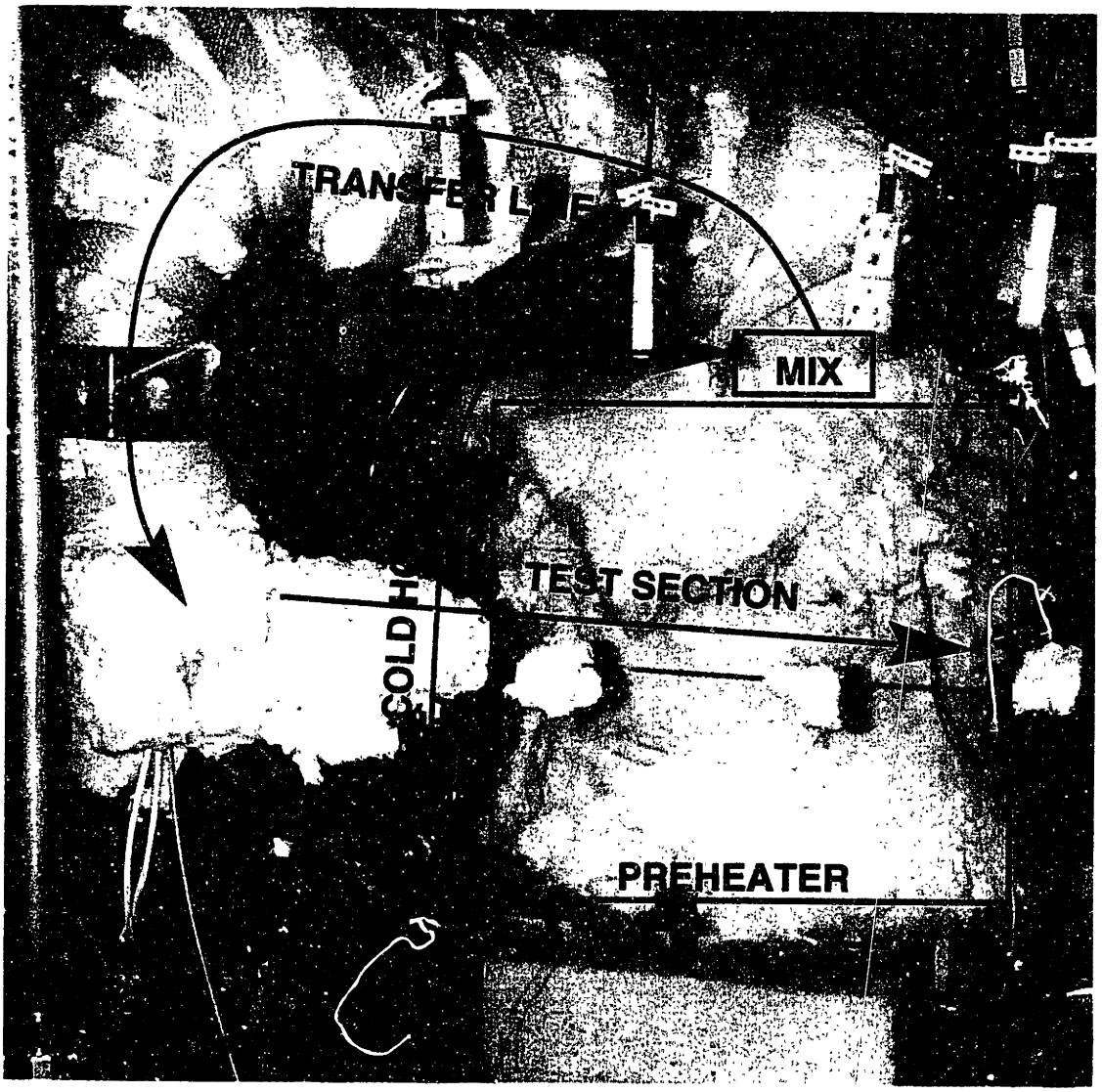

Figure 4-8 Photograph of cooling-tube apparatus.

Nom. Outer Diameter	Wall thickness	Grain Size	Vickers Microhardness	Processing
1/16"	0.010"	29 μm	228±7	Inco Alloys: Heat #Z2226CG; ASTM-B-626 1994B, Class II B (Welded, cold-worked, and solution-annealed)
1/8"	0.035"	120 μm	190±8	Salem Tube: Heat #054077; ASTM-B-626 1994B, Class III BW (Welded, cold-worked, and solution-annealed)

Table 4.4 Processing conditions for tubing tested. (Vickers microhardness was measured with 100 g weight and 15 s dwell time.)

	Composition (wt %)											
Size	C	Co	Cr	Fe	Mn	Mo	Ni	P	S	Si	V	W
1/16"	<0.01	0.24	15.39	5.96	0.40	15.44	58.69	0.007	<0.001	0.031	0.01	3.82
1/8"	0.007	0.10	15.4	6.8	0.60	15.5	57.9	0.001	0.04	0.04	0.15	3.6

Table 4.5 Composition of tubing tested.

otherwise noted, the remainder of the discussion will refer exclusively to Runs 3 and 5.

The feed to the test section is 365 ppm aqueous HCl (ambiently-measured pH of 2.0). The oxygen concentration in the feed stream is 2.9×10^{-4} M, based on Henry's Law equilibrium (Perry and Green 1984, p. 3-103) with atmospheric oxygen in the feed carbuoys. The average flow rate is 2.0 g/min, and is laminar, with a maximum Reynolds number of 12.8 at the first measurement point in Run 5. (Tables 4.7 and 4.8 contain details of the flow conditions, temperatures, and corrosion measurements.) The pressure pulses caused by the two-head displacement pump are damped by the water's increased compressibility when the system is at operating temperature. Since this is a flow system and the corrosion reactions occur relatively slowly, ionic concentrations are assumed to be constant (approximately zero for all except HCl and O_2 species). The steady-state temperature profile was constantly monitored by computer. The mean temperatures $\bar{T}$ and standard deviations σ_T were computed using a time-weighted average:

$$\bar{T} = \frac{\sum_{i=2}^{N} \frac{1}{2} (T_i + T_{i-1}) (t_i - t_{i-1})}{(t_N - t_1)} \tag{4.5}$$

Run #	Date	Tube OD	Tube Wall	Time (h)	TC bracket
1	Fall 1996	1/16"	0.010"	17.0	(a)
2	Feb 1997	1/8"	0.035"	21.5	(a)
3	Apr 1998	1/8"	0.035"	49.5	(b)
4	Jul 1998	1/16"	0.010"	22.0	(b)
5	Jan 1999	1/16"	0.010"	19.5	(b)

Table 4.6 Corrosion experiment runs. The time column indicates time of exposure to HCl. TC bracket (a) was a large copper bracket used to affix the tip of a 1/16-in thermocouple to a bead of Omega thermally-conductive cement on the tube. Bracket (a) introduced significant measurement error due to conductive losses from tube to thermocouple, and from local cooling induced by the copper bracket and TC shaft acting as a fin. This was replaced by scheme (b), in which a 0.010"-diameter TC was wrapped around the tube four to six times and then cemented with a stainless-steel-filled epoxy.

$$\sigma_T = \sqrt{\frac{\sum_{i=2}^{N} \left[\frac{1}{2}\left(T_i + T_{i-1}\right) - \bar{T}\right]^2 \left(t_i - t_{i-1}\right)}{\left(t_N - t_1\right)}} \tag{4.6}$$

where T_i is the temperature sampled at the start of period i and t_i is the time at which the interval starts. These equations assume linear behavior over the intra-sample period.

In Run 3, the 1/8-in (3.17 mm) OD tube was exposed to hydrothermal HCl fluid for 49.5 h. In Run 5, the 1/16-in (1.59 mm) OD test section was exposed to the fluid at experimental conditions for 22 h. After exposure, each tube was removed from the system, filled with epoxy, sectioned, and mounted for metallography. Metal from the locations of each thermocouple was mounted and polished as described in Appendix A. Details regarding each exposure test are given in Tables 4.7 and 4.8.

4.2.1 Metallography Results

Even before exposure there are large differences in the metallurgy of the two sizes of nominally-identical Hastelloy C-276 tubing. First and foremost is a striking difference between the grain sizes (Figure 4-9). The average diameter of the grains was computed from the number density of grains on micrographs, after the technique of Fullman (1953). The grains from the 1/8-in tube have a diameter of approximately 120 μm, are are about four times the size of the grains in the 1/16-in tube (approximately 29 μm). This grain size difference is may be due to differences in annealing such as time, temperature, or starting point. The starting point may be different due

	Thermocouple							
	1	2	3	4	5	6	7	
Position	12.7	17.5	23.8	31.4	42.5	52.1	61.3	cm
mean $\bar{T}$	395.2	386.3	382.1	376.3	357.9	325.2	292.0	°C
σ_T	1.9	0.9	0.6	0.7	3.2	4.9	7.1	°C
min. T	390	384	381	371	334	317	258	°C
max. T	398	388	383	378	365	335	301	°C
D_s at $T_{\max}$	2.5	4.0	6.5	9.3	12.5	17.1	21.5	–
-log K_w at $T_{\max}$	19.2	17.0	14.8	13.3	12.3	11.5	11.1	log(mol/kg^2)
ρ	173	241	386	476	567	669	741	kg/m^3
$\mu\times10^3$	2.94	3.34	4.59	5.51	6.54	7.89	9.13	Pa-s
Velocity	125.	90.0	56.2	45.6	38.3	32.4	29.3	mm/s
$Re(T_{\max})$	10.3	9.08	6.60	5.50	4.64	3.84	3.32	–
Model T	–	385	382	374	335	293	255	°C
	–	389	385	382	367	336	300	°C
Etch Front	11.48	13.60	15.50	22.90	13.99	20.95	23.21	mm/y
$\pm\sigma$	1.03	1.50	1.98	1.70	1.20	1.78	1.38	mm/y
Dealloying	1.84	1.39	1.01	1.29	2.02	1.80	0.17	mm/y
$\pm\sigma$	0.33	0.68	0.38	0.35	0.31	0.45	0.26	mm/y

Table 4.7 Data for Run 3. A 1/8-in Hastelloy C-276 tube of 0.035-inch wall thickness was exposed for 49.5 h to 365 ppm aqueous HCl at 246 bar pressure. Measured pressure ranged 3560-3663 psig (245-253 bar). Statistical measures of temperature are computed using Equations 4.5 and 4.6. Derived quantities use NBS data for water at 250 bar and $T_{\max}$ (Haar *et al.* 1984), mass flowrate of 2.0 g/min and initial cross sectional area A_x = 1.53×10^{-6} m^2. Penetration depths have been normalized to a mm/y rate based on exposure time to hydrothermal HCl.

	Thermocouple							
	1	2	3	4	5	6	7	
Position	9.5	20.2	30.5	41.3	53.9	65.4	76.2	cm
mean $\bar{T}$	389.0	376.7	374.7	368.2	346.7	323.9	288.4	°C
σ_T	1.3	0.4	0.6	0.4	0.5	0.7	0.7	°C
min. T	388	375	373	368	345	321	286	°C
max. T	392	378	376	370	350	327	290	°C
D_s at $T_{\max}$	3.0	9.3	10.0	11.5	15.0	18.2	22.9	–
-log K_w at $T_{\max}$	18.3	13.3	13.0	12.5	11.8	11.4	11.1	log(mol/kg^2)
ρ	201	476	496	540	626	668	761	kg/m^3
$\mu\times10^3$	3.08	5.51	5.73	6.22	7.28	8.19	9.54	Pa-s
Velocity	181.	76.5	73.4	67.4	58.2	54.5	47.9	mm/s
$Re(T_{\max})$	12.8	7.13	6.86	6.32	5.40	4.80	4.12	–
Model T	–	383	377	357	321	286	255	°C
	–	384	382	374	349	318	288	°C
Local Corr.	8.27	17.2	23.5	18.1	16.3	11.0	1.46	mm/y
Dealloying	1.79	2.03	1.99	2.09	1.17	0.18	0.06	mm/y
$\pm\sigma$	0.48	0.61	0.72	0.98	0.67	0.32	0.27	mm/y

Table 4.8 Data for Run 5. A 1/16-in Hastelloy C-276 tube of 0.010-inch wall thickness was exposed for 19.5 hours to 365 ppm aqueous HCl at 246 bar pressure. Pressure ranged 3569-3670 psig (246-253 bar) with an unintentional 10-minute excursion 3697 psig (255 bar). Statistical measures of temperature are computed using Equations 4.5 and 4.6. Same methods as in Table 4.7, with mass flowrate of 2.0 g/min and $A_x = 9.15\times10^{-7}$ m^2. "Local Corr." represents the maximum penetration in a distinctly local mode.

to additional working required to form such a thin-walled tube; it may have more severely disrupted the crystals. Microhardness tests confirm that the 1/16-in tube is harder (Table 4.4).

Another difference between the materials is the response to etchant. A pristine sample of each tube was polished and etched. The grain boundaries of the 1/8-in tube became visible because neighboring grains etched at different rates—causing a slight relief in the surface, as seen in Figure 4-9(a). In the 1/16-in tube this also occurred (Figure 4-9(b)), but was accompanied by some etch-pitting (which is attributed to attack at dislocations) and slight intergranular attack. It is speculated that the drawing which the 1/16-in tube received may have introduced into it more defects than the 1/8-in tube such that, given similar annealing times, the recovery in the 1/16-in tube (in terms of dislocations and grain boundary size) would be much less complete. These residual defects and stresses could serve as sites which would be etch-sensitive.

Unlike the post-failure analyses, the corrosion layer in the tubing from the cooling-tube experiments is devoid of striations or bands. One possible explanation for this is that the CH_2Cl_2 experiments employed many heat-up and cool-down cycles throughout the exposure lifetime of the material. The cooling-tube experiments, on the other hand, employed one continuous long-term exposure. Interestingly, a cooling-tube experiment which was operated in a multiple-exposure mode (Run 2) exhibits bands roughly commensurate with the number of operating cycles. However it cannot be distinguished whether the bands were caused by thermal cycling, water-chemistry cycles, or both.

For both runs it was confirmed that the corrosion layer was a dealloyed layer, because it exhibits grain boundaries, indicating that the layer was not redeposited from upstream. By ignoring the "singular" local corrosion features (which extended into the alloy at least 10 to 20% beyond the "flat" dealloyed layer), statistics for the dealloying rate were compiled. Five measurements of the dealloyed layer thickness were made for each micrograph; with two micrographs per site there are ten measurements of dealloyed layer thickness per site. The results for penetration rate, corrected for polishing angle and reported in annual units of mm/y, are shown in Figures 4-14 and 4-21.

Run 3 Results An 1/8-in Hastelloy C-276 tube was exposed in Run 3. Dealloying in tubing exposed at 395° C (TC_1) is shown in the elemental dot-maps in Figure 4-10, as determined by EDX. The alloy is on the right; in the middle of the photo there

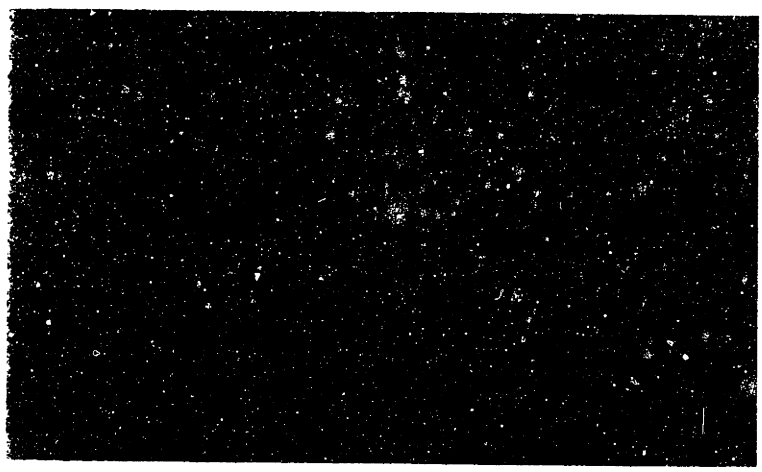

(a)

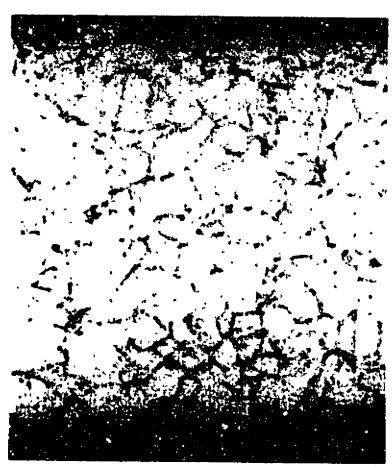

(b)

Figure 4-9 Grain sizes of metal in 1/8-in (a) and 1/16-in (b) tubing. The height of each photo is 300 μm (same scale). The contrast in (a) was enhanced to make the grain boundaries more prominent.

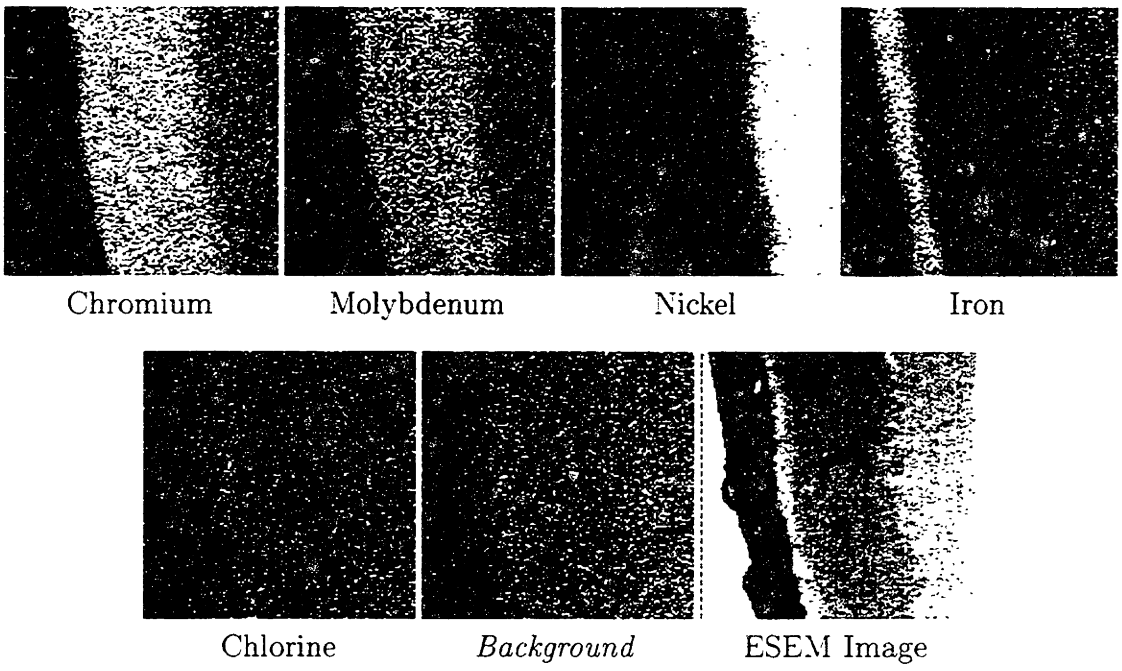

Figure 4-10 EDX analysis of an 1/8-in tube sample exposed at 395° C (TC_1, Run 3).

is the dealloyed layer. Left of this is an iron-rich redeposited layer, and on the far left, the mounting epoxy. Iron and nickel are depleted in the dealloyed layer, leaving chromium and molybdenum. The redeposited layer, which lacks grain boundaries, contains chiefly iron and nickel and was deposited during system shut-down. At the first and second thermocouples (TC_1 and TC_2), the dealloyed layer is very thick (7.8 to 10 μm) and porous (Figure 4-11). The interface between the dealloyed layer and the metal consists of many thin, hairlike (or cleavage-like) projections, shown for TC_1 in Figure 4-12. Islands of unaffected metal are also visible in the portion of the dealloyed layer nearest the alloy. The dealloyed layer is visibly porous. At TC_3 the hairlike projections persist, but they are fewer in number, and a thinner (5.7 μm) dealloyed layer is still evident. EDX analysis of the metal at TC_3 (Figure 4-13) indicates that the same dealloying behavior persists—but there is no longer any sign of a redeposited iron-rich layer. At TC_4 the interface between the dealloyed layer and the metal is relatively smooth. The dealloyed layer has grown to 7.3 μm and the hairlike projections are no longer detected. Some wider intrusions (which may correspond to a grain boundary or surface feature) are evident, but are few in number. The material at TC_4 also exhibits small, discrete islands of uncorroded material in

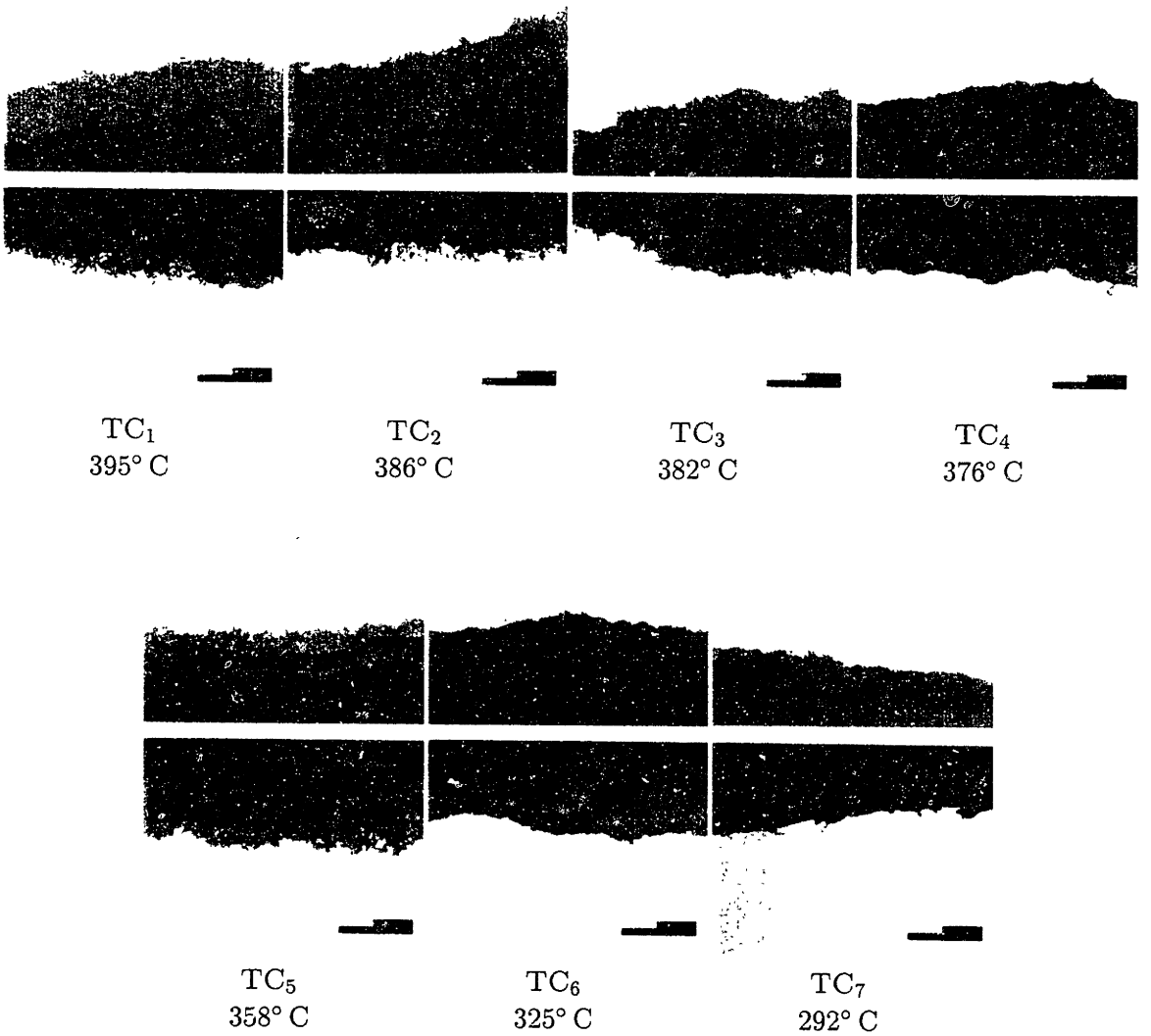

Figure 4-11 Corrosion profile of the 1/8-in tube from Run 3. Each frame corresponds to the segment of tube where thermocouples 1–7 were attached. The tubing is not etched. Each photo is approximately 76 μm wide. Position of interface in photo does *not* imply corrosion rate. Angle with radius must be considered when determining penetration depth (see Table A.1).

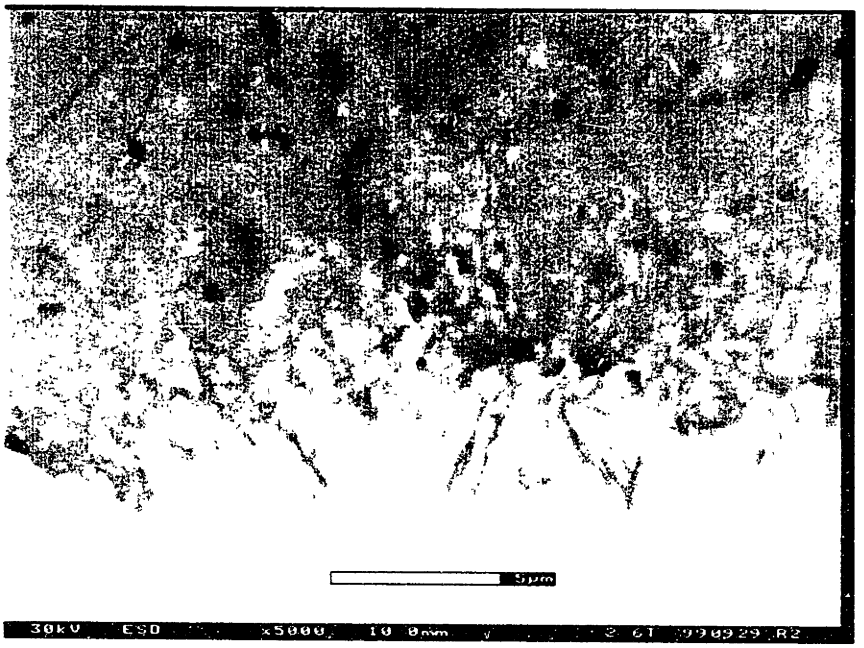

Figure 4-12 ESEM detail of the dealloying interface of an 1/8-in tube sample exposed at 395° C (TC_1, Run 3). Unaffected alloy is at the bottom of the image. See also Figure 4-11.

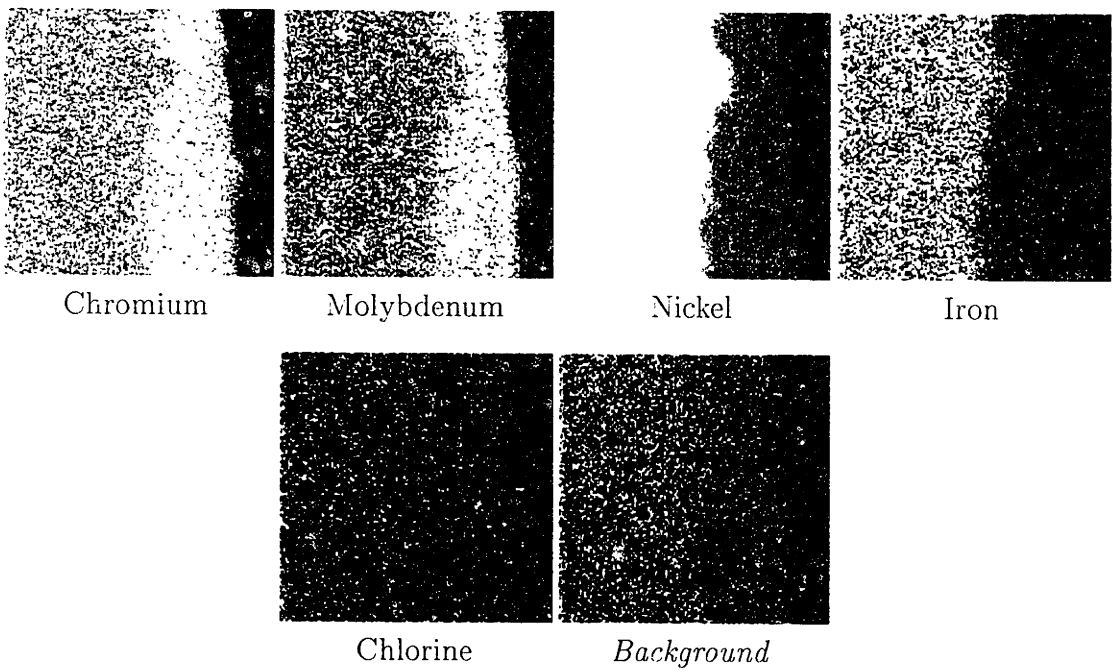

Figure 4-13 EDX analysis of an 1/8-in tube sample exposed at 382° C (TC_3, Run 3). The alloy is positioned at the left of the frame.

the dealloyed layer. At TC_5 the metal-dealloyed layer interface is once again rough, and the dealloyed layer has grown to be 11 μm thick. The roughness of the interface has a character somewhat similar to that observed from TC_1 through TC_3, but the features in the interface are shorter and thicker here. The region at TC_6 once again has a smoother interface, with a well-developed (10 μm) porous dealloyed layer. The attack appears completely uniform at this point. In contrast to all of the preceding, the TC_7 region has a *much* smaller dealloyed layer (1 μm). The smooth interface between dealloyed layer and metal exhibits signs of localized attack, but visible local penetration beyond the dealloyed layer is too small (<1 μm) to definitively identify these features as either neo-cracks or the embryonic stages of intergranular corrosion.

The apparent temperature dependence of dealloying rate is shown in Figure 4-14. From 290 to 360° C the rate increases with temperature. Above 360° C the penetration rate decreases with increasing temperature until above 380° C, where once again the dealloying rate appears to rise. Within these trends are changes in dealloying propagation, in which the corrosion front morphology changes from hairlike at high temperatures to smooth at moderate temperatures, to more-deeply-localized at still lower temperatures.

Samples from the 1/8-in tube of Run 3 were etched, to discover the extent to which the grain boundaries had become vulnerable (see Figure 4-15). The results were striking—not only was the penetration of the etched region overall *much* greater than the penetration of dealloying, but the etch-sensitive portion of the alloy was not limited to the grain boundaries. The grain centers, perhaps initially along sub-boundaries and other defects, also exhibited a remarkable amount of damage. Figure 4-16 shows the unaffected grain size next to the etch-affected zone. The damage to the metal is actually far more severe than was indicated by the dealloyed layer.

In Figure 4-17, the average etch-front penetration is shown as a function of temperature. It can be seen that the average etch-front penetration rate decreases with increasing temperature. Depending on whether the point at 376° C (TC_4) is considered an outlier, there are either one or two descending trends visible.

To determine if the etching revealed any local composition changes which had been obscured by mechanical polishing, an etched sample from the tubing at TC_3 was analyzed with EDX (see Figure 4-18). No inhomogeneous concentrations were detected. As before, iron and nickel were depleted while chromium and molybdenum were enhanced.

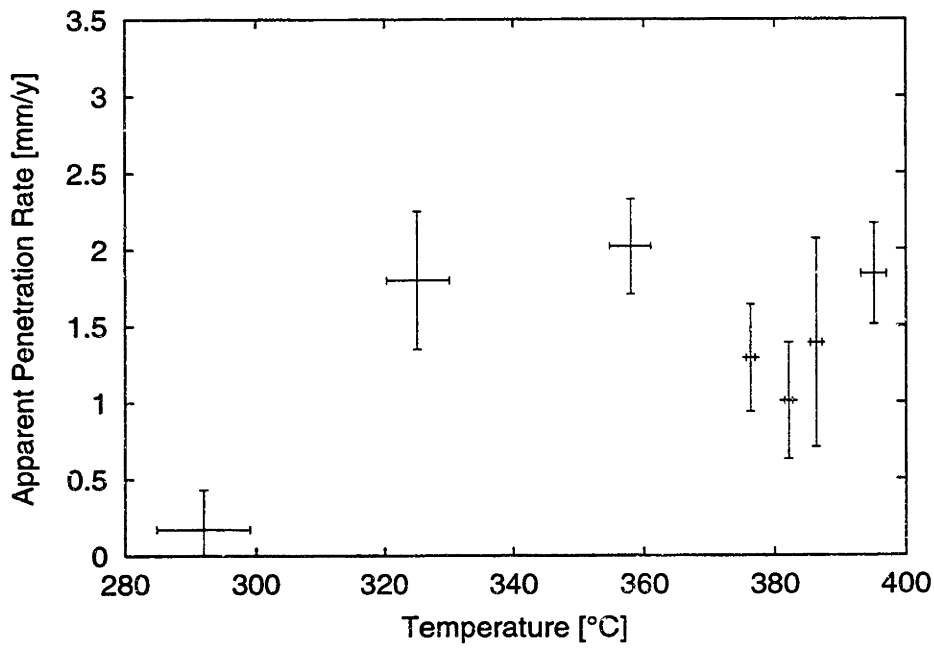

Figure 4-14 Corrosion penetration rate for the 1/8-in tube (Run 3). Error bars on temperature represent one standard deviation from the mean, as computed with Equations 4.5 and 4.6. Error bars on corrosion rate represent one standard deviation computed from five measurements on each of two micrographs per temperature point.

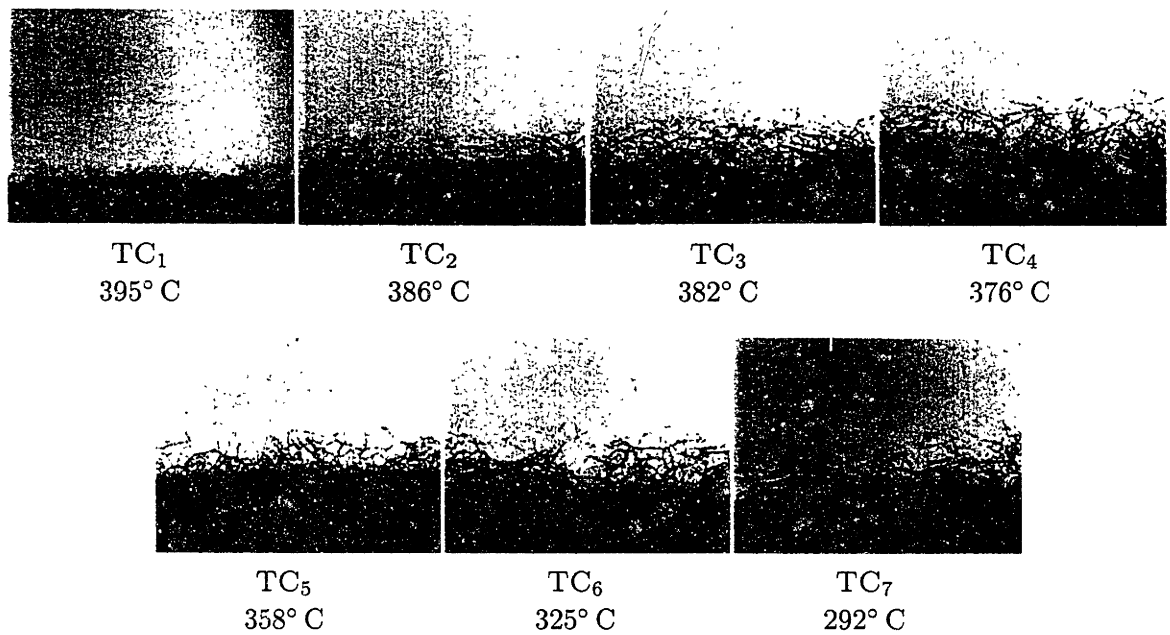

Figure 4-15 Corrosion profile of the 1/8-in tube (Run 3), as evidenced by etching. Each frame corresponds to the segment of tube where thermocouples 1–7 were attached. Each photo is approximately 570 μm wide. Position of interface in photo does *not* imply corrosion rate. Angle with radius must be considered when determining penetration depth (see Table A.1).

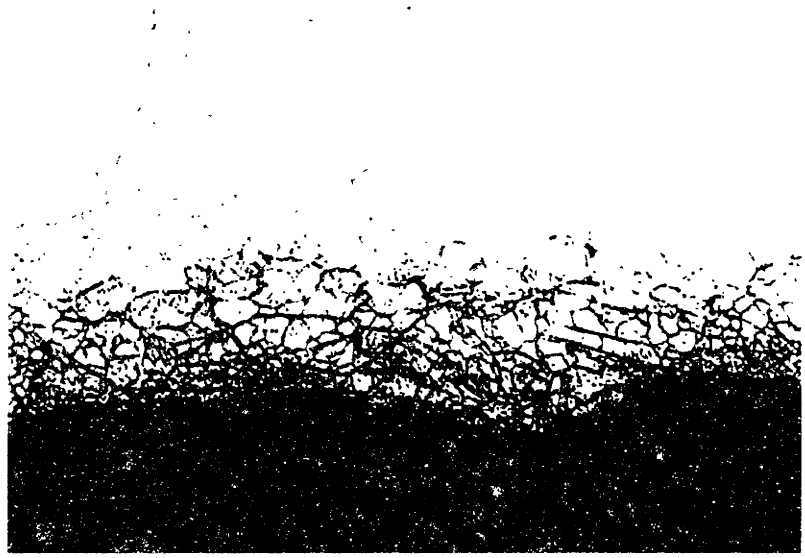

Figure 4-16 Close-up of the TC_3 sample shown in Figure 4-15. Note the size of the unaffected grains relative to the corrosion pattern.

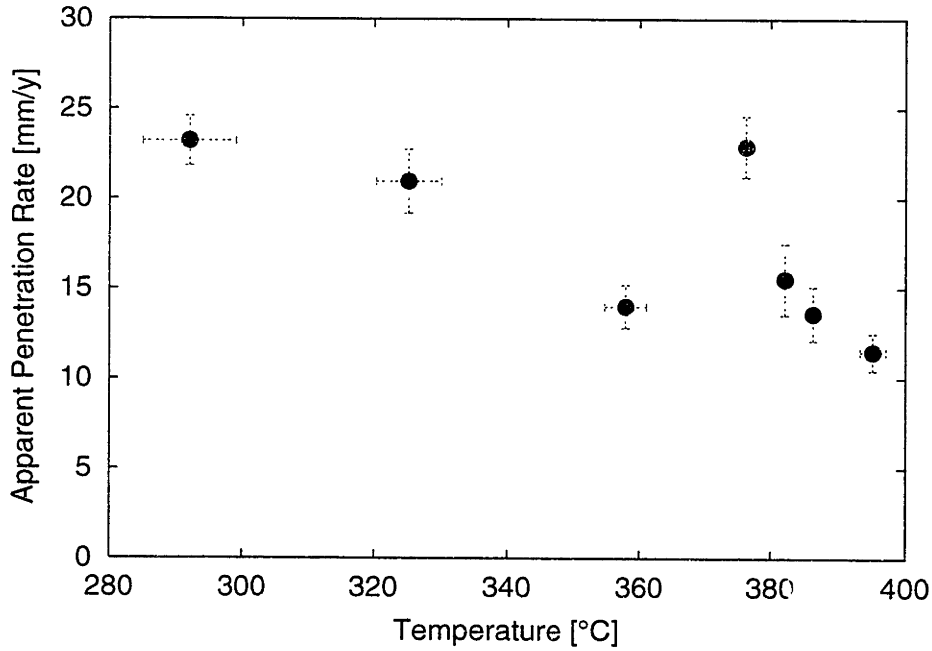

Figure 4-17 Penetration rate of "etch front" in the 1/8-in tube from Run 3. The error bars follow a convention similar to Figure 4-14. There are five measurements (one micrograph) per temperature point.

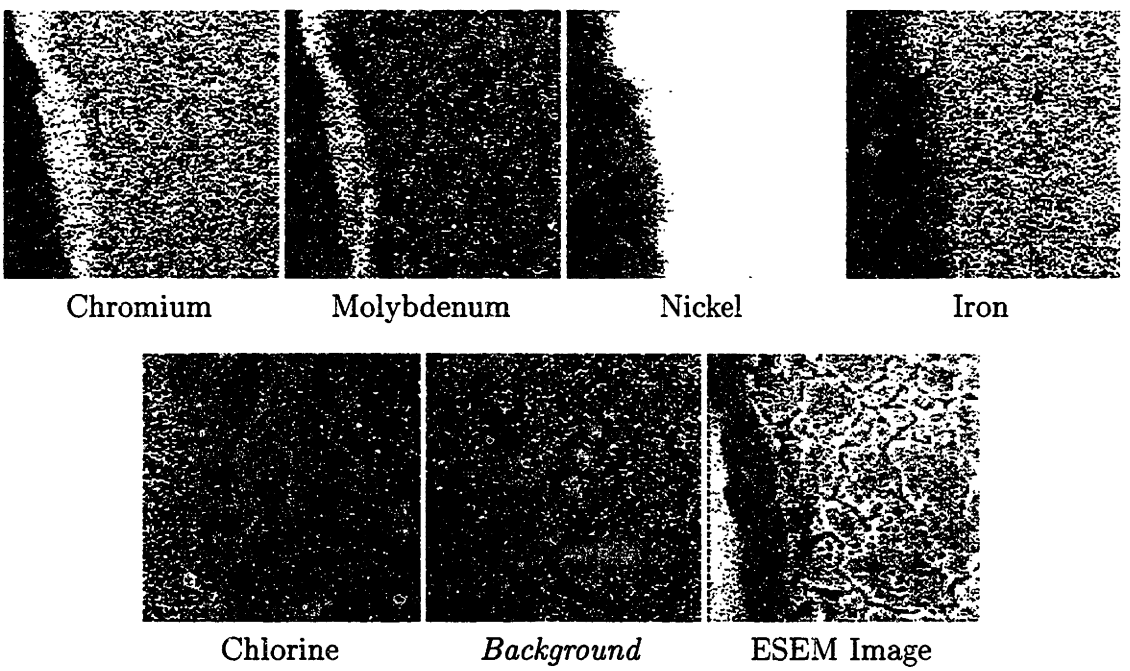

Figure 4-18 EDX analysis of etched TC_3 sample from Run 3. The etched appearance of the molybdenum image is caused by the surface sensitivity of the particular wavelength of x-rays emitted by molybdenum, and does *not* indicate a local depletion. There is a noticeable chlorine content because HCl is a component of the etchant.

Run 5 Results Polished samples from the 1/16-in tube of Run 5 are shown in Figures 4-19 (CLSM) and 4-20 (SEM). At TC_1, the corroded region of the material has many gray, hairlike projections into the metal surface, but visible penetration (3.9 μm) is not deep. No continuous dealloyed layer is observed. This behavior is similar to that seen at TC_1 of Run 3. At TC_2, the gray dealloyed layer has become a continuous layer of 4.5 μm, and although the hairlike features observed at TC_1 persist, they are not as pronounced. Instead, the corrosion front is beginning to deepen at the grain boundaries. From TC_2 to TC_4 the dealloyed layer thickness is fairly constant. TC_3 through TC_5 again exhibit a continuous dealloyed layer, but also have pronounced intrusions of the dealloying front deeper into the solid metal. These also appear to occur at the grain boundaries. Penetration is nonuniform, suggesting a gradual shift away from uniform dealloying to more-localized corrosion. At TC_2 through TC_5 there are localized intrusions of the dealloying front of 38, 52, 40, and 36 μm, respectively. While the greatest local penetration occurs at TC_3, the attack becomes increasingly narrow from the minimal damage at TC_2 to the deeper damage at TC_3 and TC_4, then to TC_5 where significant under-cutting is observed. The penetration at TC_5 is 2.6 μm, much smaller than from TC_2–TC_4. At TC_6 and TC_7 the dealloyed layer is not seen. Instead, at TC_6 the metal is corroded intergranularly with a very narrow and localized attack, penetrating visibly 25 μm into the metal. At TC_7 little corrosion effect is observed at all. The dealloying penetration is graphed in Figure 4-21. Maximum and average local penetration per site (where "local" is at least 15% deeper than the "uniform" portion of the dealloying front) is depicted in Figure 4-22.

A sample of the tubing corresponding to TC_4 from Run 5 was analyzed using EDX. Elemental maps of the dealloyed layer in Run 5 reveal a complex oxide which is depleted in nickel and iron, and enriched in chromium, molybdenum, and tungsten (see Figures 4-23 and 4-24). This indicates that the surface is covered with a porous or otherwise non-protective oxide. The composition of the oxide is apparently uniform, even 40 μm below the surface (along a grain boundary).

Chlorides were only detected in significant quantity (over background) in a piece of debris, which was neither part of the metal wall nor the oxide. The signal from the debris indicates the presence of chlorine and oxygen but none of the other elements (Cr, Fe, Ni, Mo, W), and is most likely an organic contaminant in the resin.

Samples of the 1/16-in tube from Run 5 were etched using the same procedure as for Run 3. However, the exposed Run 5 samples and a "blank" section of pristine 1/16-in tubing exhibited comparable attack over their entire surfaces. The attack

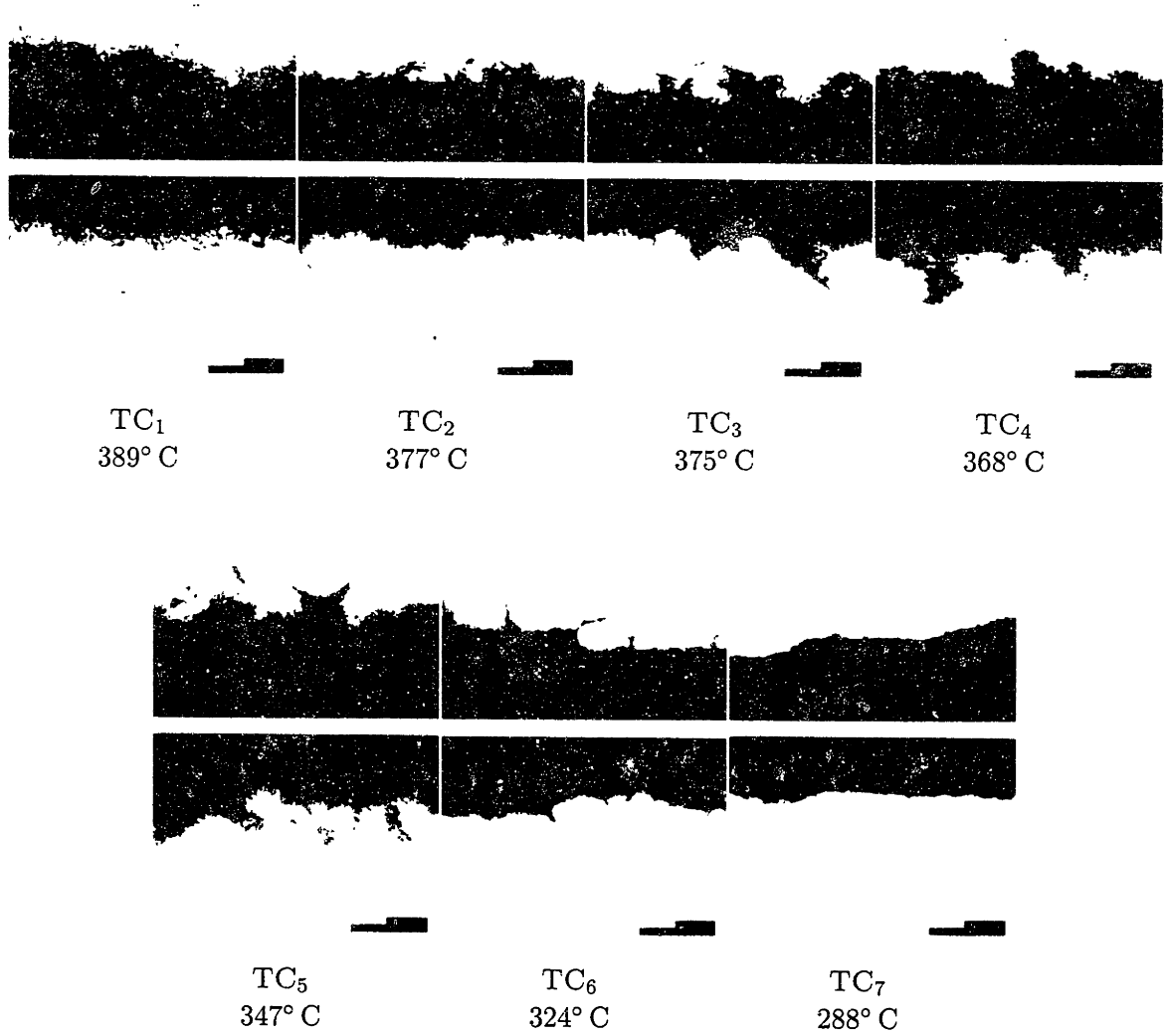

Figure 4-19 Corrosion profile of 1/16-in tube from Run 5. Each frame corresponds to the segment of tube where thermocouples 1–7 were attached. The tubing is not etched. Each photo is approximately 76 μm wide. Position of interface in photo does *not* imply corrosion rate. Angle with radius must be considered when determining penetration depth (see Table A.1).

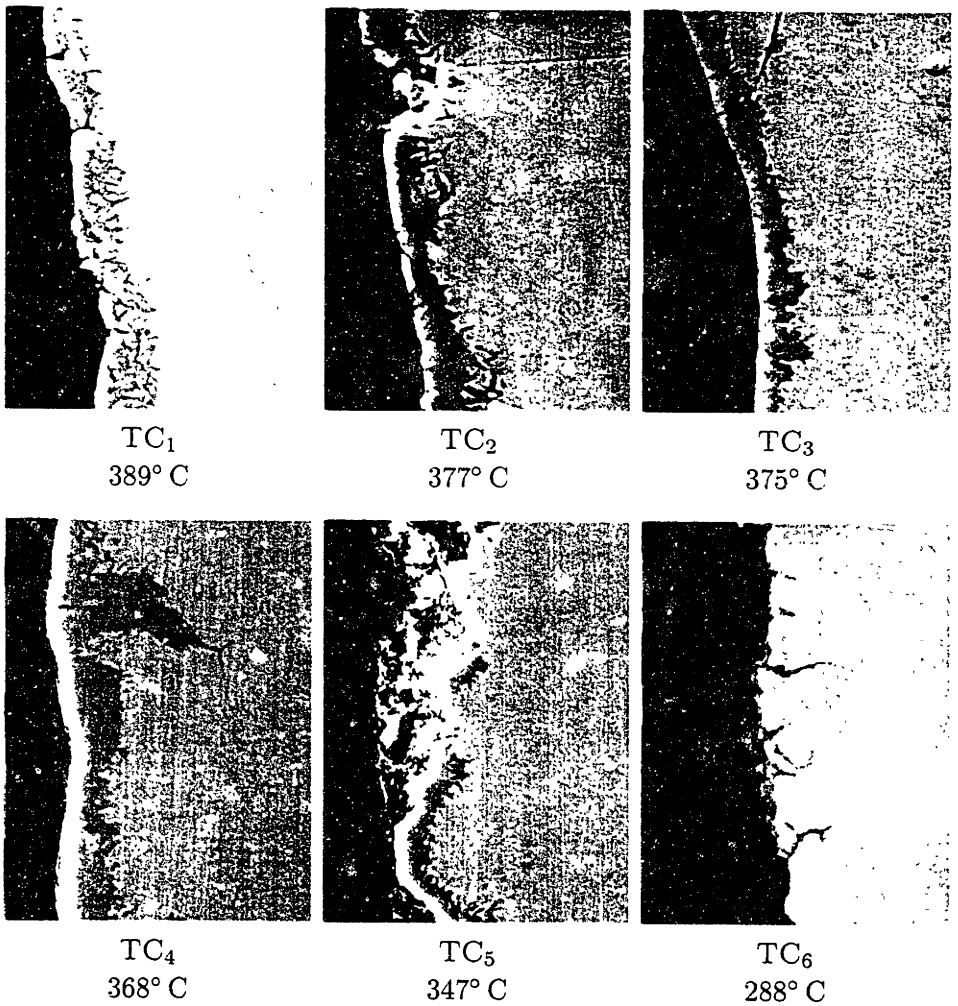

Figure 4-20 Detail of interfaces of each 1/16-in tube sample from Run 5 via SEM (see also Figure 4-19).

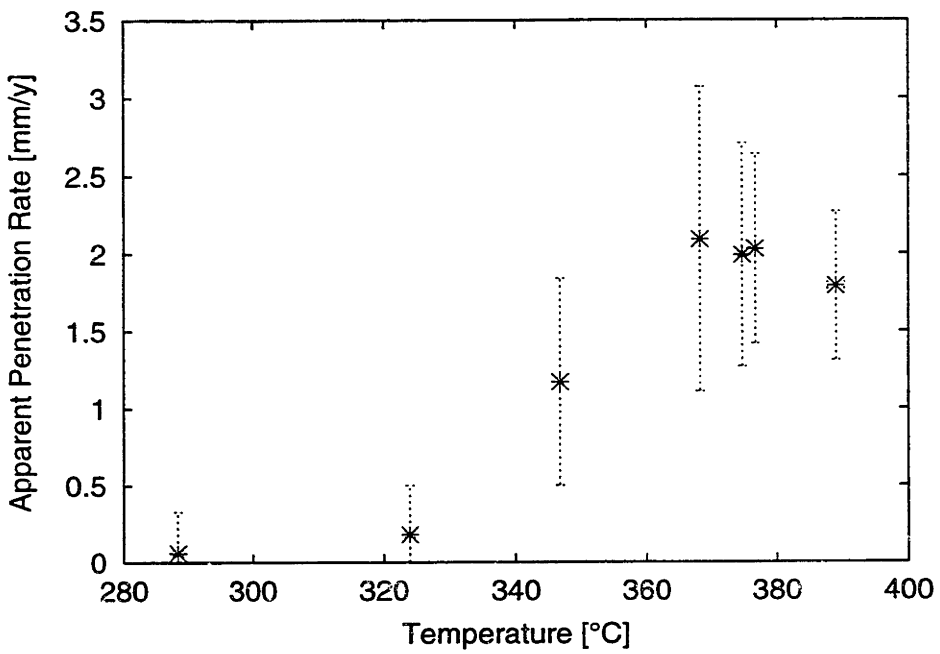

Figure 4-21 Dealloying penetration rate profile for the 1/16-in tube (Run 5).

had intergranular and etch-pit components, but there was *no* preferentially-attacked area, such as that which appeared upon the 1/8-in tube from Run 3. Because the etch-behavior of the exposed samples is indistinguishable from that found in the pristine sample, it is concluded that the 1/16-in tube did not experience any deep intergranular corrosion.

4.2.2 Heat transfer modeling

This heat transfer modeling was performed to provide mathematical confirmation that the measured temperatures are almost identical not only to the inner tube-wall temperatures, but also to the fluid itself. A second benefit is that, if needed, it allows for accurate interpolation for temperatures at points which were not directly measured by thermocouples.

Starting with the model of Section 4.1.2, a new heat transfer model was developed for the cooling tube experiment. The equations for h_o and U_i in the prior heat-transfer model were changed in order to account for the change of medium from sand bath to

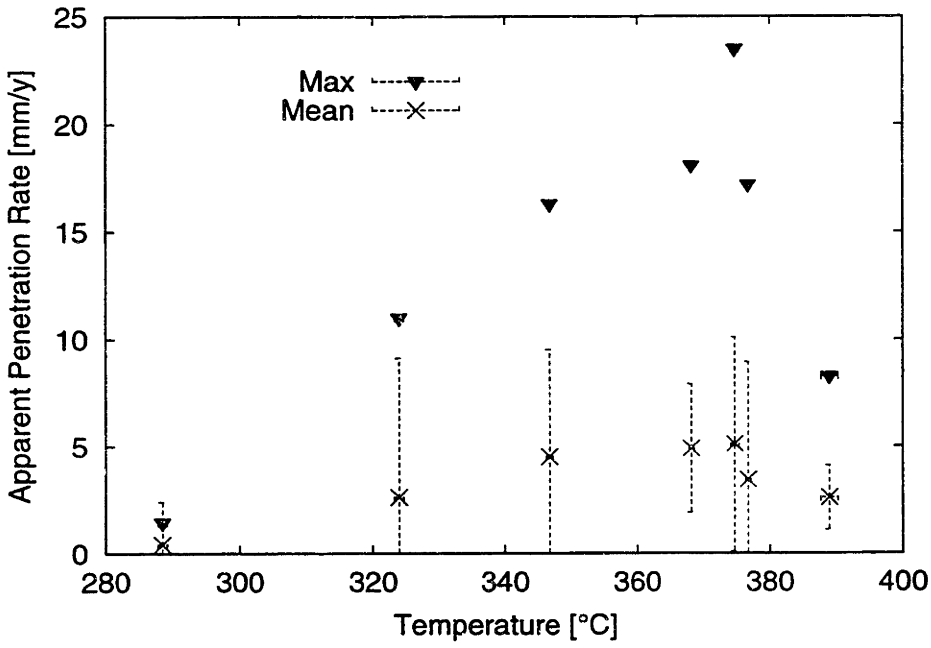

Figure 4-22 Penetration rate of nonuniform dealloying in the 1/16-in tube (Run 5). Data series "Max" have no y-error bars because these points represent the deepest penetrations (of local character) per sample. The error bars on temperature do not appear because they are smaller than the chart symbols. The "Mean" data series is the average penetration length of the seto of penetrations >15% beyond uniform. The mean data are a very rough statistic due to the small sample size, and so the error bars are only a proportional indication to the actual variation.

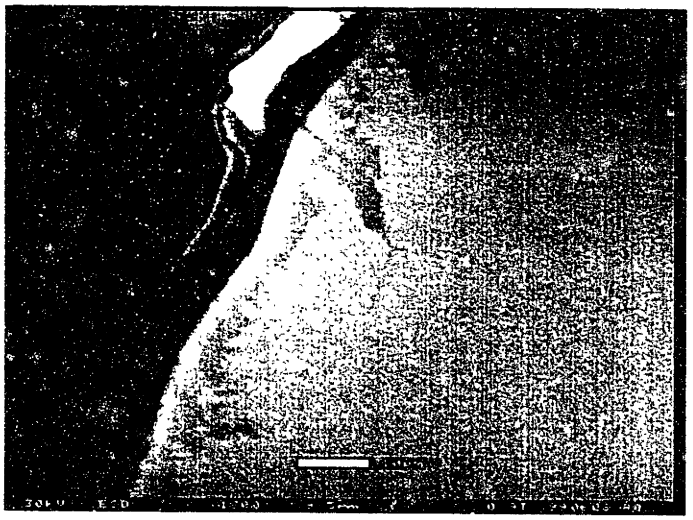

Figure 4-23 ESEM image of the a 1/16-in tube tube exposed at 368° C (TC_4 from Run 5).

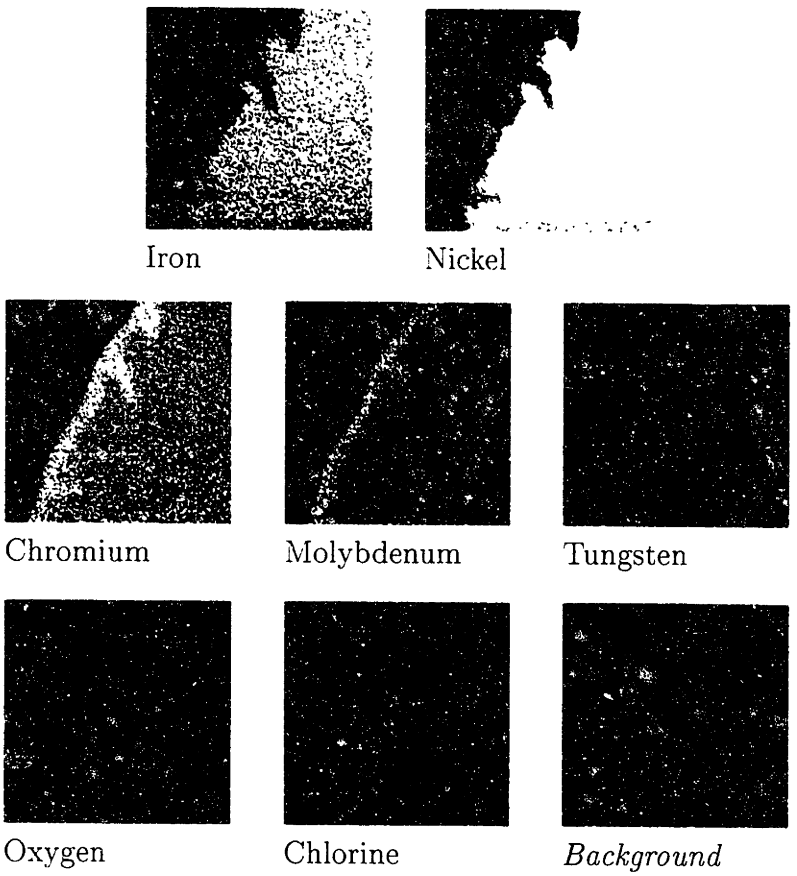

Figure 4-24 Element dot-maps from EDX of the sample in Figure 4-23. Sample is from Run 5, TC_4. Alloy surface is on the right.

air and for heat lost by radiation. The new flux equation is

$$\frac{q}{A} = U_i \Delta T + \epsilon \sigma T_m^4 \tag{4.7}$$

where U_i is similar to the U_i in Equation 4.3 (here h_o corresponds to an air film instead of a sand bath), ϵ is the metal surface emissivity, σ is the Stefan-Boltzmann constant, ΔT is $(T_{air} - T)$, and T_m is the metal surface temperature.

In the medium of air, the external heat transfer (via convection and radiation) is most important. The external heat transfer coefficient h_o is approximately 25 W/m^2-K along the entire length of the tube, while the internal coefficient h_i is two to three orders of magnitude larger (and $d_o/d_i \sim 1$); thus h_o is limiting. The Morgan correlation for convective heat transfer from a horizontal cylinder was combined with the Stefan-Boltzmann equation for gray-body radiation to determine the heat transfer external to the tube.

For the small insulated segments covering the thermocouples, effects of radiation and the external air film are neglected. The thermal conductivity of the insulation is variable (due to small differences in density and how it was attached to the tubing), but the small size of the affected area limits its impact upon the model output.

Initial temperature was set using the first thermocouple (TC_1) measurement. Emissivity was not measured, and so was considered an adjustable parameter. In order to explore how the model compares to the data, two scenarios were computed for each experiment (3 and 5):

- A "maximum temperature" curve, in which radiative heat transfer is essentially turned off ($\epsilon = 0.001$), and initial temperature T_i is set to the maximum reading from TC_1.
- A "minimum temperature" curve, in which $\epsilon = 0.2$, and T_i is set to the minimum reading from TC_1.

Thermocouple readings and model output are presented in Tables 4.7 and 4.8. The choices of emissivity were determined by the condition of the metal, which ranged from a shiny non-mirror-like silvery finish to a dull metallic sheen—but at no time did the exposed surfaces of the metal oxidize visibly to darker colors.

Model outputs are presented in the latter rows of Tables 4.7 and 4.8 and are plotted in Figure 4-25. One finds remarkable agreement between model and data for Run 3, especially for the maximum-temperature curve, which is always within 4° of the measurement. The agreement for Run 5, which used the thinner tubing used in

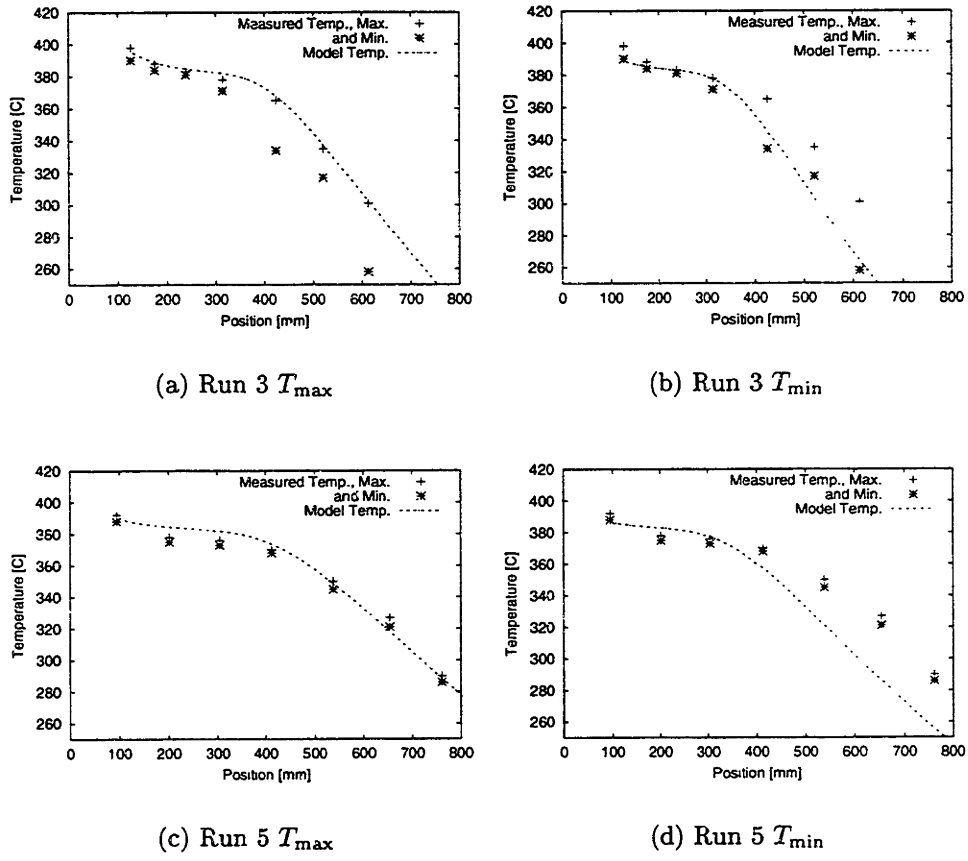

(a) Run 3 $T_{\max}$

(b) Run 3 $T_{\min}$

(c) Run 5 $T_{\max}$

(d) Run 5 $T_{\min}$

Figure 4-25 Maximum and minimum temperature curves generated by the heat transfer model for the cooling-tube experiment. For max. temp. runs, ϵ=0.001; for min. temp. runs, ϵ=0.2.

Section 4.1, is not quite as good. In this case, the "maximum temperature" curve, after the first data point (to which it is set) initially rises above the data, but then at approximately 45 cm realigns with the measurements. One might suspect that the warmer end of the tube had built up enough oxide to increase the emissivity. The emissivity, however, is not the key to the problem, as in Figure 4-25(d) for the "minimum temperature" ($\epsilon = 0.2$) curve, one sees that the temperatures for thermocouples 2 and 3 are still overestimated. This finding only emphasizes the necessity of actual temperature measurements under these experimental conditions.

In the case of the cooling-tube experiment, heat transfer was clearly dominated by the external coefficient. Following the trend in Figure 4-4 (page 82), in which a smaller $h_o\, d_o/d_i$ means a U_i less influenced by solvent properties, it is clear that the external heat transfer coefficient h_o (with $h_o\, d_o/d_i$ of 38 to 55 W/m^2-K) dominates

the overall profile. Because of this, the bulk fluid temperature is negligibly different from the metal temperature, making external measurements accurate measures of the corrosion temperature.

4.3 Discussion

Within these reaction systems there are two main modes of corrosion: *dealloying* and *intergranular* corrosion. Dealloying refers to the selective dissolution of iron and nickel as evidenced by EDX analysis, and produces what appears in the micrographs as a gray product which abuts the bright alloy. Intergranular corrosion refers to the corrosion in the 1/8-in tube which was evidenced by etching. The intergranular corrosion preferentially attacks grain boundaries, sub-boundaries and defects. Each of these modes of corrosion has its own complex behavior with different dependencies upon the environment. These will be reviewed in terms relevant to this experiment.

Review of Intergranular Corrosion

- The intergranular corrosion moves through channels so narrow that diffusion must have a significant effect upon its progress. Diffusion-limited behavior in supercritical water is subject to the electrostriction effects computed by Oelkers and Helgeson (1989) (and recently modeled by Balbuena *et al.* (1998)) in combination with viscosity changes, as per Stokes-Einstein theory.

$$D = \frac{kT}{\zeta} \qquad \zeta = \sigma \pi \eta_s R \tag{4.8}$$

  where D is the ion diffusivity, σ is a constant, η_s is the solvent viscosity, and R is an ion radius. Electrostriction artificially increases R by binding or complexing water molecules to an ion in a tenacious solvation shell. The driving force for diffusive flux includes both the standard Fick's law concentration gradient but also the electric field produced by the electrochemical potential.

- The chemistry in the penetrating front will be somewhat isolated from the chemistry of the bulk. It is expected that these reactions will have phenomenology similar to pitting or cracking. The mechanical relaxation about the intergranular damage is not significant enough to be visible under microscopy of mechanically polished specimens before etching, either because of its small magnitude or because the corroded channels closed when the internal pressure was removed.

The damage can be seen using the ESEM at two magnifications in Figure 4-26.

- There is also an issue of stress. The observed corrosion appears to be very similar in nature to intergranular stress corrosion cracking (IGSCC): the attack is very deep, along very narrow channels. The possibility of the stress enhancing the propagation rate is very real. Stress can influence the rate by (1) increasing the diameter of the channel or pore and therefore increasing diffusive flux, and (2) depending on whether there is nontrivial mechanical relaxation, stress may either expose fresh material at the crack tip or simply alter the local electrochemical potential of the alloy at the channel tip. Another factor to consider is that, as the IGSCC penetrates more deeply, the tube wall thickness decreases, making the tangential stress larger—thus accelerating the crack propagation rate mechanically with decreasing assistance from the water chemistry.

Overall then the reaction rate for the intergranular corrosion is expected to show dependence on diffusivity, reaction thermodynamics, and mechanical stress. The possibility that the reaction becomes less polarized and thus slows down also cannot be eliminated *a priori*. Figure 4-17 on page 101 shows that these effects combine somehow to encourage intergranular corrosion at temperatures lower than 325° C and also perhaps at temperatures near 376° C.

Review of Dealloying The second major effect is the dissolution rate of nickel and iron in the sub- and supercritical water, as evidenced by the uniform dealloying statistics. Here it may be helpful to review the effects of competition between diffusion and kinetics upon the the visible corrosion.

For a given heterogeneous reaction, there are regimes of kinetics and diffusion which have different physical characteristics. (It is assumed that, at least for the cooling-tube experiments, the heat transfer limitation has little role here.) The regimes are classified as fast-reaction and slow-reaction.

- In the case of a slow reaction, the environment is saturated with the proper ions and charges and is just waiting for a reaction to occur; this would encourage attack at any point to which the solvent has access. For instance, the network of channels carved by the intergranular corrosion, where they are wide enough not to be diffusion-limiting, would provide such access. *The slow reaction supports nonuniform attack.* This nonuniform attack occurs not just at the surface but along grain boundaries and through pores and channels. The slow reaction

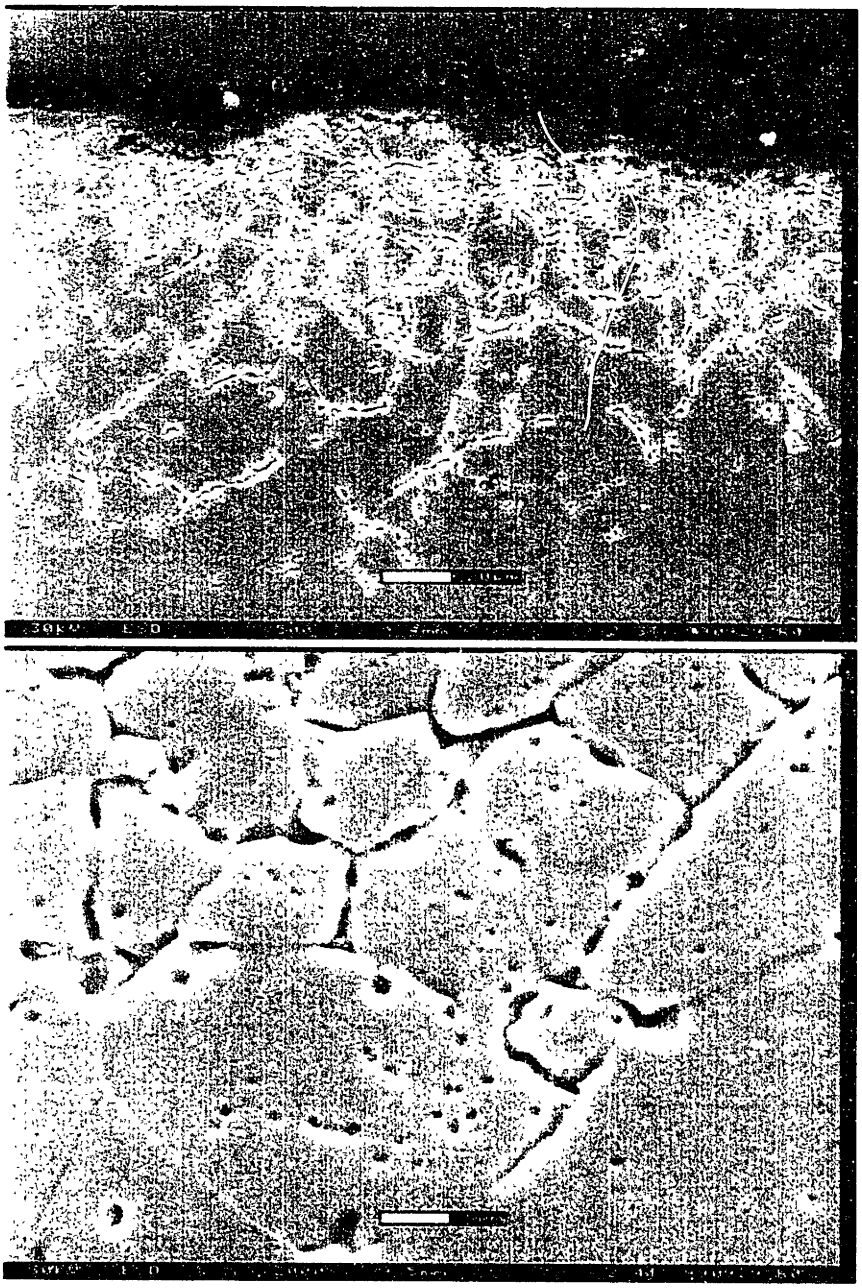

Figure 4-26 ESEM images of etch front on sample of 1/8-in tubing at lower and higher magnifications, respectively (TC_3, Run 3).

is sensitive to changes in polarization. If diffusivity decreases or polarization increases then we may enter the regime of the fast reaction.

- In the case of a fast reaction, the environment is depleted in the ions necessary to carry out the reaction. The reaction would then occur preferentially at points where there is the smallest diffusion barrier. The diffusion may also be especially enhanced (given a barrier of constant properties) by the electric field of the electrochemical reaction at points where the diffusion barrier is physically thin. *The fast reaction supports the uniform reaction front.* The fast reaction will be sensitive to changes in diffusivity. If the diffusivity increases or the polarization drops, the system will revert to the slow-reaction regime.

Dealloying is similar to general corrosion except for the presence of a matrix of insoluble species. If it is not in a diffusion limited regime, its rate is expected to obey the Tafel equation,

$$\eta = \beta \log \frac{i}{i_0} \qquad \text{Tafel} \tag{4.9}$$

where i is the current density required to charge the ions, i_0 is the exchange current density which depends on temperature and surface conditions, β is a solvent- and diffusion-dependent parameter and η is the polarization of the electrode away from its open-circuit potential. The exchange current density comes from an equilibrium reaction system. For an electron-transfer reaction,

$$\mathrm{M}^+ + e^- \rightleftarrows \left[M^+ + e^-\right]^\ddagger \rightleftarrows M \tag{4.10}$$

there are simultaneous forward and reverse reactions, proceeding at forward and reverse reaction rates k_f and k_r, respectively. The forward and reverse reactions are each activated reactions, such that

$$k_f = A_f \exp(-\Delta G_f^\ddagger / RT) \tag{4.11}$$

$$k_r = A_r \exp(-\Delta G_r^\ddagger / RT) \tag{4.12}$$

The reactant concentrations are not explicit here, because they affect the rate by electrically polarizing the system through the Nernst equation. As an open circuit, the metal M is in equilibrium with itself.

$$k_f = k_r = \frac{i_0 a}{n\mathbb{F}} \tag{4.13}$$

When polarized, these reaction rates k_f and k_r do not balance, and charge is diverted to another location (*e.g.*, a hydrogen electrode). A thorough explanation of electrochemical kinetics can be found in Jones (1996, Chapter 3).

Note that i and i_0 are current *densities* and so are implicitly dependent on the surface area. Thus the rate of dealloying depends on i, which is a function of area, as well as T, diffusivity D_{AB}, density ρ, and concentrations $\{C_i\}$ through β, η, and i_0.

Intergranular Corrosion and Dealloying of Hastelloy C-276 Tubes The 1/16-in tube does not exhibit the intergranular corrosion observed in the 1/8-in tube. However, the two tubes were exposed to the same environment and have the same composition. Two possibilities must be addressed: (1) the mechanical properties unique to the 1/16-in tube prevent intergranular corrosion, or (2) the intergranular corrosion does not immediately start in the 1/8-in tube, but rather, as the dealloyed layer thickens, suddenly and rapidly initiates and propagates (and thus is not observed in the shorter exposure time of the 1/16-in tube).

To address the first possibility, consider the grain boundary size and its relevance to mechanical relaxation and SCC mechanisms. In general, grain boundaries prevent slip and thus add strength and rigidity to a material. The yield stress of a polycrystalline solid can be predicted using the Hall-Petch equation (Dieter 1986, p. 189):

$$\sigma_0 = \sigma_i + \frac{k}{\sqrt{D_{GB}}} \qquad \text{Hall-Petch} \tag{4.14}$$

where σ_0 is the yield stress, σ_i is the "friction stress" or overall resistance of the crystal lattice to dislocation movement, k is a "locking parameter" which gauges the relative hardening contribution of the grain boundaries, and D_{GB} is the grain boundary diameter. That the metal in the 1/16-in tube has a D_{GB} of one-fourth the size of the 1/8-in tube material indicates that, assuming k and σ_i are constant for a given material, the yield stress σ_0 is larger for the 1/16-in-tube metal. Further, Vickers microhardness tests confirm that the 1/16-in tube is measurably harder than the 1/8-in tube (Table 4.4.

From Equation 4.14 it can be reasoned that, for a singular mechanical defect, the relaxation of the 1/8-in tube will be greater than the 1/16-in tube. In SCC, the mechanical relaxation of the alloy is important to propagation rate. Thus it may be the grain boundary size which decides whether or not the intergranular corrosion can gain a foothold and propagate into the alloy.

Complicating this line of reasoning is the fact that the tangential stress (or hoop

Parameter	Run 3	Run 5	
R_o	0.0625	0.03125	in
R_i	0.0285	0.02125	in
P_i	15		psia
P_o	15		psia
$S_t(r = R_i)$	5403	6715	psia

Table 4.9 Computed tangential stress for thick-walled tubes in Runs 3 and 5.

stress) is larger for the 1/16-in tube. The tangential stress S_t in the tube (relevant for seam-tearing or stress corrosion cracking) is described by the Lamé formula for cylindrical thick-walled tubing:

$$S_t = \frac{R_i^2 P_i - R_o^2 P_o}{R_o^2 - R_i^2} + \frac{R_i^2 R_o^2 (P_i - P_o)}{r^2 (R_o^2 - R_i^2)} \tag{4.15}$$

where P_i is the internal pressure, P_o is the outside or atmospheric pressure, R_i is the inner tube radius, R_o is the outer tube radius, and r is the radius at which the stress is computed. (For a pristine tube, the r of interest is $r = R_i$.) Table 4.9 shows the tangential wall stress applicable to the tubes in Runs 3 and 5, for perfectly-formed smooth tubes with no cracks or other defects. A notch or other singularity will cause a concentration of stresses into the metal adjacent to the defect. This becomes important after the crack is already started, but prior to that, the Lamé formula is more purely applicable.

Finally there are also effects of temperature, residual stresses, and annealing. The 1/16-in tube, which seems to be at a lower degree of annealing "recovery" would be expected to have larger residual stresses. It is also under higher applied tangential stress during the experiment.

If residual or applied tangential stress alone were the cause, then the 1/16-in tube would be expected to corrode intergranularly first. Instead, the local plasticity of the 1/8-in tube encourages (or fails to discourage) local propagation. Thus the elastic modulus of the 1/16-in tube may protect it from the intergranular corrosion (IGC).

At the higher temperatures, the Young's modulus will decrease and deformation will increase (some). This decrease in elastic modulus may help explain the hair-like morphology of the dealloying front in Runs 3 and 5 at their respective TC_1's. Issues of Young's modulus and alloy hardness thus compete against applied stress and defect

concentration.

To address the second possibility, some 1/8-in tubing from Run 2 was etched. This tubing was exposed to the same hydrothermal HCl environment as in Run 3, but only for 21.5 h. The presence of significantly etched regions indicates that, at an exposure time comparable to that of Run 5, intergranular corrosion had already begun in the 1/8-in tubing. It is most likely that the difference in behavior is due to the differences in mechanical response, as discussed above. That the mechanical response of the tubing plays an important role suggests that the mechanism of corrosion in the 1/8-in tube is intergranular SCC.

In contrast to the intergranular corrosion, dealloying is present and measurable in each of the tubes. Assuming that the dealloyed layer has similar composition and porosity on each tube, one can see from Run 5 and detailed micrographs from Run 3 that the dealloying proceeds in the *slow-reaction* regime. Evidence includes islands of unaffected material and visible penetration into thin, hairlike features (*e.g.*, see Figure 4-12 on page 97).

The dealloying rates in the 1/8-in and 1/16-in tubing are not as comparable as might be expected (Figure 4-27). In general the dealloying is slow to nil (<0.5 mm/y) below 300° C for each tube. But at the intermediate temperatures, the dealloying in the 1/8-in tube exceeds that of the 1/16-in tube. And for the points available near the critical point of pure water, the dealloying rate in the 1/16-in tube exceeds that of the 1/8-in tube. It is speculated that these rate differences are due to initial surface roughness, differences in available surface area due to intergranular corrosion, and mechanical relaxation. For instance, at higher temperature the uniform dealloying rate is more difficult to characterize due to the many overlapping cleavage-like features and small, undercut islands. At intermediate temperatures (Run 3 TC_6 vs. Run 5 TC_6) it may be speculated that the rate disparity is due to increased porosity of the dealloying interface due to IGC. However, this does not apply to TC_7, where the lack of corrosion in *both* cases implies a thermal activation barrier.

For temperatures at and above the critical point ($T \geq 374°$ C) there is an intriguing similarity between the maximum sitewise local dealloying penetration rates of the 1/16-in tube and the intergranular corrosion rates seen in the 1/8-in tube (Figure 4-28). This suggests that the mechanism of penetration in the nonuniform dealloying may be related to the mechanism of the intergranular corrosion observed in the 1/8-in tube. It is speculated that, whereas in the 1/8-in tube the mechanical relaxations were sufficient for the intergranular corrosion reaction to progress, in the 1/16-in tube, which is harder, the relaxations alone do not increase the diameter of the channels

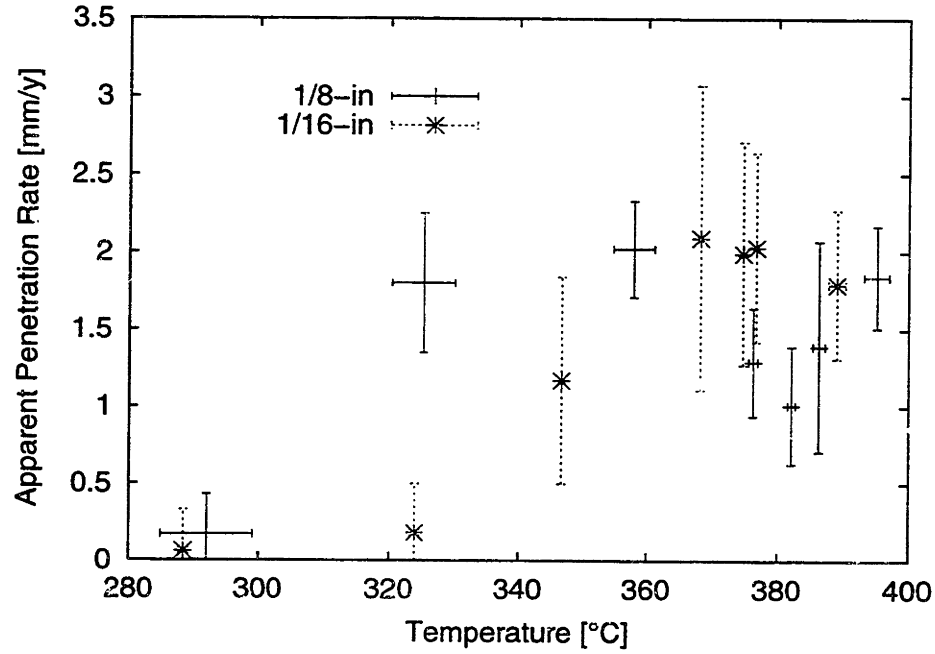

Figure 4-27 Comparison of the uniform dealloying rates in the 1/8-in and 1/16-in tubes from Runs 3 and 5.

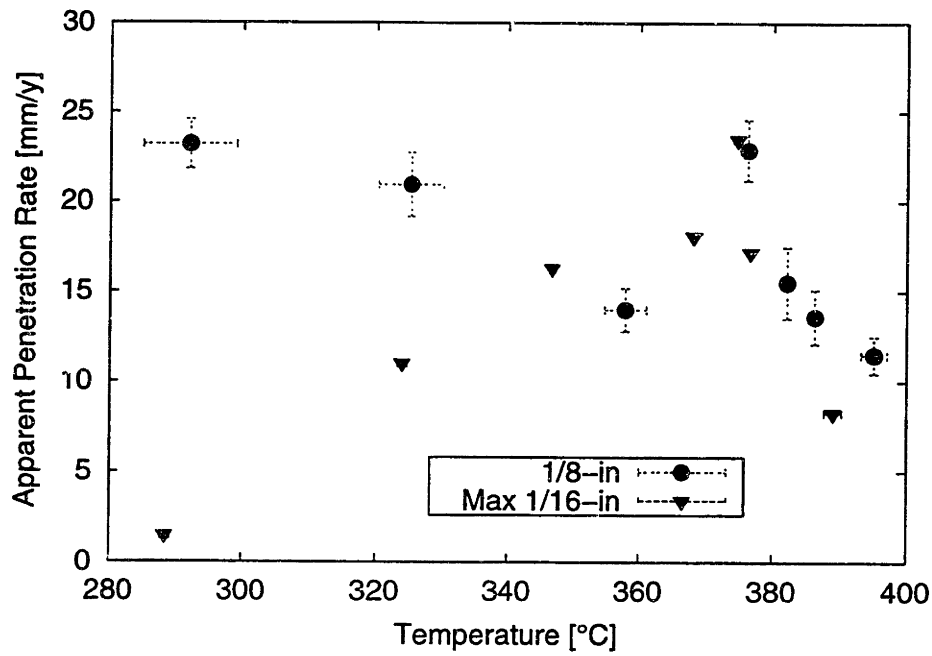

Figure 4-28 Comparison of intergranular corrosion rate in the 1/8-in tube and the maximum localized dealloying rates in the 1/16-in tube.

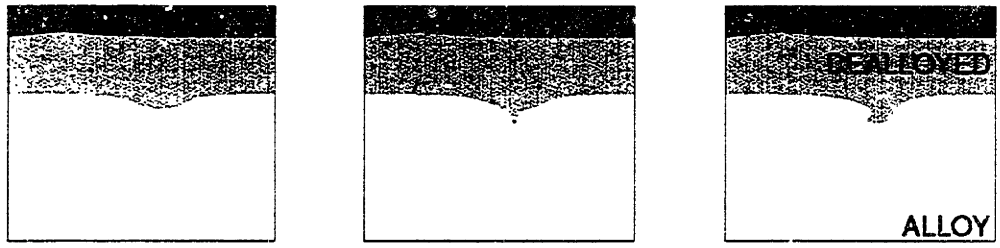

Figure 4-29 Proposed mechanism of dealloying which thwarts intergranular cracking. A singularity develops, but is blunted by dealloying.

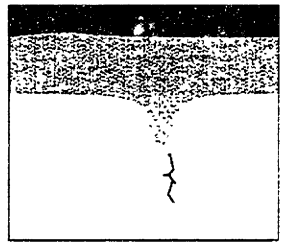

Figure 4-30 Ultimate fate of nonuniform dealloying.

enough to allow intergranular corrosion to propagate. Dealloying is required in order to increase the porosity of the material around the intergranular-corrosion initiation site and therby supply the intergranular-corrosion reactions with the required ion flux. Because the dealloying occurs in the slow-reaction regime, there is enough access for ions between bulk and singularity-tip that significant dealloying may occur. The dealloying has the effect of widening the channel and blunting the tip of the singularity, thwarting the diffusion-limited chemistry and the mechanical stress that the intergranular-corrosion mechanism requires to propagate—to an extent (Figure 4-29). This is similar to a mechanism described by Sieradzki and Newman (1987). As the cycle proceeds, the singularity becomes progressively deeper and, eventually, the diffusion barrier presented by the dealloyed metal surrounding the intergranular-corrosion channel becomes large enough that the widening and blunting afforded by dealloying are not enough to retard propagation, and the corrosion switches to a SCC regime (Figure 4-30), as seen in the preheater post-failure analyses.

Figure 4-31 is a zeroth-order Arrhenius plot of the dealloying penetration rate. A

purely thermally-activated reaction would exhibit a straight line, but the observed rates seem independent of temperature at the higher temperatures. Changes in dealloying rate can be attributed to changes in electrochemical potential, exchange current density, or surface area. As the dielectric constant of water changes, the free energy of solvation of aqueous ions changes. (Refer to Debye-Hückel theory, summarized in Section 3.4.3, to see the functional form of the dependence.) This would change the polarization of the reaction, changing the rate through the η term of the Tafel Equation 4.9. Similarly, if the transition state of the exchange-current reaction is zwitterionic, the exchange-current density i_0 may also be affected by the solvent dielectric strength. Kirkwood (1934) showed that the free energy of solvation of a charge distribution in a dielectric continuum (with respect to vacuum) can be expressed as

$$\begin{aligned}\Delta\overline{G}_{D/D_0} &= \frac{Q_0}{2b}\left(\frac{1-D}{D}\right) + \frac{Q_1}{2b^3}\left(\frac{1-D}{2D+1}\right) + \cdots \\ &\approx \frac{(ze)^2}{8\pi\epsilon_0 b}\,\frac{1-D_s}{D_s} + \frac{|\mu|^2}{4\pi\epsilon_0 b^3}\,\frac{1-D_s}{2D_s+1}\end{aligned} \tag{4.16}$$

where D is the dielectric constant of the solvent, b is the radius of the spherical solvent-less cavity around the zwitterion, and the $\{Q_i\}$ are functions in a multipole expansion. For a simple dipole, $Q_0 = 0$, $Q_1 = |\mu|^2$, and the higher-order $\{Q_i\}$ are negligible. Kirkwood further shows that a direct consequence of Equation 4.16 is that the log of the ratio of the solubility of a zwitterion in dielectric D_s=D to its solubility at D_s=D_0 is a linear function of $1/D$. In Figure 4-32 is a zeroth-order Arrhenius plot of the penetration rate scaled by the dielectric constant. While the plot still retains a good deal of scatter, the trend appears to be linear. (In Figure 4-32, the sensitivity of the dielectric strength to the error in temperature was not assessed, and is not shown in the error bars.) This is an empirical fit based on theoretical intuition. Finally, while the surface area can affect the dealloying rate, a good measure of the porosity and relative surface area would be difficult to obtain, and therefore here is not a factor in the mathematical analysis.

For the 1/8-in tube of Run 3 there appear two distinct trends in the depth of intergranular corrosion (recall Figure 4-17). Because the peak in the IGC corresponds closely with a peak in local corrosion in the 1/16-in tube, let us assume that it is not an outlier. Then, each of these apparent trendlines shows a decreasing corrosion rate with temperature. The noticeable discontinuity near the critical point suggests that a change in the chemistry or the mechanisms of the intergranular corrosion takes place there. The low-temperature regime has a gentle negative slope; the high-temperature

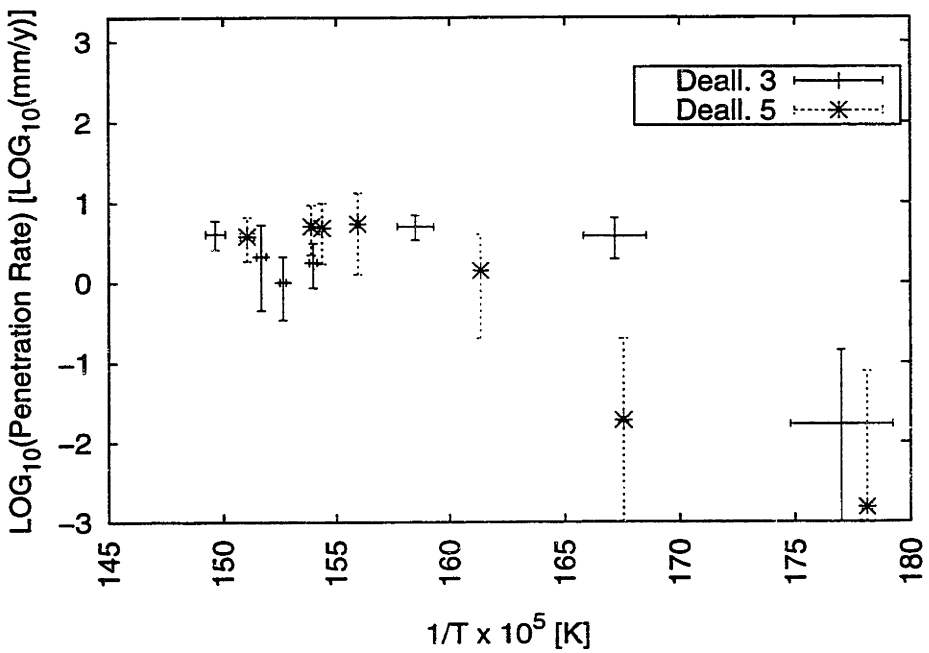

Figure 4-31 Arrhenius plot of uniform dealloying rates in the 1/8-in and 1/16-in tubes.

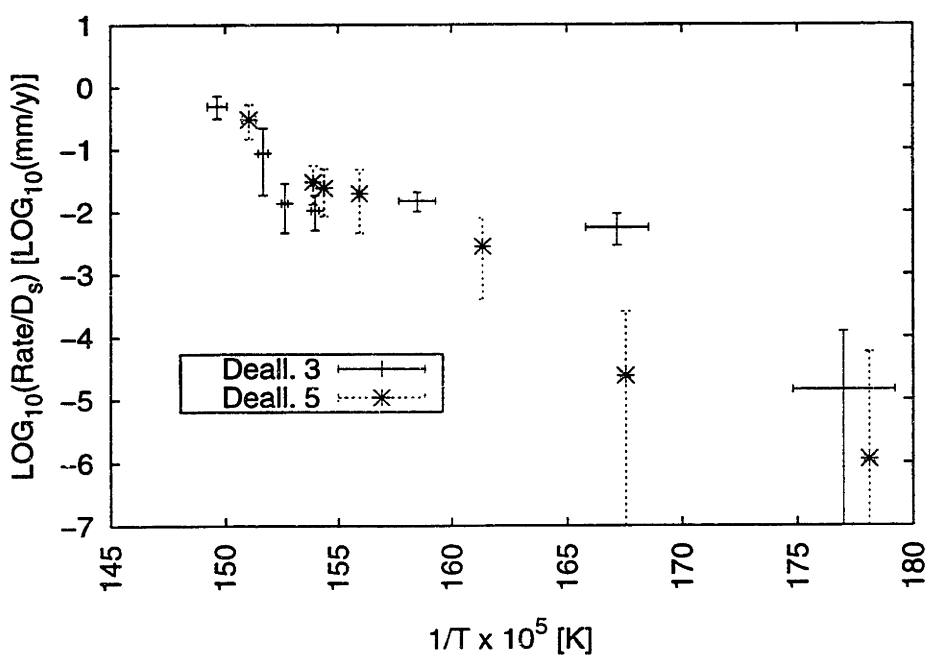

Figure 4-32 Arrhenius plot of uniform dealloying rates in the 1/8-in and 1/16-in tubes, scaled by the dielectric constant of water.

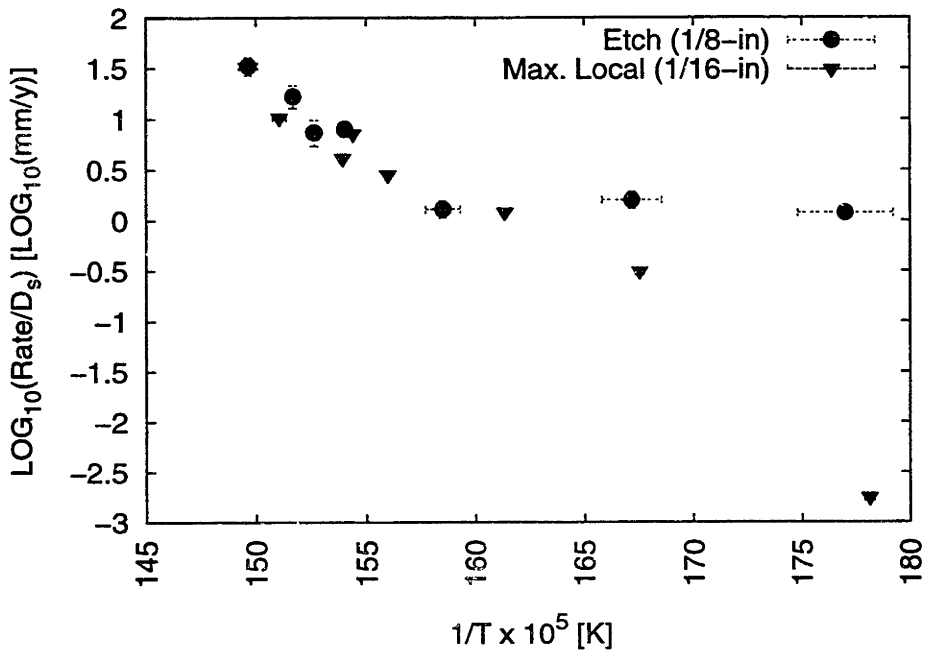

Figure 4-33 Arrhenius plot of maximum observed non-uniform dealloying rates in the 1/16-in tube *and* intergranular corrosion in the 1/8-in tube, scaled by the dielectric constant of water.

regime has a much larger negative slope. Each segment is approximately linear. It is speculated that the second (high-temperature) segment actually asymptotically approaches the first, representing an excursion near the critical point from a "usual" behavior found in the remainder of the tube.

Applying a dielectric-scaling to the intergranular corrosion *and* the nonuniform dealloying, a linearization is effected (Figure 4-33), particularly for the maximum observed nonuniform dealloying penetration. The similarity in rates between dealloying and intergranular corrosion at higher temperatures is plainly apparent. Also visible is the point of departure, where differences in propagation mechanism (due to mechanical phenomena in the tube wall) affect penetration rate. However, because the possibility of diffusion limitations has not been eliminated, the apparent linearity may be fortuitous.

It is proposed that the intergranular corrosion follows a mechanism similar to the nonuniform dealloying. As before, a singularity develops on the surface at a grain boundary (Figure 4-34). But instead of dealloying, the metal deforms, allowing access to an intergranular channel. With a narrow channel available in which local diffusion-limited chemistry can become established, intergranular penetration can propagate.

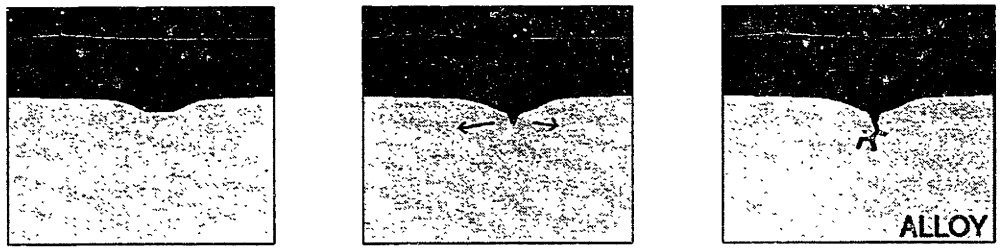

Figure 4-34 Proposed mechanism of deformation which promotes intergranular cracking. A singularity develops, and the stress pulls a crack open.

Differences in intergranular corrosion rate can be caused by variations in the material properties or the interplay between material and environment. In terms of materials properties, the time-temperature history of the material can play a role, because, for instance, chromium carbide precipitates can deplete the chromium concentration in the grain boundaries, making them chemically different from the bulk material. In general, for the cooling tube experiment, the outward heat flux is limited by the *external* heat transfer coefficient. This means that the entirety of a tube slice is essentially at one temperature. Since the interior of the tube cannot have a significantly different time-temperature history than the exterior of the tube, the preferential etch sensitivity near the inner radius can not have been caused by heat sensitization.

Residual and applied stresses can also impact the rate of intergranular corrosion by mechanical relaxation, in a mechanism of IGSCC. Stress effects are also affected by temperature, as alloys generally soften at higher temperatures. In this case, temperature-influenced deformation may be a factor in the development of the hair-like intrusions seen at higher temperatures (TC_1). At higher temperatures, annealing and stress-relief is a possibility. However, no change in grain size was detected in the test sections during these experiments. Annealing effects must still be considered for longer exposure periods.

4.4 Conclusions

In this study two different sizes of Hastelloy C-276 tubing were exposed to a hydrothermal aqueous HCl solution. It was found that the 1/16-in tube exposed in the controlled experiment exhibited corrosion behavior similar to the 1/16-in tubes used

for preheaters, as examined under post-failure analysis. The corrosion observed was a selective dissolution of of iron and nickel from the Hastelloy C-276 matrix. This dealloying was coupled with an intergranular corrosion mechanism. The intergranular corrosion in the 1/16-in tube was thwarted by the blunting effect of the dealloying and the rigidity of the metal matrix, which prevented propagation of diffusion-limited intergranular corrosion. As evidenced by the preheater failure analysis, eventually the penetration of dealloyed singularities is deep enough that diffusion-limited propagation can take place, either because the dealloyed layer is acting as a diffusion barrier or because the dealloyed layer failed under the stress and injected a crack into the alloy. The deepest penetration in the controlled experiment was found to occur between 370 and 380° C.

The 1/8-in tube exhibited uniform dealloying, but also deep intergranular corrosion which was only evident after etching. It is believed that the dealloying rate was slightly enhanced by the additional surface porosity afforded by the intergranular corrosion. The intergranular corrosion was found to propagate in the 1/8-in tube but not in the 1/16-in tube because of measurable differences in the hardness of the alloys, due to grain size differences. Intergranular attack was most dramatic at ≈370° C and also at ≈290° C, which was the lowest temperature for which intergranular corrosion rate was assessed.

The uniform-front dealloying in both tubes was found to be thermally activated with an inverse dependence on the dielectric constant of water. The dependence on D_s is attributed to changes in activity of the dissolved species and also in the exchange current density. (In the case of the exchange current density, the reaction transition state, under conventional transition state theory, would be the affected species.)

At supercritical temperatures, the temperature-dependent rate of nonuniform dealloying in the 1/16-in tube was very similar to the rate of intergranular corrosion in the 1/8-in tube. This suggests that at these temperature the mechanisms are very strongly coupled.

While the dealloying rate can be estimated as a function of temperature and solvent dielectric constant, the true danger of the corrosion is in the localized phenomena which are still not well characterized. While it is obvious that susceptibility to local corrosion in a given environment varies from material to material, this investigation demonstrates that even different forms of the same material may have different local corrosion susceptibilities. The 1/16-in tube is superior to the 1/8-in tube in terms of intergranular corrosion. However, the 1/16-in tube is still susceptible to local penetration when the dealloyed layer is large enough. The critical depth of the dealloyed

layer is expected to vary as temperature changes. Finally, it is recommended that further studies regarding local corrosion distinguish between materials with different metallurgical properties, such as hardness or grain boundary size.

Bibliography

Alloy Digest, Inc. (1985). *Data on INCO Alloy C-276.* NJ.

Balbuena, P. B., K. P. Johnston, P. J. Rossky, and J.-K. Hyun (1998). Aqueous ion transport properties and water reorientation dynamics from ambient to supercritical conditions. *J. Phys. Chem. B* **102** (19), 3806–3814.

Cline, J. A., P. A. Marrone, D. B. Mitton, R. M. Latanision, and J. W. Tester (2000, January). Corrosion mechanisms of Hastelloy C-276 in hydrothermal HCl solutions: Failure analysis and exposure studies. To be submitted to *Corrosion.*

Dieter, G. E. (1986). *Mechanical Metallurgy.* New York: McGraw-Hill.

Fullman, R. L. (1953). *Trans. AIME* **197**, 447 and 1267.

Haar, L., J. S. Gallagher, and G. S. Kell (1984). *NBS/NRC Steam Tables.* Hemisphere Publishing Corp.

Holgate, H. R., P. A. W. J. W. Tester, and R. K. Helling (1992). Carbon monoxide oxidation in supercritical water: The effects of heat transfer and the water-gas shift reaction on observed kinetics. *Energy & Fuels* **6** (5), 586.

Jackson, J. D. and W. B. Hall (1979). *Turbulent Forced Convection in Channels and Bundles*, Volume 2, pp. 563ff. Washington: Hemisphere Publishing Corp.

Jones, D. A. (1996). *Principles and Prevention of Corrosion.* Upper Saddle River, NJ: Prentice Hall.

Kelly, R. G., A. J. Young, and R. C. Newman (1993). Electrochemical impedance: Analysis and interpretation. In J. R. Scully, D. C. Silverman, and M. W. Kendig (Eds.), *ASTM STP 1188*, pp. 94. American Society for Testing Materials.

Kirkwood, J. G. (1934). Theory of solutions of molecules containing widely separated charges with special applications to zwitterions. *J. Chem. Phys.* **2** (7), 351.

Marrone, P. A. (1998). *Hydrolysis and oxidation of model organic compounds in sub- and supecritical water: Reactor design, kinetics, measurements, and modeling.* PhD thesis in Chemical Engineering, Massachusetts Institute of Technology, Cambridge, MA.

Marrone, P. A., T. A. Arias, W. A. Peters, and J. W. Tester (1998). Solvation effects on kinetics of methylene chloride reactions in sub- and supercritical water: Theory, experiment, and *ab initio* calculations. *J. Phys. Chem. A* **102** (35), 7013–28.

Marrone, P. A., R. P. LaChance, J. L. DiNaro, B. D. Phenix, J. C. Meyer, J. W. Tester, W. A. Peters, and K. C. Swallow (1995). Methylene chloride oxidation and hydrolysis in supercritical water. In K. W. Hutchenson and N. Foster (Eds.), *Innovations in Supercritical Fluids: Science and Technology*, ACS Symposium Series #608. Washington, D.C.: American Chemical Society.

Mitton, D. B., J. C. Orzalli, and R. M. Latanision (1995). Corrosion studies in supercritical water oxidation systems. In K. P. Johnston and J. M. L. Penninger (Eds.), *Innovations in Supercritical Fluids: Science and Technology*, ACS Symposium Series #608. Washington, DC: American Chemical Society.

Mitton, D. B., S.-H. Zhang, M. S. Quintana, J. A. Cline, N. Caputy, P. A. Marrone, and R. M. Latanision (1998). Corrosion mitigation in SCWO systems for hazardous waste disposal. In *Corrosion 98*, Number 414, Houston, TX. NACE.

Oelkers, E. H. and H. C. Helgeson (1989). Calculation of the transport properties of aqueous species at pressures to 5 KB and temperatures to 1000° C. *J. Solution Chem.* **18** (7), 601–640.

Perry, R. H. and D. Green, eds. (1984). *Perry's Chemical Engineers' Handbook* (6th ed.). McGraw-Hill.

Press, W. H., S. A. Teukolsky, W. T. Vetterling, and B. P. Flannery (1992). *Numerical Recipes in C: The Art of Scientific Computing* (2nd ed.). Cambridge University Press.

Protopopov, V. S. (1977). Generalizing relations for the local heat-transfer coefficients in turbulent flows of water and carbon dioxide at supercritical pressure in a uniformly heated circular tube. *High Temperature* **15** (4), 687.

Sieradzki, K. and R. C. Newman (1987). Stress-corrosion cracking. *J. Phys. Chem. Solids* **48** (11), 1101–13.

Tester, J. W., P. A. Marrone, M. D. DiPippo, K. Sako, M. T. Reagan, T. A. Arias, and W. A. Peters (1998). Chemical reactions and phase equilibria of model halocarbons and salts in sub- and supercritical water. *J. Supercrit. Fluids* **13**, 225–240.

Vreedenberg, H. A. (1958). Heat transfer between a fluidized bed and a horizontal tube. *Chem. Eng. Sci.* **9**, 52.

Watts, M. J. and C. T. Chou (1982). Mixed convection heat transfer to supercritical pressure water. In *Proceedings of the Seventh International Heat Transfer Conference*, Volume 3, Munich, Fed. Rep. of Germany, pp. 495.

Chapter 5

A Density-Functional Theory Model of α-Cr_2O_3

5.1 Modeling of Chromium Oxide

Chromium oxide is the least understood and studied of the transition metal oxides in terms of surface electronic structure properties (Henrich and Cox 1994). It is useful as a catalyst in many applications including internal combustion engine emission technology (Harrison *et al.* 1998) and the dehydrogenation of alkanes (Bond 1974; Mentasty *et al.* 1999). Cr_2O_3 is also the primary constituent of passive films protecting stainless steels and other high performance industrial alloys (Alstrup *et al.* 1994; Figueiredo *et al.* 1994; Ryan *et al.* 1994). It is known that chloride promotes corrosion initiation, penetrating the passivating Cr_2O_3 surface but the associated atomic-level mechanisms remain enigmatic (Mitton *et al.* 1998; Burstein and Mattin 1992; Newman and Sieradzki 1994).

As the problem of chloride-enhanced corrosion is of widespread industrial relevance, many techniques have been used to investigate the nature and ancillary causes of chloride-enhanced corrosion. Theoretical treatments such as percolation and fracture models have been used to treat the propagation of the resulting cracks, but until now there has been no theoretical technique which could capture the critical interactions between the solid oxide surface and the chlorinated medium.

Quantum mechanics provides means for determining the electronic structure of the oxide surface, which in conjunction with the theory of local chemical softness/hardness (Yang and Parr 1985) can be used to assess and explore chemical reactivity. However, full quantum mechanical treatments of such a complex system have been, until recently, so computationally demanding so as to be impossible to perform. Advances in

computer technology, in conjunction with developments of quantum-mechanical treatments such as density functional theory, have now made such a quantum-mechanical treatment of a metal oxide reasonable to perform.

5.1.1 Density Functional Theory

Density functional theory, developed by the recent Nobel laureate Walter Kohn (Hohenberg and Kohn 1964; Kohn and Sham 1965), is a method which is equivalent to numerically solving the Schrödinger equation. The Schrödinger equation is oft expressed in condensed form as the eigenvalue problem

$$\hat{\mathrm{H}}\Psi = E\Psi \tag{5.1}$$

where $\hat{\mathrm{H}} = \hat{\mathrm{T}} + \hat{\mathrm{V}}$ is the Hamiltonian operator ($\hat{\mathrm{T}}$ is the kinetic energy operator, $\hat{\mathrm{V}}$ is the potential energy operator) and Ψ is the many-body wavefunction. The potential energy operator is a combination of energies from the electron-electron interactions, the electron-ion interactions, and the ion-ion interactions.[1]

$$\hat{\mathrm{V}} \equiv \hat{\mathrm{V}}_{e-e} + \hat{\mathrm{V}}_{e-I} + \hat{\mathrm{V}}_{I-I} \tag{5.2}$$

In general, because the mass of the electrons is so much smaller than the mass of nuclei, the electrons respond much more quickly to outside forces. Because of this mass disparity, most *ab initio* calculations employ the Born-Oppenheimer approximation, in which the nuclei are assumed to be standing still with respect to the electrons. Under the Born-Oppenheimer approximation, the ion-ion interaction is constant, and therefore is irrelevant to the variational calculation; as such, the ion-ion energy is computed "off-line."

$$\hat{\mathrm{V}} = \hat{\mathrm{V}}_{e-e} + \hat{\mathrm{V}}_{e-I} \qquad \text{under DFT} \tag{5.3}$$

Now we consider only the electron-electron and electron-ion interactions. It was proven that the potential energy in the system can be expressed in terms solely of

[1] In this text, the word "ion" is often used to indicate an ionic core, or a nucleus.

the local electron density $\rho(\boldsymbol{r})$ (Hohenberg and Kohn 1964; Kohn and Sham 1965).

$$\rho(\boldsymbol{r}) = N_{\text{el}} \int \|\Psi(\boldsymbol{r}, \boldsymbol{r}_2, \boldsymbol{r}_3, \cdots, \boldsymbol{r}_N)\|^2 \; d\boldsymbol{r}_2 \, d\boldsymbol{r}_3 \, \cdots \, d\boldsymbol{r}_N \tag{5.4}$$

$$\hat{\mathrm{V}}[\rho(\boldsymbol{r})] = E_{\text{potential}} \tag{5.5}$$

This implies that the potential energy of the system does not depend on the separate contributions of each body, but only of the total charge density at each point. Thus the multi-particle wavefunction Ψ *can* be factored into individual-particle wavefunctions $\{\psi_n\}$. I emphasize *can* because this simplification comes at the price of changing the potential energy operator. The motions, spins, and positions of the electrons are correlated, and this is accounted for explicitly in the many-body wavefunction Ψ. When the individual $\{\psi_n\}$ are treated separately, a certain energy of exchange and correlation in the potential and kinetic energies is overlooked, which must be replaced by a correction. The exact exchange-correlation functional is proven to exist, but has no known analytic functional form. Thus the exchange-correlation functions are computed and parameterized (Perdew and Zunger 1981) from more complex calculations. The equivalent Hamiltonian operator under density functional theory is

$$\hat{\mathrm{H}} = \hat{\mathrm{T}} + \hat{\mathrm{V}}_H + \hat{\mathrm{V}}_{e-I} + \hat{\mathrm{V}}_{\mathrm{XC}} \tag{5.6}$$

where $\hat{\mathrm{V}}_{e-e}$ has been replaced by the Hartree potential operator $\hat{\mathrm{V}}_H$ and the exchange-correlation potential $\hat{\mathrm{V}}_{\mathrm{XC}}$ is included. The equivalent Kohn-Sham Hamiltonian for each electron in the many-electron system is

$$\hat{\mathrm{H}}\psi_i = \hat{\mathrm{T}}\psi_i + \left(\hat{\mathrm{V}}_H[\rho(\boldsymbol{r})] + \hat{\mathrm{V}}_{e-I}[\rho(\boldsymbol{r})] + \hat{\mathrm{V}}_{\mathrm{XC}}[\rho(\boldsymbol{r})]\right)\psi_i = \varepsilon_i \psi_i \tag{5.7}$$

where ε_i is the eigenenergy of the wavefunction ψ_i. The Hamiltonian is only indirectly dependent on the individual ψ_i by their contribution to the charge density (and the resulting electric field), and is computed to self-consistency through iteration.

The outputs of density functional theory include the total energy of the system, the eigenenergies of the wavefunctions $\{\psi_i\}$, and the charge density of the system. Additional derived quantities include the electrostatic forces upon the nuclei, the mechanical response of the system (derived from the partial derivative of energy with respect to the lattice vectors or the positions of ions), the magnetic order of the system (when using a spin-dependent exchange-correlation functional), and the spatial

distributions of the bands. Overall, density functional theory provides a reasonable computational method for determining the interactions of an oxide with other chemical species explicitly in terms of electronic states and bonding, allowing exploration of the responses of the multi-atom system to various mechanical and chemical stimuli.

5.1.2 Application of Density Functional Theory to Cr_2O_3

Experimentally, metal oxide surfaces are harder to study than pure metal surfaces (Foord and Lambert 1986). Theoretically, transition metal oxides are computationally demanding to model using *ab initio* methods because of the large number of valence electrons and the manifold of tightly bound *d*-states (Henrich and Cox 1994; Cox 1992). Manassidis *et al.* (1993) were the first to use *ab initio* density functional theory (DFT) in the local density approximation (LDA) to study the structure and energetics of the basal plane surface of Al_2O_3. They found very large surface relaxations which resulted in a reduction of the surface energy by a factor of two. Wang *et al.* (1998) used spin-DFT with the generalized gradient approximation and a full potential linearized augmented plane wave (FP-LAPW) basis set to study the α-Fe_2O_3 (0001) surface as a function of oxygen pressure. An important finding was that the oxygen-terminated surface becomes more stable than the iron-terminated surface in an oxygen rich environment. Veliah *et al.* (1998) also employed DFT with both the local spin-density approximation (LSDA) and non local LSDA (NLSDA) to study Cr_mO_n clusters. *Ab initio* periodic unrestricted Hartree-Fock (UHF) was carried out by both Catti *et al.* (1996), who studied bulk Cr_2O_3, and Rehbein *et al.* (1998), who modeled the chromium-terminated α-Cr_2O_3 (0001) and (0112) surfaces. Recently, Rohr *et al.* (1997) simulated the molecular dynamics of a hybrid Cr_2O_3 (0001) surface with half a layer of chromium ions using classical interatomic potentials.

Below, results of *ab initio* DFT calculations are reported for bulk Cr_2O_3 using LSDA, and for comparison, LDA (see also (Cline *et al.* 1999)). These results strongly support the use of the LSDA as a robust approximation for calculation of the Cr_2O_3 (0001) surface in vacuum. To gain insight into the interaction of the Cr_2O_3 surface with adsorbed species (chloride and sulfide) and to better understand both aqueous chloride-initiated corrosion at the atomic level and the catalytic activity of the Cr_2O_3 surface, the oxygen-terminated surface is studied. Results for atomic, electronic, and magnetic structure are presented. The relaxation which we find for the surface involves a contraction of the outermost oxygen layer with a rotational reconstruction.

The work described below paves the way ultimately to an *ab initio* understanding of the electrochemistry, halogen-sensitivity, and loss of catalytic activity of the Cr_2O_3 surface.

5.2 Methodology

The calculations are carried out within the *ab initio* pseudopotential density-functional formalism to provide a first-principles quantum-mechanical treatment. This approach has been applied successfully in the past to a wide variety of solid-state and surface systems. (See Payne *et al.* (1992) for a review.) Three approximations are necessary to make the calculations tractable. First, the surface is treated as a periodic array of slabs of finite thickness at finite separation in order to maintain periodic boundary conditions so that fast Fourier transform (FFT) techniques may be employed. Next, the pseudopotential, or "frozen-core," approximation is used at a given plane wave cutoff to describe the effect of the ionic cores on the valence electronic system. Finally, density functional theory as outlined in Section 5.1.1 is in principle exact, but the exact exchange-correlation functional is unknown and is approximated in this work using LDA as parameterized in Szotek *et al.* (1993) and LSDA as parameterized in Perdew and Wang (1992).

For the bulk calculations described below, both the ten-atom corundum-structure primitive cell of Cr_2O_3 and a larger, thirty-atom hexagonal cell (which is commensurate with our slab geometry for the surface studies) is used. For the ten-atom cell, the Brillouin zone is sampled with an eight $\boldsymbol{k}$-point Monkhorst-Pack (1976) mesh, which folds to four points under time-reversal symmetry. This corresponds to a reciprocal-space sampling density of 0.37 bohr^{-1}, which is commonly used to treat silicon, which is expected to be more than sufficient for this even more ionically-bonded system. For both the thirty-atom bulk cell and the surface calculations, four $\boldsymbol{k}$-points (which fold to two) in the plane perpendicular to the c-axis of the cell are employed, which yields a similar sampling in reciprocal space. The thirty-atom supercell contains six bilayers of chromium and six layers of oxygen, which was found sufficient for the description of Fe_2O_3 surfaces (Wang *et al.* 1998).

The pseudopotentials which represent the chromium and oxygen ionic cores in the study are of the non-local Kleinmann-Bylander separable form (1982), and are generated using the optimized pseudopotential procedure of Rappe *et al.* (1990). Preliminary calculations carried out on small atomic clusters showed that the states of the argon shell are relatively close in energy to the $2s$ states of oxygen. Out of con-

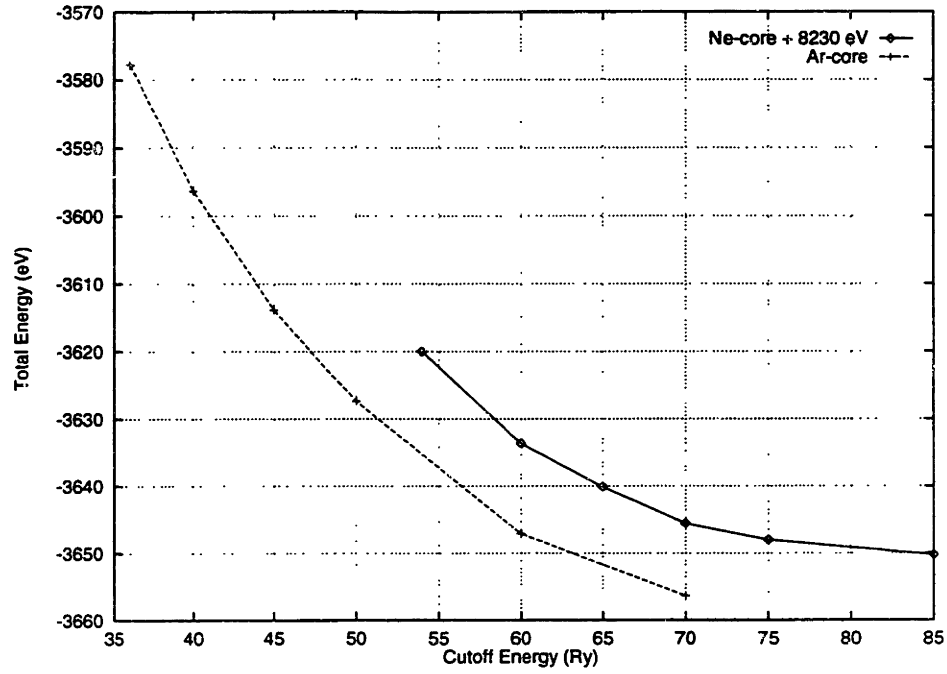

Figure 5-1 Convergence comparison of a 10-atom Cr_2O_3 cell using Ar- and Ne-core pseudopotentials.

cern for the possible mixing of the argon-shell electrons of chromium with the oxygen valence shell, the argon-shell electrons are explicitly included in the calculation as valence electrons and only the neon core of chromium is moved into the pseudopotential. Convergence tests (Figure 5-1) show that both pseudopotentials are well-converged at a plane wave cutoff of 80 rydbergs, which is used for all results reported in this thesis. Figure 5-2 compares the band-structure of chromium metal as calculated with the neon-core pseudopotential employed in this work with a comparable argon-core pseudopotential and the results of LAPW calculations (Papaconstantopoulos 1986). The LDA and LSDA results agree well with the LAPW results; including the argon-shell of electrons improves the results. The oxygen pseudopotential employed in this work has been used and tested in a variety of other works (Rappe *et al.* 1992).

Finally, the choice of exchange-correlation functional represents the third approximation in the *ab initio* calculations. To evaluate the efficacy of various functionals in treating the present material, the lattice constant and bulk modulus of Cr_2O_3 within both LDA and LSDA were evaluated for the ten-atom bulk cell. The results, described in detail in the next section, show that the LSDA gives a quite acceptable description of these properties. Further, LDA computations were performed, which

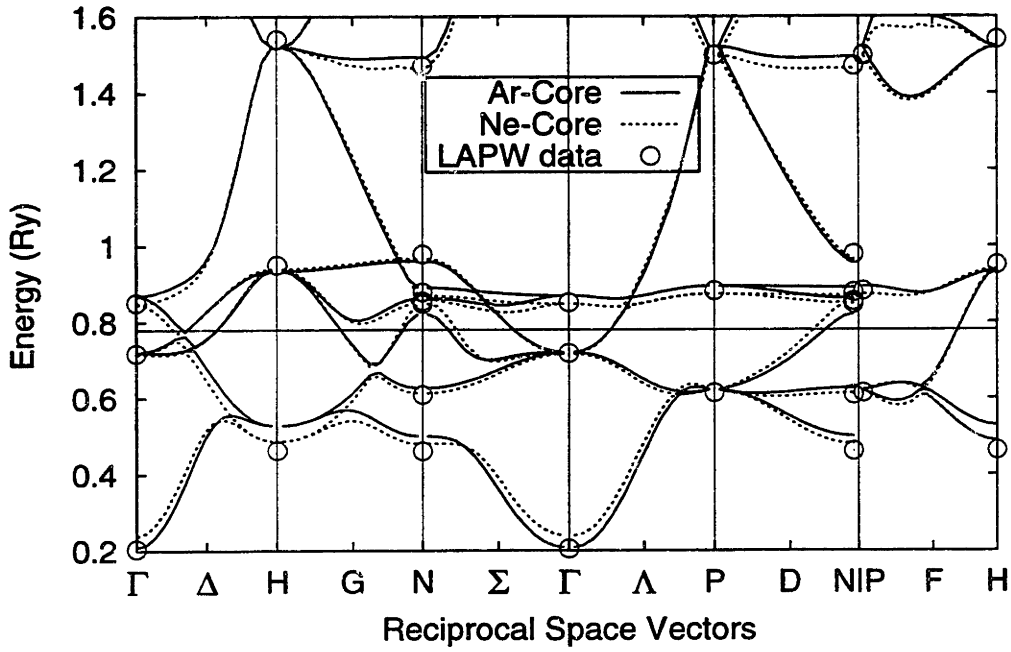

Figure 5-2 Comparison of LDA band structure results, calculated with linear augmented plane waves [LAPW] (Papaconstantopoulos 1986) (circles), and with pseudopotentials based upon an argon core (solid line) and neon core (dashed line), respectively. Reciprocal-space vectors are enumerated in Section D.2.

show that the removal of spin effects from the system greatly influences the predicted equilibrium crystal symmetry and mechanical response. After evaluating LSDA with the 10-atom cell, the 30-atom bulk and 28-atom surface calculations are performed under the LSDA exclusively.

Within the above approximations, the quantum state of the system is determined by minimizing the total energy over all possible sets of orthonormal electronic wavefunctions using the analytically-continued functional approach (Payne *et al.* 1992; Arias *et al.* 1992), which has been recently shown to be nearly optimal in a rigorous mathematical sense (Edelman *et al.* 1998). From the resulting electronic wavefunctions, calculate the total energies, electronic charge and spin densities, chemical softness fields, and forces on the atomic cores are calculated. The calculations are performed using the MIT-developed `dft++` software (Ismail-Beigi and Arias 1998) which uses a new, very general matrix language for density functional theory (Ismail-Beigi and Arias 1998; Arias 1999). This language makes the use of different physical descriptions (LDA, LSDA, SIC, Hartree-Fock, etc.) relatively simple to explore and provides both high portability to different computational platforms and good computational performance.

5.3 Results and Discussion

5.3.1 Bulk Cr_2O_3

As described above, the electronic structure, spin densities, bulk modulus, and chemical reactivity were computed for the bulk material within both LDA and LSDA. As shown below, spin is critical to a proper description of even the most basic properties, such as mechanical response as gauged by the bulk modulus.

The crystal structure of Cr_2O_3 is important for understanding the relaxation of the internal coordinates of the unit cell, the magnetic ordering of the bulk, and the structure of the surface. Cr_2O_3 assumes a corundum-type structure (space group $R\bar{3}$ c), which has a ten-atom primitive cell, equivalent to a thirty-atom cell on a hexagonal lattice. The structure consists of layers perpendicular to the c-axis which alternate between oxygen layers and chromium bilayers. Each chromium bilayer consists of two perfectly planar triangular lattices arranged so that their combined projection forms an ideal honeycomb structure, whose two-element basis consists of one member from each sublayer. (See Figure 5-3.) The difference between the crystallographic parameter "z(Cr)" (Hahn 1995) and one-third measures the distance between the

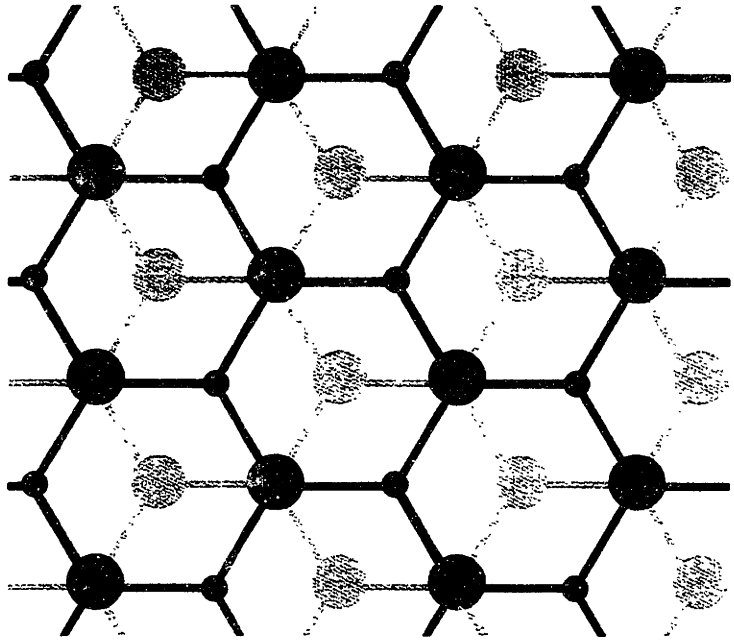

Figure 5-3 Schematic projection of the metal atoms in the corundum structure, viewed atop the (0001) surface, showing chromium atoms only. The chromium atoms in the structure arrange in a sequence of bilayers with honeycomb structure, three of which are shown, colored according to depth. The upper and lower chromium atoms of each bilayer appear as large and small circles, respectively.

planes which make up the bilayer. Chromium bilayers align in an ABC stacking sequence along the c-axis. Each sublayer of a chromium bilayer arranges such that its atoms align with the holes of the honeycomb structure of the bilayer nearest to it and directly with the atoms of the further sublayer of the second nearest bilayer. All oxygen atoms in a layer lie in exactly the same plane and form an approximate triangular lattice, with a slight contraction of triangles centered on the chromium atoms of neighboring bilayers which are directly aligned along the c-axis, namely the further chromium sublayers of the bilayers which sandwich the oxygen layer. The difference between the crystallographic parameter "x(O)" (Hahn 1995) and one-third measures this contraction.

It is known experimentally that, unlike Fe_2O_3 and V_2O_3, both Al_2O_3 and Cr_2O_3 contract nearly isotropically (within tenths of a percent) under hydrostatic pressure (Sato and Akimoto 1979). Accordingly, for our LDA and LSDA calculations, bulk moduli and unit cell volumes were determined by holding the ratio c/a between the crystal axes constrained to the experimental value of 2.7407 (Hellwege 1975, p. 469). At each volume, a standard Pulay stress correction (Froyen and Cohen 1985; Dacosta *et al.* 1986) for changes in finite-basis size was applied, and the internal coordinates of the unit cell were optimized until the Hellmann-Feynman forces on all atoms were less than 0.03 eV/Å in each coordinate direction. The location of the minimum and the curvature of the energy as a function of lattice constant give the unit-cell volume and bulk modulus.

Table 5.1 compares the results for bulk modulus, unit cell volume, cohesive energy (atomization energy to neutral atoms), and internal cell coordinates with published values from experiments and unrestricted Hartree-Fock results. Whereas the LDA calculations are in error by about -10% and 44% for unit cell volume and bulk modulus, respectively, the corresponding errors for UHF are +5% and +13% and for LSDA are -1.7% and within experimental error, 5%, respectively. Moreover, there is a reduction in the error of the cohesive energy, determined from Born-Haber cycle data for Cr_2O_3 (Sherman 1932) and the bond strength of molecular oxygen (Lide 1999), in going from LDA to LSDA from -12% to -6%, respectively. (Catti *et al.* (1996) do not provide a value of the cohesive energy.)

The variations quoted in the final digits of the internal coordinates x(O) and z(Cr), computed at the *ab initio* cell volume, reflect the differences among the individual atoms in the relaxed cell due to the small residual forces remaining after the relaxation procedure. The LDA prediction of the internal coordinates of the unit cell are in significant error. Note that x(O) for the LDA structure is nearly one-third, indicating

Model	B [Mbar]	V [Å^3]	E [eV]	1/3 - x(O)	z(Cr) - 1/3
		Computed Values			
LDA(10)	3.39(10)	43.34(04)	23.63	-0.004(2)	0.00626(1)
LSDA(10)	2.35(12)	47.19(14)	25.24	0.03133(8)	0.01647(1)
LSDA(30)	—	—	25.49	0.02212(16)	0.01196(4)
		Computed Values from Literature			
UHF (Catti *et al.* 1996)	2.66(10)	50.5	—	0.03273	0.01722
		Experimental Values from Literature			
Finger and Hazen (1980)	2.38(12)	47.997(5)	—	—	—
Sato and Akimoto (1979)	2.31(30)	48.0	—	0.0282	0.01437
Sherman (1932)	—	—	26.87†	—	—
Sawada (1994)	—	—	—	0.02763	0.01417

Table 5.1 Comparison of computed bulk modulus, volume, and cohesive energy in ten- and thirty-atom cells of Cr_2O_3 with experimental values. Volume and cohesive energies (relative to isolated atoms) are per Cr_2O_3 formula unit. The thirty-atom results were obtained at the optimal volume found in the ten-atom calculation.

† Computed with Born-Haber cycle. (See text.)

a tendency toward a perfect triangular lattice in each O layer. The LSDA results, on the other hand, are in much better accord with experiment, showing in the 10-atom cell even somewhat better agreement than reported for UHF (Catti *et al.* 1996).

In conclusion, there is a dramatic improvement relative to the experimental values when going from non-spin polarized calculations (LDA) to calculations which account for spin (LSDA, UHF). The LSDA also appears to perform better for these properties than does UHF. The results calculated for the thirty-atom cell, for both cohesive energy and internal coordinates, agree well with the results from the ten-atom cell, reflecting the good $\boldsymbol{k}$-point convergence of the calculations. Given the success of the LSDA description and its clear superiority over the LDA (and UHF), all results reported below are computed within LSDA.

Next, we turn our attention to the magnetic structure of bulk Cr_2O_3. Figure 5-4(b) presents our prediction for the ground-state spin density. The figure shows two contour surfaces, one light and one dark, which correspond to spin densities of equal magnitude but opposite sign. The spin polarization in the bulk material is concentrated almost entirely on the chromium atoms, leaving the oxygen atoms spin-neutral. Thus, the large, closed surfaces in the plot correspond precisely to the locations of the chromium atoms in the structure. The bilayer structure is evident in the figure. We find an antiferromagnetic intra-bilayer ordering among nearest neighbors in each bilayer honeycomb, so that all atoms in a given sublayer of a bilayer share the

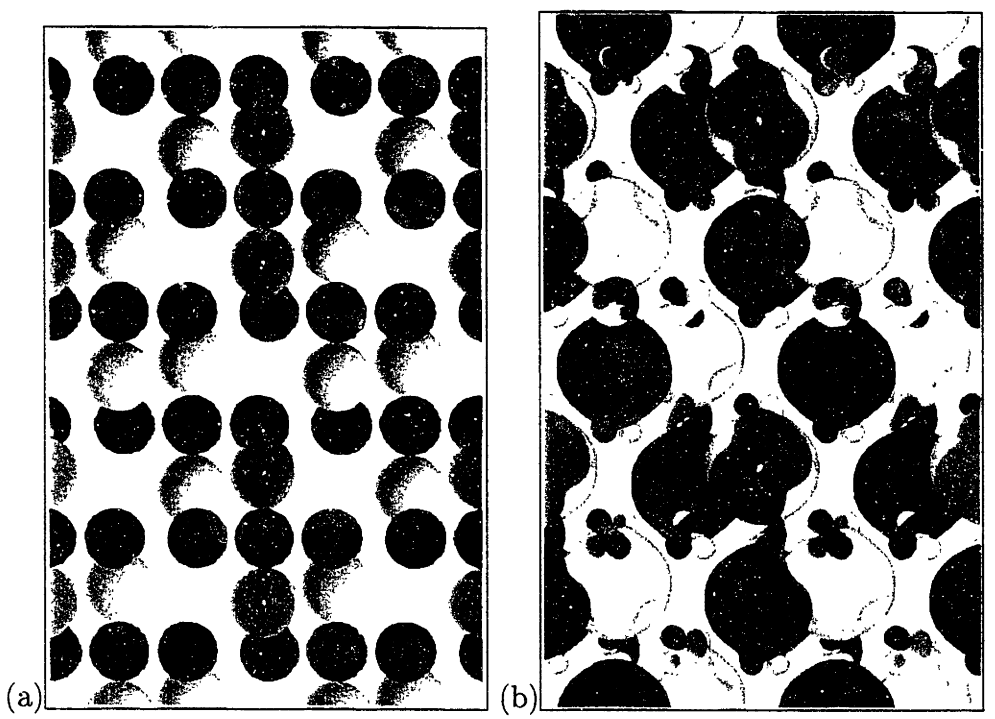

Figure 5-4 LSDA predictions for a thirty atom cell of bulk Cr_2O_3. Left panel (a) shows a single isosurface of the predicted total electron density ($n_\uparrow + n_\downarrow$), with the surface colored according to proximity to chromium atoms (white) and oxygen atoms (charcoal). Right panel (b) shows the spin polarization, $n_\uparrow - n_\downarrow$, for bulk Cr_2O_3 within LSDA (thirty atom calculation): contour of net up-spin (white), contour of net down-spin (charcoal). In this panel, large dimpled contours surround chromium atoms, and small p-orbital shapes appear at the oxygen sites. Note that for both panels some atoms are cut-off at the cell boundary, which reveals their darker-shaded interiors.

same spin direction. Moreover, there is an inter-bilayer ordering such that that spin-up/spin-down sequence along the c-axis is identical for each bilayer. These results are in complete accord with neutron diffraction experiments (Brockhouse 1953).

To confirm that the state shown in Figure 5-4(b) is the ground state within LSDA, the wavefunctions were relaxed from a random configuration. This resulted in a spin state in which the magnetic order *within* each bilayer was the same as described above, suggesting that the antiferromagnetic spin order within bilayers is quite stable. This time, the random initial wavefunctions lead to a local energy minimum (Figure 5-5) in which the spin-up/spin-down sequence of the bilayers reverses from one ground state (phase A) to the spin-flip related ground state (phase B) over a portion of the supercell, corresponding to the presence of two antiferromagnetic solitons in the supercell. LSDA ascribes a positive energy to this excitation, confirming that the spin ordering shown in Figure 5-4(b) represents the ground state. We extract the first *ab initio* estimate for the (0001) c-axis coupling constant $J_{AB} \approx 150\,\mathrm{cm}^{-1}$ from these results. Experiments provide estimates for this coupling constant but over a fairly wide range of values, from about $J_{AB} \approx 250\,\mathrm{cm}^{-1}$ to $\approx 350\,\mathrm{cm}^{-1}$ (Poole and Itzel 1964).

Finally, Figure 5-6 shows contour surfaces of the electron density of the highest occupied molecular orbitals (HOMOs) and the lowest unoccupied molecular orbitals (LUMOs), in the bulk material. These quantities represent the *local chemical softness* (Yang and Parr 1985). Species which tend to accept electrons will tend to move toward regions with strong HOMO concentration—both the oxygen and chromium atoms (Figure 5-6a). On the other hand, species which tend to donate electrons will tend selectively toward the chromium atoms, which represent the strong LUMO regions (Figure 5-6b). These results reflect the fact that the oxygen atoms, already carrying a significant negative charge, cannot accept more electrons, whereas the chromium atoms, in contrast, can relatively readily accept or donate electrons.

5.3.2 (0001) Surface

The oxygen-terminated (0001) surface of Cr_2O_3 is studied because of its relevance in oxygen-rich environments, including supercritical water oxidation (but also may in general extend to room-temperature ambient exposures of stainless steels). Although one might naïvely expect such a surface to be extremely polar and thus energetically unfavorable, the O_3-termination of a similar M_2O_3 system, the α-Fe_2O_3 (0001) surface, was found to be quite stable in oxygen-rich environments (Wang *et al.* 1998).

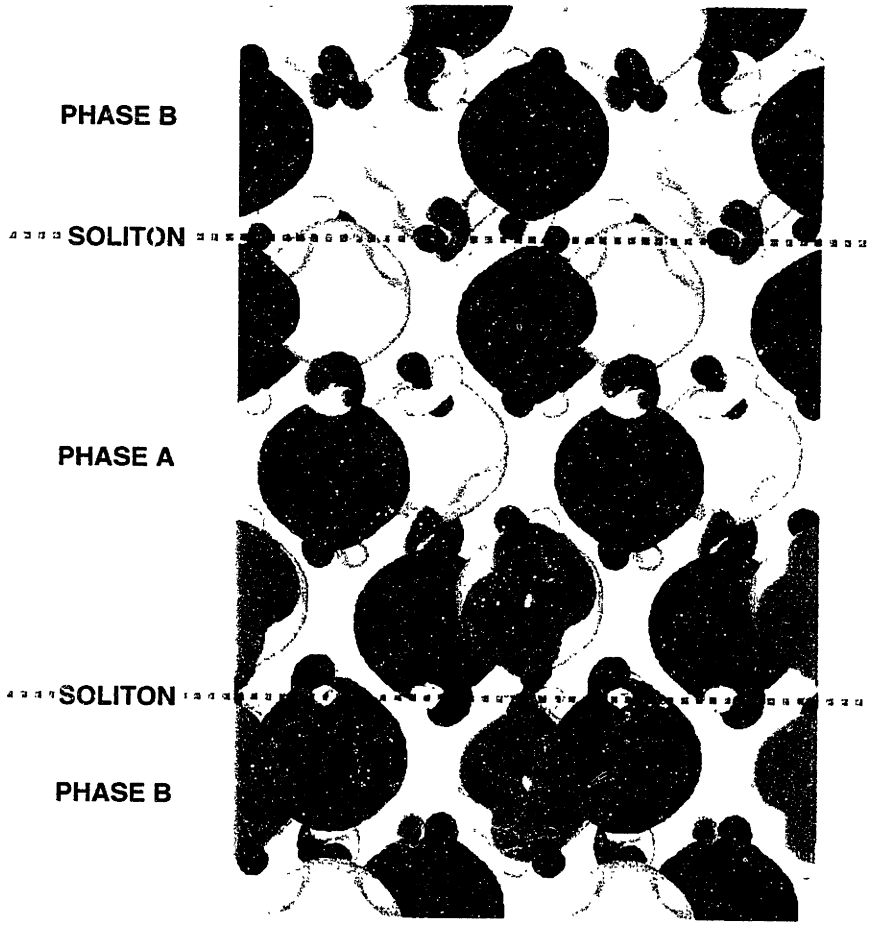

Figure 5-5 Antiferromagnetic solitons in Cr_2O_3 within LSDA (same conventions as Figure 5-4(b)).

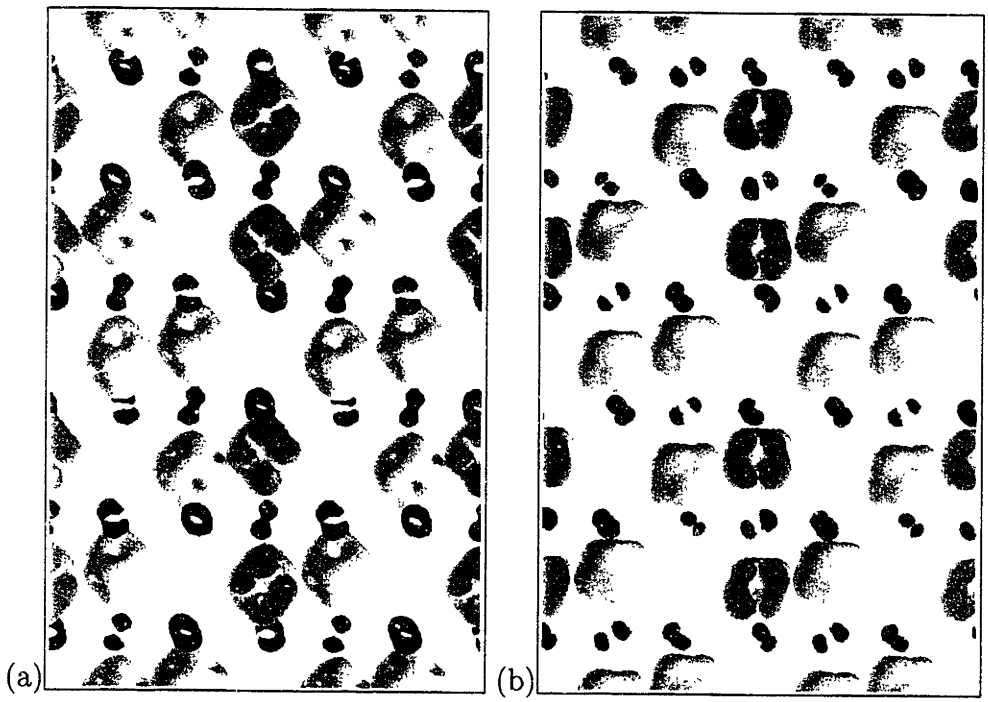

Figure 5-6 Local chemical softness map of bulk Cr_2O_3. Portrayed are the HOMOs (a) and LUMOs (b) as calculated within LSDA. The figure shows a single isosurface of local softness, which is colored according to proximity to either chromium (white) or oxygen (charcoal) atoms.

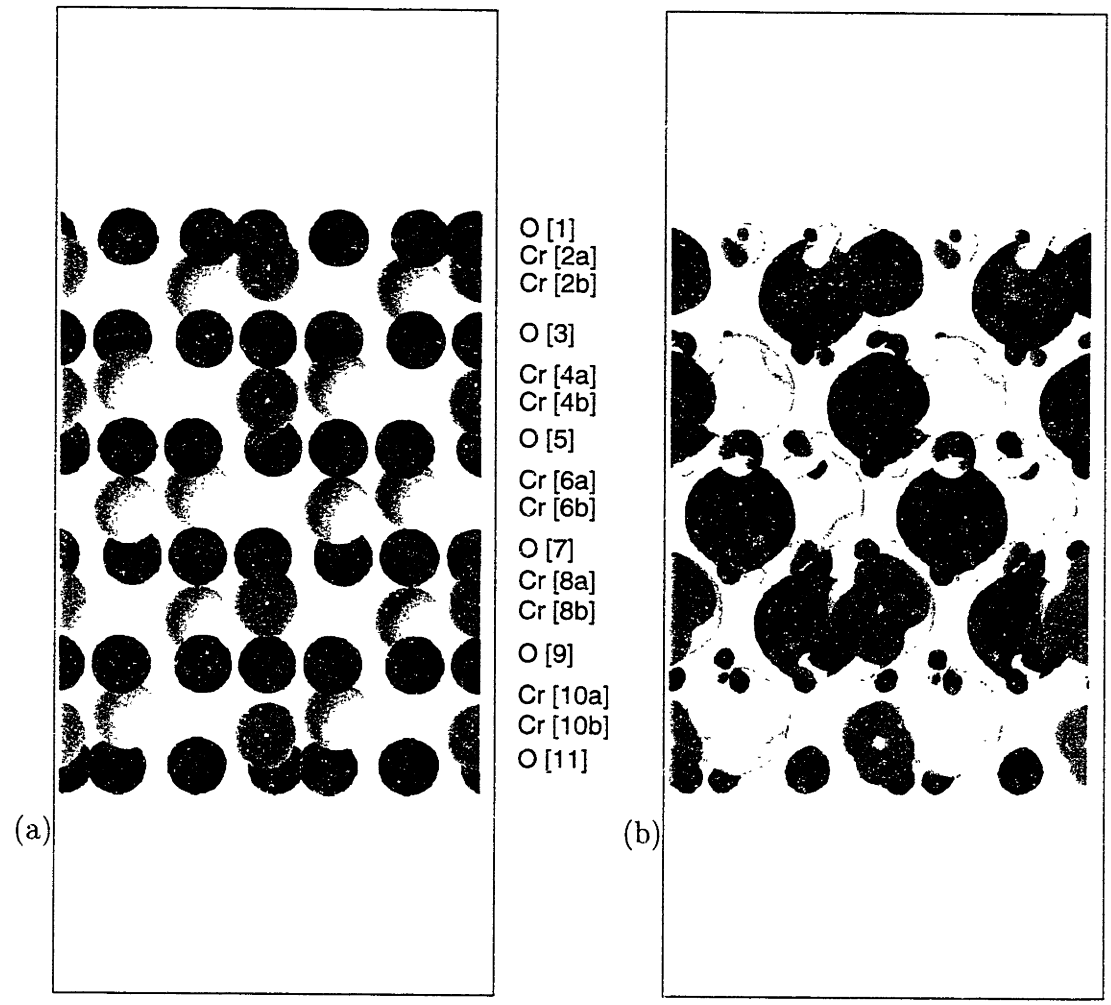

Figure 5-7 LSDA predictions for a twenty-eight atom surface slab of Cr_2O_3: electron density (a) and spin polarization (b) (same conventions as Figure 5-4.)

To form the surface slabs for our supercell calculations, one begins with the thirty-atom bulk cell at its *ab initio* lattice constants and then extends the cell with 7 Å of vacuum along the *c*-axis and removes one bilayer of chromium atoms. This forms a slab of twenty-eight atoms arranged in six oxygen layers and five chromium bilayers with two oxygen-terminated surfaces, such that there is no net electric-dipole moment in the unit cell (Figure 5-7a). The final, fully relaxed structure is then determined by moving the atoms along their Hellmann-Feynman forces until the maximum force on each atom is less than 0.03 eV/Å in each component direction.

The primary structural change associated with the surface relaxation is a significant motion of surface oxygen atoms (layer O[1] in Figure 5-7(a)) toward the outer

Layer pair	Bulk Crystallographic Spacing [Å] (Hahn 1995)	LSDA Spacing [Å]	Experimentally Determined Surface Spacing [Å] (Rohr *et al.* 1997)
–	0.94	–	0.58
O[1]–Cr[2a]	0.94	0.63	0.50
Cr[2a]–Cr[2b]	0.39	0.40	0.29
Cr[2b]–O[3]	0.94	1.05	1.04
O[3]–Cr[2b]	0.94	0.92	–

Table 5.2 Comparison of computed and experimentally observed interlayer spacing at the (0001) α-Cr_2O_3 surface. Although the surface terminations are different, corresponding O-Cr spacings are qualitatively similar.

chromium atoms in the outermost bilayer of the structure (layer Cr[2a]). This motion involves a lateral component along the surface which makes oxygen triangles appear to rotate about the deeper chromium atoms of the outermost bilayer (layer Cr[2b]) by 6.5(1)°, similar to the rotation of 10° reported for Fe_2O_3 (Wang *et al.* 1998). This lateral motion brings the oxygen atoms away from two classes of chromium sites, those associated with the nearest chromium atoms of the first of the removed layers and those about which the oxygen atoms had previously participated in superexchange. The vertical motion brings the outer oxygen atoms 33% closer to the outermost chromium sublayer, reducing the interplanar distance by 0.3 Å. Both components of the motion are consistent with the oxygen-chromium bonding on the surface becoming primarily ionic in character. The second most significant change is an increase of 9%, or 0.12 Å, in the distance between the outermost chromium bilayer and the next deeper oxygen layer. All other shifts in the structure are less than 0.06 Å. Table 5.2 summarizes the interlayer spacing results.

The only relevant experimental data found were for LEED experiments on Cr_2O_3 (0001) surfaces cleaved between the two sublayers of a chromium bilayer, leaving an oxygen terminated surface with a half-bilayer of adsorbed chromium (Rohr *et al.* 1997). As Table 5.2 shows, despite the different terminations, there are similar qualitative trends between the O-Cr spacing in experimentally observed structures and the computed structure. In particular, there is a significant contraction of the outermost oxygen layer O[1] into the underlying chromium bilayer Cr[2ab], and a slight separation of the outer oxygen-chromium double layer O[1]-Cr[2ab] from the underlying crystal.

Figure 5-8 shows the mean potential for electrons as a function of distance from the

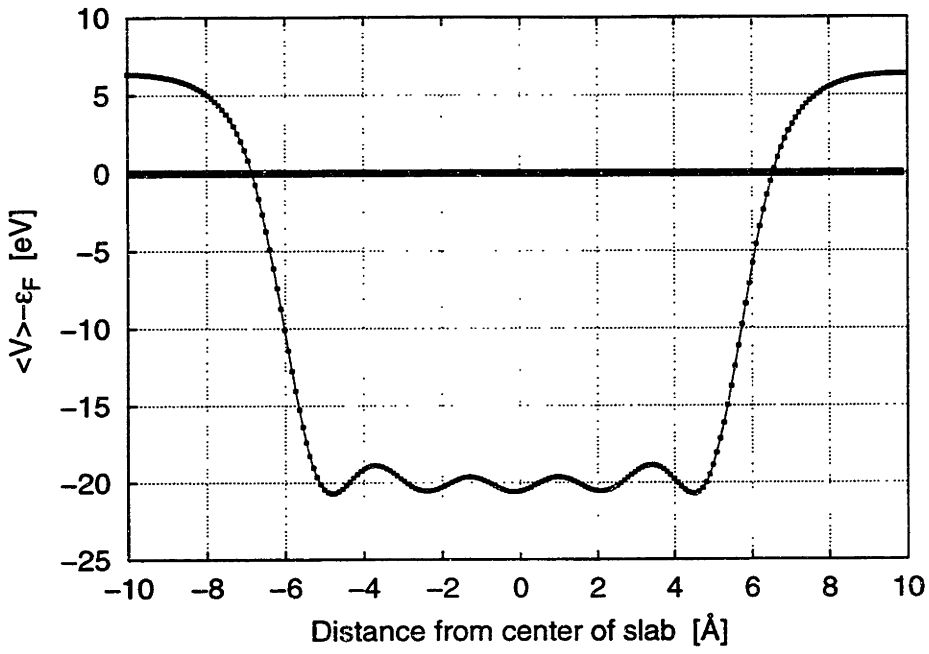

Figure 5-8 Self-consistent Kohn-Sham potential relative to Fermi Level for a twenty-eight atom surface slab of Cr_2O_3 within LSDA.

center of the slab. Comparing this potential to the Fermi level of the slab, the work function of the oxygen-terminated surface in vacuum is estimated at approximately 6.3 eV. Experiment gives a range of values of 3.6 to 5.9 eV depending upon annealing temperature (500 to 900° C) and atmospheric pressure (10^{-5} to 760 torr) for the work function. Given the range of experimental values and that they are not for any specific surface, the agreement is satisfactory.

Figure 5-7b shows the spin structure of the surface in the same format and geometry as Figure 5-4 does for the bulk. The magnetic structure of the surface is significantly different from that of the bulk. In particular, with the antiferromagnetic superexchange partners of the Cr[2b] atoms missing from the surface, the terminal oxygen atoms now exhibit a noticeable spin polarization, an effect similar to that found in Wang *et al.* (1998) for the same surface of Fe_2O_3. Note also that the Cr[2a] atoms, towards which the spin-opposed oxygen atoms move, now have a significantly reduced spin density, as evidenced by the shrinkage of the contours. Finally, after exploring different spin configurations on the surface, it is confirmed that the ordering of the spin ground state is *ferromagnetically* aligned within the Cr[2] surface layer, quite different than the antiferromagnetic ordering in the bulk planes.

Figures 5-9(a) and (b) show the HOMO and LUMO states of the surface slab. These figures show a remarkable spatial separation between the filled and empty states near the Fermi level. In particular, the chemical softness for the donation of electrons (represented by the LUMOs) is well-localized on the surface, whereas chemical softness for acceptance of electrons is concentrated in the interior of the slab. Negatively charged species, such as chloride ions, coming in to contact with this surface will occupy spatial locations which accommodate their excess electrons with the lowest energy cost: the regions of high LUMO density. Such species would be expected to prefer the surface. Moreover, when sharing their electrons with these surface states, our results suggest that such species will preferentially disrupt the electronic structure of the surface. Note also that lowering the Fermi-level, by p-type doping, might help to transfer the new LUMOs to the interior, thereby protecting the surface.

Figures 5-10(a) and (b) show the spin dependence of the slab's HOMO and LUMO states, respectively. Comparing Figure 5-10(a) and (b) with Figure 5-7(b), while the net overall spin polarization of the terminal oxygens is net *opposite* of the underlying ferromagnetic chromium bilayer, the HOMOs and LUMOs show that the states near the Fermi level are aligned *with* the ferromagnetic chromium bilayer. In general, the oxygens do not spin polarize—but here they lack the extra electrons shared with the missing chromium layer. Figure 5-10(b) also exhibits a clear symmetry in the ferromagnetism of the surfaces. This ferromagnetism may have implications for chemical reactivity, for, in any given orbital, there is a maximum of one spin-up and one spin-down electron. Thus a reaction with a Cr_2O_3 (0001) surface of this spin ordering is restricted with respect to which electrons participate in bonding or transfer without undergoing a spin-flip. It is speculated that this ordering could play a role in electron-mediated spin interactions with adsorbed species. For instance, this effect may influence the catalytic conversion of parahydrogen to orthohydrogen over Cr_2O_3, which was experimentally observed to diminish when the Néel temperature was exceeded (Arias and Selwood 1973).

5.4 Conclusions

An *ab initio* model for bulk Cr_2O_3 was constructed using density functional theory under the local spin-density approximation. This model was validated against experimentally determined crystal structures and thermodynamic data (bulk modulus and Born-Haber cycle), where agreement with experiment was found to be reasonable,

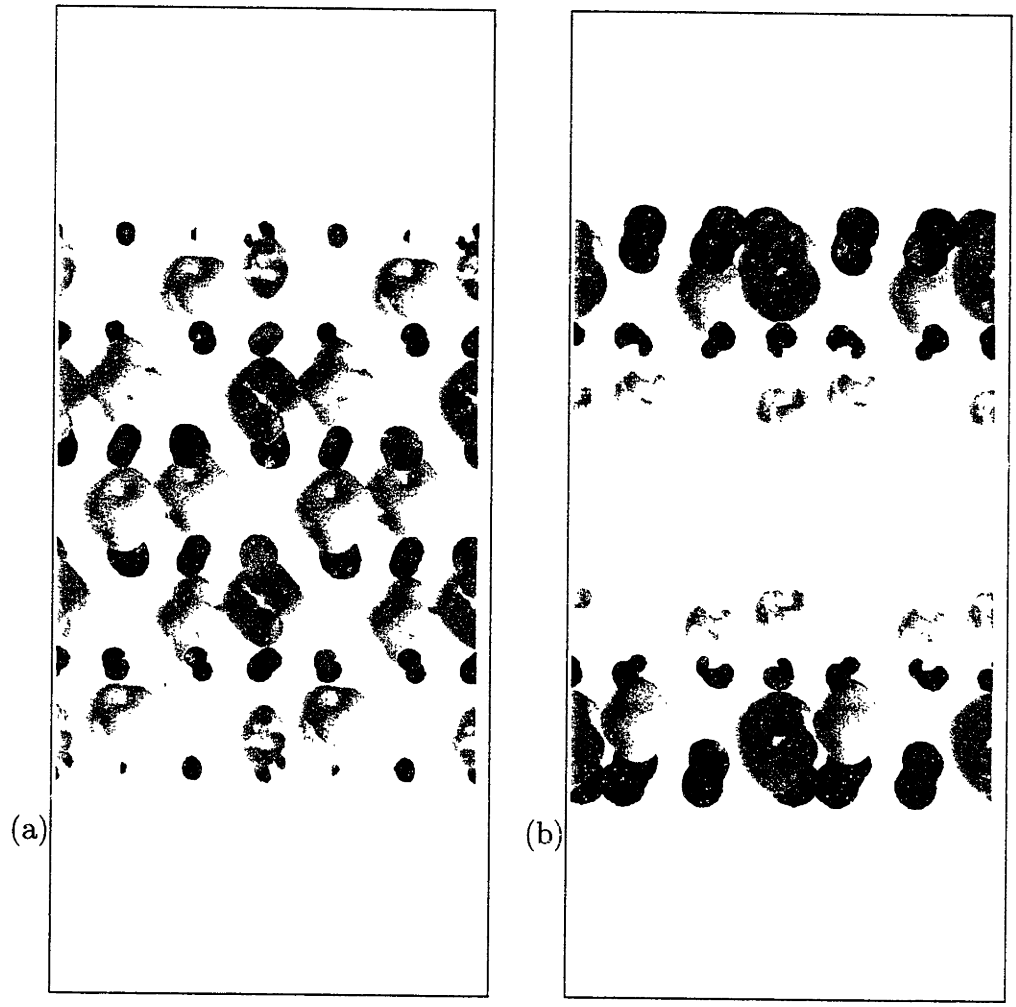

Figure 5-9 Local chemical softness map for a twenty-eight atom surface slab of Cr_2O_3 within LSDA (same conventions as Figure 5-6). Figure shows a clear surplus of unoccupied states and deficit of occupied states at the surface, indicating chemical sensitivity to attack by electron-rich species.

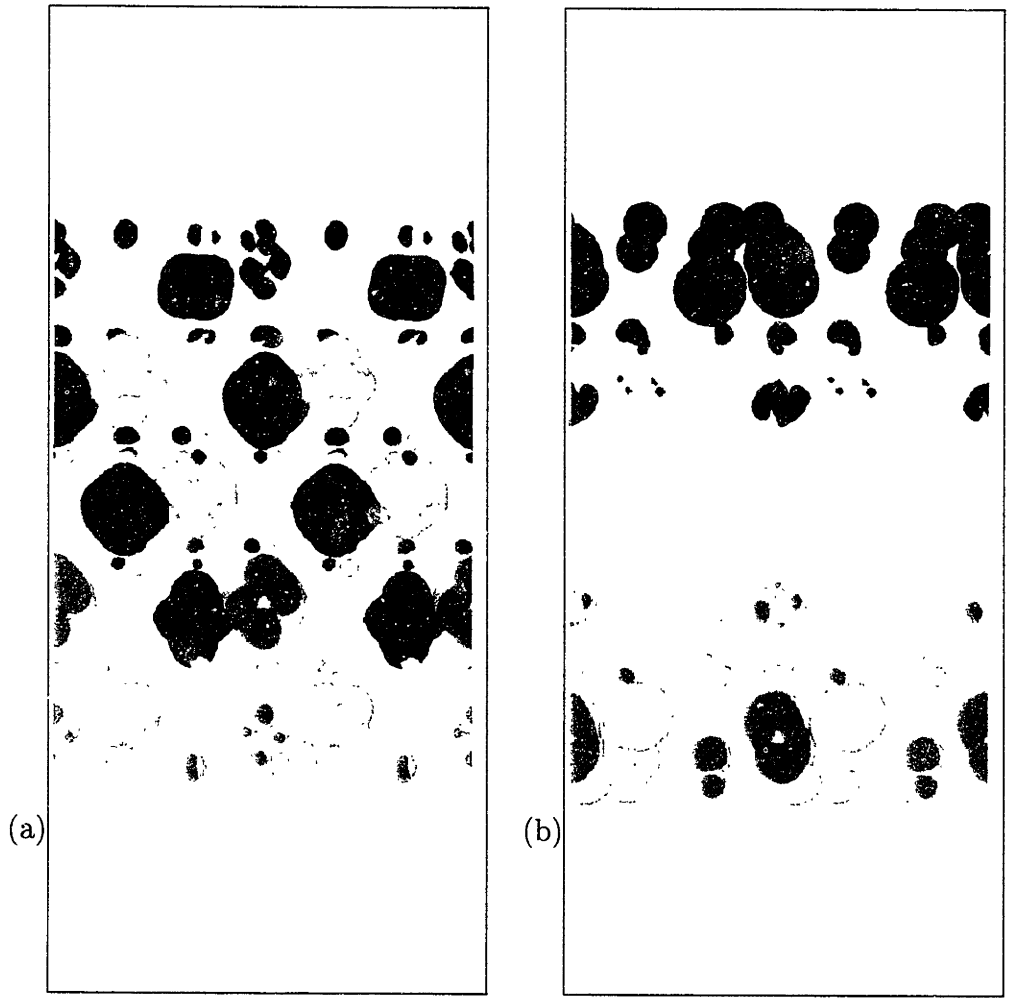

Figure 5-10 Spin-dependence of the local chemical softness map for the twenty-eight atom surface slab of Cr_2O_3 within LSDA (same conventions as Figure 5-4(b)).

and its performance with respect to other theoretical models was superior. With a validated first-principles model for the bulk crystal, a Cr_2O_3 slab was constructed for use in exploring surface chemistry.

The oxygen-terminated Cr_2O_3 surface was compared to the bulk material by calculating the atomic, electronic and magnetic structure of both. Although the differences in atomic structure between bulk and surface are noteworthy (outer oxygen atoms are 33% closer to the outermost chromium sublayer), the differences in electronic and magnetic structure are even more significant. The oxygen-terminated surface of Cr_2O_3 is a region of high LUMO density where negatively charged species such as Cl^- and S_2^- should be well accommodated. Spatial arrangement of the surface slab's HOMOs and LUMOs suggests that p-doping may in fact help reduce its chemical reactivity. The oxygen atoms of the surface have a noticeable spin polarization and the adjacent Cr[2] surface layer is ferromagnetic, quite different from the antiferromagnetic ordering of the Cr atoms in the bulk material. By restricting the spin of the electrons which can transfer to LUMO or from HOMO states at the Cr_2O_3 (0001) surface, the magnetic ordering may indeed be a contributor to the catalytic action of Cr_2O_3.

Bibliography

Alstrup, N. C., N. Langrad, and I. Chorkendorff (1994, July). AES and SAM studies of oxide formation on Inconel 600 at high temperatures. *Surface and Interface Analysis* **22** (1), 441–4.

Arias, J. A. and P. W. Selwood (1973). Parahydrogen conversion over chromiagel near the Néel point. *J. Catal.* **30**, 255–9.

Arias, T. A. (1999, January). Multiresolution analysis of electronic structure: Semicardinal and wavelet bases. *Reviews of Modern Physics* **71** (1), 267–311.

Arias, T. A., M. C. Payne, and J. D. Joannopoulos (1992, August). *Ab Initio* molecular dynamics: Analytically continued energy functionals and insights into iterative solutions. *Phys. Rev. Lett.* **69** (7), 1077–80.

Bond, G. C. (1974). *Heterogeneous Catalysis: Principles and Applications.* Oxford Chemistry Series. Oxford: Clarendon Press.

Brockhouse, B. N. (1953). Antiferromagnetic structure in Cr_2O_3. *J. Chem. Phys.* **21**, 961–2.

Burstein, G. T. and S. P. Mattin (1992). Nucleation of corrosion pits on stainless steel. *Phil. Mag. Let.* **66**, 127.

Catti, M., G. Sandrone, G. Valerio, and R. Dovesi (1996). Electronic, magnetic, and crystal structure of Cr_2O_3 by theoretical methods. *J. Phys. Chem. Solids* **57**, 1735.

Cline, J. A., A. A. Rigos, and T. A. Arias (1999, December). *Ab initio* study of magnetic structure and chemical reactivity of Cr_2O_3 and its (0001) surface. Submitted to *J. Phys. Chem. B.*

Cox, P. A. (1992). *Transition Metal Oxides.* Oxford: Clarendon Press.

Dacosta, P. G., O. H. Nelson, and K. Kunc (1986). *J. Phys. C* **19**, 3163.

Edelman, A. S., T. A. Arias, and S. T. Smith (1998). *Society for Industrial and Applied Mathematics Journal on Matrix Analysis and Applications* **20**, 303.

Figueiredo, M. O., A. C. dos Santos, H. Carmezim, M. Abbate, F. M. F. deGroot, H. Petersen, and W. Braun (1994). *Analyst* **119**, 609.

Finger, L. W. and R. M. Hazen (1980). Crystal structure and isothermal compression of Fe_2O_3, Cr_2O_3, and V_2O_3 to 50 kbars. *J. Appl. Phys.* **51**, 5362.

Foord, J. S. and R. M. Lambert (1986). *Surface Science* **169**, 327.

Froyen, S. and M. L. Cohen (1985). *J. Phys. C* **19**, 2623.

Hahn, T. (Ed.) (1995). *International Tables for Crystallography*, Volume A. Boston: Kluwer Academic Publishers.

Harrison, P. G., N. C. Lloyd, and W. Daniell (1998). The nature of the chromium species formed during thermal activation of chromium-promoted tin(IV) oxide catalysts: An EPR and XPS study. *J. Phys. Chem.* **102**, 10672.

Hellwege, K.-H. (Ed.) (1975). *Crystal Structure Data of Inorganic Compounds*, Volume 7 of *Landolt-Börnstein.* Berlin: Springer-Verlag.

Henrich, V. E. and P. A. Cox (1994). *The Surface Science of Metal Oxides.* Cambridge: Cambridge University Press.

Hohenberg, P. and W. Kohn (1964). *Phys. Rev.* **136**, 864B.

Ismail-Beigi, S. and T. A. Arias (1998). In C. E. Leiserson (Ed.), *Proceedings of the 1998 MIT Student Workshop on High-Performance Computing in Science and Engineering*, Number 737. MIT Laboratory for Computer Science.

Kleinman, L. and D. M. Bylander (1982). *Phys. Rev. Lett.* **4**, 1425.

Kohn, W. and L. J. Sham (1965). Self-consistent equations including exchange and correllation effects. *Phys. Rev.* **140**, 1133A.

Lide, D. R. (Ed.) (1999). *CRC Handbook of Chemistry and Physics* (79th ed.). New York: CRC Press.

Manassidis, I., A. De Vita, and M. J. Gillan (1993). Structure of the (0001) surface of α-Al_2O_3 from first principles calculations. *Surf. Sci. Let.* **285**, L517.

Mentasty, L. R., O. F. Gorriz, and L. E. Cadus (1999). Chromium oxide supported on different Al_2O_3 supports: Catalytic propane dehydrogenation. *Ind. Eng. Chem. Res.* **38**, 396.

Mitton, D. B., S.-H. Zhang, M. S. Quintana, J. A. Cline, N. Caputy, and R. M. Latanision (1998). Corrosion mitigation in SCWO systems for hazardous waste disposal. In *Corrosion 98*, Number 414, Houston, TX. NACE. Meeting Location: San Diego, CA.

Monkhorst, H. J. and J. D. Pack (1976). Special points for Brillouin-zone integrations. *Phys. Rev. B* **13** (12), 5188–92.

Newman, R. C. and K. C. Sieradzki (1994). *Science* **263**, 1708.

Papaconstantopoulos, D. A. (1986). *Handbook of the Band Structure of Elemental Solids.* New York: Plenum Press.

Payne, M. C., M. P. Teter, D. C. Allan, T. A. Arias, and J. D. Joannopoulos (1992). Iterative minimization techniques for *ab initio* total-energy calculations: Molecular dynamics and conjugate gradients. *Reviews of Modern Physics* **64** (4), 1045–97.

Perdew, J. P. and Y. Wang (1992). Accurate and simple analytic representation of the electron-gas correlation energy. *Phys. Rev. B* **45** (23), 13244–9.

Perdew, J. P. and A. Zunger (1981). *Phys. Rev. B* **23**, 5048.

Poole, C. P. and J. F. Itzel (1964, July). Electron spin resonance study of the antiferromagnetism of chromia alumina. *J. Chem. Phys.* **41** (2), 287–95.

Rappe, A. M., A. Dal Pino, Jr., M. Needels, and J. D. Joannopoulos (1992, September). Mixed-basis pseudopotential method applied to iterative diagonalization techniques. *Phys. Rev. B* **46** (12), 7353–7.

Rappe, A. M., K. M. Rabe, E. Kaxiras, and J. D. Joannopoulos (1990). Optimized pseudopotentials. *Phys. Rev. B* **41**, 1227.

Rehbein, C., F. Michel, N. M. Harrison, and A. Wander (1998). *Ab Initio* total energy studies of the α-Cr_2O_3 (0001) and $(01\bar{1}2)$ surfaces. *Surface Review and Letters* **5** (1), 337–40.

Rohr, F., M. Bäumer, H.-J. Freund, J. A. Meijas, V. Staemmler, S. Müller, L. Hammer, and K. Heinz (1997). Strong relaxations at the Cr_2O_3 (0001) surface as determined via low-energy electron diffraction and molecular dynamics simulations. *Surface Science* **372**, L291–L297.

Ryan, M. P., R. C. Newman, and G. E. Thompson (1994, August). A scanning tunnelling microscopy study of structure and structural relaxation in passive oxide films on Fe–Cr alloys. *Philosophical Mag. B* **70** (2), 241–51.

Sato, Y. and S. Akimoto (1979). Hydrostatic compression of four corundum-type compounds: α-Al_2O_3, V_2O_3, Cr_2O_3 and α-Fe_2O_3. *J. Appl. Phys.* **50**, 5285.

Sawada, H. (1994). Residual electron density study of chromium sesquioxide by crystal structure and scattering factor refinement. *Materials Research Bulletin* **29** (3), 239–45.

Sherman, J. (1932). Crystal energies of ionic compounds and thermochemical applications. *Chemical Reviews* **11** (1), 93–170.

Szotek, Z., W. M. Temmerman, and H. Winter (1993). *Phys. Rev. B* **47**, 4029.

Veliah, S., K.-H. Xiang, R. Pandey, J. M. Recio, and J. M. Newsam (1998). Density functional study of chromium oxide clusters: Structures, bonding, vibrations, and stability. *J. Phys. Chem. B* **102**, 1126.

Wang, X.-G., W. Weiss, S. K. Shaikhutdinov, M. Ritter, M. Petersen, F. Wagner, R. Schlögl, and M. Scheffler (1998, August). The hematite (α-Fe_2O_3) (0001) surface: Evidence for domains of distinct chemistry. *Phys. Rev. Lett.* **81** (5), 1038–1041.

Yang, W. and R. G. Parr (1985). *Proc. Natl. Acad. Sci. USA* **82**, 6723.

Chapter 6

Examining the Influence of a Dielectric Upon the Surface Chemistry of Cr_2O_3

The ultimate objective of the density functional calculations is to construct a rigorous and flexible model for Cr_2O_3 which will be useful for investigating corrosion initiation and other surface chemistries. A key property of the model is that it can account not only for the changes in charge density and bonding at the oxide surface, but also for the changes in solvent properties that occur within supercritical water oxidation (SCWO) process streams.

In Chapter 5, an *ab initio* model was formulated, validated, and used to gain insight into the chemical nature of the Cr_2O_3 surface. These results represent its surface chemistry in a vacuum, and so are most applicable to heterogeneous reactions with low-density gas-phase systems. They can presumably be applied to conditions similar to vacuum, such as under dilute gases at low pressure. Ultimately the calculation is targeted for examining surface reactions and corrosion in SCWO systems, in which the environment is much denser. Typical densities range from 0.2 to 1.0 $g \cdot cc^{-1}$. At these higher densities, water, a very polar solvent, can by rearrangement of its dipolar molecules support atomic and electronic configurations which are not feasible in vacuum.

The *in vacuo* calculation results cannot be directly applied with any obvious reliability to the case of a dense aqueous system, because the high density of the polar solvent provides a medium with a dielectric constant ($D_s \equiv \epsilon/\epsilon_0$) as high as 80. The influence of this dielectric is expected to be especially significant when aqueous or adsorbed species become involved. Since corrosion and other surface reactions involve

aqueous and adsorbed species, it thus becomes necessary to provide in the model the capability of accounting for the effects of the medium.

In principle, a completely *ab initio* treatment of these effects is possible with *ab initio* molecular dynamics calculations using a large number of water molecules to represent the solvent. However, because in such a simulation most of the water molecules remain relatively inert entities, their full quantum-mechanical description is unnecessary and would represent a major commitment of computational resources. Such a detailed analysis would not only involve numerous water molecules but would also require compilation of ensemble averages, necessarily making the computation much more involved.

The primary effects of a highly polar solvent such as water on a quantum mechanical system can be explored using dielectric continuum theory. Although the structureless-dielectric description of the solvent accounts neither for localized solvent clustering nor the details of hydrogen bonding, it does capture the electrostatic effects of the polarizable medium upon the energy and orbitals of the system at hand. This description allows one to contrast the chemical behavior of Cr_2O_3 passive films from ambient to supercritical conditions, where the solvent changes its dielectric constant through about two orders of magnitude, from 80 to less than 2. Although this is a very simplified model for water, it is intended to show the general qualitative changes in the local surface chemistry that occur with variation in the solvent's dielectric constant and provide a mechanism for including a more rigorously-constructed and detailed solvent model. After showing the response of the bare surface to the simple dielectric, a research path is outlined in which the surface can be exposed to hydrogen and chlorine atoms in order to determine their responses under vacuum or an arbitrary dielectric medium.

6.1 Methodology for *Ab Initio* Calculations in a Dielectric

The response of the density-functional system to changes in the surrounding medium (from vacuum D_s=1 to high dielectric strength D_s=80) is computed using the following procedure:

1. The full charge density of the system is computed. The surface slab used as the basis for these calculations is the same as that described earlier in Chapter 5, and is pictured in Figure 5-7 on page 142.

2. Next, the dielectric strength $D_s(\boldsymbol{r})$ profile of the dielectric medium is determined as a function of position $\boldsymbol{r}$. For reasons to be developed below, the dielectric does not overlap with regions of strong charge density—thus the dielectric shape is determined by the charge density of the *in vacuo* system. The charge density in the cell is never zero, but for positions which are not near atoms, the charge density is very small. To account for this nonzero-but-negligible charge density, a parameter for the maximum charge density overlapped by the dielectric (n_{cutoff}) must be set. This parameter is rather small. For all investigations within this work the value used for n_{cutoff} is 1.15×10^{-3} electrons/bohr^3.

   In this implementation of the dielectric field, the $D_s(\boldsymbol{r})$ array, which has the same dimensions as the charge-density array, is initialized thus:

$$D_s(\boldsymbol{r}) = \begin{cases} 1.0 & n(\boldsymbol{r}) > n_{\text{cutoff}} \\ D_s \text{ of bulk solvent} & n(\boldsymbol{r}) \leq n_{\text{cutoff}} \end{cases} \tag{6.1}$$

   Note that, in the `dft++` native atomic units of bohrs and hartrees, ϵ_0=1. With the array initialized, it was then smoothed via 3-D convolution with a Gaussian of width σ_{Ds}, a second adjustable parameter for this procedure. For results presented in this chapter, σ_{Ds}=0.25 bohr as used in Tester *et al.* (1998) unless otherwise noted.

3. The Poisson-Boltzmann equation is solved to determine the polarization of the dielectric. For a system of charges[1] in an arbitrary dielectric field:

$$\nabla \cdot [D_s(\boldsymbol{r})\, \nabla\phi(\boldsymbol{r})] = 4\pi\, n_{\text{free}}(\boldsymbol{r}) \tag{6.2}$$

   where $\phi(\boldsymbol{r})$ is the potential which is computed from $n_{\text{free}}(\boldsymbol{r})$, the charge density of all of the electrons and nuclei. For this application, the free charge is the charge as computed in Chapter 5. Equation 6.2 is solved numerically for the system with the imposed dielectric. It is equivalent to view the potential as the effect of an induced-charge distribution $n_{\text{ind}}(\boldsymbol{r})$ superimposed upon the free charge to create a virtual total charge $n_{\text{vir}}(\boldsymbol{r})$. The Laplacian of potential is

[1] The charge density $n(\boldsymbol{r})$ is an electron-oriented representation of the conventional charge density $\rho(\boldsymbol{r})$ such that $n(\boldsymbol{r}) = -\rho(\boldsymbol{r})$.

related directly to the virtual total charge by Gauss' Law:

$$\nabla \cdot \nabla\phi(\boldsymbol{r}) = 4\pi\, n_{\text{vir}}(\boldsymbol{r}) \tag{6.3}$$

Since $n_{\text{free}} + n_{\text{ind}} = n_{\text{vir}}$ and knowing that Equations 6.2 and 6.3 are linear, one can by subtraction obtain the induced charge density and its contribution to the electrical potential, $\phi_{\text{ind}}(\boldsymbol{r})$.

$$\nabla \cdot \nabla\phi_{\text{ind}}(\boldsymbol{r}) \equiv \nabla \cdot [D_s(\boldsymbol{r}) - 1]\, \nabla\phi(\boldsymbol{r}) = -4\pi\, n_{\text{ind}}(\boldsymbol{r}) \tag{6.4}$$

In order to compute this induced potential, there are some practical considerations which impact its implementation. While the valence-electron charge density is easily accessible in an array, the contribution from the pseudopotentials is not. Due to the spherical symmetry of the pseudopotentials, they can without altering the field external to a cutoff-sphere, be replaced with a simple Gaussian-smoothed representation of the net core charge less the charges of the non-valence (or "pseudized") electrons. This incurs another adjustable parameter, the Gaussian smoothing parameter σ_{core}, which was taken to be 0.25 bohr for the purposes of this work. All of the smoothing parameters are taken from a previous study, in which they were optimized (Tester *et al.* 1998; Reagan *et al.* 1999).

4. The computed polarization field of the dielectric is transformed into a `dft++`-compatible external potential. The resulting file for ϕ_{ind} is input as an external potential into the density-functional calculation by incorporating it into the pseudopotential field. At this stage the polarization energy can be estimated from

$$(\Delta E)_{\text{polarization}} \doteq \int_{\Omega} \left(\phi_{\text{free}} n_{\text{ind}} + \phi_{\text{ind}} n_{\text{ind}} + \phi_{\text{ind}}\, n_{\text{free}}\right)\, dV \tag{6.5}$$

This relation is approximate because the charge density n_{free}, from the Chapter 5 calculations, is fixed. Also, the $\phi_{\text{free}} n_{\text{free}}$ term is constant, and cancels out of the equation. Polarization energies computed in this manner appear in Table 6.2.

5. As a first extension to the previous step, the wavefunctions from the bare-surface computations may be used as an initial guess to compute the charge density n_{free} of the surface under the influence of the induced potential ϕ_{ind}. This extra step was only performed for the bare Cr_2O_3 surface. For large changes in the charge

density, even this step will not generate a self-consistent n–ϕ system. A method for achieving a self-consistent system is proposed in Section 6.4. However, as established below, these changes are quite small.

This procedure was presented without showing how the external potential is incorporated into the density-functional model. The explanation of the density functional theory presented in Chapter 5 is simplified and does not show the explicit implementation of the pseudopotential approximation in the Hamiltonian. This will now be discussed in terms of the density-functional Lagrangian.

$$\begin{aligned}\mathcal{L}_{\mathrm{LDA}}(\{\psi_i\},\phi) &= \frac{1}{2}\sum_i f_i \int d\boldsymbol{r}\, \|\nabla\psi_i(\boldsymbol{r})\|^2 \\ &+ \int d\boldsymbol{r}\, \epsilon_{\mathrm{XC}}[n_\uparrow(\boldsymbol{r}), n_\downarrow(\boldsymbol{r})]\, n(\boldsymbol{r}) - \int d\boldsymbol{r}\, \phi(\boldsymbol{r})\,[n(\boldsymbol{r}) - n_0] \\ &- \frac{1}{8\pi}\int d\boldsymbol{r}\, D_s(\boldsymbol{r})\, \|\nabla\phi(\boldsymbol{r})\|^2 + \int d\boldsymbol{r}\, V_{\mathrm{ion}}(\boldsymbol{r})\, n(\boldsymbol{r}) \quad (6.6)\end{aligned}$$

The only term which depends explicitly on the wavefunctions is the kinetic energy, contained in the first term ($\frac{1}{2}\sum_i f_i \int d\boldsymbol{r}\, \|\nabla\psi_i\|^2$). The factor f_i is a filling factor, such that $0 \le f_i \le 1$ (or $0 \le f_i \le 2$ if not spin-dependent). Next is the exchange-correlation term ($\int d\boldsymbol{r}\, \epsilon_{\mathrm{XC}}(n_\uparrow, n_\downarrow)\, n$), shown here as a spin-dependent exchange correlation function. This depends only on the local electron density and spin channel. Next is the electron-electron interaction, also called the Hartree energy ($-\int d\boldsymbol{r}\,(n - n_0)\,\phi$), where ϕ is the electric field caused by charge density n. The constant n_0 is a neutralizing charge background which is used in conjunction with the Ewald sum (for $\hat{\mathrm{V}}_{I-I}$, computed "off-line") to produce the correct total electrostatic energy. The second-to-last term is the electric field self-energy term ($-1/8\pi \int d\boldsymbol{r}\, D_s \|\nabla\phi\|^2$). The electron-ion energy term, when not using the pseudopotential approximation, is simply the $z_i/|\boldsymbol{r} - \boldsymbol{r}_i|$ potentials for the nuclei. In the case of the pseudopotential approximation, the nuclear charge is replaced with a combined nuclear and core-electron potential.

As described in Step 5 above, the induced potential ϕ_{ind} does not change during the density-functional calculation.

$$\left[\overbrace{\int d\boldsymbol{r}\, \phi_{\mathrm{ind}}(\boldsymbol{r})\, n(\boldsymbol{r})}^{\text{new term}} + \int d\boldsymbol{r}\, V_{\mathrm{ion}}(\boldsymbol{r})\, n(\boldsymbol{r}) \right] \longrightarrow \int d\boldsymbol{r}\, V_{\mathrm{ion+ind}}(\boldsymbol{r})\, n(\boldsymbol{r}) \quad (6.7)$$

The similarities between this potential and the V_{ion} potential allow for a small modification of the `dft++` code in order to execute Step 5.

6.2 Ionicity of the Surface *In Vacuo*

Recall Section 5.3.2, in which significant relaxations of the α-Cr_2O_3 (0001) surface were evident. Let us now examine the accompanying rearrangements of the electronic structure. The (0001) α-Cr_2O_3 surface, in vacuum, is not only significantly relaxed atomically, but also exhibits a surface dipole reduction greater than that expected under the classical picture, in which the charges of the surface atoms are formally identical to those in the bulk. Spatial Mulliken population analysis was performed using program `one4one.c` (discussed in Section C.2). Table 6.1 shows that the change in the surface electronic structure reduces the ionicity of the outermost oxygens to 0.71 times the bulk value, thus reducing the surface dipole strength. This effect combines with the reduction of the spacing between the terminal oxygens and the next lowest chromium sublayer to 0.68 times its original length, to produce a reduction in surface dipole strength of approximately 50%. At the surface the oxygens are electron-depleted compared to their bulk-phase counterparts. The upper sublayer of the underlying chromium bilayer, layer Cr[2a], is also electron-depleted relative to inner layers.[2] Although the oxygens' net charge is negative, the self-consistent potential shows that on average the surface has an *affinity* for electrons.

The 28-atom slab used for the remainder of the calculations in this chapter has a magnetic phase boundary at the O[7] oxygen plane. Recall that for the bulk thirty-atom cell in Chapter 5 that there was a magnetic excitation pictured in Figure 5-5; a similar excitation is present in this system. This magnetic phase boundary is useful for investigating the effects of magnetic order on chemical reactivity. The excitation provides an asymmetry in the behaviors of the two surfaces.

6.3 The Effect of the Aqueous Dielectric

To ascertain the effects of a liquid water environment on the structure and energetics of the α-Cr_2O_3 (0001) surface, the procedure outlined in Section 6.1 was applied to the 28-atom Cr_2O_3 surface cell. Although the dielectric slab's induced polarization field influences the charge distribution in the bare Cr_2O_3 surface, the effect is so subtle that it is of little practical consequence for the bare surface. First-order-approximate computations applied to surfaces with adsorbates, however, suggest that the influence of the induced field around adsorbing species such as chlorine may be significant.

[2] Slab layers are named according to Figure 5-7 nomenclature, page 142.

Table 6.1 Spatial Mulliken population analysis for Cr_2O_3, as computed using program `one4one.c` (Section C.2).

	Charge per Atom			
Atom	Bulk	Surface (D_s=1)	Surface† (D_s=80)	Position
Chromium atoms				
0	1.59	1.63	1.62	
1	1.59	1.63	1.63	
2	1.58	1.92	1.92	Cr[2a]/Cr[10b]
3	1.59	1.94	1.91	Cr[2a]/Cr[10b]
4	1.58	1.61	1.63	
5	1.59	1.60	1.61	
6	1.58	1.76	1.77	Cr[2b]/Cr[10a]
7	1.59	1.61	1.61	
8	1.58	1.76	1.78	Cr[2b]/Cr[10a]
9	1.59	1.60	1.59	
10	1.58			
11	1.59			
Oxygen atoms				
0	-1.06	-1.04	-1.03	
1	-1.06	-1.04	-1.04	
2	-1.06	-1.04	-1.03	
3	-1.06	-1.03	-1.04	
4	-1.05	-1.03	-1.04	
5	-1.06	-1.03	-1.03	
6	-1.05	-0.75	-0.74	O[1]/O[11]
7	-1.05	-0.75	-0.75	O[1]/O[11]
8	-1.06	-0.75	-0.75	O[1]/O[11]
9	-1.06	-1.05	-1.06	
10	-1.05	-1.05	-1.04	
11	-1.05	-1.06	-1.05	
12	-1.06	-1.06	-1.06	
13	-1.05	-1.06	-1.06	
14	-1.06	-1.06	-1.06	
15	-1.06	-0.74	-0.75	O[1]/O[11]
16	-1.06	-0.75	-0.76	O[1]/O[11]
17	-1.06	-0.75	-0.75	O[1]/O[11]

†The surface supercell used in this calculation was based upon the magnetically-excited bulk cell in Figure 5-5. While the physical asymmetries in the cell might lead one to expect asymmetrical Mulliken results, no such asymmetries are evident.

Figure 6-1 portrays the change in charge density of the 28-atom slab when going from vacuum to a dielectric medium of D_s=80. On average, electrons on each atom recede from the surface. This effect is observed (at the ±0.001 electron/bohr^3 contours) as deep as the second chromium bilayer from the surface. Note that this very subtle effect *only* appears at contour levels as low as ±0.001 electron/bohr^3—two orders of magnitude smaller than what is normally used to visualize total charge density (0.3 electron/bohr^3). The electrons recede symmetrically despite the aforementioned asymmetric magnetic ordering in this cell.

In the HOMOs and LUMOs (Figure 6-2), however, the behavior is not as symmetric. Here it was discovered that the magnetic ordering of the cell (illustrated in Figure 6-3) exerts an influence (albeit small) not just upon the internal HOMO states, but also upon the chemical reactivity of the surface. Within two chromium bilayers of the magnetic phase boundary (*i.e.*, ignoring the Cr[2] bilayer[3]), there is an antisymmetric influence reflecting through the phase boundary: the HOMOs deplete "below" the phase boundary (bilayers Cr[8], Cr[10]), and are enhanced "above" it (bilayers Cr[4], Cr[6]).

Consider the "top" surface of the slab. The HOMOs of the outer Cr sublayer, layer Cr[2a], experience a population enhancement while the slightly deeper Cr[2b] HOMOs deplete. At the "bottom" portion of the slab, the situation is different. The HOMOs in the shallower Cr[10b] layer are unaffected, while the terminal oxygens O[11] and deeper-sublayer chromiums Cr[10a] are depleted in population. No enhancement occurs in the HOMOs "beneath" the magnetic soliton. In the LUMOs the O[1] and Cr[2b] layers are enhanced while the Cr[2a] layer depletes; in their case the symmetry does carry over to the other surface, except that the O[11] layer does not enhance as the O[1] layer does. Even the LUMOs, then, which are concentrated at the surfaces, are influenced by the magnetic phase boundary.

The atomic positions were not relaxed after the charge density reacted to the induced field of the dielectric. The changes in charge density computed in this very approximate study, however, are far too subtle to cause any significant changes in bonding, chemical reactivity, or crystal structure. That the induced field does not strongly affect the surface might suggest that the reactivity of a Cr_2O_3 surface is well-described by density functional theory independently of the environment. Examination of the polarization energies of some surfaces with adsorbates leads to a contrary conclusion, however.

[3] Here again the nomenclature of Figure 5-7 on page 142 is used.

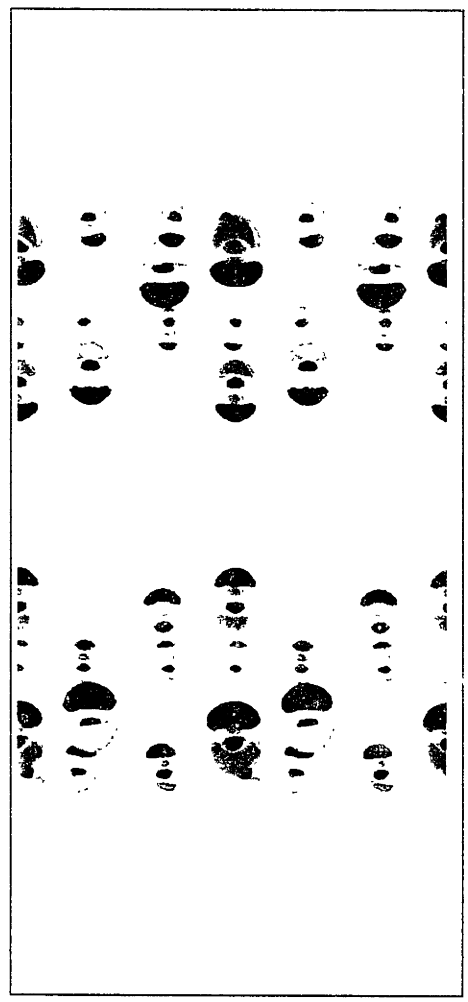

Figure 6-1 Change in total Cr_2O_3 charge density in going to a polarized state from a non-polarized ($n_{D_s=80} - n_{\text{vacuum}}$) state. The dark fields are the positive results, indicating enhancement in population, and the white fields are the negative results, indicating depletion. The isosurfaces are at $\Delta n = \pm 0.001$ electron/bohr^3. As in prior figures, some shapes are cut by the front plane of the cell, revealing their darker shaded interiors.

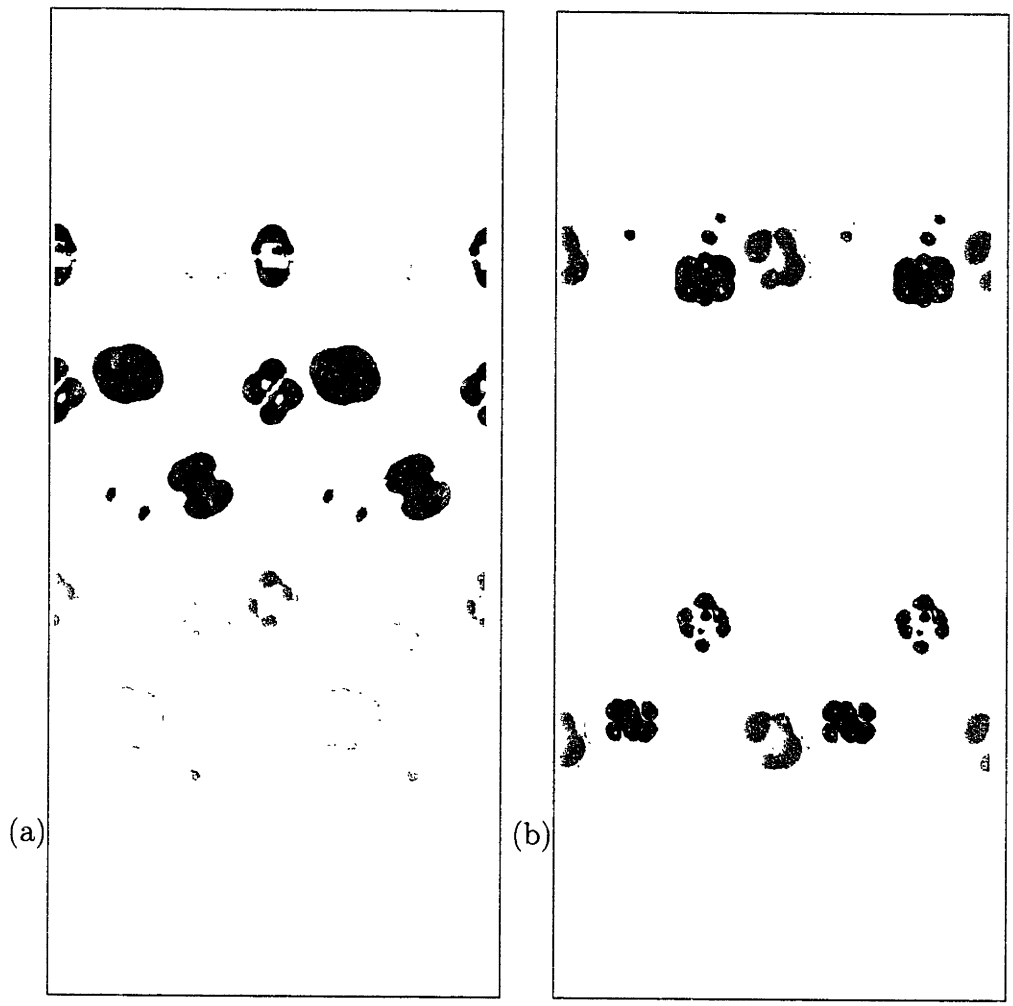

Figure 6-2 Effect of dielectric polarization field on the HOMOs (a) and LUMOs (b) of the 28-atom α-Cr_2O_3 surface slab. Electron charge density decreased in the spaces denoted by white shapes and increased in the spaces denoted by the darker shapes. In the HOMOs the effect is asymmetrical from surface to surface; this asymmetry is most likely due to the magnetic excitation in this surface slab. In the LUMOs however, there is a trend at both surfaces for the lowest energy states to recede from the surface. As in prior figures, some shapes are cut by the front plane of the cell, revealing their darker shaded interiors.

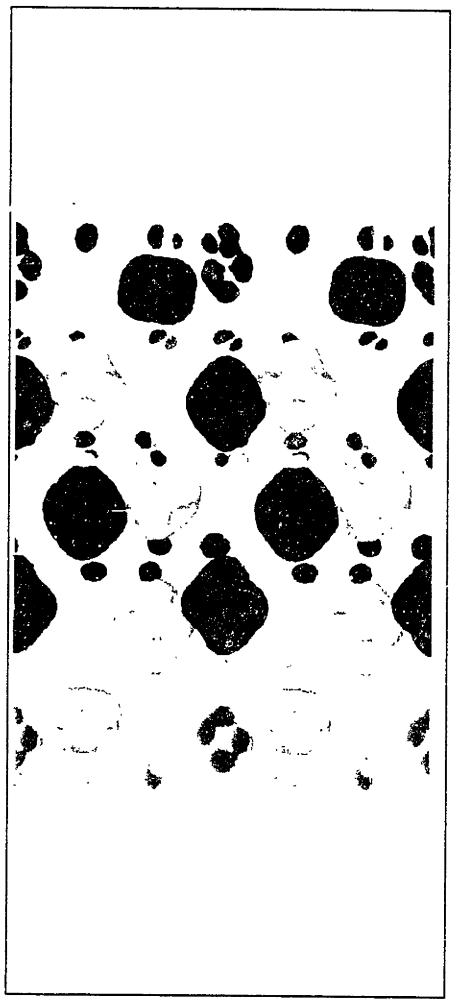

Figure 6-3 Spin polarization in the HOMOs of the magnetically-excited 28-atom α-Cr_2O_3 surface slab.

Table 6.2 Polarization energies from LSDA (Equation 6.5). Energies reflect the effects of polarization energy per surface (corresponding to one adsorption site).

System	$E_{D_s=80} - E_{D_s=1}$ [eV]
bare Cr_2O_3	-0.037
H-adsorbed Cr_2O_3	-0.314
H alone	-0.017
Cl alone	-0.023
Cl-adsorbed Cr_2O_3	-5.05

NOTE: H- and Cl-adsorbed surfaces are *not* at their relaxed positions and so may exhibit unrealistically strong dipoles.

With this picture for the bare surface in mind, similar calculations are performed to explore adsorption energies and the effect of the dielectric upon them. To gauge the effect of the dielectric on adsorbed species, total energy calculations of the adsorption of H and Cl on the Cr_2O_3 surface were performed on H- and Cl-adsorbed surfaces in various stages of mechanical relaxation. (These configurations were borrowed from another study-in-progress, but also employ the surface slab which has the magnetic phase boundary.) While these adsorbates have not fully reached relaxed positions on the Cr_2O_3 surface, they are close enough to allow us to gain insight into the effects of the presence of water on the adsorption energies. In order to have a point of comparison for the adsorption energy, separate total-energy calculations were performed for atomic H and Cl using exactly the same conditions ($\boldsymbol{k}$-point set, cell size, *etc.*) as used in the 28-atom surface slab calculations. Table 6.2 lists the energies of polarization of five systems.

To gauge solvation effects, the solvation energy of the surface alone was computed as a reference and then compared with the solvation energy of the surface with adsorbed species. The adsorption of H onto Cr_2O_3 increases the magnitude of the solvation effect calculated for the surface, lowering the system's energy by 0.3 eV, whereas the adsorption of Cl enhances the solvation effect to a much greater extent, 5.5 eV. Of the two configurations, the Cl-adsorbed surface was the least converged—and so a large dipole may exaggerate the effects of the solvent. But this non-equilibrium scenario corresponds to a species reacting with the surface, where it is evident that the solvent effects are very important.

Another effect which may be enhancing the solvation energy of the adsorbed chlo-

rine system is the electronegativity of the chlorine atom, which may be great enough to extract an electron from the crystal beneath. This would further exaggerate the dipole and would excite a stronger induced electric field in the dielectric continuum.

6.4 Implications and Recommendations

The preceding work has created a technique which combines a highly-detailed spin-dependent density functional calculation with the external influence of an electrostatic continuum due to the presence of a solvent of variable dielectric strength. While the continuum is chosen in this case to be a structureless dielectric, it can easily be replaced by a more structured dielectric once the proper model has been employed to compute it. While the simplicity of the model may exaggerate the effect of the presence of liquid water upon the Cr_2O_3 system, it is entirely appropriate for contrasting the general trends in behavior of the surface under the dielectric with results for vacuum conditions.

The influence of the dielectric upon the HOMOs and LUMOs of the bare Cr_2O_3 surface is negligible. However, when dealing with species which are capable of producing large dipoles at the surface, the energy-reducing effect of the induced field can be significant.

This work has discovered an intriguing relationship between the magnetic ordering in the system and the electronic structure of the HOMOs and LUMOs. This suggests that under certain conditions the magnetic order at or below the oxide surface may have an effect on the catalytic activity or other chemical reactivity at the surface. Because this portion of the computation was approximate, it cannot yet be used to quantify these effects or even describe trends, because the magnitude of these effects are very small.

While the techniques in this chapter help elucidate the interactions between a bare α-Cr_2O_3 surface and a variable-dielectric-constant medium, they are still very qualitative in nature and lack the detail required for quantitative characterization of these interactions. Part of the inadequacy is due to the lack of self-consistency between the charge density and the polarization field computed for the dielectric, particularly in the cases with adsorbing species Cl^- and H^+. Still another flaw is the magnetic phase boundary, which, while it allows exploration of chemo-magnetic effects, is not the true ground state of the material.

For future work, it is proposed that the assignment of the shape of the dielectric and its polarization field computation be merged into the `dft++` code. This would

allow iterative optimization of the orbitals in the context of the changing dielectric. The specific changes required include a modification of the pseudopotential to treat the core charge not as a point but as a Gaussian, which would allow direct representation and therefore computation of the dielectric polarization within the mechanisms already existing in the `dft++` code. The Ewald sum correction would be turned off as there are no more core point-charges to deal with. And, of course, the now-separate routines which construct the dielectric medium and solve the Poisson-Boltzmann equation would be integrated directly into the main iterative loop. With these modifications, large changes in the surface structure such as relaxations of terminal oxygens or hydroxyls could be handled without manually changing the shape of the dielectric each time the atoms were moved along their Hellmann-Feynman forces.

Additionally, a thorough examination of the parameters (n_{cutoff}, σ_{Ds}, σ_{core}) is in order. Although these were optimized during a previous study of a methylene chloride transition state (Tester *et al.* 1998), their transferability to this particular system has not been rigorously established, nor has the sensitivity of the results to the parameters been measured. In order for the calculation to provide solid quantitative results, the results must be fairly insensitive to the tunable parameters, and the calculation must be carefully validated against experimental data.

Bibliography

Reagan, M., J. Harris, and J. W. Tester (1999). Molecular simulations of dense hydrothermal NaCl-H_2O solutions from subcritical to supercritical conditions. *J. Phys. Chem. B* **103** (37), 7935–7941.

Tester, J. W., P. A. Marrone, M. D. DiPippo, K. Sako, M. T. Reagan, T. A. Arias, and W. A. Peters (1998). Chemical reactions and phase equilibria of model halocarbons and salts in sub- and supercritical water. *J. Supercrit. Fluids* **13**, 225–240.

Chapter 7

Conclusions, Recommendations, and Future Work

7.1 Experiments

E1. The failure of multiple Hastelloy C-276 CH_2Cl_2 preheaters was reviewed and interpreted. The preheaters experienced dealloying as well as stress corrosion cracking (SCC). Corrosion was most severe at positions exposed to hot, subcritical solution, but determination of peak conditions is not possible because of the range of conditions to which the tubes were exposed. Some cracking was also observed at sites with a low ($\approx$150° C) nominal temperature. Potential mechanisms for SCC initiation and propagation include the film-induced cleavage (Kelly *et al.* 1993), local chemistry changes, and local chemistry at physical defects (Mitton *et al.* 1997).

E2. An apparatus was developed which corrosion-tests an alloy in an entire profile of temperatures in one experiment. The test proceeds at constant pressure and composition, and is capable of internal pressures up to 4000 psig and test-section temperatures of up to 410° C. It is computer-controlled and logged (using `LabView`®) to allow safe high-temperature high-pressure multiple-day exposures with minimal human intervention. It uses a cooling profile rather than a heating profile to (1) ease construction, (2) obviate deposition of corrosion products during elevation to supercritical temperatures, and (3) ensure that the heat-transfer profile is externally limited.

E3. This system was used to expose Hastelloy C-276 tubes of 1/8-in and 1/16-in OD to a 365 ppm hydrothermal HCl solution at 250 bar and temperatures ranging

approximately 280–400° C. These conditions were chosen because they were typical of the conditions to which the failed Hastelloy C-276 preheater tubes of Section 4.1 had been exposed. This closely-controlled exposure developed a corrosion profile which could be correlated very accurately to a measured steady-state temperature profile.

E4. The 1/16-in tubing exhibited a corrosion profile similar to the preheater tube. The main component was of selective dissolution of iron and nickel. This dealloying was coupled with an intergranular corrosion mechanism. The intergranular corrosion was thwarted by the blunting effect of the dealloying and the rigidity of the metal matrix, which prevented a diffusion-limited intergranular corrosion propagation. The deepest penetration in the controlled experiment was found to occur between 370 and 380° C.

E5. The pseudo-zeroth-order rates of dealloying in the tubing were found to depend on temperature and dielectric constant. The dielectric constant may affect rate by changing the polarization of the corrosion reactions through contributions to the free energies of ionic species, or by influencing the exchange current density at the interface between the alloy and the porous dealloyed layer.

E6. The alloy in the 1/8-in tube was softer than in the 1/16-in tube; their grain boundary sizes differed by a factor of four, measurably influencing the hardness and therefore the yield stress. The apparent differences in elasticity, perhaps in combination with tensile residual stresses, allowed a deep intergranular corrosion to develop in the 1/8-in tube. This intergranular corrosion was not visible until the tubing was etched.

E7. It is expected that, even in the 1/16-in tube, once the dealloying front reaches a certain critical distance from the solvent, that the diffusion-limited chemistry will be supported, and the tube will crack. This is supported by the morphology of the corrosion seen in Figure 4-2.

It is clear from these results that when considering a material which must be resistant to localized corrosion, not only does its composition matter but also its microstructure.

For future work regarding investigation of similar systems:

- To eliminate intergranular corrosion, the metallurgy of the Hastelloy C-276 used in SCWO systems should more closely resemble the 1/16-in tube and not the 1/8-in tube.

- Each of these experiments provides only one time-dependent data point. The experiment should be repeated with different exposure times in order to fully characterize the rates. In particular, the deep intergranular corrosion may require an incubation time before it starts.

- There must be a limiting small-grain-size microstructure which is the best compromise between mechanical strength, toughness, and corrosion resistance. Experiments should be performed with material of different grain sizes.

- At higher water densities, the dealloying rate is not expected to drop off, because ions remain soluble. If a high dealloying rate can be tolerated, it may be possible to keep the alloy in the uniform-dealloying-dominated regime and suppress local cracking. A caveat is that the high-density operation would incur a mechanical stress expense, which may defeat any cracking resistance you gain.

- From the set of factors including residual and applied stresses, material hardness, and changes in aqueous-phase diffusivity, the immediate causes of the high intergranular corrosion rates seen in Run 3 should be identified. If it can be defeated, then intergranular corrosion at supercritical temperatures will not be a problem, and 120 μm-grained Hastelloy C-276 (like the 1/8-in tube) can be used in SCWO systems.

7.2 Theoretical Modeling

T1. A new neon-core pseudopotential for chromium was constructed using the methods of Rappe *et al.* (1990). The pseudopotential was validated by using it to calculate the electronic structure of bulk chromium metal under the local density approximation, and the comparing it with calculations performed without a pseudopotential.

T2. The chromium pseudopotential was combined with a well-tested oxygen pseudopotential (from another study) to compute *ab initio* the system of bulk Cr_2O_3 within the local spin-density approximation (LSDA) and also the local density approximation (LDA) under density functional theory. The LSDA calculations were found to describe the mechanical response, crystal asymmetries, thermodynamic and magnetic properties of Cr_2O_3 satisfactorily in comparison to experimental data and unrestricted Hartree-Fock calculations. The LDA results,

when compared with the LSDA results, showed that the effects of spin polarization in Cr_2O_3 help define even basic properties such as bulk modulus.

T3. The oxygen-terminated (0001) surface of α-Cr_2O_3 was computed under LSDA. It was found that, compared to their bulk positions, the terminal oxygens experience a significant inward relaxation. The terminal oxygens and underlying chromiums are depleted in electrons relative to their deeper counterparts. The HOMO states of the surface slab were located in the deeper layers, while the LUMO states tended to concentrate at the surface. The surface is thus vulnerable to electron-rich species, where any donated electrons would occupy the surface LUMO states and disrupt the bonding.

T4. The capability of computing the atomic-resolution effects of a dielectric upon the surface chemistry of Cr_2O_3 was developed in conjunction with the *ab initio* model. The *bare* Cr_2O_3 surface showed no significant changes in surface chemistry when a strong dielectric was present. Rough calculations of adsorption energies of chlorine onto the surface showed a dramatic decrease in energy in the presence of a dielectric. The dielectric is thus expected to have its strongest effect when the surface interacts with ions, creating strong dipoles which are geometrically accessible to the solvent.

This computational work has developed a tool which can be used to explore the surface chemistry of Cr_2O_3, the main constituent on passive films in popular corrosion-resistant alloys. This tool is now ready to be used to develop an *ab initio* density-functional description of the physical and chemical interactions between chlorine and Cr_2O_3 to explore mechanisms for chemical disruption of this passive film.

Although the model was originally targeted to explain loss of passivity of Cr_2O_3-protected materials in chloride-containing streams of SCWO systems, its utility reaches far beyond this application. Not only does Cr_2O_3 appear on very popular and widely-used alloys such as stainless steels, but also in catalytic applications. The density-functional model of Cr_2O_3 thus also may be used to develop an electron-level understanding of catalytic activity, catalytic reactions and transition states, and the mechanisms of catalyst poisoning.

For the future development and application of the density-functional description of Cr_2O_3, the following are recommended:

- It is now possible to explore reduction of the *ab initio* results to classical models for use in molecular dynamics (MD) computations. With such a model it may

be possible to quickly perform MD simulations of solvated ions near the Cr_2O_3 surface. This would be used to search for collisions likely to cause a chemical reaction. (Of course, the full *ab initio* potential could be used, but would slow the calculations considerably.) The full density-functional model could then be used to examine in detail the possible chemical reaction.

- The surface area available in model is too small for computing the adsorptions of all but the tiniest of molecules. As larger-scale computing power becomes available, the surface area should be increased.

- In a similar vein, when *much* higher computing power becomes available, the effect of oxide thickness should be assessed in the following manner: Sandwiched within two relatively thin oxide layers is a single-crystal metal. The oxide thickness can then be reduced to a monolayer, or expanded to multiple layers without loss of the internal electron reservoir of the "bulk" states.

- There was a remarkable influence of the magnetic ordering on the HOMOs and LUMOs in the Cr_2O_3 (0001) surface. The impact of the magnetic ordering upon catalytic activity and selectivity should be investigated.

- A full sensitivity analysis of the polarization energy of Cr_2O_3 with adsorbed species be performed, with respect to the parameters σ_{Ds}, σ_{core} and n_{cutoff}. While the general effects of the dielectric field have been observed with the techniques of Chapter 6, they cannot be considered quantitatively reliable without more thorough sensitivity analysis and validation and, where possible, validation with experiment.

Bibliography

Kelly, R. G., A. J. Young, and R. C. Newman (1993). Electrochemical impedance: Analysis and interpretation. In J. R. Scully, D. C. Silverman, and M. W. Kendig (Eds.), *ASTM STP 1188*, pp. 94. American Society for Testing Materials.

Mitton, D. B., S.-H. Zhang, K. E. Hautanen, J. A. Cline, E.-H. Han, and R. M. Latanision (1997). Evaluating stress corrosion and corrosion aspects in supercritical water oxidation systems for the destruction of hazardous waste. In *Corrosion 97*, Number 203, Houston, TX. NACE.

Rappe, A. M., K. M. Rabe, E. Kaxiras, and J. D. Joannopoulos (1990). Optimized pseudopotentials. *Phys. Rev. B* **41**, 1227.

APPENDIX

Appendix A

Metallography

A.1 Mounting, Polishing and Etching

Tube samples were cold mounted in epoxy mixed from Shell EPON 828 resin and a TETA initiator in a 100:13 mass ratio. The samples were then ground and wet-polished from the side, leaving a longitudinal cross-section of the tube visible. Care was taken to indicate the original orientation of the tube when mounting. The polishing was performed such that the longitudinal cross section exposes the top and bottom surfaces of the tube (Figure A-1). Samples were polished with SiC paper and water, down to 1200 grit, then with 1 μm diamond paste. After polishing, a portion of each sample was etched for 20 minutes to expose the metal grain boundaries. The etchant was prepared freshly and consisted of 15 mL concentrated hydrochloric acid, 10 mL glacial acetic acid, 5 mL concentrated nitric acid, and two *drops* of glycerol. After exposure for 20 minutes, the samples were rinsed with distilled water and immersed in a saturated sodium bicarbonate solution.

A.2 Determination of Penetration Depth

Samples are often polished to a plane P which is not quite dead center ($\Delta y \neq 0$, see Figure A-2). In order to interpret the apparent penetration depth (as seen from micrographs), it is necessary to correct for the angle α that the polished surface makes with the norm of the tube surface.

For small Δy it is possible to approximate that the triangle made by the apparent thickness t_a with the inner surface of the tube at radius r and the connecting line

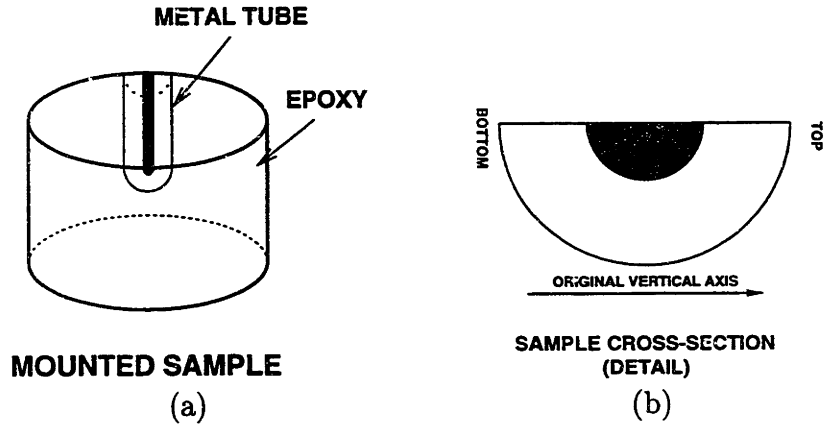

Figure A-1 Orientation of sample for metallography.

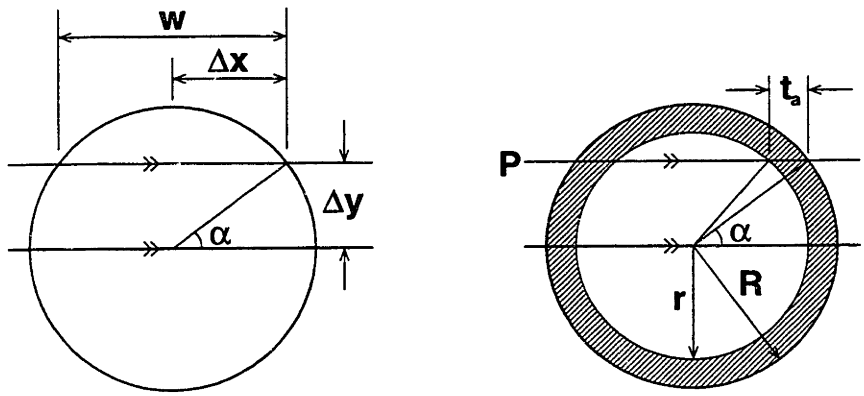

Figure A-2 Geometry of a tubular sample.

segment $t \equiv R - r$ (not labeled) is a right triangle. Then it follows that

$$\cos(\alpha) = \frac{t}{t_a} \tag{A.1}$$

The measured variables are apparent thickness t_a and cross-sectional width at the polished surface plane, w. Nominal radius R is also known from the tubing specifications. We solve for α with

$$\cos(\alpha) = \frac{\Delta x}{R} = \frac{w}{2R} \tag{A.2}$$

For a more exact computation we must determine the location of the intersection of the polished surface P with the inner radius r. This can be computed by recognizing that the line P is displaced from the centerline by Δy, and that the inner radius can be described by the circle equation,

$$(\widehat{\Delta x})^2 + (\widehat{\Delta y})^2 = r^2 \tag{A.3}$$

By inspection, the following are also true:

$$\widehat{\Delta x} = \Delta x - t_a = \frac{w}{2} - t_a \tag{A.4}$$

$$\widehat{\Delta y} = \Delta y \tag{A.5}$$

$$\tan(\alpha) = \frac{\Delta y}{\Delta x} \tag{A.6}$$

Substituting, one finds that

$$t = R - \sqrt{\left(\frac{w}{2} - t_a\right)^2 + \left(\frac{w}{2}\tan\alpha\right)^2} \tag{A.7}$$

where $\alpha = \cos^{-1}(w/2R)$. Completely in terms of measured quantities,

$$\boxed{t = R - \left\{\left(\frac{w}{2} - t_a\right)^2 + \left(\frac{w}{2}\tan\left[\cos^{-1}\frac{w}{2R}\right]\right)^2\right\}^{1/2}} \tag{A.8}$$

Table A.1 shows Equation A.8 applied to the values for each sample (Cline 1999, pp. 41–44).

Applying the correction to the polished samples, the true penetration depth of corrosion phenomena such as dealloying, intergranular corrosion, and so-called "singular" dealloying can be determined. These data are presented in Table A.2.

Run	Sample	w [mm]	t_a [mm]	α [°]	t	t/t_a
3	1	2.894	1.143	23.3	0.894	0.7822
3	2	2.877	1.175	24.0	0.895	0.7616
3	3	2.860	1.220	24.8	0.894	0.7327
3	4	2.977	1.024	19.1	0.894	0.8729
3	5	3.009	0.990	17.2	0.894	0.9024
3	6	2.894	1.143	23.3	0.894	0.7822
3	7	2.961	1.044	20.0	0.894	0.8565
5	1	1.353	0.331	31.5	0.254	0.7677
5	2	1.417	0.304	26.8	0.254	0.8344
5	3	1.517	0.271	17.1	0.253	0.9346
5	4	1.477	0.284	21.5	0.254	0.8948
5	5	1.360	0.327	31.1	0.253	0.7724
5	6	1.460	0.288	23.1	0.253	0.8788
5	7	1.397	0.313	28.4	0.254	0.8117

Table A.1 Geometric parameters of polished samples from Runs 3 and 5. **Note:** The scale on the microscope for Run 3 was imprecise, and so the absolute lengths should not be compared here. The ratio t/t_a has little ($< 1\%$) error, and can safely be used. The scale used for Run 5 is exact.

Run 3 (49.5 h)	Dealloying (μm)	IGC Penetration
TC_1	10.4 ± 1.9	64.8 ± 5.8
TC_2	7.8 ± 3.8	76.8 ± 8.5
TC_3	5.7 ± 2.1	87.6 ± 11.2
TC_4	7.3 ± 2.0	129.3 ± 9.6
TC_5	11.4 ± 1.7	79.0 ± 6.8
TC_6	10.1 ± 2.5	118.3 ± 10.0
TC_7	1.0 ± 1.5	131.1 ± 7.8

Run 5 (19.5 h)	Dealloying (μm)	Maximum Observed Singular Dealloying (μm)
TC_1	4.0 ± 1.1	18.4
TC_2	4.5 ± 1.4	38.4
TC_3	4.4 ± 1.7	52.3
TC_4	4.6 ± 2.2	40.2
TC_5	2.6 ± 1.9	36.4
TC_6	0.4 ± 0.7	24.6
TC_7	0.1 ± 0.6	3.3

Table A.2 Observed penetration depths of corrosion phenomena, corrected for polishing angle.

Bibliography

Cline, J. A. (1997–1999). Laboratory notebook of Jason Cline. MIT.

Appendix B

Major Changes to Density-Functional Model

B.1 Addition of Spin to `dft++` Code

A key task required to use spin-dependent density functional theory was to implement spin in the existing local density approximation (LDA) codes. This was accomplished with the following modifications to the code:

1. separate spin-up and spin-down charge densities, in addition to the total,
2. separate spin-up and spin-down self-consistent local Hamiltonians,
3. a new spin-dependent exchange-correlation function,
4. an analytic gradient to the exchange-correlation function,
5. a change in the input interface to account for spin,
6. separate sets of spin-up and spin-down wavefunctions, and
7. a maximum band filling of 1.0.

This was accomplished by duplicating the Bloch-theorem $\boldsymbol{k}$-points in the LDA system such that each LDA $\boldsymbol{k}$-point has two "virtual" LSDA $\boldsymbol{k}$-points. This implementation exploits a natural division in the code, requiring only very minor changes to effect the complete modification.

The exchange-correlation potential V_{xc} was split into two potentials, $V_{xc}^{\uparrow}$ and $V_{xc}^{\downarrow}$. These took the form

$$V_{xc}^{\uparrow} = \frac{\partial(\varepsilon_{xc} n)}{\partial n_{\uparrow}} = \frac{\partial \varepsilon_{xc}}{\partial n_{\uparrow}} \cdot n_{\uparrow} + \varepsilon_{xc} + n_{\downarrow} \frac{\partial \varepsilon_{xc}}{\partial n_{\uparrow}} \tag{B.1}$$

$$= \left(\frac{\partial \varepsilon_{xc}}{\partial n_{\uparrow}} \right) (n_{\uparrow} + n_{\downarrow}) + \varepsilon_{xc} \tag{B.2}$$

and the exchange-correlation energy

$$E_{xc} = \int_{\Omega} (n_{\uparrow} + n_{\downarrow}) \, \varepsilon_{xc} \tag{B.3}$$

Appendix C

Programming

C.1 Minor dft++ Core Code Modifications

While the major changes in the code are documented in Chapter B, there are many lesser modifications which were required to make the LSDA version of dft++ work properly.

For example, another code modification, which was required to construct higher-resolution electronic structure maps, was to update the program allbands to be compatible with the LSDA code.

The original LDA allbands program reads the total charge density of a previous dft++ run, then reconstructs the self-consistent Hamiltonian ($V_{sc,loc}$) from it. Next it minimizes the eigenvalues of the orthogonal wavefunctions by varying the wavefunction basis-expansion coefficients.

The LSDA-compatible code would not be able to use the total charge density to compute $V_{sc,loc}$, because $V_{sc,loc}$ was now spin dependent ($\{V_{sc,loc\uparrow}, V_{sc,loc\downarrow}\}$). Rather, the new allbands program reads in the actual $V_{sc,loc}$'s produced by the previous dft++ run, then uses them directly as the Hamiltonians upon which to minimize the wavefunctions.

C.2 Utilities for dft++ Suite

In order to properly interpret the data generated by the dft++ code, it was necessary to write a few utility programs which digest the data. To benefit possible continuation of the research, these mini-programs are documented here.

- p2f.c converts the 3-D output arrays (which are in general represented in non-

orthogonal crystallographic coordinates) from `dft++` into a form which can be read by AVS.[1] `p2f.c` was originally written to interpret data from the `md` program (written in CM FORTRAN); thus data provided to `p2f.c` for processing must be transposed into the FORTRAN array convention. This is accomplished using the `n2asc_cline` program (originally written as `n2asc.c` by Sohrab Ismail-Beigi).

- `n2asc_cline.c` converted the binary output files generated by `dft++` into ASCII files. These ASCII number lists could then be transported between platforms for plotting and/or re-instantiation as binary files for future `dft++` runs.

- `endian.c` is a July 1999 code which converts binary file formats (for standard ANSI C double-precision arrays) between little-endian and big-endian formats. This program greatly expedited the transfer of data between DEC Alpha and Cray/SGI Origin 2000 computers. Cumbersome and time-consuming conversions of 300+ Mb binary files to ASCII, and transport of the resulting huge (800–1000 Mb) ASCII files over crowded 10 Mbps EtherNet was eliminated.

- `mulliken.c` sums up charge for a given ion in an ever increasing radius for each ion in the system. It reads the total charge density and ion coordinates, then numerically integrates

$$q(r) = -e \int_0^r \int_0^\pi \int_0^{2\pi} n(r', \theta, \phi)\, r' \sin\theta \, d\phi \, r' \, d\theta \, dr' \qquad \text{(C.1)}$$

  I naïvely expected to see obvious plateaus which would indicate a cutoff radius delimiting the various ions from each other—making the formal charge on an atom obvious. In fact, no such cutoff point surfaced, probably due to the continuity of the electron orbitals through covalent bonding.

- `one4one.c` uniquely assigns each volume-pixel of the FFT box to the nearest ion ("nearestness," if necessary, can be weighted by a per-species effective-radius factor), then reports the total charge sum for each ion. This was the alternative to `mulliken.c`. This essentially sums charge in the Wigner-Seitz cell of each atom.

[1] AVS is a visualization and plotting program. AVS's chief competitor is DataExplorer, which has recently been released by IBM as free software.

- `spinflip.c` is a utility, based on `one4one.c`, which reads the self-consistent Hamiltonian ($V_{sc,loc}$) and "flips the spin" or exchanges the up and down $V_{sc,loc}$'s vicinal to selected ions. (These flipped $V_{sc,loc}$'s are then fed as input to the allbands program, which generates wavefunctions corresponding to the new spin arrangement. (See Section C.1 for details.)

- `linresp.c`, a utility which extrapolates (or interpolates) linearly a set of wave functions or atomic coordinates (or any other set of equal-sized arrays) based on an arbitrary coefficient α. This program is used to take advantage of the linear relationship between the wavefunction coefficients $\{c_{\boldsymbol{G},n,\boldsymbol{k},s}\}$ and the ion positions $\boldsymbol{R}$ and the cell vectors $\boldsymbol{\tau}$. This was particularly useful for the bulk modulus calculations, where the parameter α was an expansion-or-contraction factor for the lattice coordinates:

$$\boldsymbol{\tau}' = \alpha\boldsymbol{\tau} \tag{C.2}$$

  After obtaining the first two points of a bulk modulus by solving from random wavefunctions, the remaining bulk modulus points had a very good predictor both for the wavefunctions and for the atomic positions.

$$\boldsymbol{R}_2 = \frac{\boldsymbol{R}_1 - \boldsymbol{R}_0}{\alpha_1 - \alpha_0}(\alpha_2 - \alpha_0) + \boldsymbol{R}_0 \tag{C.3}$$

  and similarly for the wavefunction coefficients.

- `plotz.c` is a program which, given a `dft++` cell whose c-axis is orthogonal to the other two, it delivers a plot of the charge density in the cell, as a function of the c (or z) coordinate. The charge-density information produced by `dft++` is in terms of electron number density, in ($-$e·bohr^{-3}) units.

- `plotz_pot.c` is a similar to `plotz.c` but delivers a plot of an average potential ϕ in the cell as a function of z. It is important to note the normalization convention in `dft++`. The energy is

$$E = \int_\Omega \rho(\boldsymbol{r})\phi(\boldsymbol{r})\,d\boldsymbol{r} \tag{C.4}$$

$$= \sum_i \rho_i \phi_i v \tag{C.5}$$

  where ρ is the charge density, ϕ is the potential, v is the finite-element volume, and Ω is the total cell volume. In the `dft++` code, the potential array is *not* ϕ

but rather $\hat{\phi}_i \equiv \phi_i v$, so that

$$E = \sum_i \rho_i \hat{\phi}_i \tag{C.6}$$

For the purposes of `plotz_pot.c`, then, the average potential in an xy slice is described by

$$\overline{(\phi_{xy})}_z = \frac{1}{\Omega_{xy}} \sum_{x,y} \phi_{x,y,z} v \tag{C.7}$$

$$= \frac{1}{\Omega_{xy}} \sum_{x,y} \hat{\phi}_{x,y,z} \tag{C.8}$$

C.3 HOMO/LUMO Plots

To make plots of the highest occupied and lowest occupied molecular orbitals of the system, they must first be identified by examining the output of the last `dft++` run. For the purposes of plotting, the top four HOMOs and bottom four LUMOs in each $\boldsymbol{k}$-point are identified and recorded. The program `dumpbanddens` is then employed to dump the probability density ($|\psi|^2$) of the wavefunctions of each band—these dumps are in binary format. The binary files are next converted to ASCII using `n2asc_cline` (see above). The ASCII-dumps of the probability densities are then summed using `awk`. A simple `awk` script is employed piecewise to obtain the HOMOs and LUMOs for each $\boldsymbol{k}$-point, and then the HOMOs and LUMOs summed across $\boldsymbol{k}$-points.

The following program takes the ASCII dumps (named `n.{kpoint}.{band}`) and sums them for $\boldsymbol{k}$-point 1:

```
paste n.1.{5,6,7} | awk '{ \
    sum=0; \
    for (i=1;i<NF;i++) sum+=$i; \
    print sum; \
    }' > n.1.HOMO
```

This is repeated for all $\boldsymbol{k}$-points, and then the same awk script is used again to sum HOMOs and LUMOs for the entire system.

The HOMO/LUMO dumps are then transferred to a computer which has AVS installed. The program `p2f` (above) is run for the data set, and AVS is used (through use of an "isosurface" contour) to render the orbitals.

Appendix D

Theoretical Modeling Parameters and Data

D.1 Reporting Conventions

D.1.1 Lattice Vectors

The lattice matrix $\mathbf{L}$ is quickly constructed by multiplying the diagonal matrix of lattice parameters $\mathbf{A}$ with the matrix of nondimensional lattice vectors $\boldsymbol{\tau}$.

$$\mathbf{L} = \mathbf{A}\boldsymbol{\tau} \tag{D.1}$$

$$\mathbf{L} = \begin{bmatrix} a & 0 & 0 \\ 0 & b & 0 \\ 0 & 0 & c \end{bmatrix} \left[\begin{pmatrix} \vdots \\ \boldsymbol{\tau}_1 \\ \vdots \end{pmatrix} \begin{pmatrix} \vdots \\ \boldsymbol{\tau}_2 \\ \vdots \end{pmatrix} \begin{pmatrix} \vdots \\ \boldsymbol{\tau}_3 \\ \vdots \end{pmatrix} \right] \tag{D.2}$$

For convenience, lattice vectors will be presented as a the matrix compatible with the dft++ file `lattice.in`, which is in bohr units. The unit lattice matrix $\boldsymbol{\tau}$ and the lattice parameters a and c are reported. For all Cr_2O_3 supercells in this appendix, $b = a$ so b is not reported separately.

D.1.2 Position

Positions are reported in nondimensional crystallographic coordinates, as defined by a lattice matrix $\mathbf{L}$ in which the unit cell vectors are column vectors expressed in units

of bohrs.[1]

$$\mathbf{L}\boldsymbol{a} = \boldsymbol{x} \tag{D.3}$$

where $\mathbf{L}$ is the lattice matrix (column vectors), $\boldsymbol{a}$ is the nondimensional lattice coordinate vector, and $\boldsymbol{x}$ is the coordinate vector in real orthogonal space. (Also note that $\boldsymbol{a}$ and $\boldsymbol{x}$ are column vectors.) The cell volume is the determinant of matrix $\mathbf{L}$.

The coordinates for the positions are formatted in matrices of row vectors. Thus in order to convert them to orthogonal coordinates, the entire equation is transposed (generally done in MatLab®).

$$\mathbf{A}\mathbf{L}^{\dagger} = \mathbf{X} \tag{D.4}$$

where $\mathbf{A}$ and $\mathbf{X}$ are the row-vector-formatted nondimensional and real-space vector arrays, respectively.

D.1.3 Energy

Energies in the raw dft++ output are expressed in hartree units.[2] However, many of the results involve digested information, which is rendered in electron volts (eV). Energy units will be explicitly written.

D.1.4 Force

The Hellmann-Feynman forces are computed natively by dft++ in hartrees/bohr. Almost all of the digested data reported force in eV/Å.[3]

D.2 Chromium Pseudopotential

During this study a chromium pseudopotential was constructed. Figure D-1 shows the pseudo wavefunctions for the s, p and d electrons.

Table D.1 shows the reciprocal-space vectors used in testing the chromium pseudopotentials in Chapter 5.

---

[1] 1 bohr = 0.529177 Å.

[2] 1 hartree = 2 rydbergs = 27.2113961 eV.

[3] 1 eV/Å= $1.60217733 \times 10^{-9}$ N.

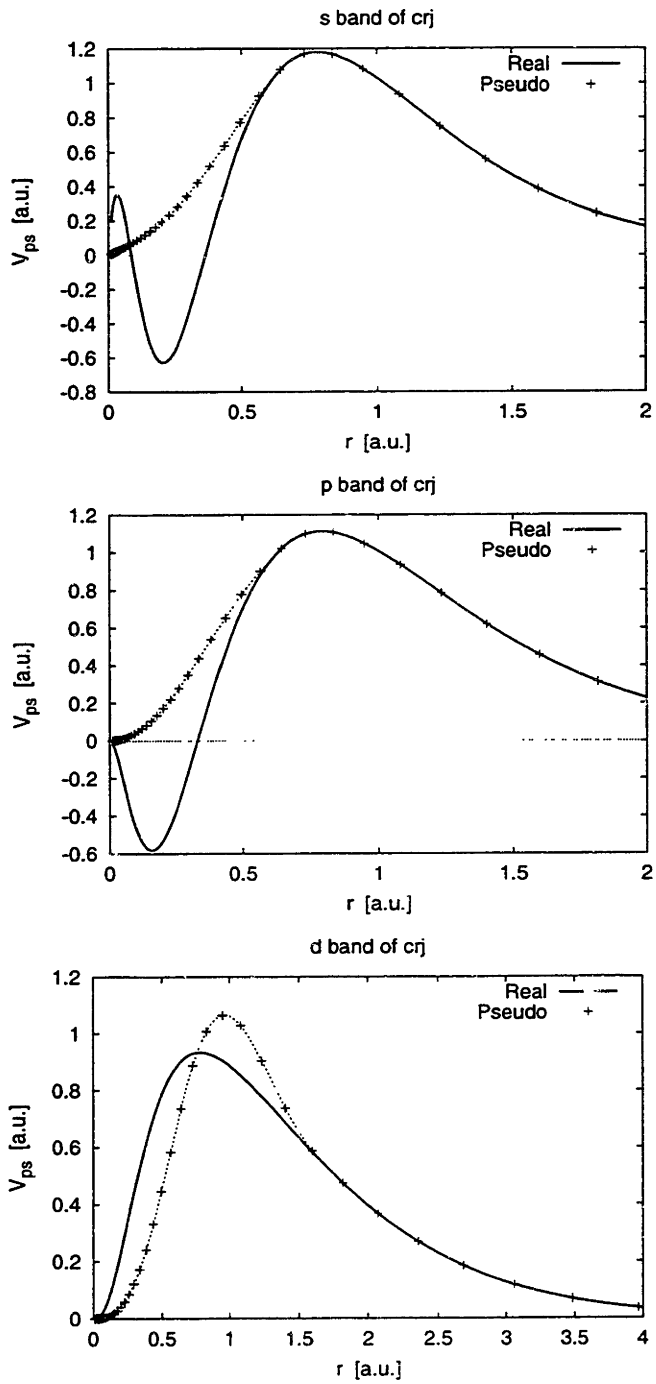

Figure D-1 Real potentials and pseudopotentials for the s, p, and d channels in chromium. Note the change in the r-scale in the d graph.

Γ	$(0, 0, 0)$	G	$(-\frac{1}{4}, \frac{1}{4}, \frac{1}{2})$
H	$(-\frac{1}{2}, \frac{1}{2}, \frac{1}{2})$	Σ	$(0, 0, \frac{1}{4})$
P	$(\frac{1}{4}, \frac{1}{4}, \frac{1}{4})$	Λ	$(\frac{1}{8}, \frac{1}{8}, \frac{1}{8})$
N	$(0, 0, \frac{1}{2})$	D	$(\frac{1}{8}, \frac{1}{8}, \frac{3}{8})$
Δ	$(-\frac{1}{4}, \frac{1}{4}, \frac{1}{4})$	F	$(-\frac{1}{8}, \frac{3}{8}, \frac{3}{8})$

Table D.1 Reciprocal-space vectors used for chromium band structure.

D.3 Pulay Stress

In general, density functional computations are run at a specific cutoff energy, beyond which energy the contribution of the eigenfunctions to the total energy of the system is negligible. This limits the total number of basis functions required for the minimization.

$$\psi(\boldsymbol{r}) = \sum_{G=0}^{G_{max}} c_G \varphi_G(\boldsymbol{r}) \tag{D.5}$$

For the case of a three-dimensional plane wave basis set, the following expressions relate cutoff energy and number of basis functions:

$$E_{cut} = \frac{\hbar G_{max}^2}{2m} \tag{D.6}$$

$$\frac{4\pi}{3} G_{max}^3 = \left(\frac{2\pi}{L_x} \cdot \frac{2\pi}{L_y} \cdot \frac{2\pi}{L_z}\right) \tilde{N}_{pl} \tag{D.7}$$

where Equation D.6 is the kinetic energy of a free plane wave and Equation D.7 equates the volume of a sphere of radius G_{max} in $\boldsymbol{G}$-space with the number of basis functions times the basis functions' allotted volume in $\boldsymbol{G}$-space. Note that $\tilde{N}_{pl}$ is not guaranteed to be an integer, and so the actual N_{pl} is greater than or equal to $\tilde{N}_{pl}$.

Bulk modulus computations involve stretching or compressing the simulation cell (via parameters $\{L_i\}$), thus increasing or reducing the number of plane waves required for computation. As the computation always uses the optimum basis set, the number of basis functions required changes. Since the basis function set is a discrete set, only integer quantities of basis functions may be added or subtracted—and this is often much more than what $\tilde{N}_{pl}$ dictates. Hence, when the coefficients of the newly added or removed basis functions are not small, as is the case when the contribution of the higher-energy basis functions to the total energy drops off suddenly, a change

$\langle N_{pl} \rangle_k$	E [eV]	Cutoff [Ry]
4341	-11850.0217231620	54
5121	-11863.6459709582	60
5721	-11870.1495428669	65
6503	-11875.5514282850	70
7049	-11878.0172189306	75
7909	-11880.2429231588	85

Table D.2 Convergence in LDA cell energy for a 10-atom Cr_2O_3 cell with a Ne-core pseudopotential as a function of basis set size.

Cutoff [Ry]	E [eV]
36	-3577.7997037223
40	-3596.3063655015
45	-3613.8944989271
50	-3627.3799701779
60	-3647.0743415513
70	-3656.3646658127

Table D.3 Convergence in LDA cell energy for a 10-atom Cr_2O_3 cell with a Ar-core pseudopotential as a function of basis set size.

in computed energy occurs.

In the case of practical computations, there is an optimization of speed vs. accuracy, and hence the value of the coefficients near the cutoff energy is often nonzero. This thus introduces energy errors into the bulk modulus curve. These errors can be corrected by running the full computation at various values of E_{cut} to develop an E_{total} vs. E_{cut} curve.

$$E_{corrected} = E_{computed} + \frac{\partial E_{cell}}{\partial E_{cut}} \left(E_{cut} - \tilde{E}_{cut} \right) \tag{D.8}$$

$\tilde{E}_{cut}$ is the cutoff energy computed using $\tilde{N}_{pl}$ in Equations D.6 and D.7.

For applications in which multiple Bloch-theorem $\boldsymbol{k}$-points have different $\{N_{pl}^k\}$, we use $\langle N_{pl} \rangle_k$.

D.4 10-atom Cr_2O_3 Cell

D.4.1 Initial Crystallographic Lattice Vectors

The following vectors are consistent with Hahn (1995).

$$\begin{bmatrix} 8.11339657713771 & 0 & 5.40893122968307 \\ -4.68427388189585 & 9.36854776379170 & 0 \\ 0 & 0 & 8.55882394618247 \end{bmatrix}$$

$$a = 4.95762\,\text{Å} \qquad c = 4.52913\,\text{Å} \qquad \boldsymbol{\tau} = \begin{bmatrix} \frac{\sqrt{3}}{2} & 0 & \frac{2}{3} \\ -\frac{1}{2} & 1 & 0 \\ 0 & 0 & 1 \end{bmatrix}$$

D.4.2 Initial Atom Positions

The ideal crystallographic positions for the atoms in the 10-atom cell are described by the following (x and z are compound-dependent crystal parameters).

Cr: (z, z, z), $(\bar{z} + \frac{1}{2}, \bar{z} + \frac{1}{2}, \bar{z} + \frac{1}{2})$, $(\bar{z}, \bar{z}, \bar{z})$, $(z + \frac{1}{2}, z + \frac{1}{2}, z + \frac{1}{2})$

O: $(x, \bar{x} + \frac{1}{2}, \frac{1}{4})$, $(\bar{x}, x + \frac{1}{2}, \frac{3}{4})$, $(\frac{1}{4}, x, \bar{x} + \frac{1}{2})$, $(\frac{3}{4}, \bar{x}, x + \frac{1}{2})$, $(\bar{x} + \frac{1}{2}, \frac{1}{4}, x)$, $(x + \frac{1}{2}, \frac{3}{4}, \bar{x})$

The initial coordinates for these atoms (for files `crj.pos` and `O.pos`) are below.

Chromium Atoms			Oxygen Atoms		
0.302680	0.651427	0.045908	0.803584	0.749668	0.750053
0.697407	0.348644	0.953931	0.499772	0.053669	0.750115
0.302537	0.151292	0.546031	0.195807	0.445918	0.750083
0.697373	0.848691	0.454112	0.196295	0.250299	0.249922
			0.500290	0.946265	0.249869
			0.804289	0.554225	0.249909

The final coordinates at each bulk-modulus volume-point are not enumerated here, but can be reconstructed from the x(O) and z(Cr) information in Figure D-2.

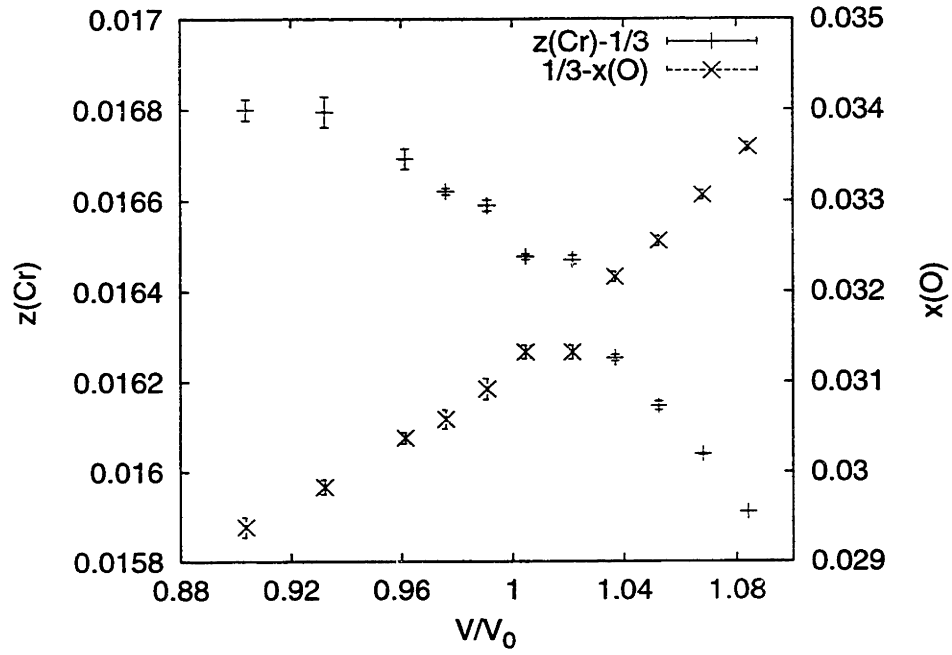

Figure D-2 Crystal asymmetry parameters under LSDA, as a function of volume change. V_0 here is the crystallographic specific volume.

D.4.3 Bloch-Theorem k-Points

The k-vectors used for this cell are:

$$\begin{pmatrix} \frac{1}{4} \\ \frac{1}{4} \\ \frac{1}{4} \end{pmatrix} \quad \begin{pmatrix} \frac{1}{4} \\ \frac{1}{4} \\ -\frac{1}{4} \end{pmatrix} \quad \begin{pmatrix} \frac{1}{4} \\ -\frac{1}{4} \\ \frac{1}{4} \end{pmatrix} \quad \begin{pmatrix} \frac{1}{4} \\ -\frac{1}{4} \\ -\frac{1}{4} \end{pmatrix}$$

and each was weighted at $\frac{1}{4}$.

D.4.4 *Ab Initio* Equilibrium Lattice Vectors

These are essentially the same lattice vectors as adapted from Hahn (1995), except that they are rescaled to the *ab initio* equilibrium volume. Below are two results, one for LDA and the other for LSDA.

D.5 30-atom Cr_2O_3 Cell

D.5.1 Lattice Vectors

Lattice vectors used in the 28-atom surface slabs (as listed in `lattice.in`) were:

$$\begin{bmatrix} 8.06877665804 & 0 & 0 \\ -4.65851037555 & 9.31702075109 & 0 \\ 0 & 0 & 25.5352423513 \end{bmatrix}$$

$$a = 4.93035\,\text{Å} \qquad c = 13.5127\,\text{Å} \qquad \boldsymbol{\tau} = \begin{bmatrix} \frac{\sqrt{3}}{2} & 0 & 0 \\ -\frac{1}{2} & 1 & 0 \\ 0 & 0 & 1 \end{bmatrix}$$

D.5.2 Initial Atom Positions

The positions of the atoms as determined by symmetry and crystallography are determined by adding the following offsets to the coordinates of the Cr and O atoms.

offset: $(0, 0, 0)$, $(\frac{2}{3}, \frac{1}{3}, \frac{1}{3})$, $(\frac{1}{3}, \frac{2}{3}, \frac{2}{3})$

Cr: $(0, 0, z)$, $(0, 0, \bar{z} + \frac{1}{2})$, $(0, 0, \bar{z})$, $(0, 0, z + \frac{1}{2})$

O: $(x, 0, \frac{1}{4})$, $(0, x, \frac{1}{4})$, $(\bar{x}, \bar{x}, \frac{1}{4})$, $(\bar{x}, 0, \frac{3}{4})$, $(0, \bar{x}, \frac{3}{4})$, $(x, x, \frac{3}{4})$

The initial coordinates for these atoms (for files `crj.pos` and `O.pos`) are below.

Chromium Atoms

0.000000	0.000000	0.236082
0.000000	0.000000	0.443288
0.000000	0.000000	0.575766
0.000000	0.000000	0.103604
0.333300	0.666700	0.216855
0.333300	0.666700	0.349332
0.333300	0.666700	0.556540
0.666700	0.333300	0.462515
0.666700	0.333300	0.122830
0.666700	0.333300	0.330038

Oxygen Atoms

0.306000	0.000000	0.169843
0.000000	0.306000	0.169843
0.694000	0.694000	0.169843
0.694000	0.000000	0.509527
0.000000	0.694000	0.509527
0.306000	0.306000	0.509527
0.639300	0.666700	0.622779
0.333300	0.972700	0.622779
0.027300	0.360700	0.622779
0.027300	0.666700	0.283093
0.333300	0.360700	0.283093
0.639300	0.972700	0.283093
0.972700	0.333300	0.396277
0.666700	0.639300	0.396277
0.360700	0.027300	0.396277
0.360700	0.333300	0.056591
0.666700	0.027300	0.056591
0.972700	0.639300	0.056591

The final coordinates follow:

Chromium Atoms

0.00022691258527	0.00005503435251	0.65180483825778
0.00006795902099	0.00022242117702	0.84249603472163
0.66663736103324	0.33314548661333	0.48528945497258
0.66647325900701	0.33329758214243	0.67579610563035
0.66688239744493	0.33339103858347	0.98531451404904
0.66672664201251	0.33355509521587	0.17589987867712
0.33331009060631	0.66646642702512	0.81852566096784
0.33314910870443	0.66662903981022	0.00910660636052
0.33356224620475	0.66672431018415	0.31862082568943
0.33339930676839	0.66687975568548	0.50912673863573
0.99996911927502	0.99980206216891	0.15192629880461
0.99980387197553	0.99996675037314	0.34262236341758

Oxygen Atoms

0.68882266132310	0.00003527047442	0.74711158932680
0.66660701740240	0.02187808375448	0.08058078730864
0.35554806231369	0.02211814044688	0.58048892946717
0.31093679380767	0.31099611685218	0.74711020023182
-0.00012726410045	0.31114681887789	0.24728202019795
0.97812413443404	0.33335946181179	0.58049214566326
0.35536912875789	0.33360330112904	0.08058705490259
0.33357440574635	0.35535066261397	0.41388520163940
0.02208605404111	0.35558062430498	0.91381507026954
0.97793652015054	0.64444992606667	0.08057591755605
0.66648478376900	0.64468599157183	0.58050071360228
0.64465934670348	0.66640240073675	0.91380548045064
0.02190021015984	0.66663816275124	0.41389267970065
1.00018203437183	0.68887992039886	0.74711029459999
0.68909169827362	0.68903607183446	0.24728118142016
0.64447155096676	0.97791903602863	0.41389600138505
0.33344861119518	0.97815396673260	0.91381064637177
0.31119851874678	0.99996990513769	0.24727994357566

D.5.3 Bloch-Theorem k-Points

The k-vectors used for this cell are:

$$\begin{pmatrix} \frac{1}{4} \\ \frac{1}{4} \\ 0 \end{pmatrix} \qquad \begin{pmatrix} \frac{1}{4} \\ -\frac{1}{4} \\ 0 \end{pmatrix}$$

and each was weighted at $\frac{1}{2}$.

D.6 28-atom Cr_2O_3 (0001) Surface Slab

D.6.1 Lattice Vectors

Lattice vectors used in the 28-atom surface slabs (as listed in `lattice.in`) were:

System	Total Energy (D_s=1) [hartree]	[eV]	$E_{D_s=80}-E_{D_s=1}$ [hartree]	[eV]
bare Cr_2O_3	-1.139543061×10^{3}	-31008.5576	-2.7×10^{-3}	-7.4×10^{-2}
H-adsorbed Cr_2O_3	-1.140730235×10^{3}	-31040.8622	-2.3×10^{-2}	-6.3×10^{-1}
H alone	$-4.768732112\times10^{-1}$	-12.9763	-1.2×10^{-3}	-3.3×10^{-2}
Cl alone	-1.489783460×10^{1}	-405.3909	-1.7×10^{-3}	-4.6×10^{-2}
Cl-adsorbed Cr_2O_3	-1.170709560×10^{3}	-31856.6415	-4.1×10^{-1}	-1.1×10^{1}

Table D.4 Total energies and polarization energies from LSDA. The energies of polarization are computed using Equation 6.5. Energies reflect the effects of polarization of the entire cell, which has *two* surfaces (top and bottom). Many significant figures are reported due to the small size of the polarization energies compared to the total electronic energy.

NOTE: H- and Cl-adsorbed surfaces are not at their relaxed positions and so may exhibit unrealistically strong dipoles.

$$\begin{bmatrix} 8.06877665804 & 0 & 0 \\ -4.65851037555 & 9.31702075109 & 0 \\ 0 & 0 & 37.7945197716 \end{bmatrix}$$

$$a = 4.93035\,\text{Å} \qquad c = 20.0000\,\text{Å} \qquad \boldsymbol{\tau} = \begin{bmatrix} \frac{\sqrt{3}}{2} & 0 & 0 \\ -\frac{1}{2} & 1 & 0 \\ 0 & 0 & 1 \end{bmatrix}$$

D.7 Adsorption Energies

The initial coordinates used were the final coordinates of the 30-atom bulk cell. The final coordinates for the relaxed surface follow:

Chromium Atoms

0.00006173295241	0.00026759464479	0.23615941424240
0.00008799849577	-0.00025424202576	0.44325932954691
0.00066069268497	0.00024421971833	0.57894722329295
-0.00096989702106	-0.00037325150092	0.10047105674861
0.33300589507760	0.66649429454680	0.21901271568630
0.33356367479049	0.66693220728604	0.34786304829472
0.33487237500179	0.66720441211165	0.55885386651549
0.66703273655427	0.33348110927123	0.46031578610217
0.66502505668171	0.33281366830464	0.12057280407346
0.66660145002424	0.33299412123419	0.33150272201472

Oxygen Atoms

0.30849238464805	0.00068117171602	0.17303753180168
-0.00114075764699	0.30768460122012	0.17292636953904
0.69312570091739	0.69196962967911	0.17306868471158
0.69149397872315	-0.00077282971495	0.50632245965563
0.00105548162145	0.69229525942699	0.50646071317406
0.30704207153264	0.30820903111164	0.50628433480522
0.66542245332674	0.70863544058012	0.61075096128193
0.29366316248777	0.95777703463652	0.61028280626852
0.04325673670090	0.33551734795302	0.61046111648697
0.02254739387725	0.66644436967398	0.28382776216660
0.33376412582827	0.35610199612422	0.28381266849087
0.64389537248224	0.97733134826739	0.28377100181353
0.97759373580171	0.33346799239172	0.39552005195268
0.66648113728086	0.64391592564405	0.39552599076488
0.35617681180390	0.02258089856339	0.39558464733230
0.33436780660747	0.29142742148547	0.06874615319253
0.70608326302902	0.04218332872057	0.06914743781761
0.95647337388879	0.66445449535560	0.06892449433219

Bibliography

Hahn, T. (Ed.) (1995). *International Tables for Crystallography*, Volume A. Boston: Kluwer Academic Publishers.

Bibliography

Alloy Digest, Inc. (1985). *Data on INCO Alloy C-276.* NJ.

Anderko, A. and K. S. Pitzer (1993). Equation-of-state representation of phase equilibria and volumetric properties of the system NaCl-H_2O above 573 K. *Geochim, [Comochim], Aeta* **57**, 1657–80.

Anderko, A., S. J. Sanders, and R. D. Young (1997). Real-solution stability diagrams: A thermodynamic tool for modeling corrosion in wide temperature and concentration ranges. *Corrosion* **53** (1), 43–53.

Balbuena, P. B., K. P. Johnston, and P. J. Rossky (1996). Molecular dynamics simulation of electrolyte solutions in ambient and supercritical water. 2. Relative acidity of HCl. *J. Phys. Chem.* **100** (7), 2716–22.

Balbuena, P. B., K. P. Johnston, P. J. Rossky, and J.-K. Hyun (1998). Aqueous ion transport properties and water reorientation dynamics from ambient to supercritical conditions. *J. Phys. Chem. B* **102** (19), 3806–3814.

Bellissent-Funel, M.-C., T. Tassaing, H. Zhao, D. Beysens, B. Guillot, and Y. Guissani (1997). The structure of supercritical heavy water as studied by neutron diffraction. *J. Chem. Phys.* **107** (8), 2942–2949.

Biswas, R. and B. Bagchi (1998). Ion solvation dynamics in supercritical water. *Chem. Phys. Lett.* **290** (1–3), 223–228.

Blaney, C. A., L. Li, E. F. Gloyna, and S. U. Hossain (1996). Supercritical water oxidation of pulp and paper mill sludge (as an alternative to incineration). In *Minimum Effluent Mills Symp.*, pp. 79–93. TAPPI Press, Atlanta, GA.

Born, V. M. (1920). Volumen und Hydrationswärme der Ionen. *Zeitschr. Physik* **1**, 45–48.

Botti, A., F. Bruni, M. A. Ricci, and A. K. Soper (1998). Neutron diffraction study of high density supercritical water. *J. Chem. Phys.* **109** (8), 3180–4.

Boukis, N., N. Claussen, K. Ebert, R. Janssen, and M. Schacht (1997). Corrosion screening tests of high-performance ceramics in supercritical water containing oxygen and hydrochloric acid. *J. Eur. Ceram. Soc.* **17** (1), 71–77.

Boukis, N., G. Franz, C. Friedrich, W. Habicht, and K. Ebert (1996). Corrosion screening tests with Ni-base alloys in supercritical water containing hydrochloric acid and oxygen. In *Proceedings of the ASME Heat Transfer Division*, Number 4, pp. 159–167.

Brock, E. E., Y. Oshima, P. E. Savage, and J. R. Barker (1996). Kinetics and mechanism of methanol oxidation in supercritical water. *J. Phys. Chem.* **100** (39), 15834–15842.

Brock, E. E. and P. E. Savage (1995). Detailed chemical kinetics model for supercritical water oxidation of C_1 compounds and H_2. *AIChE Journal* **41** (8), 1874–88.

Chen, C. C., H. I. Britt, J. F. Boston, and L. B. Evans (1982). Local composition model for excess Gibbs energy of electrolyte solutions. Part 1: Single solvent, single completely dissociated electrolyte systems. *AIChE Journal* **28** (4), 588–596.

Chialvo, A. A. and P. T. Cummings (1996). Microstructure of ambient and supercritical water. Direct comparison between simulation and neutron scattering experiments. *J. Phys. Chem.* **100** (4), 1309–16.

Chialvo, A. A., P. T. Cummings, and H. D. Cochran (1996). Solvation structure, hydrogen bonding, and ion pairing in dilute supercritical aqueous NaCl mixtures. *Int. J. Thermophys.* **17** (1), 147–56.

Cline, J. A. (1997–1999). Laboratory notebook of Jason Cline. MIT.

Cline, J. A., P. A. Marrone, D. B. Mitton, R. M. Latanision, and J. W. Tester (2000, January). Corrosion mechanisms of Hastelloy C-276 in hydrothermal HCl solutions: Failure analysis and exposure studies. To be submitted to *Corrosion*.

Cline, J. A., A. A. Rigos, and T. A. Arias (1999, December). *Ab initio* study of magnetic structure and chemical reactivity of Cr_2O_3 and its (0001) surface. Submitted to *J. Phys. Chem. B*.

Connolly, J. (1966). Solubility of hydrocarbons in water near the critical solution temperature. *J. Chem. Eng. Data* **11** (1), 13.

Criss, C. M. and J. W. Cobble (1964). The thermodynamic properties of high temperature aqueous solutions. IV. Entropies of the ions up to 200°C and the correspondence principle. *J. Am. Chem. Soc.* **86**, 5390.

Croiset, E. and S. F. Rice (1998). Direct observation of H_2O_2 during alcohol oxidation by O_2 in supercritical water. *Ind. Eng. Chem. Res.* **37** (5), 1755–1760.

Croiset, E., S. F. Rice, and R. G. Hanush (1997). Hydrogen peroxide decomposition in supercritical water. *AIChE Journal* **43** (9), 2343–2352.

Dieter, G. E. (1986). *Mechanical Metallurgy.* New York: McGraw-Hill.

DiNaro, J. L. (1999). PhD thesis in Chemical Engineering, Massachusetts Institute of Technology, Cambridge, MA.

DiNaro, J. L., J. W. Tester, K. Swallow, and J. B. Howard (1999). Experimental measurements of benzene oxidation in supercritical water. To be submitted to *AIChE Journal.*

Ding, K. and W. E. Seyfried, Jr. (1996, 14 June). Direct pH measurement of NaCl-bearing fluid with an in situ sensor at 400°C and 40 megapascals. *Science* **272**, 1634–6.

Downey, K. W., R. H. Snow, D. A. Hazlebeck, and A. J. Roberts (1995). Corrosion and chemical agent destruction: Research on supercritical water oxidation of hazardous military wastes. In K. P. Johnston and J. M. L. Penninger (Eds.), *Innovations in Supercritical Fluids: Science and Technology*, ACS Symposium Series #608. American Chemical Society.

Eklund, K., S. N. Lvov, and D. D. Macdonald (1997). The measurement of Henry's constant for hydrogen in high subcritical and supercritical aqueous systems. *J. Electroanal. Chem.* **437** (1–2), 99–110.

Fells, I. and E. A. Moelwyn-Hughes (1958). The kinetics of the hydrolysis of methylene dichloride. *J. Chem. Soc.*, 1326.

Fullman, R. L. (1953). *Trans. AIME* **197**, 447 and 1267.

Garcia, K. M. (1996). Data acquisition testing in supercritical water oxidation using machine cutting oils and metals. In *Proceedings of the ASME Heat Transfer Division*, Volume 4, pp. 169–176.

Garcia, K. M. and R. E. Mizia (1995). Corrosion investigation in supercritical water oxidation process environments. See Heat Transfer Division (Am. Soc. Mech. Eng.) (1995), pp. 299–309.

Gloyna, E. F. and L. Li (1995). Supercritical water oxidation research and development update. *Environ. Prog.* **14** (3), 182–92.

Gorbaty, Y. E. and R. B. Gupta (1998). The structural features of liquid and supercritical water. *Ind. Eng. Chem. Res.* **37** (8), 3026–3035.

Gorbaty, Y. E. and A. G. Kalinichev (1995). Hydrogen bonding in supercritical water. 1. Experimental results. *J. Phys. Chem.* **99**, 5336–40.

Haar, L., J. S. Gallagher, and G. S. Kell (1984). *NBS/NRC Steam Tables.* Hemisphere Publishing Corp.

Hanush, R. G., S. F. Rice, T. B. Hunter, and J. D. Aiken (1996). Operation and performance of the supercritical fluids reactor (SFR). Technical Report SAND96-8203, Sandia National Laboratories, Livermore, CA.

Haroldsen, B. L., D. Y. Ariizumi, B. E. Mills, B. G. Brown, and D. C. Rousar (1996). Transpiring wall supercritical water oxidation test reactor design report. Technical Report SAND96-8213, Sandia National Laboratories, Livermore, CA.

Heat Transfer Division (Am. Soc. Mech. Eng.) (1995). *Proceedings of the ASME Heat Transfer Division*, Volume 2. Heat Transfer Division (Am. Soc. Mech. Eng.).

Hodes, M. S. (1998, September). *Measurements and Modeling of Deposition Rates from Near-Supercritical, Aqueous, Sodium Sulfate and Potassium Sulfate Solutions to a Heated Cylinder.* PhD thesis in Mechanical Engineering, Massachusetts Institute of Technology, Cambridge, MA.

Hodes, M. S., K. A. Smith, W. S. Hurst, W. J. Bowers, Jr., and P. Griffith (1997). Measurements and modeling of deposition rates from a near supercritical aqueous sodium sulfate solution to a heated cylinder. In *ASME Proceedings of the National Heat Transfer Conference*, Volume 12, pp. 107–119.

Hohenberg, P. and W. Kohn (1964). *Phys. Rev.* **136**, 864B.

Holgate, H. R. (1993). *Oxidation Chemistry and Kinetics in Supercritical Water: Hydrogen, Carbon Monoxide, and Glucose.* PhD thesis in Chemical Engineering, Massachusetts Institute of Technology, Cambridge, MA.

Holgate, H. R. and J. W. Tester (1993). Fundamental kinetics and mechanisms of hydrogen oxidation in supercritical water. *Comb. Sci. and Tech.* **88**, 369–97.

Holgate, H. R. and J. W. Tester (1994). Oxidation of hydrogen and carbon monoxide in sub- and supercritical water: Reaction kinetics, pathways, and water-

density effects. 2. Elementary reaction modeling. *J. Phys. Chem.* **98**, 810–22.

Holgate, H. R., P. A. W. J. W. Tester, and R. K. Helling (1992). Carbon monoxide oxidation in supercritical water: The effects of heat transfer and the water-gas shift reaction on observed kinetics. *Energy & Fuels* **6** (5), 586.

Holliday, R. L., B. Y. M. Jong, and J. W. Kolis (1998). Organic synthesis in subcritical water. Oxidation of alkyl aromatics. *J. Supercrit. Fluids* **12** (3), 255–260.

Holliday, R. L., J. W. King, and G. R. List (1997). Hydrolysis of vegetable oils in sub- and supercritical water. *Ind. Eng. Chem. Res.* **36** (3), 932–935.

Hong, G. T. (1995). Hydrothermal oxidation: Pilot scale operating experiences. In *Off. Proc.—Int. Water Conf.*, pp. 489–96.

Hong, G. T., F. J. Armellini, and J. W. Tester (1995). The NaCl-Na_2SO_4-H_2O system in supercritical water. See White (1995).

Huang, S., K. Daehling, T. E. Carleson, P. Taylor, C. Wai, and A. Propp (1989). Thermodynamic analysis of corrosion of iron alloys in supercritical water. In K. P. Johnston and J. M. L. Penninger (Eds.), *Supercritical Fluid Science and Technology*, ACS Symposium Series #406. American Chemical Society.

Hunter, T. B., S. F. Rice, and R. G. Hanush (1996). Raman spectroscopic measurement of oxidation in supercritical water. 2. Conversion of isopropyl alcohol to acetone. *Ind. Eng. Chem. Res.* **35** (11), 3984–3990.

Ikushima, Y. (1997). An *in situ* laser Raman spectroscopy study on the structure of supercritical water. *Koatsuryoku no Kagaku to Gijutsu* **6** (1), 24–29.

Ikushima, Y., K. Hatakeda, N. Saito, and M. Arai (1998). An in-situ Raman spectroscopy study of subcritical and supercritical water: The peculiarity of hydrogen bonding near the critical point. *J. Chem. Phys.* **108** (14), 5855–5860.

Jackson, J. D. and W. B. Hall (1979). *Turbulent Forced Convection in Channels and Bundles*, Volume 2, pp. 563ff. Washington: Hemisphere Publishing Corp.

Japas, M. L. and E. U. Franck (1985b). High pressure phase equilibria and PVT-data of the water–nitrogen to 673K and 250 MPa. *Ber. Bunsenges Phys. Chem.* **89**, 793.

Japas, M. L. and E. U. Franck (1985a). High pressure phase equilibria and PVT-data of the water–oxygen system including water–air to 673K and 250 MPa. *Ber. Bunsenges Phys. Chem.* **89**, 1268.

Johnson, J. W., E. H. Oelkers, and H. C. Helgeson (1992). SUPCRT92: A software package for calculating the standard molal thermodynamic properties of minerals, gases, aqueous species, and reactions from 1 to 5000 bar and 0 to 1000° C. *Computers and Geosciences* **18** (7), 899–947.

Johnston, K. P., P. B. Balbuena, T. Xiang, and P. J. Rossky (1995). Simulation and spectroscopy of solvation in water from ambient to supercritical conditions. In K. P. Johnston and J. M. L. Penninger (Eds.), *Innovations in Supercritical Fluids: Science and Technology*, ACS Symposium Series #608, pp. 77–92. American Chemical Society.

Jones, D. A. (1982). Localized corrosion. In R. N. Parkins (Ed.), *Corrosion Processes*, Chapter 4, pp. 161–207. New York: Applied Science Publishers.

Jones, D. A. (1996). *Principles and Prevention of Corrosion.* Upper Saddle River, NJ: Prentice Hall.

Kalinichev, A. G. and J. D. Bass (1997). Hydrogen bonding in supercritical water. 2. Computer simulations. *J. Phys. Chem. A* **101** (50), 9720–9727.

Kelly, R. G., A. J. Young, and R. C. Newman (1993). Electrochemical impedance: Analysis and interpretation. In J. R. Scully, D. C. Silverman, and M. W. Kendig (Eds.), *ASTM STP 1188*, pp. 94. American Society for Testing Materials.

Kirkwood, J. G. (1934). Theory of solutions of molecules containing widely separated charges with special applications to zwitterions. *J. Chem. Phys.* **2** (7), 351.

Kohn, W. and L. J. Sham (1965). Self-consistent equations including exchange and correllation effects. *Phys. Rev.* **140**, 1133A.

Krader, T. and E. U. Franck (1987). The ternary sytems H_2O-CH_4-NaCl and H_2O-CH_4-$CaCl_2$ to 800K and 250 MPa. *Ber. Bunsenges. Phys. Chem.* **91**, 627.

Krammer, P., S. Mittelstadt, and H. Vogel (1999, February). Investigating the synthesis potential in supercritical water. *Chemical Engineering & Technology* **22** (2), 126–130.

Kriksunov, L. and D. Macdonald (1997). Potential-pH diagrams for iron in supercritical water. *Corrosion* **53** (8), 605–611.

Kriksunov, L., D. D. Macdonald, and P. J. Millett (1994, November). Tungsten/tungsten oxide pH sensing electrode for high temperature aqueous environments. *J. Electrochem. Soc.* **141** (11), 3002–5.

Kriksunov, L. B. and D. D. Macdonald (1995a). Corrosion testing and prediction in SCWO environments. See Heat Transfer Division (Am. Soc. Mech. Eng.) (1995), pp. 281–288.

Kriksunov, L. B. and D. D. Macdonald (1995b, Feb. 6–9). Development of Pourbaix diagrams for metals in supercritical aqueous media. In *Proceedings of First International Workshop on Supercritical Water Oxidation*, Jacksonville, FL.

Kutney, M. C., V. S. Dodd, K. A. Smith, H. J. Herzog, and J. W. Tester (1997). A hard-sphere, volume-translated van der Waals equation of state for supercritical process modeling: Part I, pure components. *Fluid Phase Equilibria* **128**, 149–171.

LaJeunesse, C. A., B. L. Haroldsen, S. F. Rice, and B. G. Brown (1997). Hydrothermal oxidation of Navy shipboard excess hazardous materials. Technical Report SAND97-8212, Sandia National Laboratories, Livermore, CA.

le Clercq, M. (1996, June). Ceramic reactor for use with corrosive supercritical fluids. *AIChE Journal* **42** (6), 1798.

Lee, A., O. S. Saulters, C. S. Connon, and H. G. Castillo (1996). Destruction of ammonia and acetic acid by hydrothermal oxidation. In *Proceedings of the ASME Heat Transfer Division (335)*, Volume 4, pp. 189–201. HTD (Am. Soc. Mech. Eng.).

Lee, D. S., K. S. Park, Y. W. Nam, Y.-C. Kim, and C. H. Lee (1997). Hydrothermal decomposition and oxidation of *p*-nitroaniline in supercritical water. *J. Hazard. Mater.* **56** (3), 247–256.

Lee, J. B. (1981, August). Elevated temperature potential-pH diagrams for the Cr-H_2O, Ti-H_2O, Mo-H_2O, and Pt-H_2O systems. *Corrosion* **37** (8), 467.

Lee, J. H. and N. R. Foster (1996). Direct partial oxidation of methane to methanol in supercritical water. *J. Supercrit. Fluids* **9** (2), 99–105.

Lide, D. R. (Ed.) (1999). *CRC Handbook of Chemistry and Physics* (79th ed.). New York: CRC Press.

Lin, K. S., H. P. Wang, and M. C. Li (1998). Oxidation of 2,4-dichlorophenol in supercritical water. *Chemosphere* **36** (9), 2075–2083.

Liu, C., D. D. Macdonald, E. Medina, J. J. Villa, and J. M. Bueno (1994, September). Probing corrosion activity in high subcritical and supercritical water through electrochemical noise analysis. *Corrosion Science* **50** (9), 687.

Liu, C., S. R. Snyder, and A. J. Bard (1997). Electrochemistry in near-critical and supercritical fluids. 9. Improved apparatus for water systems (23-385°C). The oxidation of hydroquinone and iodide. *J. Phys. Chem. B* **101** (7), 1180–1185.

Lvov, S. N. and D. D. Macdonald (1997). Potentiometric studies of supercritical water chemistry. In *Proc. Electrochem. Soc., High Temperature Materials Chemistry*, Volume 39, pp. 746–754.

Macdonald, D. D. (1997, January). Defining the corrosion chemistry of supercritical water oxidation systems. In *Proc. of the Tri-Service Conference on Corrosion*, Volume 1, Springfield, VA. National Technical Information Service.

Macdonald, D. D. and P. Butler (1973). The thermodynamics of the aluminum-water system at elevated temperatures. *Corrosion Science* **13**, 259–74.

Marrone, P. A. (1998). *Hydrolysis and oxidation of model organic compounds in sub- and supecritical water: Reactor design, kinetics, measurements, and modeling.* PhD thesis in Chemical Engineering, Massachusetts Institute of Technology, Cambridge, MA.

Marrone, P. A., T. A. Arias, W. A. Peters, and J. W. Tester (1998). Solvation effects on kinetics of methylene chloride reactions in sub- and supercritical water: Theory, experiment, and *ab initio* calculations. *J. Phys. Chem. A* **102** (35), 7013–28.

Marrone, P. A., R. P. LaChance, J. L. DiNaro, B. D. Phenix, J. C. Meyer, J. W. Tester, W. A. Peters, and K. C. Swallow (1995). Methylene chloride oxidation and hydrolysis in supercritical water. In K. W. Hutchenson and N. Foster (Eds.), *Innovations in Supercritical Fluids: Science and Technology*, ACS Symposium Series #608. Washington, D.C.: American Chemical Society.

Marshall, W. L. and E. U. Franck (1981). Ion product of water substance, 0–1000°C, 1–10,000 bars. *J. Phys. Chem. Ref. Data* **10** (2), 295–304.

Mather, A. E. and E. U. Franck (1992). Phase equilibria in the system carbon dioxide–water at elevated pressures. *J. Phys. Chem.* **96** (1), 6.

McKrell, T. J. and J. M. Galligan (1995). Kinetic study of the passive film on 304 stainless steel using a scanning tunneling microscope. In R. Sharma, P. L. Gai, M. Gajdardziska-Josifovska, R. Sinclair, and L. J. Whitman (Eds.), *In Situ Electron and Tunneling Microscopy of Dynamic Processes*, Pittsburgh, PA, pp. 199–204. Materials Research Society. Meeting in Boston, MA, 27–30 November, 1995.

Meissner, H. P. and J. W. Tester (1972). Activity coefficients of strong electrolytes in aqueous solutions. *Ind. Eng. Chem. Proc. Des. Dev.* **11** (1), 128–133.

Mitton, D. B., Y. S. Kim, J. H. Yoon, S. Take, and R. M. Latanision (1999). Corrosion of SCWO constructional materials in Cl^- containing environments. In *Corrosion 99*, Number 257, Houston, TX. NACE. Meeting Location: San Antonio, TX.

Mitton, D. B., P. A. Marrone, and R. M. Latanision (1996, March). Interpretation of the rationale for feed modification in SCWO systems. *J. Electrochem. Soc.* **143** (3), L59–L61.

Mitton, D. B., J. C. Orzalli, and R. M. Latanision (1995). Corrosion studies in supercritical water oxidation systems. In K. P. Johnston and J. M. L. Penninger (Eds.), *Innovations in Supercritical Fluids: Science and Technology*, ACS Symposium Series #608. Washington, DC: American Chemical Society.

Mitton, D. B., S.-H. Zhang, K. E. Hautanen, J. A. Cline, E.-H. Han, and R. M. Latanision (1997). Evaluating stress corrosion and corrosion aspects in supercritical water oxidation systems for the destruction of hazardous waste. In *Corrosion 97*, Number 203, Houston, TX. NACE.

Mitton, D. B., S.-H. Zhang, M. S. Quintana, J. A. Cline, N. Caputy, P. A. Marrone, and R. M. Latanision (1998). Corrosion mitigation in SCWO systems for hazardous waste disposal. In *Corrosion 98*, Number 414, Houston, TX. NACE.

Mizan, T. I., P. E. Savage, and R. M. Ziff (1995). A molecular dynamics investigation of hydrogen bonding in supercritical water. In K. P. Johnston and J. M. L. Penninger (Eds.), *Innovations in Supercritical Fluids: Science and Technology*, ACS Symposium Series #608, pp. 47–64. American Chemical Society.

Mizan, T. I., P. E. Savage, and R. M. Ziff (1996a). Comparison of rigid and flexible simple point charge water models at supercritical conditions. *J. Comput. Chem.* **17** (15), 1757–1770.

Mizan, T. I., P. E. Savage, and R. M. Ziff (1996b). Temperature dependence of hydrogen bonding in supercritical water. *J. Phys. Chem.* **100** (1), 403–8.

Newman, R. C. and K. C. Sieradzki (1994). *Science* **263**, 1708.

Odenweller, T. (1990, August). On the theory of the semiconductor/electrolyte-interface (I). *J. Electrochem. Soc.* **137** (8), 2457–61.

Oelkers, E. H. and H. C. Helgeson (1989). Calculation of the transport properties of aqueous species at pressures to 5 KB and temperatures to 1000° C. *J. Solution Chem.* **18** (7), 601–640.

Oelkers, E. H., H. C. Helgeson, E. L. Shock, D. A. Sverjensky, J. W. Johnson, and V. A. Pokrovskii (1995). Summary of the apparent standard partial molal Gibbs free energies of formation of aqueous species, minerals, and gases at pressures 1 to 5000 bars and temperatures 25 to 1000°C. *J. Phys. Chem. Ref. Data* **24** (4), 1401.

Oshima, Y., K. Hori, M. Toda, T. Chommanad, and S. Koda (1998). Phenol oxidation kinetics in supercritical water. *J. Supercrit. Fluids* **13** (1–3), 241.

Perdew, J. P. and A. Zunger (1981). *Phys. Rev. B* **23**, 5048.

Perry, R. H. and D. Green, eds. (1984). *Perry's Chemical Engineers' Handbook* (6th ed.). McGraw-Hill.

Peters, ed., W. A. (1996). Data needs to support modeling of supercritical water oxidation reactors and processes for chem demil applications. Technical Report MIT-EL 96-002, MIT Energy Laboratory, Cambridge, MA.

Phenix, B. D. (1998). *Hydrothermal oxidation of simple organic compounds.* PhD thesis in Chemical Engineering, Massachusetts Institute of Technology, Cambridge, MA.

Phenix, B. D., J. L. DiNaro, J. W. Tester, J. B. Howard, and K. A. Smith (1999). The effects of mixing and oxidant choice in laboratory-scale measurements of supercritical water oxidation kinetics. To be submitted to *Ind. Eng. Chem. Res.*

Pomelli, C. S. and J. Tomasi (1997). *Ab Initio* study of the S_N2 reaction $CH_3Cl + Cl^- \rightarrow Cl^- + CH_3Cl$ in supercritical water with the polarizable continuum model. *J. Phys. Chem. A* **101** (19), 3561–3568.

Pourbaix, M. (1964). *Atlas of Electrochemical Equilibria.* London: Pergamon Press.

Press, W. H., S. A. Teukolsky, W. T. Vetterling, and B. P. Flannery (1992). *Numerical Recipes in C: The Art of Scientific Computing* (2nd ed.). Cambridge University Press.

Protopopov, V. S. (1977). Generalizing relations for the local heat-transfer coefficients in turbulent flows of water and carbon dioxide at supercritical pressure in a uniformly heated circular tube. *High Temperature* **15** (4), 687.

Reagan, M., J. Harris, and J. W. Tester (1999). Molecular simulations of dense hydrothermal NaCl-H_2O solutions from subcritical to supercritical conditions. *J. Phys. Chem. B* **103** (37), 7935–7941.

Rebert, C. J. and W. B. Kay (1959). The phase behavior and solubility relations of the benzene–water system. *AIChE Journal* **5**, 285.

Rehbein, C., F. Michel, N. M. Harrison, and A. Wander (1998). *Ab Initio* total energy studies of the α-Cr_2O_3 (0001) and $(01\bar{1}2)$ surfaces. *Surface Review and Letters* **5** (1), 337–40.

Rice, S. F., R. R. Steeper, and C. A. LaJeunesse (1994). Supercritical water oxidation of colored smoke, dye, and pyrotechnic compositions. Technical Report SAND94-8203, Sandia National Laboratories, Livermore, CA.

Rohr, F., M. Bäumer, H.-J. Freund, J. A. Meijas, V. Staemmler, S. Müller, L. Hammer, and K. Heinz (1997). Strong relaxations at the Cr_2O_3 (0001) surface as determined via low-energy electron diffraction and molecular dynamics simulations. *Surface Science* **372**, L291–L297.

Salvatierra, D., J. D. Taylor, P. A. Marrone, and J. W. Tester (1999). Kinetic study of hydrolysis of methylene chloride from 100 to 500° C. Accepted for publication in *Ind. Eng. Chem. Res.*

Schacht, M., N. Boukis, N. Claussen, E. Dinjus, K. Ebert, R. Janssen, and F. Meschke (1997). Reactor for investigations of the corrosion of ceramics in HCl containing SCWO environments and first experimental results. In *Proceedings of the 4th International Symposium on Supercritical Fluids (ISSF97)*, pp. 147–150. Meeting date: 11-14 May, 1997 in Sendai, Japan.

Schacht, M., N. Boukis, E. Dinjus, K. Ebert, R. Janssen, F. Meschke, and N. Claussen (1998). Corrosion of zirconia ceramics in acidic solutions at high pressures and temperatures. *J. Europ. Ceram. Soc.* **18**, 2373–76.

Shock, E. L. and H. C. Helgeson (1988). Calculation of the thermodynamic and transport properties of aqueous species at high pressures and temperatures: Correlation algorithms for ionic species and equation of state predictions to 5 kb and 1000°C. *Geochimica et Cosmochimica Acta* **52**, 2009.

Sieradzki, K. and R. C. Newman (1987). Stress-corrosion cracking. *J. Phys. Chem. Solids* **48** (11), 1101–13.

Steeper, R. R. and S. F. Rice (1995). Optical monitoring of the oxidation of methane in supercritical water. See White (1995), pp. 652–4.

Sunkara, M. K., A. K. Rawat, and P. J. Moran (1996). Corrosion monitoring in supercritical water media. In R. H. Jones and D. R. Baer (Eds.), *Proc. Symp. New Tech. Charact. Corros. Stress Corros.*, pp. 303–313. Minerals, Metals & Materials Society, Warrendale, PA.

Tanger, IV, J. C. and H. C. Helgeson (1988). Calculation of the thermodynamic and transport properties of aqueous species at high pressures and temperatures: Revised equations of state for the standard partial molal properties of ions and electrolytes. *American Journal of Science* **288**, 19.

Taylor, J. D. and J. W. Tester (1999). Experimental measurements of MTBE hydrolysis and oxidation in supercritical water. Work in progress.

Tester, J. W. and J. A. Cline (1999). Hydrolysis and oxidation in sub- and supercritical water: Connecting process engineering science to molecular interactions. In *Corrosion 99*, Number 252, Houston, TX. NACE. Meeting Location: San Antonio, TX.

Tester, J. W., H. R. Holgate, F. J. Armellini, P. A. Webley, W. R. Killilea, G. T. Hong, and H. E. Barner (1991). Oxidation of hazardous organic wastes in supercritical water: A review of process development and fundamental research. In D. W. Tedder and F. G. Pohland (Eds.), *Emerging Technologies for Hazardous Waste Management III*, ACS Symposium Series #518, pp. 35–76. American Chemical Society.

Tester, J. W., P. A. Marrone, M. D. DiPippo, K. Sako, M. T. Reagan, T. A. Arias, and W. A. Peters (1998). Chemical reactions and phase equilibria of model halocarbons and salts in sub- and supercritical water. *J. Supercrit. Fluids* **13**, 225–240.

Tester, J. W. and M. Modell (1997). *Thermodynamics and Its Applications* (3rd ed.). Upper Saddle River, NJ: Prentice Hall.

Tester, J. W., P. A. Webley, and H. R. Holgate (1993). Revised global kinetic measurements of methanol oxidation in supercritical water. *Ind. Eng. Chem. Res.* **32** (1), 236–9.

Thammanayakatip, C., Y. Oshima, and S. Koda (1998). Inhibition effect in supercritical water oxidation of hydroquinone. *Ind. Eng. Chem. Res.* **37** (5), 2061–2063.

Townsend, Jr., H. E. (1970). Potential-pH diagrams at elevated temperature for the system Fe-H_2O. *Corrosion Science* **10**, 343–58.

Uematsu, M. and E. U. Franck (1980). Static dielectric constant of water and steam. *J. Phys. Chem. Ref. Data* **9** (4), 1291–1306.

Vreedenberg, H. A. (1958). Heat transfer between a fluidized bed and a horizontal tube. *Chem. Eng. Sci.* **9**, 52.

Wang, X.-G., W. Weiss, S. K. Shaikhutdinov, M. Ritter, M. Petersen, F. Wagner, R. Schlögl, and M. Scheffler (1998, August). The hematite (α-Fe_2O_3) (0001) surface: Evidence for domains of distinct chemistry. *Phys. Rev. Lett.* **81** (5), 1038–1041.

Watts, M. J. and C. T. Chou (1982). Mixed convection heat transfer to supercritical pressure water. In *Proceedings of the Seventh International Heat Transfer Conference*, Volume 3, Munich, Fed. Rep. of Germany, pp. 495.

Webley, P. A. (1990). *Fundamental oxidation kinetics of simple compounds in supercritical water.* PhD thesis in Chemical Engineering, Massachusetts Institute of Technology, Cambridge, MA.

Webley, P. A., H. R. Holgate, D. M. Stevenson, and J. W. Tester (1990). Oxidation kinetics of model compounds of metabolic waste in supercritical water. In *20th Intersociety Conference on Environmental Systems*, #901333, Warrendale, PA. Society of Automotive Engineers. Meeting Location: Williamsburg, VA.

Webley, P. A. and J. W. Tester (1991). Fundamental kinetics of methane oxidation in supercritical water. *Energy and Fuels* **5**, 411–419.

Webley, P. A., J. W. Tester, and H. R. Holgate (1991). Oxidation kinetics of ammonia and ammonia-methanol mixtures in supercritical water in the temperature range 530–700°C at 246 bar. *Ind. Eng. Chem. Res.* **30** (8), 1745–54.

White, Jr., H. J. (Ed.) (1995). *Physical Chemistry of Aqueous Systems, Proceedings from the 12th International Conference on the Properties of Water and Steam*, New York. Begell House.

Wofford, W. T., E. F. Gloyna, and K. P. Johnston (1998). Boric acid equilibria in near-critical and supercritical water. *Ind. Eng. Chem. Res.* **37** (5), 2045–2051.

Xiang, T., K. P. Johnston, W. T. Wofford, and E. F. Gloyna (1996). Spectroscopic measurement of pH in aqueous sulfuric acid and ammonia from sub- to supercritical conditions. *Ind. Eng. Chem. Res.* **35** (12), 4788–4795.

THESIS PROCESSING SLIP

FIXED FIELD: ill. _____ name _____

index _____ biblio _____

▶ COPIES: (Archives) Aero Dewey Eng Hum

Lindgren Music Rotch (Science)

TITLE VARIES: ▶☐ _____

_____

_____

NAME VARIES: ▶☐ _____

_____

IMPRINT: (COPYRIGHT) _____

_____

▶ COLLATION: 207 l

_____

▶ ADD: DEGREE: _____ ▶ DEPT.: _____

SUPERVISORS: _____

_____

_____ _____

_____ _____

_____ _____

_____ _____

_____ _____

_____ _____

_____ _____

NOTES:

_____ cat'r: _____ date:

page: F 47

▶ DEPT: _____

▶ YEAR: 2000 ▶ DEGREE: _____

▶ NAME: _____

_____